PHD

Synthesis and Characterisation of Metal-Organic Frameworks

Sebestyen, Vio

Award date:
2015

Awarding institution:
University of Bath

Synthesis and Characterisation of Metal-Organic Frameworks

Viorica Marinela Sebestyen

A thesis submitted for the degree of Doctor of Philosophy

University of Bath

Department of Chemistry

December 2015

For Andreas Sebestyen, Marius Andrei Sebestyen and Violica Pop.

Table of Contents:

Acknowledgements

I am deeply thankful to my supervisor Dr. Andrew Burrows, for giving me the opportunity to work in his group, stimulating suggestions and encouragement throughout the course of my PhD.

I am grateful to have had the opportunity to get the best expertise in crystallography from Dr. Mary Mahon and Dr. G. Kociok-Köhn, University of Bath.

I would also like to thank to my colleagues Dr. Luke Keenan, Dr. Laura Fisher and Dr. Anna Warren for their enlightening discussions. Thanks go to our collaborators Prof. Tina Düren and Dr. Peyman Z. Moghadam from Institute for Materials and Processes, School of Engineering, The University of Edinburgh and to Dr. Sean Bew, Dominika Bachera and Dr. Sean Thurston from University of East Anglia.

I am beyond grateful to my husband Andrei Marius Sebestyen for selflessly helping me during my PhD and his encouragements. I also would like to thank our one year old now son Andreas who empowered me to cross the finish line.

„Mulțumesc frumos mamă!"

Last but not least the EPSRC are gratefully acknowledged for financial support of this project.

Declaration of work done in conjunction with others

The synthesis of ligand **L1** was carried out as part of this project by Dominika Bachera from University of East Anglia during her PhD under supervision of Dr. Sean Bew. Also parts of H_2caldc synthesis was carried as part of this project at the University of East Anglia in collaboration with Dr. Sean Thurston during his PhD with others from Dr. Sean Bew's group.

The computational studies for the MOFs with calix[4]arene dicarboxylic acid have been carried out by Dr. Peyman Zoroufchian Moghadam during his PhD under supervision of Prof. Tina Düren at the Institute for Materials and Processes, School of Engineering, University of Edinburgh.

Magnetic measurements presented in Chapter 5 were carried out by Dr. Yanhua Lan working in the group of Prof. Annie Powell from Institut für Anorganische Chemie der Universität Karlsruhe, Karlsruhe Institute of Technology, Germany.

Abstract

The **first chapter** of this thesis includes a brief introduction to metal organic frameworks (MOFs) and the aims of this thesis.

The use of two dipyridyl-type linkers depicted in Figure 1 in combination with various benzene dicarboxylate linkers for the synthesis of mixed-linker MOFs is investigated in **chapter 2**.

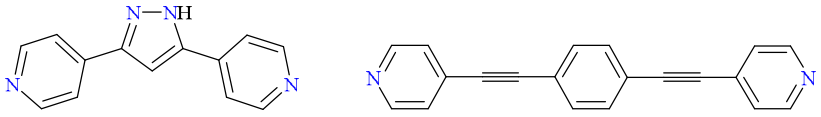

3,5-bis(4-pyridyl)-1*H*-pyrazole

HL

1,4-bis(4'-pyridylethynyl)benzene

L1

Figure 1. The functionalised dipyridyl linkers used in this work.

In **chapter 3** six new compounds containing caldc ligand (25,26,27,28-tetrapropoxycalix[4]arene-5,17-dicarboxylate) were synthesised and characterised. Adsorption of methane, hydrogen, and their equimolar mixtures were studied by molecular simulations by our collaborators from University of Edinburgh.

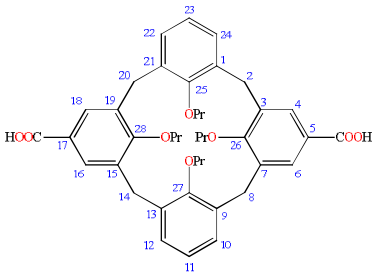

Figure 2. Representation of H_2caldc showing the numbering of carbon atoms (Pr = n-propyl).

In **chapter 4** a new molybdenum diphosphonate network structure has been prepared and structurally characterised. It shows reversible dehydration, which occurs with a structural change. The dehydrated material is able to adsorb methanol but not ethanol.

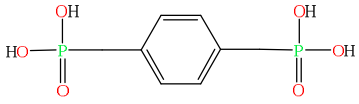

Figure 3. para-Xylylenediphosphonic acid (H_4xdp).

The synthesis, structures, and magnetic properties of three new anionic copper(II) sulfate aggregates and chains linked into 2-D and 3-D networks involving the dimethylammonium cations ($NMe_2H_2^+$) are reported in **chapter 5**.

Dissemination

The work presented in this thesis has been disseminated as follows:

1) Participation at the 1st International Conference on Metal-Organic Frameworks and Open Framework Compounds (MOF08), 8th-10th October 2008, Augsburg, Germany.

2) Viorica M. Pop and Andrew D. Burrows, *Microwave-assisted synthesis of metal-organic frameworks*, 2nd Year Postgraduate Student Talks, Dept. of Chemistry, University of Bath, 16th December 2008, Bath, UK-oral presentation.

3) Viorica M. Pop and Andrew D. Burrows, *Microwave-assisted synthesis of metal-organic frameworks*, Final Year Postgraduate Student Symposium, 13th May 2009, Dept. of Chemistry, University of Bath, Bath, UK- poster presentation.

4) Viorica M. Pop, Andrew D. Burrows and Mary F. Mahon, *Metal-Organic Frameworks Containing the 3,5-Di(4-Pyridyl)-1H-Pyrazole Linker*, Royal Society of Chemistry Coordination Chemistry Interest Group, 1st-2nd July 2010, University of Bath, Bath, UK - poster presentation.

5) Viorica M. Pop, Andrew D. Burrows, Mary F. Mahon, Sean P. Bew and Sean Thurston, *MOFs using calix[4]arene carboxylate linkers*, 2nd International Conference on Metal-Organic Frameworks and Open Framework Compounds (MOF10), 5th-8th September 2010, Marseille, France - poster presentation.

6) Viorica M. Pop and Andrew D. Burrows, *Functionalized metal-organic frameworks*, Final Year Postgraduate Student Symposium, 23rd-24th May 2011, Dept. of Chemistry, University of Bath, Bath, UK - oral presentation.

7) Andrew D. Burrows, David J. Kelly, M. Infas Haja Mohideen, Mary F. Mahon, Viorica M. Pop and Christopher Richardson, *Competition between coordination and hydrogen bonding in networks constructed using dipyridyl-1H-pyrazole ligands*, CrystEngComm, 2011, 13, 1676-1682.

8) Ayi A. Ayi, Andrew D. Burrows, Mary F. Mahon and Viorica M. Pop, *Sodium trihydrogen-1,4-benzenediphosphonate: An extended coordination network*, J. Chem. Crystallogr., 2011, 41, 1165-1168.

9) Sean P. Bew, Andrew D. Burrows, Tina Düren, Mary F. Mahon, Peyman Z. Moghadam, Viorica M. Sebestyen and Sean Thurston, *Calix[4]arene-based metal–organic frameworks: towards hierarchically porous materials*, Chem. Commun., 2012, 48, 4824–4826.

10) Andrew D. Burrows, Mary F. Mahon, Viorica M. Sebestyen, Yanhua Lan and Annie K. Powell, Synthesis, structures, and magnetic behavior of new anionic copper(II) sulfate aggregates and chains, Inorg. Chem., 2012, 51, 10983−10989

11) Ayi A. Ayi, Andrew D. Burrows, Mary F. Mahon and Viorica M. Sebestyen, A molybdenum diphosphonate network structure exhibiting reversible dehydration and selective uptake of methanol, CrystEngComm, 2013, 15, 9301–9303.

Abbreviations

The abbreviations used in this thesis are:

MOF	Metal-organic framework
ZIF	Zeolitic imidazolate framework
IRMOF	Isoreticular metal-organic framework
SBU	Secondary building unit
TGA	Thermogravimetric analysis
PXRD	Powder X-ray diffraction
BET	Brunauer, Emmett and Teller
DOE	Department of Energy
CCD	Charge-coupled device
CSD	Cambridge Structural Database
ICSD	Inorganic Chemistry Structural Database
DMF	*N*,*N*'-dimethylformamide
DEF	*N*,*N*'-diethylformamide
DMSO	dimethylsulfoxide
DCM	dichloromethane
4,4'-bipy	4,4'-bipyridine
H_3btc	1,3,5-benzenetricarboxylic acid
H_3btt	1,3,5-benzenetristetrazol-5-yl
H_3btb	1,3,5-benzenetribenzoic acid
H_4btec	1,2,4,5-benzenetetracarboxylic acid
1,4-H_2bdc	1,4-benzenedicarboxylic acid (terephthalic acid)
1,4-H_2bdc-NH_2	2-amino-1,4-benzenedicarboxylic acid (2-aminoterephthalic acid)
1,4- H_2bdc- Br	2-bromo-1,4- benzenedicarboxylic acid (2-bromoterephthalic acid)
1,4-H_2bdc-I	2-iodo-1,4-benzenedicarboxylic acid (2-iodoterephthalic acid)
1,3-H_2bdc	1,3-benzenedicarboxylic acid (isophthalic acid)
1,3-H_2bdc-Me	5-methyl-1,3-benzenedicarboxylic acid (5-methylisophthalic acid)
H_2bpdc	4,4'-biphenyldicarboxylic acid
1,4-H_2ndc	1,4-naphthalenedicarboxylic acid
2,6-H_2ndc	2,6-naphthalenedicarboxylic acid

dabco	1,4-diazabicyclo[2.2.2]octane
OAc	acetate
en	ethylenediamine
PTSA	p-toluene sulfonic acid
HL	3,5-bis(4-pyridyl)-1*H*-pyrazole
L1	1,4-bis(4'-pyridylethynyl)benzene
KOtBu	potassium tert-butoxide
H_2caldc	25,26,27,28-tetrapropoxycalix[4]arene-5,17-dicarboxylic acid

Chapter 1. Introduction

1.1. Definition of a MOF

Metal-organic frameworks (MOFs) have recently emerged as an important family of porous materials due to their unique structural and functional properties.[1-8] MOFs can exhibit nano-sized cavities and/or open channels. Among the numerous attractive features of MOFs are their well-characterized crystalline architectures and record-high surface areas.

MOFs are a new class of crystalline solids that are currently attracting considerable interest because of their potential for porosity, which has implications for applications such as gas storage, catalysis, and drug delivery. Compared to conventionally used microporous inorganic materials such as zeolites, MOFs have the potential for more flexible rational design, through control of the architecture and functionalization of the pores.

MOFs have structures that are based on a scaffold-like network of corner units and linkers[2, 4] as illustrated schematically in Figure 1-1. The corners are generally metal ions or metal clusters, and the linkers are organic molecules or ions able to bridge between metal centres.

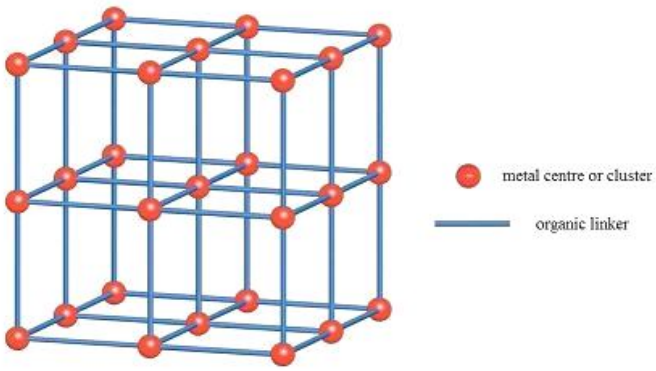

Figure 1-1 Schematic representation of a MOF.

In 1965, roughly three decades before the commonly assumed birth year of MOFs, Tomic mentioned materials which would nowadays be called MOFs, metal–organic polymers or supramolecular structures.[9] Bi- and trivalent aromatic carboxylic acids were used to form

frameworks with zinc, nickel, iron, aluminium, thorium and uranium. Some interesting features of MOFs, like high thermal stability and high metal content were already reported. Also in 1965, Biondi *et al.* reported on Cu(II) tricyanomethanide being a crystalline, polymeric compound.[10] In 1990, Hoskins and Robson reported on, the design of scaffold-like materials using Cu(I) centres and tetracyanotetraphenylmethane.[1]

The group of Yaghi published in 1999[11] the structure of the archetypal MOF-5, with formula $Zn_4O(1,4\text{-bdc})_3$. In MOF-5, Zn_4O cationic units are linked by the 1,4-benzenedicarboxylate (1,4-bdc) anions to form the cubic neutral framework shown in Figure 1-2. The zinc carboxylate unit has the formula $Zn_4O(CO_2)_6$, and the six carboxylate carbons are at the vertices of a regular octahedron.

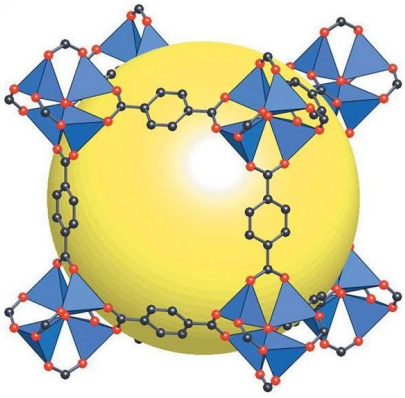

Figure 1-2. The MOF-5 structure shown as ZnO_4 tetrahedra (blue polyhedra) joined by benzene dicarboxylate linkers (O = red and C = black) to give an extended 3-D cubic framework with 12 Å pore (yellow sphere) diameter. (The yellow sphere represents the largest sphere that can occupy the pores without coming within the van der Waals size of the framework).[3]

The number of papers which feature the term MOF has increased dramatically over the last decade. However, there is some debate over the meaning of the term MOF but in general two main ideas can be distinguished. Some scientists as Férey[8] apply the term coordination polymer to MOFs and others as Yaghi and O'Keeffe[12] define MOFs as materials built by linking polyatomic clusters entirely by strong covalent bonds and thus not including coordination polymers, which have some generally weaker bonds and lower stability. Robson argued that the distinction between MOFs and coordination polymers is unnecessary.[13] A number of other names are also in usage for MOFs such as metal-

organic materials (MOMs) by Perry[14], porous coordination polymers (PCPs) by Kitagawa[6], porous coordination networks (PCNs) by Ma[15], hybrid organic–inorganic materials or organic zeolite analogues.[8] Today, many of the boundaries between supramolecular chemistry, inorganic chemistry and MOFs chemistry have become increasingly more difficult to distinguish.

The term MOF is used throughout this thesis to describe any extended structure based on metals and organic bridging ligands.

Scheme 1-1 illustrates some of the simplest architectures that can be generated by using commonly available metal moieties and linking them with spacer ligands.

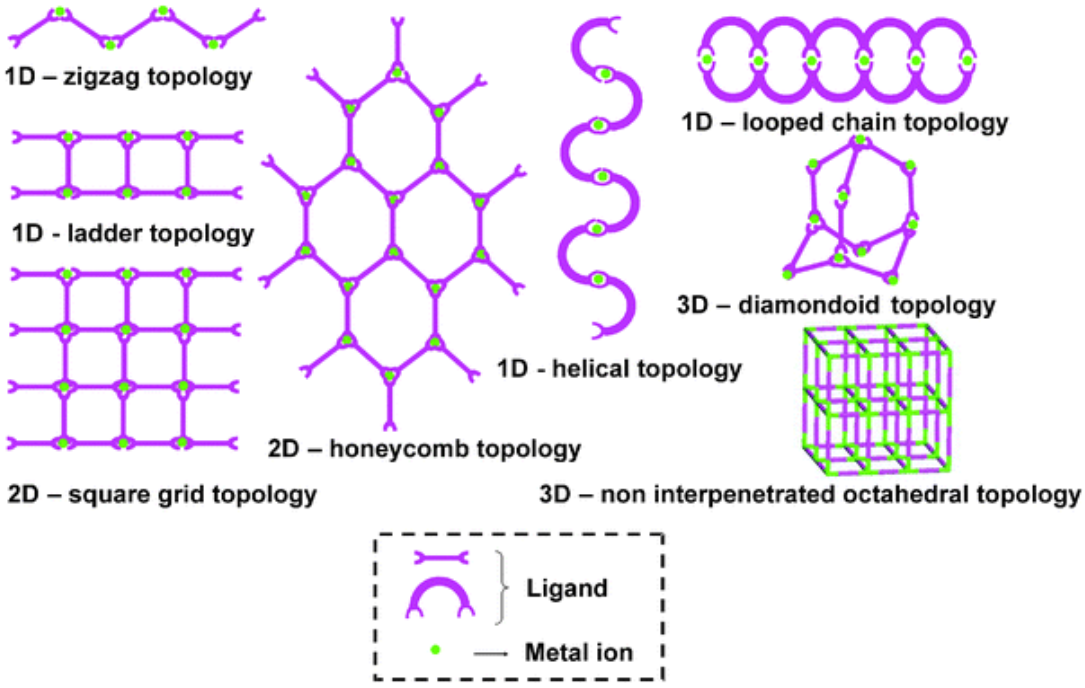

Scheme 1-1. Various topological networks observed in MOFs.[16]

Since the earliest days of crystallography, crystal structures have been described in terms of nets in which atoms are the vertices and the bonds are the links (edges) between them. Considerable effort, most notably by A. F. Wells,[17] has been devoted to describing the structures of such nets. MOFs can be represented as a special kind of graph called a periodic net where polyatomic groups act as the vertices and edges of the net. Yaghi *et al.*[18] have developed a system of nomenclature for common nets and some of their

properties are conveniently accessed through a web-based database known at the Reticular Chemistry Structure Resource (RCSR).

Among all the MOFs, charge-neutral MOFs usually attract the most attention but, recently, it was demonstrated that some ionic species could significantly enhance the framework affinity towards gas molecules, particularly H_2, due to stronger interactions between the charges and the induced dipoles, therefore charged MOFs, could also be valuable synthetic targets. Fedin believes that the addition of soluble ionic salts to the reaction medium might promotes the formation of charged MOFs.[19] His group reported two 3-D anionic framework structures built from zinc(II) carboxylate layers linked by carboxylate anions. These were synthesized by heating a DMF solution of $Zn(NO_3)_2 \cdot 6H_2O$, $[NH_2(CH_3)_2]Cl$ and organic carboxylic acids.

1.2. Terms used in MOF chemistry

1.2.1. Secondary building unit (SBU)

In order to aid the process of structure prediction, the concept of secondary building units (SBUs) as structural entities was adopted in MOF chemistry from zeolite chemistry. SBUs are simple geometric figures representing the inorganic clusters or coordination spheres (known as primary building units) that are linked together by the organic components to form a framework.

Examples of some SBUs that are commonly encountered in metal carboxylate MOFs are illustrated in Figure 1-3: a) the triangle, b) the square paddle-wheel, c) the tetrahedron, d) the octahedral zinc acetate cluster and e) the trigonal prismatic oxo-centred trimer. The SBUs are connected into MOFs by linking the carboxylate carbons with organic units, but may also be linked by replacement of terminal ligands.

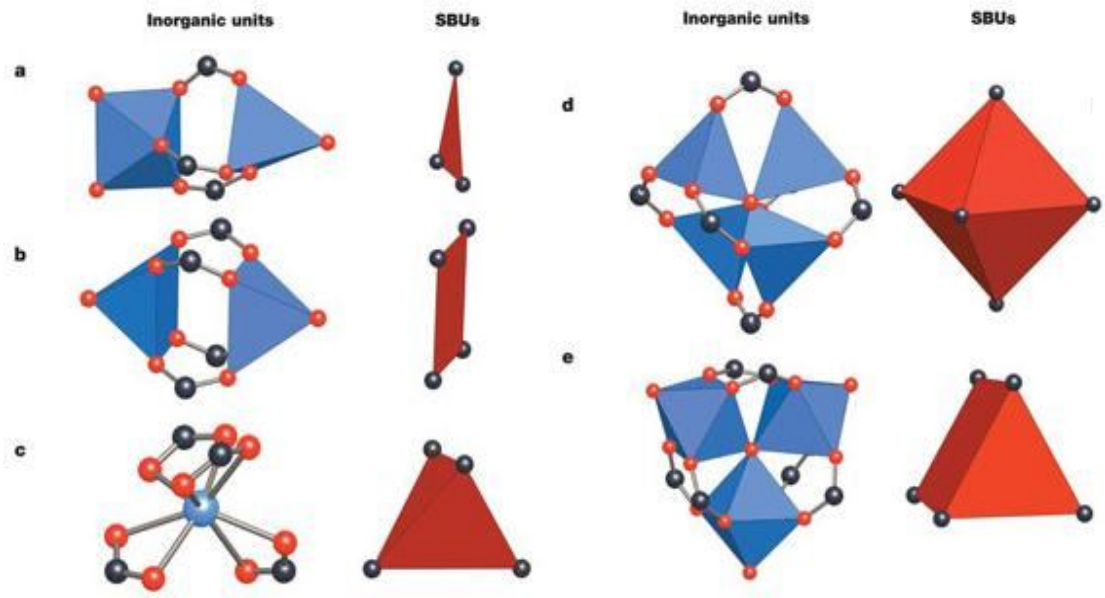

Figure 1-3. Examples of SBUs from carboxylate MOFs. O = red; C = black. In inorganic units metal-oxygen polyhedra are shown blue, and the polygon or polyhedron defined by carboxylate carbon atoms (SBUs) are red [3]

Chui *et al.*[20] reported $Cu_3(btc)_2(H_2O)_3$ (btc = 1,3,5-benzenetricarboxylate) (known as HKUST-1[20] or MOF-199[21]). The SBU in HKUST-1 is a paddle-wheel unit (Figure 1-4) with Cu_2 dimers at its six vertices and four btc ions tetrahedrally disposed as panels for four of the eight triangular faces of an octahedron.

These SBUs are connected with other units through corner sharing of a octahedra forming the HKUST-1 framework (Figure 1-4).

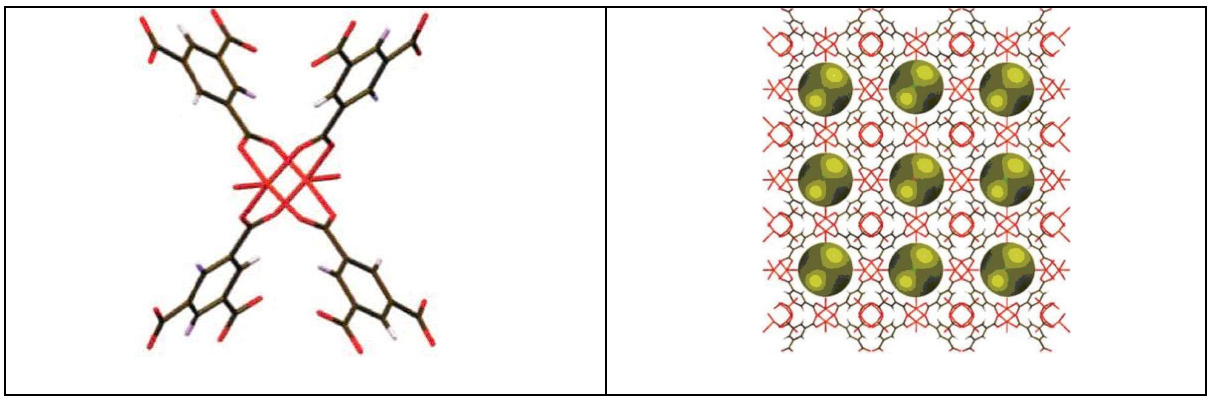

Figure 1-4. HKUST-1: Left: Paddle-wheel Cu (II) tetracarboxylate building block for HKUST-1 framework showing nanochannels. The empty space is represented as yellow spheres. (Cu = orange; O = red; C = brown; H = white).

This polymer forms face-centred-cubic crystals that contain a 3-D system of large square-shaped pores (9Å × 9Å). The main pores contain up to 10 additional water molecules per formula unit. The material has a reasonable degree of thermal stability (up to 240°C) and a capacity for chemical functionalization of the channel. Terminal water ligands, bound to the copper ions, are directed towards the interior of these pores. Removal of the three copper-bound water molecules allows access to the Lewis acidic copper sites and the catalytic properties of HKUST-1 have been explored.

The $Cr_3F(H_2O)_2O(1,4\text{-bdc})_3$ material, designated as MIL-101 as illustrated in Figure 1-5, is constructed from the corner-sharing of tetrahedral SBUs, which consist of chromium trimers and 1,4-bdc anions. Its structure exhibits several unusual features: a large free aperture (12 Å for pentagonal windows and 16 Å × 14.5 Å for hexagonal windows), mesoporous cages (29 Å and 34 Å), and a very high nitrogen sorption capacity ($S_{Langmuir}$ ~ 5900 m^2/g).[22, 23]

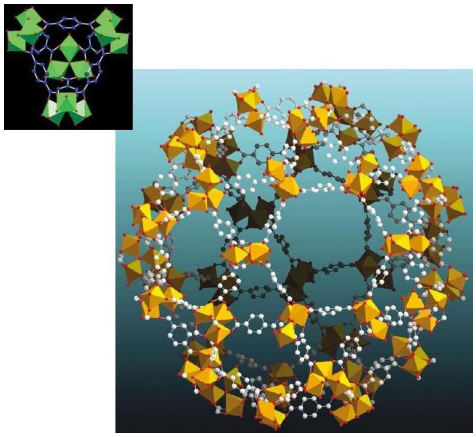

Figure 1-5. Structure of MIL-101 showing: (left) SBU [22] and (right) fragment of the giant pore. Cr = orange polyhedron; C = white; O = red. Hydrogen atoms are omitted for clarity[24]

1.2.2. Isoreticular MOFs

Yaghi and coworkers[3] relate the term reticular synthesis to the conceptual approach by which a MOF is designed and assembled and is based upon identification of how building blocks come together to form a net. The reticular synthesis approach have been applied in 2002 by Yaghi *et al.* to prepare the first [25] isoreticular series of MOFs (IRMOFs) in which octahedral-shaped metal-containing ("inorganic") SBUs were joined with a variety of linear ditopic carboxylate linkers to form 16 distinct MOFs which shares the same cubic topology as MOF-5 (Figure 1-6). These 16 IRMOFs were formulated as $Zn_4O(link)_3(DEF)_x$. The links differ both in functionality of the pendant groups (IRMOF-1 to IRMOF-7) and in length (IRMOF-8 to IRMOF-16). While expansion of the links increases the internal void space (represented by yellow spheres in Figure 1-6), it also allows the formation of catenated phases (IRMOF-9, IRMOF-11, IRMOF-13 and IRMOF-15). MOF-5 was used to demonstrate that its 3-D porous framework can be functionalized with the organic groups -Br, $-NH_2$, $-OC_3H_7$, $-OC_5H_{11}$, $-C_2H_4$, and $-C_4H_4$ and that its pore size can be expanded with the long linkers biphenyl, tetrahydropyrene, pyrene, and terphenyl.

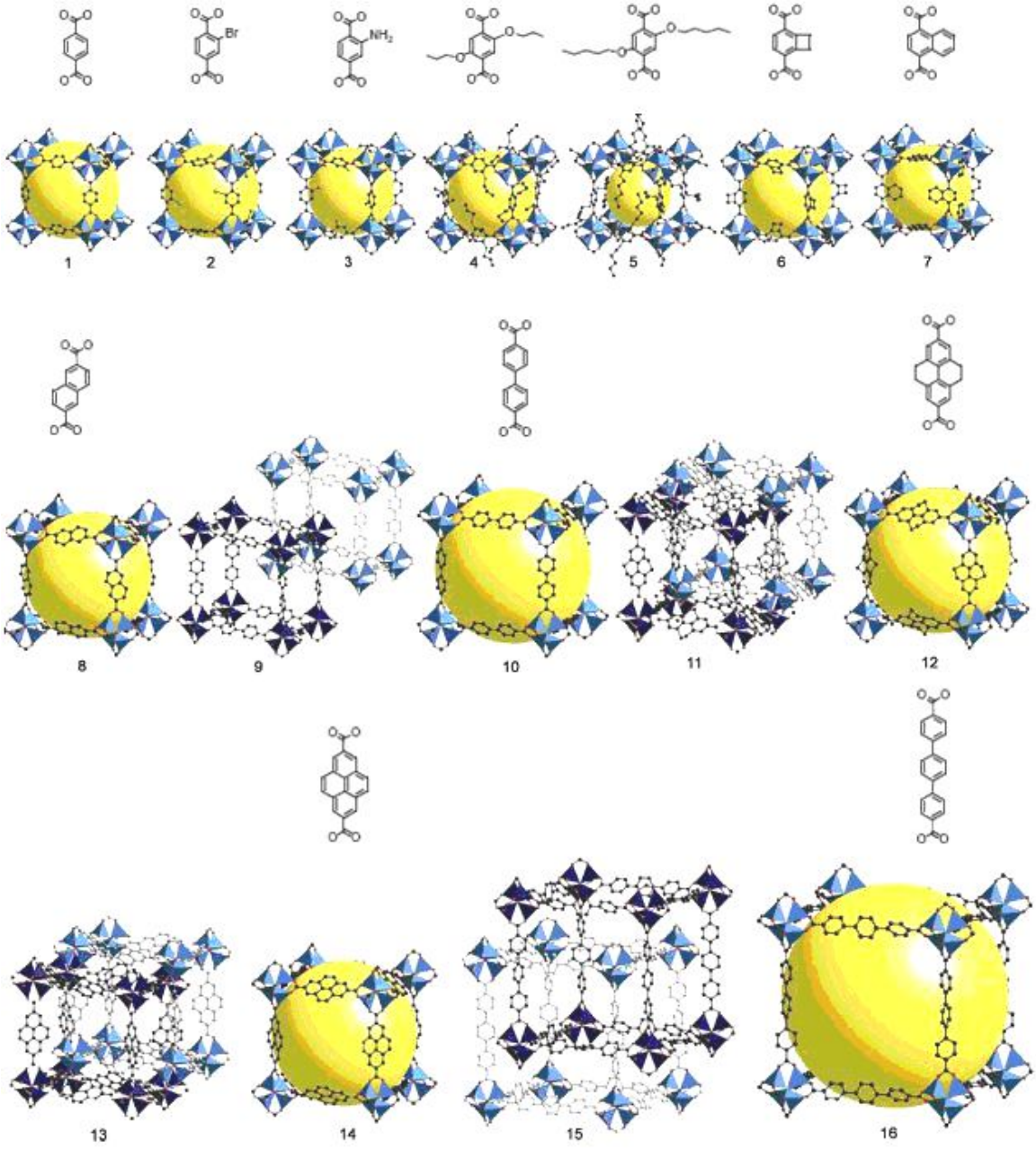

Figure 1-6. Organic linkers (top) and IRMOF series (bottom). The internal void space is represented by yellow spheres.[26]

Several examples of isorecticular series have now been reported [27, 28] The concept and occurrence of isoreticular series of MOFs is reviewed by Yaghi *et al.* [28] for various tritopic carboxylates and Cu_2 paddlewheel units as depicted in Figure 1-7. Expansion from btc^{3-} (1,3,5-benzenetricarboxylate) to bbc^{3-} (4,4',4''-benzene-1,3,5-tryil-tribenzoate) led to enlargement of unit cell length from 26.34Å in HKUST-1 (MOF-199) to 68.31 Å in MOF-399, which corresponds to a volume expansion by a factor of 17. Accordingly, MOF-399

had the highest porosity (94 %) and lowest density (0.126 $g \cdot cm^{-3}$) of any recorded MOF when reported in 2011. They consider that "the isoreticular expansion is one of the promising approaches to achieve the high surface area materials".

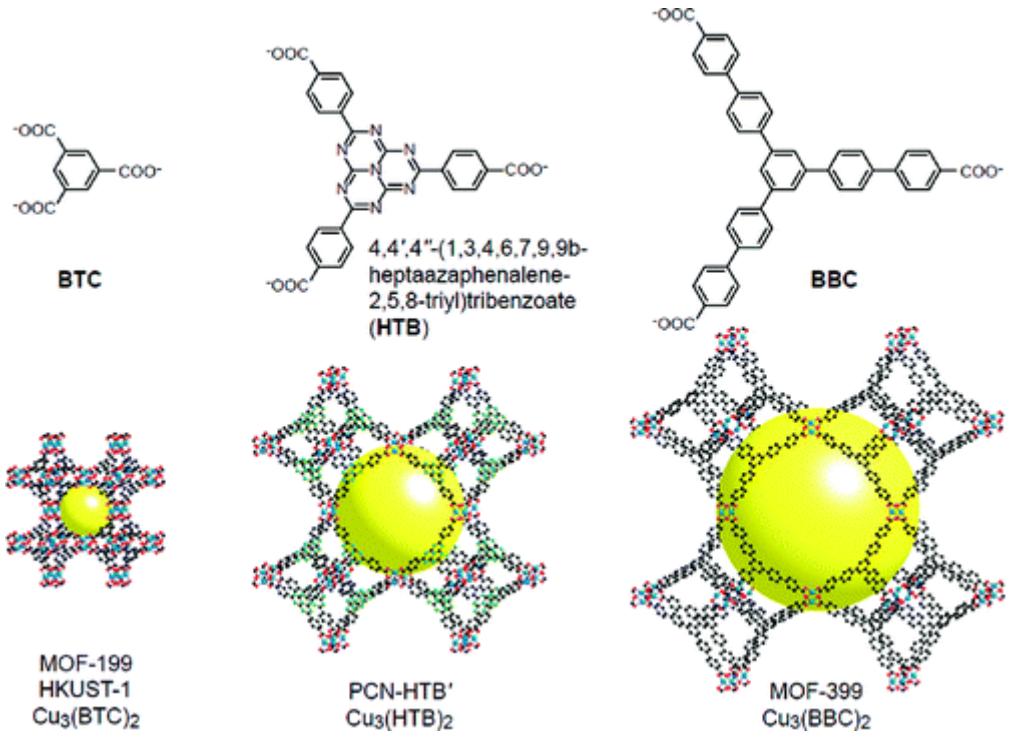

Figure 1-7. Organic linkers (top) and structures of MOF-199, PCN-HTB', and MOF-399 (bottom). The internal void space is represented by yellow spheres. Cu, blue; C, black; O, red; and N, green. Hydrogen atoms are omitted for clarity. [28]

1.2.3. Interpenetration

The phenomenon where two or more identical frameworks are intergrown at the expense of pore volume is called catenation (sometimes refered as interlocking) and this may take the form of interpenetration[29] (where the networks are maximally displaced from each other) or interweaving[30] (where they are minimally displaced).

Interpenetration is defined as occurring when two or more networks are not chemically bound to each other but cannot be separated without the breaking of bonds.[29]

Among other entangled systems, the phenomenon of self catenation (also known as self-penetration, self-entanglement, and polyknotting) is rare and unpredicted. The term of self

catenation proposed by Proserpio describes a special single network in which the smallest topological rings are penetrated by the rods belonging to the same net.
The extended 3-D framework of crystalline MOF-9, $Tb_2(1,4\text{-bdc})_3(DMSO)_4$ illustrates another aspect of SBUs: namely, their ability to support the existence of large free volume in interpenetrating structures, which are often assumed to form assemblies containing very little or no free volume.[31]

There are few advantages resulting from interpenetration. The size of a pore is found to be critical to the adsorption affinity for light gases. Within a certain range, a slight variation in pore size can cause a dramatic change in the adsorption affinity for an adsorbate. It has been reported that at low pressures, CO_2 uptake in a MOF correlates with the heat of adsorption, an index of adsorption affinity which depends on the size of a pore. The interpenetration or catenation of two or more frameworks has traditionally been considered as an obstacle to producing highly porous frameworks due to the resultant reduction of pore volume. However, the catenation of two or more frameworks with minimal displacement was found to possibly prevent some MOFs from collapse. Recently, it has been reported that interpenetration and catenation is an effective way to reduce the pore dimensions of IRMOFs as shown in Figure 1-6. The catenated IRMOFs such as IRMOF-9, IRMOF-11, and IRMOF-13 have larger CO_2 over CH_4 selectivity compared with their noninterpenetrated counterparts. Keskin and Sholl[32] also found similar results. The enhanced CO2 selectivity is considered as a result of additional small pores and adsorption sites formed by the interpenetration of framework. Cheon prepared a doubly interpenetrated Mg-based porous MOF with 3-D channels. The desolvated solid SNU-25 exhibits high thermal stability and can selectively adsorb CO_2 over CH_4 at various temperatures. Kim reported that they can synthesize either a catenated (CuTATB-60) or a non-catenated (CuTATB-30) MOF through a sonochemical route by adjusting the ultrasonic power levels. Catenation in CuTATB-60 led to both higher surface area and enhanced stability of the network than the non-catenated counterpart, CuTATB-30. Moreover, the CuTATB-60 showed higher CO_2 adsorption capacity (189 mg g-1) than the CuTATB-30 and has an excellent selectivity over N_2 (larger than 20 : 1) as well. Zhang *et al.*[33] synthesized a pillared MOF in both interpenetrated and non-interpenetrated forms and they found that high temperature and reagent concentration favored an interpenetrated crystal form.

There is a belief in MOF chemistry that non-interpenetrating networks can sustain porosity while interpenetration occurs as a natural consequence to avoid the presence of empty space.[30, 34] While this may be true in many cases, it cannot be generalized and in 2011 Kitagawa *et al.* [35] reported a series of MOFs that does not conform to the current belief that interpenetration of lattices results in highly compact structures.

1.3. Metal-organic framework Ligands

1.3.1. Carboxylate Ligands

The vast majority of MOFs are constructed from multitopic ligands bearing the carboxylate functionality. Most of these carboxylate-based ligands are either commercially available, such as 1,4-bdc and 1,3,5-benzenetricarboxylate (btc), or easily accessible through well-defined and high yielding synthetic pathways.

Carboxylic acids are also attractive as framework-forming reagents because their high acidity (pKa ~ 4) allows facile *in situ* deprotonation. In the same way, the metal–carboxylate bond formation is reversible under relatively mild conditions, which presumably facilitates the formation of well-ordered, crystalline MOFs. Being negatively charged, carboxylates are countered by the positive charge of the metal centre once coordinated in a framework structure. When this occurs, it eliminates the need for counter ions to be present in the structural pores. While accessibility and favourable thermodynamics make carboxylic acids the most popular ligand choice, it was perhaps the extensive literature on molecular metal–carboxylate systems that inspired initial work made by Yaghi and co-workers with these ligands.

The carboxylate groups have been shown to coordinate in a variety of manners. Figure 1-8 shows some of the possible binding modes of 1,4-bdc linker. It can binds through either one of the oxygen atoms or through both.

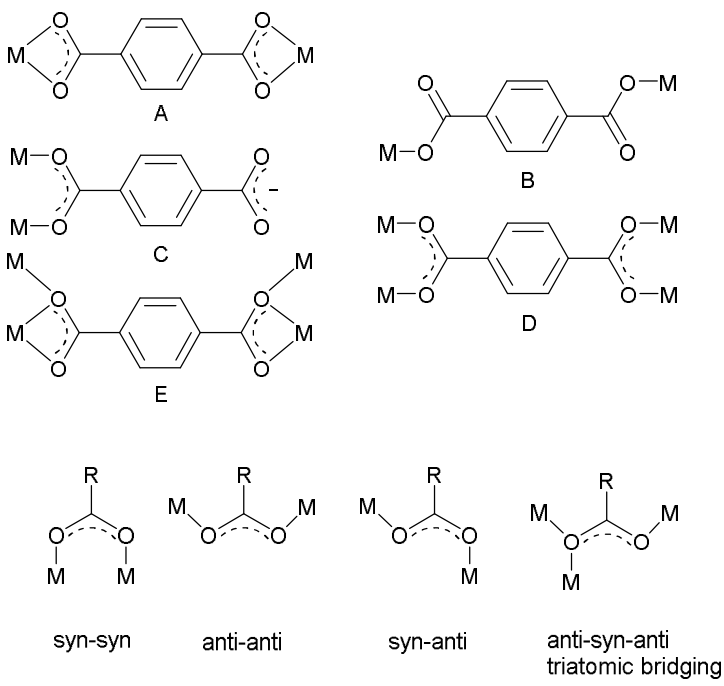

Figure 1-8. The coordination modes of 1,4-bdc: (A) chelating bis-bidentate, (B) bis-monodentate, (C) mono-syn-syn bridging/bidentate, (D) syn-syn bridging bis-bidentate, (E) chelating/bridging bis-bidentate.[36]

When the linking units are changed from dicarboxylates to tricarboxylates, the topology of the ligand is changed from a two-point-linker to a three-point-linker, therefore, different networks will be formed. Figure 1-9 shows possible binding modes of the btc linker[36].

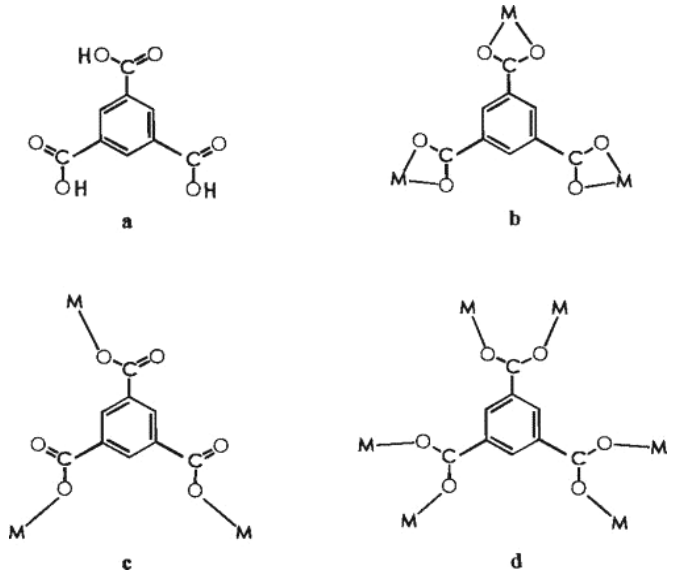

Figure 1-9. a) H_3btc and b-d) examples of multidentate coordination modes of btc.[37]

1.3.2. Nitrogen Donor Ligands

Ligands containing nitrogen, such as pyridine based liagnds, have been shown to produce stable network systems, whilst ligands containing primary amines produce less stable frameworks. Primary amines have poorer donor ability towards metal centres when forming coordination polymers. However, there are also problems associated with the metal-N bond formation with the pyridine ligands, as this bond is relatively labile, depending on the metals used. Hence rearrangement of the networks can occur, giving unexpected frameworks and this can lead to supramolecular isomerism.[38]

Unlike carboxylates, most pyridyl ligands are neutral, and once reacted with a cationic metal centre the network produced will retain a charge that must be balanced by counter ions, which occupy the pores of the network. This can be a disadvantage if the material is to be used for gas storage studies.

A lot of research has been conducted with the use of nitrogen containing ligands coordinating to silver(I) centres. Silver(I) ions are readily available and have soft metal centres with a high affinity for relatively soft nitrogen ligands, they are able to form complexes with many different geometries. Coordination numbers for Ag(I) compounds have been characterised between one and six, showing a variety of geometries.[39] Ag(I) exists with full 4d orbitals ($4d^{10}$) and the most common geometry adopted by the silver centre is tetrahedral.

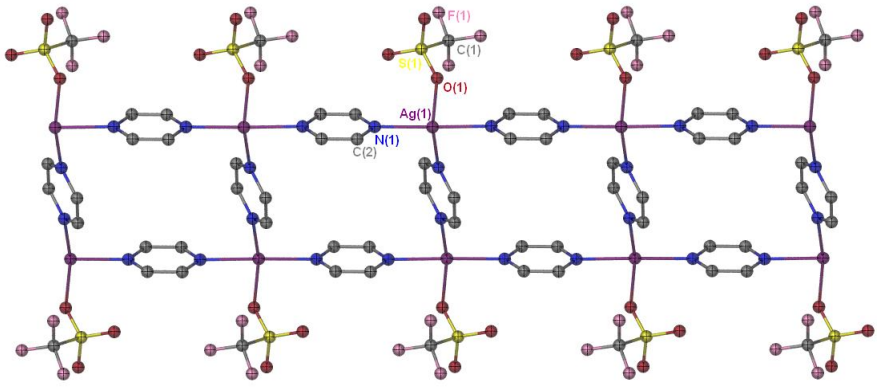

Figure 1-10. Molecular ladder of $\{[Ag_2(pyrz)_3(CF_3SO_3)_2]\}_\infty$ (pyrz = pyrazine)[40]

Figure 1-10 above shows an example of a MOF containing Ag(I) centres and nitrogen ligands, namely the molecular ladder of $\{[Ag_2(pyrz)_3(CF_3SO_3)_2]\}_\infty$ (pyrz = pyrazine). The

structure consists of chains linked by alternating pyrazine ligands and silver(I) ions, with each chain being linked to another by pyrazine, forming the rungs of the ladder. The ladder is sustained by the coordinating $CF_3SO_3^-$ anion, whereas when the reaction is conducted with PF_6^-, a non coordinating anion, only single stranded linear chains are observed.[40]

Zeolitic imidazole frameworks (ZIFs) are MOFs with exceptional chemical and thermal stability, which are largely constructed from tetrahedral zinc or cobalt ions linked to the nitrogen atom of an imidazolate (Im). In the structure of $Zn(MeIm)_2$ (named ZIF-8) (Figure 1-11) each zinc atom is tetrahedral and is bonded to four nitrogen atoms from four different 2-methylimidazolate (MeIm) ligands. Each MeIm ligand bonds through both nitrogen atoms to two different zinc centres. This creates a 3-D structure with a large open pore space within (shown in Figure 1-11 as yellow sphere with ~ 12.5 Å diameter).

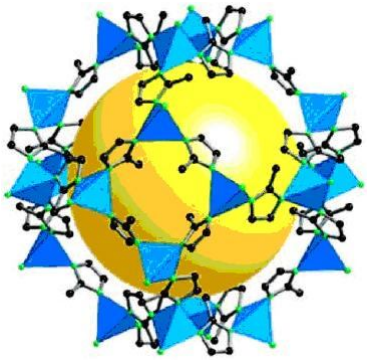

Figure 1-11. Structure of ZIF-8 where the largest cage is shown with ZnN_4 tetrahedra in blue.[41]

1.3.3. Mixed-ligand MOFs

The terminology to describe mixed-ligand MOFs has been different for different researchers. For example, mixed-ligand MOFs have been termed MIXMOFs by Baiker and co-workers,[42] multivariate MOFs (MTV-MOFs) by Yaghi and co-workers[43] and coordination polymers by Matzger and co-workers[44]. Burrows[45] places mixed-ligand MOFs (Figure 1-12) under a new termed class, namely mixed-component MOFs (MC-MOFs), where mixed-metal and core–shell MOFs were also included.

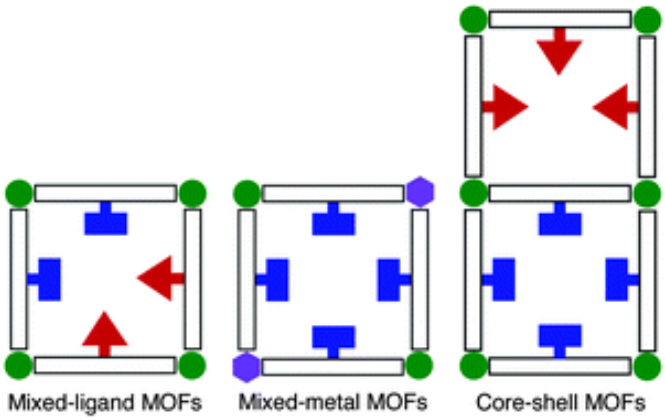

Figure 1-12. The different categories of mixed-component MOFs.[45]

Herein, the focus will be on mixed-ligand MOFs with mixed bridging ligands and the mixed-ligand synthetic strategies for the rational design and construction of this type of networks.

The bipyridine and polycarboxylate ligands represent the most reliable and typical organic connectors in construction of mixed-ligand MOFs. The explanation can be that these linkers have different functionalities and therefore each plays a distinct role into MOF formation. The neutral bipyridine ligands normally bind to the metal ions as the rod-like bidentate struts whilst the polycarboxyl bridging ligands may take the anionic or protonated form to provide various coordination modes upon binding to metals.

In this respect, Kitagawa and co-workers [46, 47] have pioneered the synthesis of mixed-ligand with pillared-layer networks. This strategy has also been applied to design and prepare a series of carboxyl-functionalized porphyrin-based framework materials with diverse bipyridine pillaring linkers, which show emerging applications in gas storage, heterogeneous catalysis, and light harvesting.

Mixed-ligand systems were classified by Due *et al.*[48], into three categories: acid–acid, base–base, and acid–base systems (the concept of acid or base in this review only indicates the Lewis acid/base ligands).

It has been demonstrated that one of the most rational methods in the construction of 3-D porous frameworks is inserting appropriate pillar moieties between the well-defined 2-D

layer compounds (Figure 1-13), which is the so-called ‘‘pillaring’’ strategy.[49] The pillar linkers can be inserted stepwise [50-54] or using a “one-pot” procedure [36, 55-63].

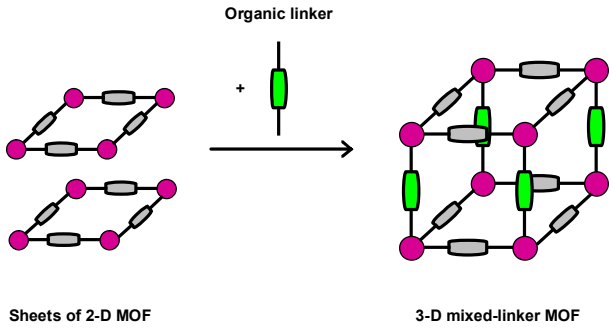

Figure 1-13. Schematic representation of a construction of 3-D porous framework by a pillar insertion strategy. The metal atoms are shown in magenta and the two different linkers are shown as grey and green rectangles.

Stepwise assembly of a MOF from a molecular polyhedron precursor is difficult because the intermediate molecular polyhedra are not always soluble, even if they can be interlinked.

The pillaring methodology has already been successfully used in the syntheses of 3-D porous MOFs [36, 52-55, 58-65]. The prototype of 3-D mixed-linker MOFs is $[Zn_2(1,4\text{-bdc})_2(dabco)]$ [65] where the 2-D square-grid sheets constructed by Zn paddle-wheel units and 1,4-bdc are connected by 1,4-diazabicyclo[2,2,2]octane (dabco) pillar ligands. Mixed-linker MOFs using bipyridyl-type linkers as 4,4’-bipy in combination with dicarboxylate linkers have been reported.[36, 55, 58, 63, 64]

A schematic illustration (Figure 1-14) showing the different cubic frameworks pillared by (a) 4,4’-bipy, (b) 4,4′-bpt, (c) bpb, (d) dfbpb, and as well as their 2-fold interpenetrating arrangements (a–d).

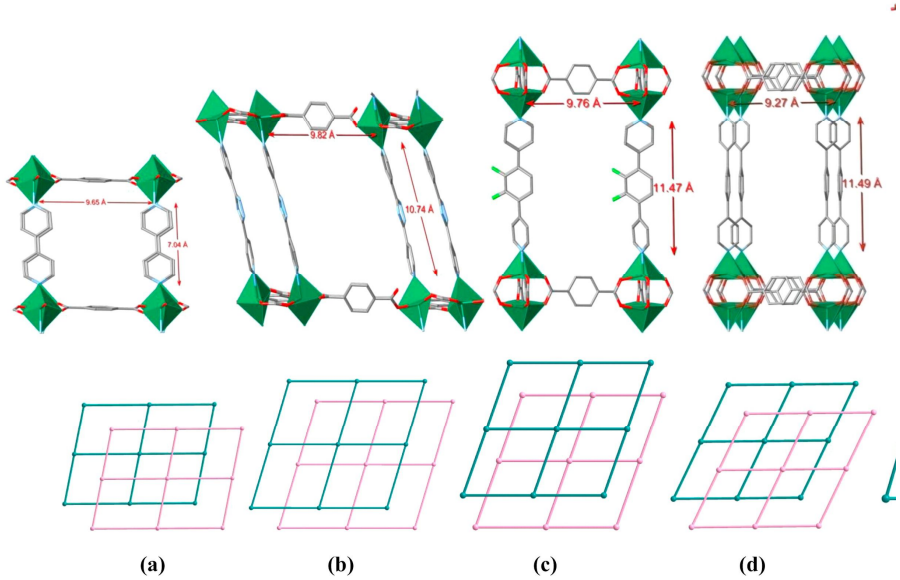

Figure 1-14. Schematic illustration showing the different cubic frameworks pillared by (a) 4,4'-bipy, (b) 4,4'-bpt, (c) bpb, (d) dfbpb, and as well as their 2-fold interpenetrating arrangements (a–d).

Kitagawa *et al.*[64] succeeded in controlling the polymorphism of $[Zn_2(1,4\text{-bdc})_2(4,4'\text{-bipy})]$ by solely adjusting the nucleation process systematically. They obtained $[Zn_2(1,4\text{-bdc})_2(4,4'\text{-bipy})]$ previously reported[58, 63] consisting of 2-D square-grid sheets constructed by zinc paddle-wheel units and 1,4-bdc are connected by bipy pillar ligands (its 2-fold interpenetrated 3-D network being shown on the left in (Figure 1-15) from a mixture of $Zn(NO_3)\cdot 6H_2O$ (0.2mmol), 1,4-H_2bdc (0.2 mmol) and bipy (0.1mmol) in DMF (20 mL) by heating at 120°C for 2 days. In the same work they reported for the first time to get a 3-D non-interpenetrated polymorph structure for $[Zn_2(1,4\text{-bdc})_2(4,4'\text{-bipy})]$ where 2-D Kagomé nets instead as layers are connected by bipy pillar ligands shown on the right in Figure 1-15. This non-interpenetrated 3-D network for $[Zn_2(1,4\text{-bdc})_2(4,4'\text{-bipy})]$ was obtained while cooling over a day at 25 °C after an 1hour heating at 120°C. They showed how the control over the nucleation process determines the framework topology of the MOFs.

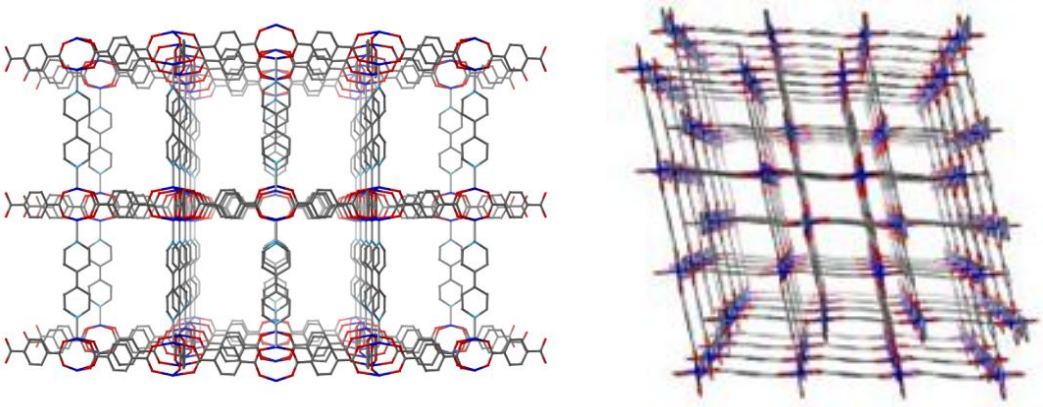

Figure 1-15. Crystal structures of [Zn_2(1,4-bdc)$_2$(4,4'-bipy)] along a axis: (left) 3-D two-fold interpenetrated network and (right) 3-D non-interpenetrated form. Hydrogen atoms and disordered guest molecules are omitted for clarity.[64]

Chen *et al.*[36] reported [Zn(1,4-bdc)(4,4'-bipy)] which have been synthesised by reacting $Zn(NO_3)_2 \cdot 6H_2O$, 1,4-H_2bdc and 4,4'-bipy (1:1:1: ratio) hydrothermally (at 180°C) for seven days, using pyridine as a base. The resulted framework (Figure 1-16) is a 3-D two fold interpenetrated similar with the interpenetrated version of Kitagawa's mentioned earlier with the difference that no paddle-wheel units are present in here. The binuclear units are interconnected through 1,4-bdc ligands and Zn_2 centres to generate a parallelogram-like sheet with dimensions of 10.28 x 10.98 Å, and is linked by the 4,4'-bipy ligands to form an infinite 3-D double interpenetrated framework. The 1,4-bdc ligands adopt two coordination modes in this structure, a chelating/bridging bis-bidentate and a bis-monodentate mode. However, the distance between zinc and uncoordinated oxygen atom of 2.617(2) Å suggests from literature[66, 67] a non-negligible interaction and therefore the bis-monodentate 1,4-bdc ligand can be described adopting a semi-chelating coordination. Hence, the zinc atoms can be also regarded as in a distorted octahedral geometry, than just the distorted trigonal bipyramidal geometry thought in first instance.

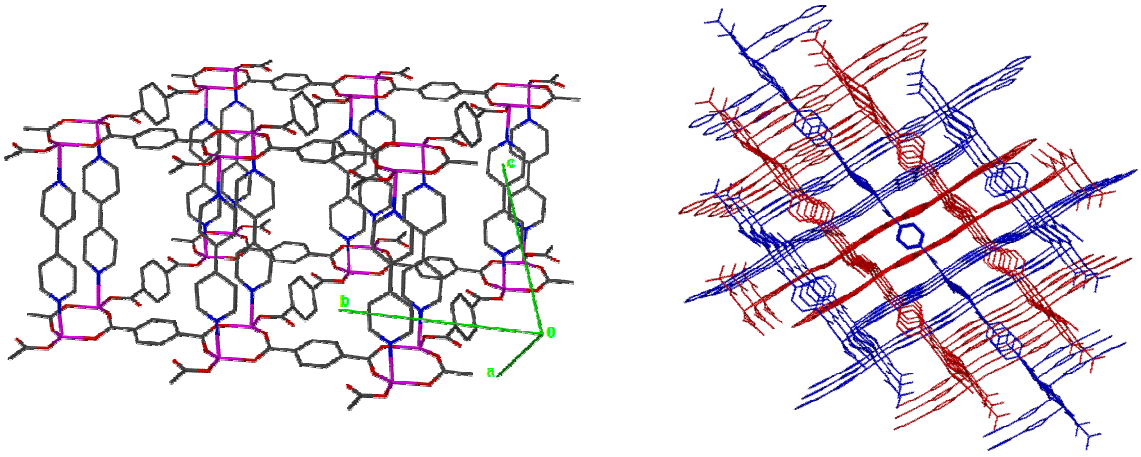

Figure 1-16. The structure of [Zn(1,4-bdc)(4,4'-bipy)] reported by Chen et al.[36] showing the 3-D framework formed of zinc-terephthalate parallelogram-like sheets pillared by 4,4'-bipy ligands (left) where Zn, C, O, N atoms are coloured in magenta, dark grey, red and blue, respectively, and twofold interpenetrated 3-D frameworks in blue and red viewed along b axis (right).

If isophthalic acid (1,3-H_2bdc) is used instead of terephthalic acid (1,4-H_2bdc) a porous MOF of $[Zn_2(1,3\text{-bdc})_2(4,4'\text{-bipy})_2]\cdot$DMF was reported by Kitagawa *et al.*[68]. This MOF was obtained from $Zn(NO_3)_2\cdot 4H_2O$, 1,3-H_2bdc and 4,4'-bipy in a DMF solution heated at 120°C for several days. Each Zn^{2+} ion is in a distorted octahedral geometry, being coordinated by two 4,4'-bipy ligands at the axial positions, two oxygen atoms from the chelate carboxylate end of the 1,3-bdc ligand and two oxygen atoms from the 1,3-bdc in the equatorial plane. The zinc centres and 1,3-bdc give rise to 1-D double-chains (Figure 1-17.a) and the further linkages of these chains via 4,4'-bipy ligands in the axial positions generate an infinite 2-D neutral layer (Figure 1-17.b). Although the distance of 3.8 Å between the planes of the nearest-neighbour 1,3-bdc ligands is too large to form π-stacking interactions, the 2-D layers are mutually interdigitated to create a stable 3-D framework (Figure 1-17.c). This type of packing called interdigitation has been reported in the literature [69-76] and the compounds adopting it can be included into a so called class of coordination polymers with interdigitated structures (CID). Hence, $[Zn_2(1,3\text{-bdc})_2(4,4'\text{-bipy})_2]\cdot$DMF is called CID-1. CID structures have been demonstrated to exhibit a certain degree of flexibility which makes them useful in application as selectivity towards different adsorbents. They have demonstrated that CID-1 adsorbs methanol and ethanol but

not benzene or water, CID-1 being therefore a hydrophobic framework showing size-based selective sorption properties via dynamic structural transformation.

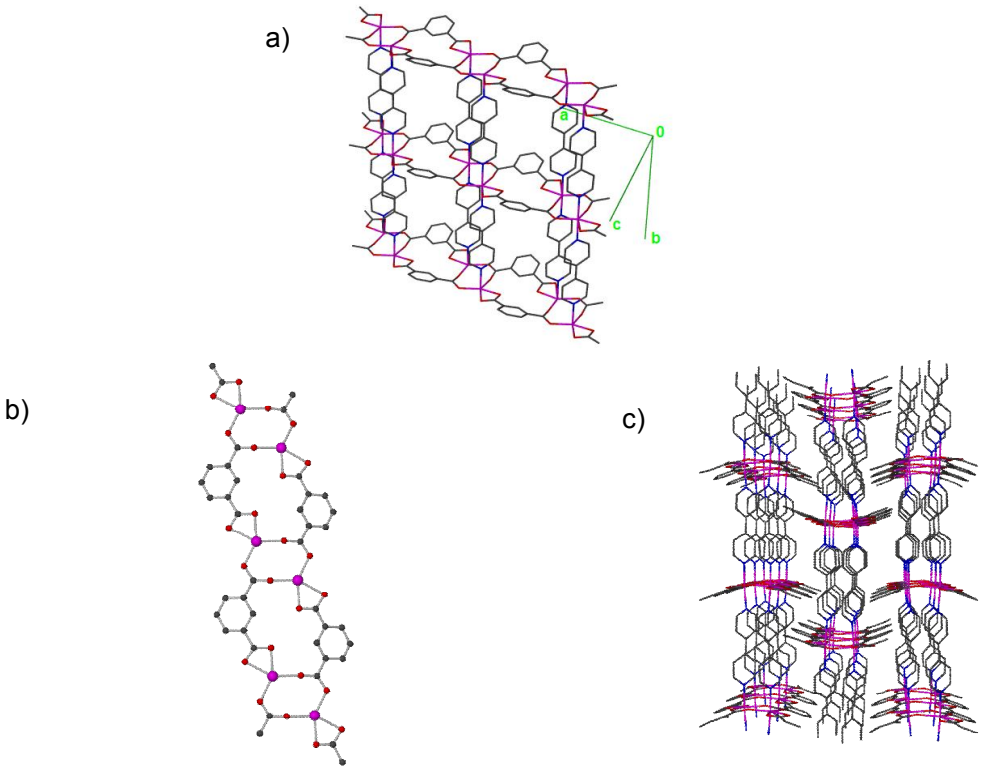

Figure 1-17. a) 2-D layer structure, b) bonding mode in the Zn–O plane along b axis and c) 3-D structure of CID-1 along a axis. Dark grey, blue, red, magenta are C, N, O and Zn, respectively; H atoms are omitted.

Substituted isophthalate ligands as 5-nitroisophthalate (NO_2-1,3-bdc)[72], 5-methoxyisophthalate (MeO-1,3-bdc)[72] and 5-azidoisopthalate (N_3-1,3-bdc)[73] have been used in conjunction with bipy and reported to form similar coordination polymers with interdigitated structures (CID). They all show similar structures to the non-substituted isophthalate detailed above, being named CID-5, CID-6 and CID-N3, respectively. Crystalline solid solutions of the layered phase [Zn(NO_2-1,3-bdc)(4,4'-bipy)]·(0.5DMF·0.5MeOH) with its isostructural MeO-1,3-bdc analog can be tailored in order to change the gate-opening pressure for water adsorption. Additionally, CO_2 absorption selectivity can be increased by adjusting the number of MeO-1,3-bdc ligands in the solid solution. The bare triplet nitrenes from CID-N_3 were shown by Kitagawa *et al.*[73] to be accessible to and reacted with adsorbed oxygen or carbon monoxide molecules,

which showed not only activation of the pore surface, but also a high probability of chemical trapping and conversion of guest molecules by light stimulation on demand.

Another approach is stepwise insertion of new linkers into MOFs. The Kitagawa and Chen groups have inserted bidentate bridging linkers into 2-D MOFs with accessible metal centers, resulting in structural transformations to 3-D MOFs. [50, 51] Zhou reported another structural transformation from a 0-D MOP to a 3-D MOF by insertion of pillaring bipyridyl linkers.[77, 78]

1.4. Porous MOFs

Finally, a note must be made concerning the terminology used to describe porosity, which is often assumed in MOFs. The most common method for examining the stability of a MOF in the absence of its original guests is a powder X-ray diffraction (PXRD) analysis of the bulk material after heating and/or evacuation. This is then correlated with thermogravimetric analysis (TGA), in which framework stability is indicated by the weight loss between the temperatures of guest desorption and framework decomposition. Importantly, neither method of analysis is sufficient on its own to demonstrate that a framework is an open one. In addition, corroborating evidence must be gained in the form of changes in elemental composition (M, C, H, N, etc.), and infrared (IR) and/or nuclear magnetic resonance (NMR) spectra. Aside from these preliminary analyses, the establishment of a material as porous requires studies evidencing the reversible flow of guests into and out of the void volume. A method which proves that the framework exhibits permanent porosity; i.e. stability in the fully evacuated state is the isothermal sorption of gases.

The porosity of MOFs is calculated from the amount of gas adsorbed by the activated MOF. The activation is the process to remove the guest solvent molecules present within the framework when it is first prepared. In order to assess most of the MOF's properties activation is required. Thermogravimetric analysis (TGA) can be used to determine how easily the guest molecules can be removed.

The establishment of porosity in MOFs has been a challenging but central goal during the development of this field since, by analogy with zeolites, it opens up possibilities for new chemical separations, ion exchange, sensing and possibly even catalytic behaviour.

Pores are classified by IUPAC according to their size as shown in Table 1-1. MOFs possess very high pore volume; most of the pores fall within the IUPAC microporous regime, but are few MOFs which pores size exceeds 20 Å falling therefore in the IUPAC mesoporous region.

Table 1-1. Classification of pores.

Pore type	Pore size (Å)
Ultramicropore	< 5
Micropore	5-20
Mesopore	20-500
Macropore	> 500

There are two ways in which gas molecules can be adsorbed onto a surface, physisorption and chemisorption. The latter involves the formation of a chemical bond between the adsorbate (gas molecule) and the adsorbent (surface the adsorbate is to be adsorbed onto).[79] Physisorption involves a gas molecule being bound to a surface by physical forces, mainly van der Waals interactions.[80] For the purposes of gas adsorption into MOFs it is physisorption that is important, because the principle of gas storage requires that the gas can be removed unchanged from the surface of the MOF.

There are six representative adsorption isotherms that reflect the relationship between porous structure and sorption type,[6] which are shown in Figure 1-18. These adsorption isotherms are characteristics of adsorbents that are microporous (type I), nonporous and macroporous (types II, III, and VI), and mesoporous (types IV and V). The differences between types II and III and between types IV and V arise from the relative strength of gas-solid and gas-gas attractive interactions. When the gas-solid attractive interaction is stronger than that of gas-gas, the adsorption isotherm should be of types II and IV, and

opposite situation leads to types III and V. The type VI isotherm represents adsorption on nonporous or macroporous solid surfaces where stepwise multiplayer adsorption occurs. In terms of gas adsorption in MOFs it is generally type I isotherms that will be seen as the materials are usually microporous.

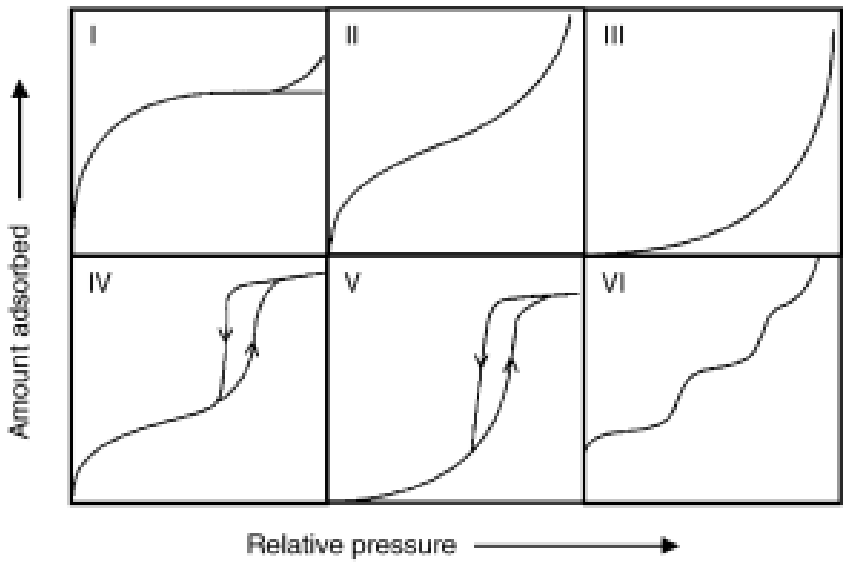

Figure 1-18. IUPAC classification of adsorption isotherms.[6]

Porous materials are very often characterized by their specific surface area (SA), which is reported as either the Langmuir surface area or the BET (Brunauer, Emmett, and Teller) surface area derived from nitrogen adsorption isotherms measured at 77 K. Both methods assume a close packing of molecules in a monolayer (Langmuir) or in multilayers (BET). Because most porous materials have large enough pores to allow more than one adsorbed layer, the Langmuir surface area leads to overestimation, and the BET surface area calculation is more reliable. It should be kept in mind that the surface area is not a direct experimental observable; it must be calculated from the nitrogen isotherm assuming a model such as BET.[81, 82] BET surface areas for a particular MOF material reported in the literature, even by the same group, vary widely and for these variations there are two possible reasons: the pressure range chosen for the BET analysis and the quality of sample.

The first material to exceed surface areas of the best activated carbons was MOF-177, $Zn_4O(btb)_2$ (Figure 1-19) in which Zn_4O clusters are linked with 1,3,5-benzenetribenzoate (btb). In 2004 Yaghi *et al.*[83] reported for MOF-177 a Langmuir surface area of 4,500 m^2/g.

Figure 1-19. A btb_3 unit linked to three Zn_4O units in MOF-177 structure (H atoms are omitted for clarity). ZnO_4 tetrahedra are shown in blue and O and C atoms are shown as red and black spheres, respectively.[83]

1.5. Flexible MOFs

Whereas many MOFs are structurally rigid, a smaller group of MOF crystals show rather unique structural flexibility not commonly associated with crystalline solids. In particular, the guest-induced "gate opening" or "breathing" behaviors of MOFs, initially discovered by the groups of Kaneko, Kitagawa, Férey, and others, are currently under extensive investigation. These intriguing MOFs can selectively respond to certain guests and, upon gas/vapor adsorption, undergo reversible structural transitions between narrow pore and large pore phases. Such a selective, stimuli-driven structural responsiveness is rarely observed in other classes of porous materials (e.g. zeolites, activated carbons, etc.) and therefore provides a unique entry into the development of functional materials for gas separation and sensing. These breathing processes can cause striking unit cell volume changes and frequently result in the appearance of steps and/or hysteresis behavior in their gas sorption isotherms. The breathing behaviour in MOFs is best exemplified by MIL-53, where crystals of the MOF can sustain a cell shrinkage of up to 32 % in volume upon hydration and where well-defined steps and hysteresis are apparent in the CO_2 sorption isotherms. On the basis of the analysis of sorption isotherms, powder X-ray diffraction (PXRD), and theoretical simulations, a better understanding of the breathing effects of MOFs has been achieved.

A study has brought forth a thermodynamic description of the breathing behavior. The first concerns frameworks which are sustained only with guest molecules and collapse on removal of the guest, most of the time irreversibly. The second generation corresponds to stable and robust porous frameworks which exhibit permanent porosity without any guest in the pores. The last category refers to flexible frameworks which change, most of the time reversibly, their structure to respond to external stimuli. The stimulus can be temperature, pressure, light, electric or magnetic field, guests. Depending on the structure itself, the input is associated with either an expansion or a contraction of the cell volume and can generate induced movements larger than 10 Å during the transformation.

An interesting type of flexibility resulting from phase transitions in which the skeleton remains the same, while distorted, is illustrated by the jungle gym MOF Zn_2(1,4-bdc)$_2$(dabco)[55, 65, 84] Its structure is composed of dinuclear Zn_2 units with a paddle-wheel structure, which are bridged by 1,4-bdc dianions to form a distorted 2-D square-grid Zn_2(1,4-bdc)$_2$ (Figure 1-20).

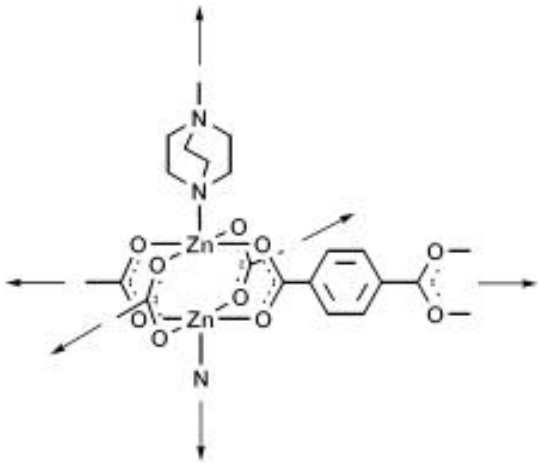

Figure 1-20. The extension of the 2-D square-grid of Zn_2(1,4-bdc$_2$) into a 3-D structure by using dabco which occupies the axial positions.[65]

The pillaring of the latter by the nitrogens of dabco ensures the 3-D structure. For example, during the adsorption of propan-2-ol,[84] distortion of the primitive unit cell first occurs after the introduction of up to three propan-2-ol molecules per cell. The volume decreases by 21% with a decrease of the length of the cell edges. The distortion corresponds to a shift of the square grids from one to the other by 16°. By increasing the amount of propan-2-ol up to 4.5 molecules per cell the original dimensions of the cell are regenerated.

MOFs that have a dynamic and flexible framework, although they have shown promising potential application in adsorption and separation, they could provide new opportunities in designing solid catalysts due to the dynamic structural change in response to guest molecules in a manner reminiscent of enzymes.[85-87]

1.6. Synthesis of MOFs

MOFs are synthesised in general using two methods: conventional and non-conventional methods. The non-conventional methods take in account using microwave or ultrasonic radiations which are well known for speeding up reactions and producing cleaner materials

In MOF chemistry due to dificulties to characterise them is preferable to obtain MOF as a single crystal and in this way when synthesing MOFs, the general rules about growing crystals should be taken in account as well. Traditionally, one of the goals of MOF synthesis has been to obtain high quality single crystals for structural analysis.

The pertinent chemical parameters of the synthesis are pH (mostly acidic), concentrations (which can vary over a large range) and temperature.

The equilibrium therefore, can be shifted to the MOF-product side by working on the concentration profiles of the solvent, liberated water and nitrate. By taking these equilibrium conditions into account, it became possible to improve the MOF quality; i.e. to increase the surface area. As the reaction can be easily driven in both directions, the stability and integrity of MOFs in their use depend on the polarity of the environment and the pH-value. The conditions under which a material is stable have to be considered on a case-by-case basis.

As mentioned above, temperature is a fundamental parameter. In some cases zero-dimensional units can be transformed to chains, sheets and 3-D structures as a function of temperature and time. As an example, by heating the zero-dimensional dimeric molecular zinc oxalate, $(C_4N_2H_{12})_3[Zn_2(C_2O_4)_5]$ $8H_2O$ (Figure 1-21), in the presence of piperazine (PIP) at different temperatures (100°C, 165°C and 180°C) for the same time (48h), compounds with different dimensionalities were obtained as is shown in Figure 1-21.[88]

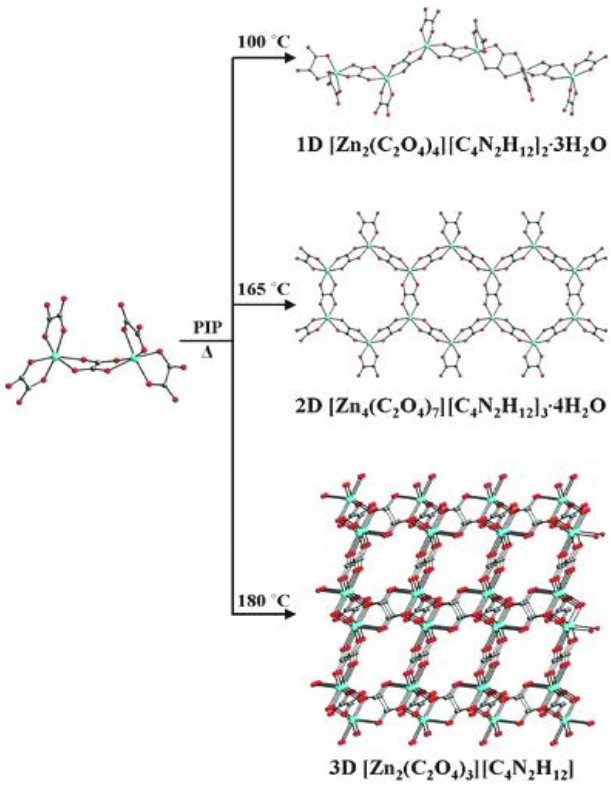

Figure 1-21. Zero-dimensional dimeric zinc oxalate species transform progressively to chain, layered and 3-D structures with increasing temperature.[88]

The solvothermal reactions of $Cu(NO_3)_2$ with H_3btc at different pH conditions yield two MOFs which exhibit different structures: an interpenetration network of $Cu_3(btc)_2(H_2O)_3(NH_3)_4$ and a 2-D bilayer structure of $Cu_4(btc)_2(OH)_2(H_2O)_2(NH_3)_4$ (Figure 1-22).[89]

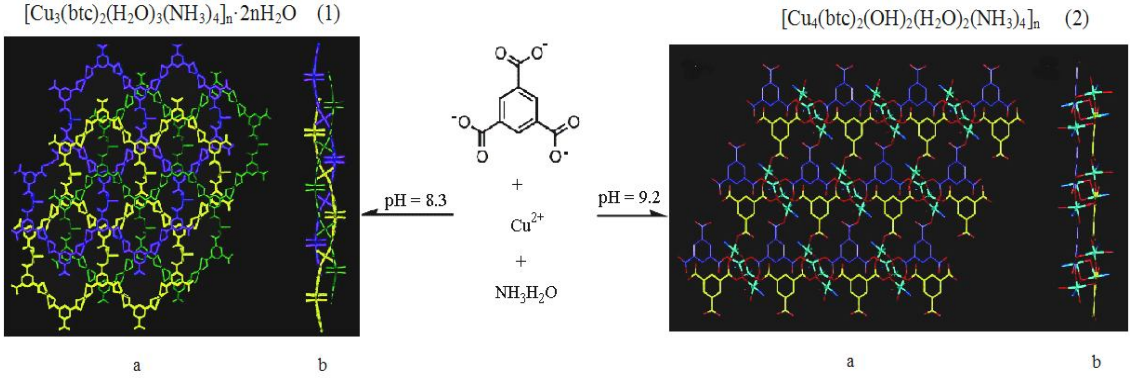

Figure 1-22. Dependence of MOF structures on the pH conditions. a) In both pictures the three layers are represented in different colours and (b) is side view of (a).[89]

Usually, MOFs are synthesized at low temperature (< 250°C). Below 100°C, the classical ways familiar to coordination chemistry are used. Above 100°C, solvothermal syntheses are required. Besides water (the most frequently used), the main solvents are alcohols, dialkyl formamides and pyridine. For many syntheses, the preparations involve the addition of amines which seem to favour the reaction without participating in the formula of the final compound.

Early efforts to produce highly crystalline MOFs involved a variety of techniques previously used to grow crystals of simple inorganic salts. These generally involved the slow introduction of the building blocks to reduce the rate of crystallite nucleation. Methods included slow evaporation of a solution of the precursors, layering of solutions, or slow diffusion of one component solution into another through a membrane or an immobilizing gel. Where a ligand needed to be deprotonated prior to coordination (such as a carboxylic acid), a volatile amine was gradually added via vapour diffusion. Just as for many of the polar solvents used, careful choice of base was necessary to avoid competitive coordination with the organic links for the available metal sites. While in some cases, blocking of metal coordination sites is necessary for the formation of a particular SBU, this occurrence has generally been regarded as leading to low-dimensional structures that are less likely to define an open framework.

As the need for more robust frameworks was recognized, greater difficulties in crystal growth were encountered. The inverse relationship between bond strength and reversible formation is directly responsible for this obstacle. Fortunately, solvothermal techniques were found to be a convenient solution to this dilemma and have largely replaced the older, often time-consuming methods involving slow coupling of the coordinating species. The precursors are typically combined as dilute solutions in polar solvents such as water, alcohols, acetone or acetonitrile and heated in sealed vessels such as Teflon-lined stainless steel bombs or glass tubes. Mixed solvent systems are often used to tune the solution polarity and the kinetics of solvent-ligand exchange, effecting enhanced crystal growth.

Exposing the growing framework to a variety of space-filling solvent molecules may also be an effective way to stabilize its defect-free construction as they efficiently pack within the channels. In cases where deprotonation of the linking molecule is necessary, gradual neutralization of a solution can be effected by thermal decomposition of an amide solvent.

Alkyl formamides and pyrrolidinones have been particularly useful to this end, as they are also excellent solubilizing agents. Finally, if high yield is desired over crystal quality, reaction times can be greatly reduced by increased concentration and agitation of the solution. Quite often microcrystalline, rather than amorphous, materials are formed under these conditions, as evidenced by electron microscopy and PXRD.

The potential number of structures that can be obtained from the combination of inorganic and organic linker moieties is vast and many are known based on triangular, square, tetrahedral and octahedral SBUs (Figure 1-3), which lead to default structural nets. MOF structures are mainly dependent upon the coordination geometry of the SBUs. MOF structures with the same net can often be made by functionalizing the organic linker units and this allows surface chemistry to be tailored. Similarly, lengthening the linker ligand also often leads to structures with the same net and this can lead to a series of structures with the same crystallographic space group but different pore sizes and volumes (see Yaghi's IRMOF series Figure 1-6). However, lengthening the linkers to increase the distance between nodes often leads to catenation and this may be a limitation for synthetic studies.[90]

The control of dimensionality is a major challenge in MOF chemistry. Even when polyfunctional ligands such as btc are used, additional ligation by water or other solvent ligands may result in low dimensionality. The dimensionality of the resulting metal–btc frameworks is mainly dependent on the solvent used in the synthesis, and the strength of base employed for the deprotonation of H_3btc, as summarized in Figure 1-23. With a strong conjugate base (i.e. the acetate anion) used for deprotonation and water acting as both a solvent and a strong coordinating ligand, a 1-D framework was obtained (Figure 1-23a). Using a less strongly coordinating solvent such as ethanol and a weaker base such as pyridine for deprotonation a 2-D structure was obtained (Figure 1-23b). Pyridine partly deprotonates H_3btc and, in the absence of water, binds strongly to metal ions, blocking the extension of the framework. For 3-D structures a stronger base, such as triethylamine, with sufficient strength to completely deprotonate H_3btc, but with a low affinity for binding to metal ions is necessary (Figure 1-23c).

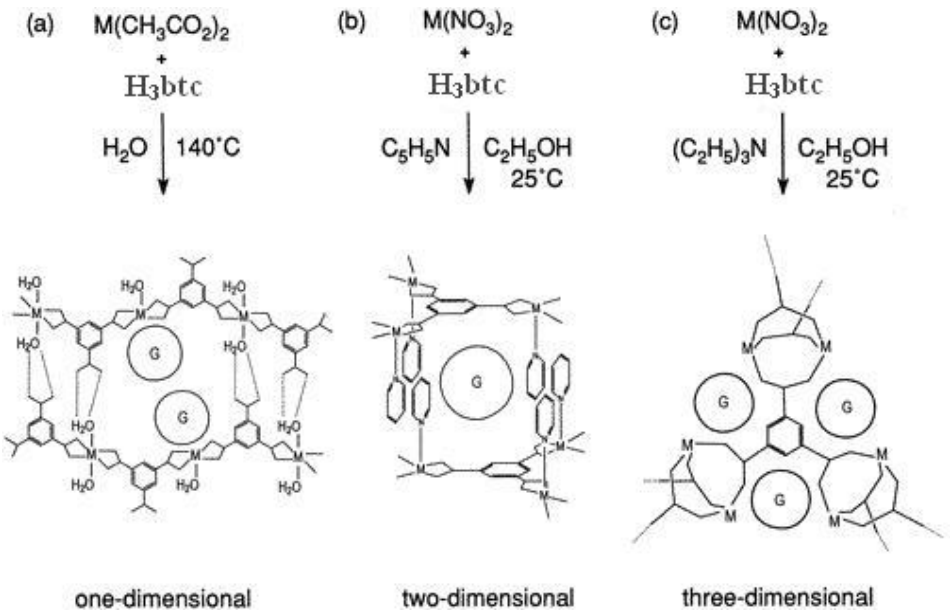

Figure 1-23. A schematic representation of (a) 1-D (b) 2-D, and (c) 3-D structures produced by reacting metal ions (M) with benzene (H_3btc), and the dependence of their dimensionality on the solvent and base employed in the reaction. For clarity, all hydrogen atoms have been omitted from the structures, with the corners representing carbon and oxygen atoms of btc.[37]

Recent years have witnessed a rapid increase in interest in alternative synthetic methods that would be faster, cleaner and less expensive. Such methods include electrochemical methods, sonochemical methods, microwave methods and mecanochemical methods.

Mueller *et al.* synthesized HKUST-1 for the first time using an electrochemical route.[7] Copper plates were used as electrodes in an electrochemical cell with the H_3btc dissolved in methanol as solvent. This procedure is especially beneficial for MOF-structures containing open metal sites, as no anions from added salts can block the access to the sites. By the same method the successful synthesis of Zn-EZIF (electrochemically made ZIF) with 2-methylimidazole (2-HMeIM) as a linker was reported.[91]

In 2008 Qiu *et al.*[92] applied for the first time the ultrasound technique for MOF synthesis, to prepare $Zn_3(btc)_2 \cdot 12H_2O$. In 2009 the same group of researchers synthesised under ultrasonic irradiation at ambient temperature and atmospheric pressure for short reaction times (5–60 min), HKUST-1 in high yields (63 – 85%).[93] These HKUST-1 nano-crystals have dimensions much smaller than those synthesized using conventional solvothermal

method. There were no significant differences in physicochemical properties, i.e. surface area, pore volume, and hydrogen storage capacity, between HKUST-1 nano-crystals prepared using ultrasonic method and the microcrystals obtained by using solvothermal methods. These researchers obtained also Zn(1,4-bdc)(H_2O) by the reaction of zinc acetate with $H_2$1,4-bdc in DMF under ultrasonic irradiation at ambient temperature and atmospheric pressure.[93]

High-throughput methods routinely used in screening for activity of drug molecules and catalysts have found their use in the synthesis of MOFs, both conventional and alternative methods. High-throughput methods in materials science permit an accelerated, systematic investigation of the reaction parameter space while consuming small amounts of reagents.[94, 95]

Biemmi *et al.* reported the systematic screening of reaction parameters of MOF-5 and HKUST-1 employing high-throughput as well as conventional methods. Thus, compositional parameters (metal salt, reagent concentrations, and pH) as well as process parameters (temperature, time) were investigated in order to establish reaction trends and fields of formation. A multiclave reaction block was used to perform the investigation of 24 different solvothermal reactions at a time. Attention was focused on the phase purity and the crystal morphology of the resulting compounds. The characterization of the samples was performed by PXRD and high resolution scanning electron microscopy (SEM). The experimental results showed that the formation, phase purity, and morphology of MOF-5 and HKUST-1 are extremely sensitive to the synthesis parameters explored.

There are examples of highly porous MOFs that have been prepared in amounts far greater than the laboratory scale[96] and for example, the BASF (Badische Anilin- und Soda-Fabrik) chemical company have investigated the use of MOFs in pilot plants on a barrel scale.[7] MOFs are commercially available from suppliers as the Sigma-Aldrich: Basolite Z1200 (which is ZIF-8), Basolite F300, Basolite A100 (which is MIL-53(Al)), Basolite C300 (which is HKUST-1), and Basosive M050. They also sell organic linkers and SBU precursors (cobalt(II) oxo pivalate, iron(III) oxo acetate perchlorate hydrate, zinc(II) oxo acetate and zirconium(IV) oxo hydroxy methacrylate).

Postsynthetic modification (PSM) is a relatively new area of research within MOF chemistry and can be defined as a late-stage chemical modification and functionalization of MOFs. The PSM idea was triggered almost a decade later from the visionary quote of Robson[97] in 1990. Postsynthetic methods enable MOFs with new physical properties or chemical behaviours. PSM of MOFs shown a very fast progress in the last five years and there are already reviews [98-100] reported about the PSM topic. Cohen *et al.*[100] divide the PSM of MOFs into three areas: (a) covalent PSM, (b) dative PSM and (c) postsynthetic deprotection (PSD), whose shemes can be seen in Figure 1-24. They take in account the type of chemical bond that is formed or broken during the postsynthetic approach.

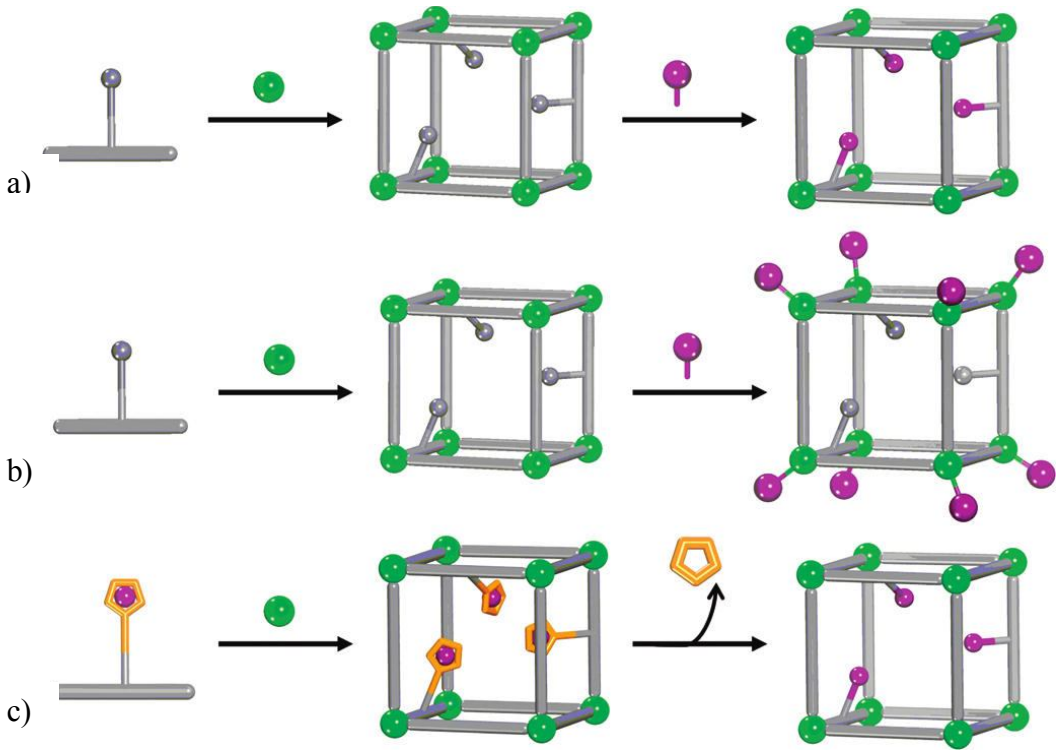

Figure 1-24. Generic schemes for (a) covalent PSM, (b) dative PSM, and (c) PSD.[100]

1.7. Gas adsorption and separation of MOFs

While the initial focus in the field of MOFs was the synthesis and structural characterization, an increasing number of MOFs are now being explored for their interesting properties, including optic,[101-106] magnetic,[107-113] and electronic properties,[114-118] as well as their various potential applications such as: gas storage,[37, 119-129]

separation,[130-133] catalysis,[134-139] ion exchange,[106, 140-142] sensing,[143-146] polymerization,[147-149] and drug delivery.[150-152]

The decrease in fossil fuel reserves urgently needs solutions of substitution and MOFs might be one, for their capacity to adsorb large amounts of strategic gases like H_2, CO_2, CH_4, CO, O_2, NOx, C_2H_2, etc. within the cages.

MOFs are ideal adsorbents for gas storage and separation due to their large surface areas, adjustable pore sizes, and controllable surface properties. These materials can potentially fill the place between other physisorbents such as activated carbon, which have similar uptake at low temperatures but low affinity for hydrogen at ambient temperature, and chemical sorbents such as hydrides, which have high hydrogen uptakes but undesirable release kinetics and thermodynamics.

The adsorption of guest molecules onto the solid surface is governed not only by the interaction between guest molecules and the surfaces but also by the pore size and shape.

For the moment, the main efforts concentrate on H_2, CH_4 and CO_2 with a striking difference between the first and the others. Indeed, MOFs adsorb large amounts of hydrogen only at 77 K; at room temperature, adsorption is negligible, at variance to CH_4 and CO_2 which exhibit interesting performances at 300 K and above.

The underlying possibility of using hydrogen as a fuel for mobile or portable fuel-cell applications raises a very high interest in hydrogen storage possibilities. MOF-storage for hydrogen works fully reversibly, avoids complicated heat treatments, and recharging proceeds within seconds or minutes. This clearly is an advantage over metal hydrides as storage materials. The US department of Energy (DoS) has set targets for hydrogen storage capacity for mobile applications that are yet to be met (6.0 wt% and 45 g/L by 2010 and 9.0 wt% and 81 g/L by 2015).[153, 154] It should be noted that these are system requirements, and not just targets for the storage capacity of the material itself.

The three best verified MOFs for hydrogen storage at 77 K are MOF-5 (5.1 wt.% at saturation, SA_{BET} = 2296 m^2g^{-1}, $SA_{Langmuir}$ = 3840 m^2g^{-1}), HKUST-1 (3.6 wt.% at saturation; SA_{BET} = 1154 m^2g^{-1}, $SA_{Langmuir}$ = 1958 m^2g^{-1}), and MIL-53 (3.8 and 4.5 wt.%

at 15 bar and at saturation, SA_{BET} = 1100 m^2g^{-1}, SALangmuir = 1540 m^2g^{-1}).[7] Yaghi *et al.*[155] showed that MOF-177 can store 7.5 wt% hydrogen with a volumetric capacity of 32 g/L at 77 K and 70bar. UMCM-2 shows an excess gravimetric H_2 uptake of 6.9 wt% at 46 bar[156], thus not greater than MOF-177.

Müller *et al.*[7, 157] from BASF showed the real efficiency of MOFs for industrial applications. Indeed, they noted that, compared to pressurizing (77 K and up to 40 bar) an empty container with hydrogen, MOF-5, MOF-177, IRMOF-8 , Zn-EZIF[91], Zeolite13X and Cu-EMOF (electrochemically-prepared HKUST-1)[7] increasingly take up higher amounts of hydrogen, all of them exceeding the standard pressure–volume–temperature (PVT) uptake curve of the empty container. MOF-177 demonstrates the most promising results for the selected MOFs (Figure 1-25).

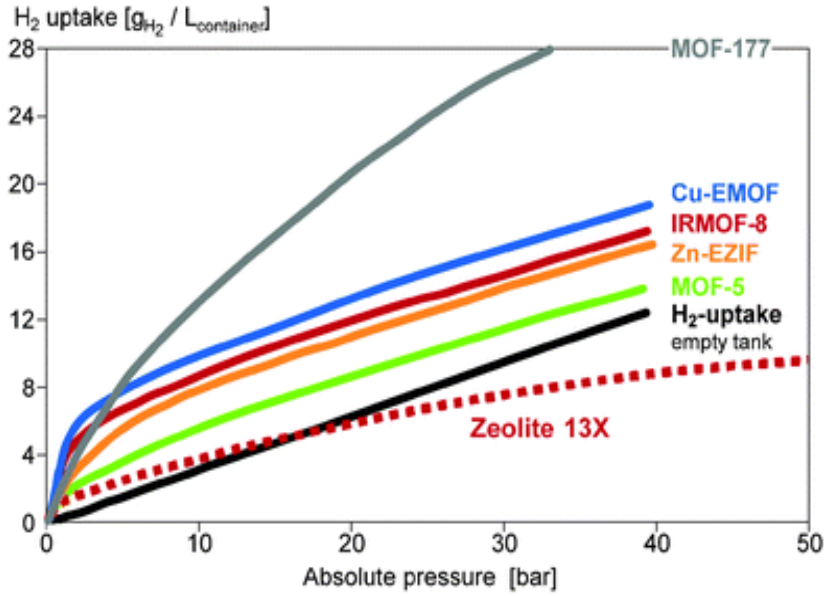

Figure 1-25. H_2-storage capacities for different MOFs (prototype trials).[157]

The first success to introduce large amounts of CH_4 in a MOF was made in 1997 by Kitagawa *et al.*[158] They showed that $Co_2(4,4'\text{-bpy})_3(NO_3)_4$ adsorbs an equivalent of 52 cm^3g^{-1} (STP) (STP = standard temperature and pressure) of CH_4 at 25°C and 30 bar. Storage of methane in MOF-filled tanks at room temperature is a promising field for improving the storage technology in adsorbing natural gas driven cars. The uptake curves reported by Müller *et al.*[157], are shown in Figure 1-26 for the storage of CH_4 at room temperature and pressures up to 200 bar in gas cylinders filled with different MOF

materials. A non-linear uptake behaviour can be monitored as the pressure is increased. At a pressure of 150 bar, it is clearly seen that about 35% more capacity is reached over the state-of-the-art filling curve. It should be noted that the benefit of enhanced capacity with MOF-filled vessels can only occur if the gas is in a true gaseous state and not in the liquid-phase. Furthermore, the density of the liquid phase is the limiting case for the storage capacity of the MOF since a MOF cannot compress gas to a higher density than its liquid state density.

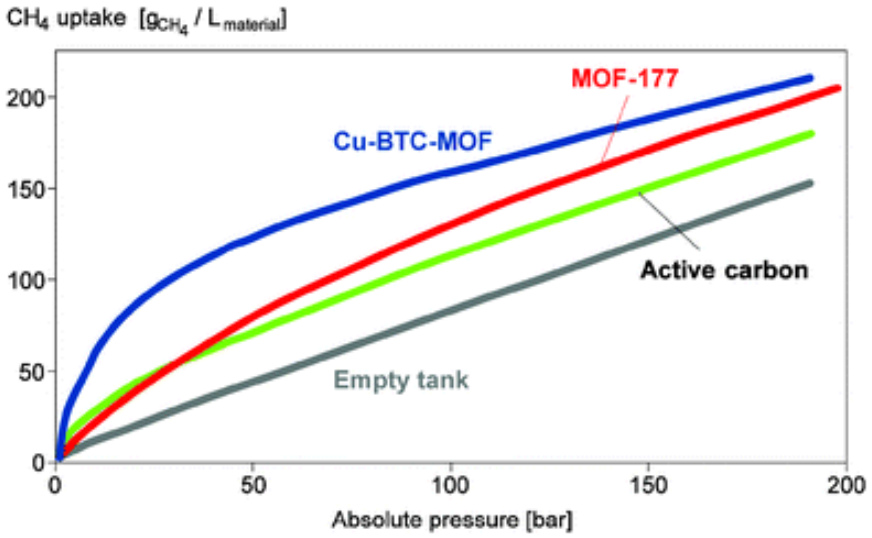

Figure 1-26. CH4-storage in MOFs (prototype trials). [157]

HKUST-1, Zn_2(1,4-bdc)$_2$dabco, and $Cr_3F(H_2O)_2O$(1,4-bdc)$_3$ (MIL-101) were evaluated as methane storage materials by Kaskel and coworkers.[159] Among the three materials, HKUST-1 shows the highest excess adsorption at 30°C (15.7 wt.%) and effective volumetric storage capacity of 228 m^3/m^3 (150 bar), whereas for Zn_2(1,4-bdc)$_2$(dabco), and MIL-101 the maximum excess adsorption is lower (14.3 and 14.2 wt.%, respectively).

Düren *et al.*[160] have used computational methods to calculate the adsorption capacity, heats of adsorption, and surface areas of various different MOFs, zeolites, and carbon materials. They indicate that the important features of materials that control methane adsorption are primarily the surface area, followed by free volume, framework density, and heats of adsorption.

The first MOF studied for CO_2 adsorption was MOF-2.[161] A total of four carboxylate units of different, but symmetrically equivalent, bdc building blocks are bonded to two zinc atoms in a di-monodentate fashion giving the known paddle-wheel structure met in HKUST-1 but here based on zinc and bdc. Each zinc is also linked to a terminal water ligand. The structure extends by having identical Zn−Zn units linked to remaining carboxylate functionalities of bdc to yield 2-D microporous layers. Stacking of the layers in the crystal leads to a 3-D network having extended pores of nearly 5Å in diameter where DMF guests reside, as shown in Figure 1-27. MOF-2 had an uptake of CO_2 of more than 2mmol/g at 1bar and 195 K.

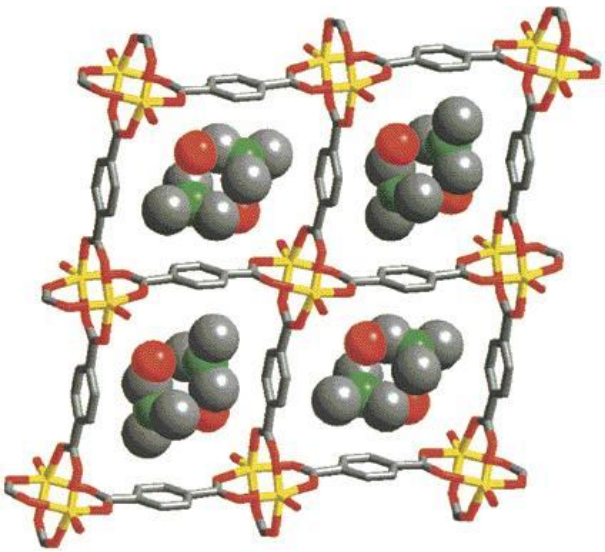

Figure 1-27. MOF-2 framework with DMF occupying the pores. (Zn = yellow; O = red; N = green; C = grey). [2]

Yaghi and co-workers have subsequently reported that many MOFs show remarkable CO2 adsorption capacities (i.e. MOF-177 exhibits a CO_2 capacity of 33.5mmol/g),[162] which exceed the capacities of zeolites and activated carbons.

The flexibility of MOFs may also be used to improve storage properties and perhaps the most interesting (although by no means highest capacity) CO_2 adsorbing materials studied are the breathing MIL-n MOFs prepared in Férey's group.[163] $Zn_2(1,4\text{-bdc})_2(dabco)$ shows as well an unusual dynamic behavior as is described in section 1.5 and this MOF exhibits also permanent porosity (the guest-accessible volume is estimated to be 62 %) and a high surface area (SA_{BET} = 1450m^2g^{-1}).[65]

1.8. Aims

Currently, there is intense interest in the introduction of chemical functionalities onto the linkers, as a means of tuning the properties of the resultant MOFs. This can be achieved either by using functionalised linkers in the synthesis, or by post-synthetic modifications (PSMs). Hence, we investigated incorporation into MOFs of two dipyridyl-based functionalised linkers, namely 3,5-bis(4-pyridyl)-1*H*-pyrazole (HL) and 1,4-bis(4′-pyridylethynyl)benzene (L1) depicted in Figure 1-28.

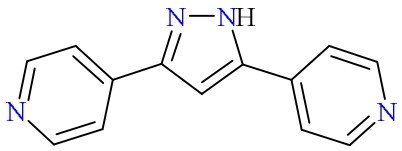

3,5-bis(4-pyridyl)-1*H*-pyrazole

HL

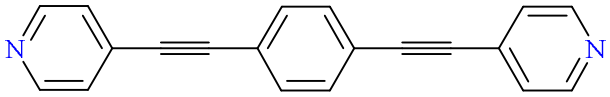

1,4-bis(4'-pyridylethynyl)benzene

L1

Figure 1-28. The functionalised dipyridyl linkers used in this work.

We reasoned that HL and L1 had the potential to act in a similar manner to other neutral *N,N′*-ditopic ligands in polycarboxylate-containing MOFs. We therefore sought to investigate the effect of the longer length of the linker with respect to 4,4'-bpy and dabco on the network structures formed. In addition, the central five-membered pyrazole ring ensures that the relative angle between the pyridyl nitrogen donors is reduced from 180° as observed in 4,4'-bpy and dabco to approximately 156° in HL, and this difference may also have structural consequences. Finally, the presence of the hydrogen bond donor and acceptor on the pyrazole ring may lead to the potential for the network to act as a selective host for guests containing complementary hydrogen bonding faces. We aimed to introduce the highly rigid long bipyridine ligand L1 with zinc dicarboxylates in order to understand the effect of interpenetration and pore generation.

The formation of MOFs with calix[4]arene-based ligands opens up the possibility of forming hierarchically-porous materials, with two levels of porosity associated with both the ligand and the structural framework. With this in mind, we aimed to synthesise MOFs using an upper-rim functionalised calix[4]arene dicarboxylic acid, namely H_2caldc (25,26,27,28-tetrapropoxycalix[4]arene-5,17-dicarboxylic acid) (Figure 2).

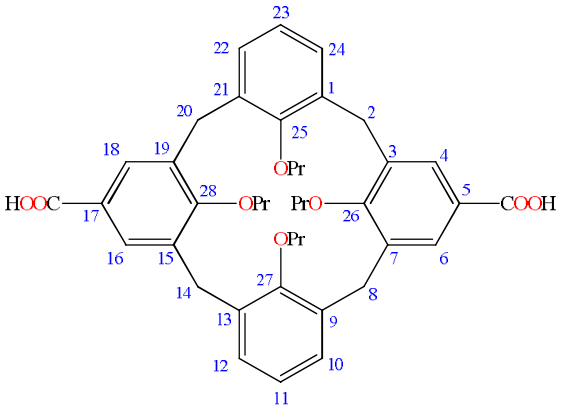

Figure 1-29. Representation of H_2caldc showing the numbering of carbon atoms (Pr = n-propyl).

Studies carried out by our collaborators Dr. Peyman. Z. Moghadam during his PhD under the supervision of Prof. Tina Düren from Institute for Materials and Processes, University of Edinburgh[164] along with other studies in the literature[165] suggested that *p-tert*-butylcalix[4]arene displays interesting adsorptive characteristics. With this in mind our collaborators characterised and tested $Cu_2(caldc)_2(DMF)_2$, $[Cd_2(caldc)_2(DMF)_2]\cdot 3DMF$ and $[Co_5(caldc)_4(OH)_2(H_2O)_4]\cdot 8DMF$ for their adsorption and separation capabilities for methane and hydrogen.

The investigation into the use of *para*-xylylenediphosphonic acid (H_4xdp) (Figure 3) to obtain mixed-metal MOFs was initiated by Dr. Ayi A. Ayi from Department of Pure and Applied Chemistry, University of Calabar, Nigeria, during his fellowship at the University of Bath. During these studies a new structure containing *para*-xylylenediphosphonate (xdp^{4-}) was obtained serendipitously as revealed by a single crystal X-ray analysis.

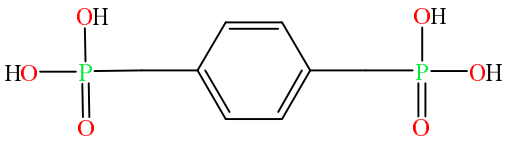

Figure 1-30. para-Xylylenediphosphonic acid (H_4xdp).

The aims for the work reported here in chapter 4 were to establish the synthesis of the new molybdenum *para*-xylylenediphosphonate MOF and to characterise this MOF through thermogravimetric analysis (TGA), powder X-ray diffraction (PXRD), infrared spectroscopy, CHN analysis and ^{1}H and ^{31}P NMR spectroscopy of the digested product.

Studies on dehydration and rehydration of the new molybdenum *para*-xylylenediphosphonate MOF have been performed and the behaviour of fully dehydrated MOF when in contact with guest molecules as methanol and ethanol has been investigated.

The final aim of this research was to investigate the synthesis and magnetic properties of new anionic copper(II) sulfate aggregates and chains linked into 2-D and 3-D networks involving the dimethylammonium cations ($NMe_2H_2^+$). The trigger for this project was one of these new dimethylammonium copper(II) sulfate frameworks which was synthesised serendipitously during the work carried out with H_2caldc ligand, reported in chapter 3.

1.9. References

[1] O. M. Yaghi, H. Li, C. Davis, D. Richardson, T. L. Groy, *Accounts of Chemical Research* **1998**, *31*, 474.

[2] M. Eddaoudi, D. B. Moler, H. Li, B. Chen, T. M. Reineke, M. O'Keeffe, O. M. Yaghi, *Accounts of Chemical Research* **2001**, *34*, 319.

[3] O. M. Yaghi, M. O'Keeffe, N. W. Ockwig, H. K. Chae, M. Eddaoudi, J. Kim, *Nature* **2003**, *423*, 705.

[4] S. L. James, *Chemical Society Reviews* **2003**, *32*, 276.

[5] C. Janiak, *Dalton Transactions* **2003**, 2781.

[6] S. Kitagawa, R. Kitaura, S.-i. Noro, *Angewandte Chemie International Edition* **2004**, *43*, 2334.

[7] U. Müller, M. Schubert, F. Teich, H. Puetter, K. Schierle-Arndt, J. Pastré, *Journal of Materials Chemistry* **2006**, *16*, 626.

[8] G. Férey, *Chemical Society Reviews* **2008**, *37*, 191.

[9] D. Bradshaw, J. B. Claridge, E. J. Cussen, T. J. Prior, M. J. Rosseinsky, *Acc. Chem. Res.* **2005**, *38*, 273.

[10] S. Kitagawa, S.-i. Noro, T. Nakamura, *Chemical Communications* **2006**, 701.

[11] H. Li, M. Eddaoudi, M. O'Keeffe, O. M. Yaghi, *Nature* **1999**, *402*, 276.

[12] O. M. Yaghi, M. O'Keeffe, D. J. Tranchemontagne, J. L. Mendoza-Cortes, *Chemical Society Reviews* **2009**, *38*, 1257.

[13] R. Robson, *Dalton Transactions* **2008**, 5113.

[14] J. Perry IV, J. A. Perman, M. J. Zaworotko, *Chemical Society Reviews* **2009**, *38*, 1400.

[15] S. Ma, H.-C. Zhou, *Journal of the American Chemical Society* **2006**, *128*, 11734.

[16] N. N. Adarsh, P. Dastidar, *Chemical Society Reviews* **2012**, *41*, 3039.

[17] A. F. Wells, *Three-Dimensional Nets and Polyhedra, Wiley-Interscience,*, New York, **1977**.

[18] J. Hafizovic, M. Bjorgen, U. Olsbye, P. D. C. Dietzel, S. Bordiga, C. Prestipino, C. Lamberti, K. P. Lillerud, *Journal of the American Chemical Society* **2007**, *129*, 3612.

[19] S. A. Sapchenko, D. N. Dybtsev, D. G. Samsonenko, V. P. Fedin, *New Journal of Chemistry*, *34*, 2445.

[20] S. S. Chui, S. M. Lo, J. P. Charmant, A. G. Orpen, I. D. Williams, *Science* **1999**, *283*, 1148.

[21] D. J. Tranchemontagne, J. R. Hunt, O. M. Yaghi, *Tetrahedron* **2008**, *64*, 8553.

[22] G. Férey, C. Mellot-Draznieks, C. Serre, F. Millange, J. Dutour, S. Surble, I. Margiolaki, *Science* **2005**, *309*, 2040.

[23] O. I. Lebedev, F. Millange, C. Serre, G. Van Tendeloo, G. Ferey, *Chemistry of Materials* **2005**, *17*, 6525.

[24] H. Birch, *Chemistry World* **2009**, 46.

[25] M. Eddaoudi, J. Kim, N. Rosi, D. Vodak, J. Wachter, M. O'Keeffe, O. M. Yaghi, *Science* **2002**, *295*, 469.

[26] J. L. C. Rowsell, O. M. Yaghi, *Microporous and Mesoporous Materials* **2004**, *73*, 3.

[27] S. Surble, C. Serre, C. Mellot-Draznieks, F. Millange, G. Ferey, *Chemical Communications* **2006**, 284.

[28] H. Furukawa, Y. B. Go, N. Ko, Y. K. Park, F. J. Uribe-Romo, J. Kim, M. O'Keeffe, O. M. Yaghi, *Inorganic Chemistry* **2011**, *50*, 9147.

[29] S. R. Batten, R. Robson, *Angewandte Chemie International Edition* **1998**, *37*, 1460.

[30] B. Chen, M. Eddaoudi, S. T. Hyde, M. O'Keeffe, O. M. Yaghi, *Science* **2001**, *291*, 1021.

[31] T. M. Reineke, M. Eddaoudi, D. Moler, M. O'Keeffe, O. M. Yaghi, *Journal of the American Chemical Society* **2000**, *122*, 4843.

[32] S. Keskin, D. S. Sholl, *Langmuir* **2009**, *25*, 11786.

[33] J. Zhang, L. Wojtas, R. W. Larsen, M. Eddaoudi, M. J. Zaworotko, *Journal of the American Chemical Society* **2009**, *131*, 17040.

[34] B. Kesanli, Y. Cui, M. R. Smith, E. W. Bittner, B. C. Bockrath, W. Lin, *Angewandte Chemie* **2005**, *117*, 74.

[35] T. Yamada, S. Iwakiri, T. Hara, K. Kanaizuka, M. Kurmoo, H. Kitagawa, *Crystal Growth & Design* **2011**, *11*, 1798.

[36] J. Tao, M. L. Tong, X. M. Chen, *Journal of the Chemical Society-Dalton Transactions* **2000**, 3669.

[37] O. M. Yaghi, C. E. Davis, G. Li, H. Li, *Journal of the American Chemical Society* **1997**, *119*, 2861.

[38] L. Carlucci, G. Ciani, D. M. Proserpio, F. Porta, *Crystengcomm* **2006**, *8*, 696.

[39] D. L. Reger, R. F. Semeniuc, C. A. Little, M. D. Smith, *Inorganic Chemistry* **2006**, *45*, 7758.

[40] D. Venkataraman, S. Lee, J. S. Moore, P. Zhang, K. A. Hirsch, G. B. Gardner, A. C. Covey, C. L. Prentice, *Chemistry of Materials* **1996**, *8*, 2030.

[41] K. S. Park, N. Zheng, A. Côté, J. Y. Choi, R. Huang, F. J. Uribe-Romo, H. K. Chae, M. O'Keeffe, O. M. Yaghi, *Proceedings of the National Academy of Sciences* **2006**, *103*, 10186.

[42] W. Kleist, F. Jutz, M. Maciejewski, A. Baiker, *European Journal of Inorganic Chemistry* **2009**, *2009*, 3552.

[43] H. Deng, C. J. Doonan, H. Furukawa, R. B. Ferreira, J. Towne, C. B. Knobler, B. Wang, O. M. Yaghi, *Science* **2010**, *327*, 846.

[44] K. Koh, A. G. Wong-Foy, A. J. Matzger, *Chemical Communications* **2009**, 6162.

[45] A. D. Burrows, *CrystEngComm* **2011**, *13*, 3623.

[46] M. Kondo, T. Okubo, A. Asami, S. I. Noro, T. Yoshitomi, S. Kitagawa, T. Ishii, H. Matsuzaka, K. Seki, *Angewandte Chemie - International Edition* **1999**, *38*, 140.

[47] T. K. Maji, K. Uemura, H.-C. Chang, R. Matsuda, S. Kitagawa, *Angewandte Chemie International Edition* **2004**, *43*, 3269.

[48] M. Du, C.-P. Li, C.-S. Liu, S.-M. Fang, *Coordination Chemistry Reviews* **2013**, *257*, 1282.

[49] G. Férey, *Chemistry of Materials* **2001**, *13*, 3084.

[50] R. Kitaura, F. Iwahori, R. Matsuda, S. Kitagawa, Y. Kubota, M. Takata, T. C. Kobayashi, *Inorganic Chemistry* **2004**, *43*, 6522.

[51] Z. Chen, S. Xiang, D. Zhao, B. Chen, *Crystal Growth & Design* **2009**, *9*, 5293.

[52] K. Seki, S. Takamizawa, W. Mori, *Chemistry Letters* **2001**, *30*, 332.

[53] K. Seki, W. Mori, *The Journal of Physical Chemistry B* **2002**, *106*, 1380.

[54] H. Chun, H. Jung, G. Koo, H. Jeong, D.-K. Kim, *Inorganic Chemistry* **2008**, *47*, 5355.

[55] K. Kim, H. Chun, D. N. Dybtsev, H. Kim, *Chemistry - A European Journal* **2005**, *11*, 3521.

[56] T. K. Maji, M. Ohba, S. Kitagawa, *Inorganic Chemistry* **2005**, *44*, 9225.

[57] J.-C. Dai, X.-T. Wu, S.-M. Hu, Z.-Y. Fu, J.-J. Zhang, W.-X. Du, H.-H. Zhang, R.-Q. Sun, *European Journal of Inorganic Chemistry* **2004**, *2004*, 2096.

[58] B.-Q. Ma, K. L. Mulfort, J. T. Hupp, *Inorganic Chemistry* **2005**, *44*, 4912.

[59] H. Chun, J. Moon, *Inorganic Chemistry* **2007**, *46*, 4371.

[60] J. Y. Lee, D. H. Olson, L. Pan, T. J. Emge, J. Li, *Advanced Functional Materials* **2007**, *17*, 1255.

[61] J. Zhang, L. Wojtas, R. W. Larsen, M. Eddaoudi, M. J. Zaworotko, *Journal of the American Chemical Society* **2009**, *131*, 17040.

[62] L.-G. Zhu, H.-P. Xiao, *Z. Anorg. Allg. Chem.* **2008**, *634*, 845.

[63] B. Chen, C. Liang Sr, J. Yang, D. S. Contreras, S. Dai, *Angewandte Chemie International Edition* **2006**, *45*, 1390.

[64] M. Kondo, Y. Takashima, J. Seo, S. Kitagawa, S. Furukawa, *CrystEngComm* **2010**, *12*, 2350.

[65] K. Kim, D. N. Dybtsev, H. Chun, *Angewandte Chemie International Edition* **2004**, *43*, 5033.

[66] C. C. Addison, N. Logan, S. C. Wallwork, C. D. Garner, *Quarterly Reviews, Chemical Society* **1971**, *25*, 289.

[67] G. Guilera, J. W. Steed, *Chemical Communications* **1999**, 1563.

[68] S. Horike, D. Tanaka, K. Nakagawa, S. Kitagawa, *Chemical Communications* **2007**, 3395.

[69] M.-H. Zeng, X.-L. Feng, X.-M. Chen, *Dalton Transactions* **2004**, 2217.

[70] D. Tanaka, K. Nakagawa, M. Higuchi, S. Horike, Y. Kubota, T. C. Kobayashi, M. Takata, S. Kitagawa, *Angew. Chem.* **2008**, *120*, 3978.

[71] D. Tanaka, K. Nakagawa, M. Higuchi, S. Horike, Y. Kubota, T. C. Kobayashi, M. Takata, S. Kitagawa, *Angewandte Chemie International Edition* **2008**, *47*, 3914.

[72] T. Fukushima, S. Horike, Y. Inubushi, K. Nakagawa, Y. Kubota, M. Takata, S. Kitagawa, *Angewandte Chemie International Edition* **2010**, *49*, 4820.

[73] H. Sato, R. Matsuda, K. Sugimoto, M. Takata, S. Kitagawa, *Nat Mater* **2010**, *9*, 661.

[74] G. Tian, G. Zhu, Q. Fang, X. Guo, M. Xue, J. Sun, S. Qiu, *Journal of Molecular Structure* **2006**, *787*, 45.

[75] J. Tao, X.-M. Chen, R.-B. Huang, L.-S. Zheng, *Journal of Solid State Chemistry* **2003**, *170*, 130.

[76] C. Ma, C. Chen, Q. Liu, D. Liao, L. Li, L. Sun, *New Journal of Chemistry* **2003**, *27*, 890.

[77] J.-R. Li, D. J. Timmons, H.-C. Zhou, *Journal of the American Chemical Society* **2009**, *131*, 6368.

[78] M. J. Zaworotko, *Nat Chem* **2009**, *1*, 267.

[79] F. Rouquerol, J. Rouquerol, S. King, *Adsorption by Powders and Porous Solids, Principles, Methodology and Applications*, Academic Press, **1999**.

[80] R. J. Hunter, *Introduction to Modern Colloid Science*, Oxford University Press, **1993**.

[81] K. S. Walton, R. Q. Snurr, *Journal of the American Chemical Society* **2007**, *129*, 8552.

[82] T. Düren, F. Millange, G. Férey, K. S. Walton, R. Q. Snurr, *Journal of Physical Chemistry C* **2007**, *111*, 15350.

[83] O. M. Yaghi, M. O'Keeffe, H. K. Chae, D. Y. Siberio-Perez, J. Kim, Y. Go, M. Eddaoudi, A. J. Matzger, *Nature* **2004**, *427*, 523.

[84] K. Uemura, Y. Yamasaki, Y. Komagawa, K. Tanaka, H. Kita, *Angewandte Chemie International Edition* **2007**, *46*, 6662

[85] S. Kitagawa, K. Uemura, *Chemical Society Reviews* **2005**, *34*, 109.

[86] K. Uemura, R. Matsuda, S. Kitagawa, *Journal of Solid State Chemistry* **2005**, *178*, 2420.

[87] D. Bradshaw, J. E. Warren, M. J. Rosseinsky, *Science* **2007**, *315*, 977.

[88] M. Dan, C. N. R. Rao, *Angewandte Chemie International Edition* **2006**, *45*, 281.

[89] W.-X. Chen, S.-T. Wu, L.-S. Long, R.-B. Huang, L.-S. Zheng, *Crystal Growth & Design* **2007**, *7*, 1171.

[90] E. Biemmi, S. Christian, N. Stock, T. Bein, *Microporous and Mesoporous Materials* **2009**, *117*, 111.

[91] U. Müller, I. Richter , M. Schubert, *Patent* **2007, WO 2007131955 A1**.

[92] L.-G. Qiu, Z.-Q. Li, Y. Wu, W. Wang, T. Xu, X. Jiang, *Chemical Communications* **2008**, 3642.

[93] Z.-Q. Li, L.-G. Qiu, T. Xu, Y. Wu, W. Wang, Z.-Y. Wu, X. Jiang, *Materials Letters* **2009**, *63*, 78.

[94] T. B. Norbert Stock, *Angewandte Chemie International Edition* **2004**, *43*, 749.

[95] K. Choi, D. Gardner, N. Hilbrandt, T. Bein, *Angewandte Chemie International Edition* **1999**, *38*, 2891.

[96] Q. M. Wang, D. Shen, M. Bülow, M. L. Lau, S. Deng, F. R. Fitch, N. O. Lemcoff, J. Semanscin, *Microporous and Mesoporous Materials* **2002**, *55*, 217.

[97] B. F. Hoskins, R. Robson, *Journal of the American Chemical Society* **1990**, *112*, 1546.

[98] S. M. Cohen, *Chemical Science* **2010**, 32.

[99] K. K. Tanabe, S. M. Cohen, *Chemical Society Reviews* **2011**, *40*, 498.

[100] S. M. Cohen, *Chemical Reviews* **2012**, *112*, 970.

[101] O. R. Evans, W. Lin, *Accounts of Chemical Research* **2002**, *35*, 511.

[102] E. Y. Lee, S. Y. Jang, M. P. Suh, *Journal of the American Chemical Society* **2005**, *127*, 6374.

[103] B. D. Chandler, D. T. Cramb, G. K. H. Shimizu, *Journal of the American Chemical Society* **2006**, *128*, 10403.

[104] W. J. Rieter, K. M. L. Taylor, H. An, L. Weili, W. Lin, *Journal of the American Chemical Society* **2006**, *128*, 9024.

[105] J.-R. Li, Y. Tao, Q. Yu, X.-H. Bu, *Chemical Communications* **2007**, 1527.

[106] L. Yan, L. Gao, L. Xing, C. Yong, *Angewandte Chemie International Edition* **2007**, *46*, 6301.

[107] G. J. Halder, C. J. Kepert, B. Moubaraki, K. S. Murray, J. D. Cashion, *Science* **2002**, *298*, 1762.

[108] D. Maspoch, D. Ruiz-Molina, J. Veciana, *Journal of Materials Chemistry* **2004**, *14*, 2713.

[109] P. D. C. Dietzel, Y. Morita, R. Blom, H. Fjellvåg, *Angewandte Chemie International Edition* **2005**, *44*, 6354.

[110] W. Ouellette, M. H. Yu, C. J. O'Connor, D. Hagrman, J. Zubieta, *Angewandte Chemie International Edition* **2006**, *45*, 3497.

[111] X.-M. Zhang, Z.-M. Hao, W.-X. Zhang , X.-M. Chen, *Angewandte Chemie International Edition* **2007**, *46*, 3456.

[112] Z. M. Wang, Y. J. Zhang, T. Liu, M. Kurmoo, S. Gao, *Advanced Functional Materials* **2007**, *17*, 1523.

[113] M. Kurmoo, *Chemical Society Reviews* **2009**, *38*, 1353.

[114] M. Alvaro, E. Carbonell, B. Ferrer, F. X. Llabrés i Xamena, H. Garcia, *Chemistry - A European Journal* **2007**, *13*, 5106.

[115] T. Okubo, R. Kawajiri, T. Mitani, T. Shimoda, *Journal of the American Chemical Society* **2005**, *127*, 17598.

[116] Q. Ye, Y.-M. Song, G.-X. Wang, K. Chen, D.-W. Fu, P. W. H. Chan, J.-S. Zhu, S. D. Huang, R.-G. Xiong, *Journal of the American Chemical Society* **2006**, *128*, 6554.

[117] Z. Xu, *Coordination Chemistry Reviews* **2006**, *250*, 2745.

[118] A. Kuc, A. Enyashin, G. Seifert, *Journal of Physical Chemistry B* **2007**, *111*, 8179.

[119] M. D. Ward, *Science* **2003**, *300*, 1104.

[120] J. L. C. Rowsell, O. M. Yaghi, *Angewandte Chemie International Edition* **2005**, *44*, 4670.

[121] X. Lin, J. Jia, P. Hubberstey, M. Schroder, N. R. Champness, *CrystEngComm* **2007**, *9*, 438.

[122] D. J. Collins, H.-C. Zhou, *Journal of Materials Chemistry* **2007**, *17*, 3154.

[123] R. E. Morris, P. S. Wheatley, *Angewandte Chemie International Edition* **2008**, *47*, 4966.

[124] S. Ma, D. Sun, J. M. Simmons, C. D. Collier, D. Yuan, H.-C. Zhou, *Journal of the American Chemical Society* **2007**, *130*, 1012.

[125] M. Dincă, J. R Long, *Angewandte Chemie International Edition* **2008**, *47*, 6766.

[126] S.-H. Cho, T. Gadzikwa, M. Afshari, S. T. Nguyen, J. T. Hupp, *European Journal of Inorganic Chemistry* **2007**, 4863.

[127] K. Sumida, D. L. Rogow, J. A. Mason, T. M. McDonald, E. D. Bloch, Z. R. Herm, T.-H. Bae, J. R. Long, *Chemical Reviews* **2012**, *112*, 724.

[128] M. P. Suh, H. J. Park, T. K. Prasad, D.-W. Lim, *Chemical Reviews* **2012**, *112*, 782.

[129] L. J. Murray, M. Dinca, J. R. Long, *Chemical Society Reviews* **2009**, *38*, 1294.

[130] Q. Min Wang, D. Shen, M. Bülow, M. Ling Lau, S. Deng, F. R. Fitch, N. O. Lemcoff, J. Semanscin, *Microporous and Mesoporous Materials* **2002**, *55*, 217.

[131] R. Custelcean, B. A. Moyer, *European Journal of Inorganic Chemistry* **2007**, *2007*, 1321.

[132] J.-R. Li, J. Sculley, H.-C. Zhou, *Chemical Reviews* **2011**.

[133] J.-R. Li, R. J. Kuppler, H.-C. Zhou, *Chemical Society Reviews* **2009**, *38*, 1477.

[134] S. Horike, M. Dincă, K. Tamaki, J. R. Long, *Journal of the American Chemical Society* **2008**, *130*, 5854.

[135] W. Lin, *Journal of Solid State Chemistry* **2005**, *178*, 2486.

[136] R.-Q. Zou, H. Sakurai, S. Han, R.-Q. Zhong, Q. Xu, *Journal of the American Chemical Society* **2007**, *129*, 8402.

[137] F. X. Llabrés i Xamena, O. Casanovaa, R. G. Tailleura, H. Garciaa, A. Corma, *Journal of Catalysis* **2008**, *255*, 220.

[138] L. Alaerts, E. Séguin, H. Poelman, F. Thibault-Starzyk, P. A. Jacobs, D. E. De Vos, *Chemistry - A European Journal* **2006**, *12*, 7353.

[139] J. Lee, O. K. Farha, J. Roberts, K. A. Scheidt, S. T. Nguyen, J. T. Hupp, *Chemical Society Reviews* **2009**, *38*, 1450.

[140] D. F. Sava, V. C. Kravtsov, F. Nouar, L. Wojtas, J. F. Eubank, M. Eddaoudi, *Journal of the American Chemical Society* **2008**, *130*, 3768.

[141] B. F. Hoskins, R. Robson, *Journal of the American Chemical Society* **2002**, *112*, 1546.

[142] L. Eunsung, K. Jaheon, H. Jungseok, W. Dongmok, K. Kimoon, *Angewandte Chemie International Edition* **2001**, *40*, 399.

[143] B. Zhao, X.-Y. Chen, P. Cheng, D.-Z. Liao, S.-P. Yan, Z.-H. Jiang, *Journal of the American Chemical Society* **2004**, *126*, 15394.

[144] B. Chen, Y. Yang, F. Zapata, G. Lin, G. Qian, E. B. Lobkovsky, *Advanced Materials* **2007**, *19*, 1693.

[145] B. Chen, L. Wang, F. Zapata, G. Qian, E. B. Lobkovsky, *Journal of the American Chemical Society* **2008**, *130*, 6718.

[146] B. V. Harbuzaru, A. Corma, F. Rey, P. Atienzar, J. L. Jordá, H. García, D. Ananias, L. D. Carlos, J. Rocha, *Angewandte Chemie International Edition* **2008**, *47*, 1080.

[147] U. Takashi, K. Ryo, O. Yusuke, N. Masataka, K. Susumu, *Angewandte Chemie International Edition* **2006**, *45*, 4112.

[148] C. J. Chuck, M. G. Davidson, M. D. Jones, G. Kociok-Kohn, M. D. Lunn, S. Wu, *Inorganic Chemistry* **2006**, *45*, 6595.

[149] U. Takashi, H. Daisuke, K. Yoshiki, T. Masaki, K. Susumu, *Angewandte Chemie International Edition* **2007**, *46*, 4987.

[150] H. Patricia, S. Christian, V.-R. María, S. Muriel, T. Francis, F. Gérard, *Angewandte Chemie International Edition* **2006**, *45*, 5974.

[151] V.-R. María, B. Francisco, A. Daniel, *Angewandte Chemie International Edition* **2007**, *46*, 7548.

[152] G. Férey, P. Horcajada, C. Serre, G. Maurin, N. A. Ramsahye, F. Balas, M. Vallet-Regi, M. Sebban, F. Taulelle, *Journal of the American Chemical Society* **2008**, *130*, 6774.

[153] *Hydrogen ,Fuel Cells & Infrastructure Technologies Program: Multi-yrear research, Development and Demonstration Plan, U. S. Department of Energy, February 2005,* http://www.eere.energy.gov/hydrogenandfuelcell/mypp/.

[154] *Basic Reearch Needs for the Hydrogen Economy, report of the Basic Energy Sciences workshop on Hydrogen, Production, Storage and Use, U. S. Department of Energy, May 13–15, 2005,* http://www.sc.doe.gov/bes/.

[155] A. G. Wong-Foy, A. J. Matzger, O. M. Yaghi, *Journal of the American Chemical Society* **2006**, *128*, 3494.

[156] A. J. Matzger, K. Koh, A. G. Wong-Foy, *Journal of the American Chemical Society* **2009**, *131*, 4184.

[157] U. Müller, A. U. Czaja, N. Trukhan, *Chemical Society Reviews* **2009**, *38*, 1284.

[158] M. Kondo, T. Yoshitomi, K. Seki, H. Matsuzaka, S. Kitagawa, *Angewandte Chemie International Edition* **1997**, *36*, 1725.

[159] I. Senkovska, S. Kaskel, *Microporous and Mesoporous Materials* **2008**, *112*, 108.

[160] T. Düren, L. Sarkisov, O. M. Yaghi, R. Q. Snurr, *Langmuir* **2004**, *20*, 2683.

[161] M. Eddaoudi, O. M. Yaghi, H. Li, T. L. Groy, *Journal of the American Chemical Society* **1998**, *120*, 8571.

[162] O. M. Yaghi, A. R. Millward, *Journal of the American Chemical Society* **2005**, *127*, 17998.

[163] G. Férey, C. Serre, *Chemical Society Reviews* **2009**, *38*, 1380.

[164] P. Z. Moghadam, PhD thesis, The University of Edinburgh **2012**.

[165] J. A. Ripmeester, G. D. Enright, C. I. Ratcliffe, K. A. Udachin, I. L. Moudrakovski, *Chemical Communications* **2006**, 4986.

Chapter 2. MOF synthesis using functionalised dipyridyl linkers

2.1. Introduction

The next most used ligands in MOF chemistry after oxygen-based ligands as discussed in Chapter 1 are the nitrogen-based ligands[1-3]. The nitrogen-based ligands usually bind metal centres via the lone pair on the nitrogen atom(s), which means that these are often neutral. The nitrogen-based ligands are known to form cationic homoleptic networks or neutral mixed-ligand networks, typically in conjunction with polycarboxylates[4-7]. The cationic homoleptic networks contain counter ions, usually coming from the metal salt used or from ionisation of the solvent, which balance the charge.

Dipyridyl-based linkers are one of the most widely used N-donor ligands which have shown a great potential to incorporate into coordination networks producing a large variety of MOFs[1, 8-12]. The most iconic of the dipyridyl ligands is 4,4′-bipyridine (4,4′-bipy) which has been used as ligand in coordination chemistry due to at least three features: its ready availability from a number of commercial sources, its structural rigidity and its suitability for a variety of metals. Dastidar and Adarsh[13] have recently reported some of the developments of coordination polymers containing functionalised dipyridyl linkers, derived from 4,4′-bipy ligand.

Recently, researchers have focused on the formation of functionalised networks as presented in Chapter 1. One of the strategies to functionalise a MOF is to use a ligand bearing a functional group that does not affect network formation and which will be prone to further chemistry processes such as interaction with a guest or even the ability to be post-synthetically converted into a more useful group[1, 14].

In this work we investigate incorporation into MOFs of two dipyridyl-based functionalised linkers, namely 3,5-bis(4-pyridyl)-1*H*-pyrazole (H**L**) and 1,4-bis(4′-pyridylethynyl)benzene (**L1**) depicted in Figure 1-28. They both encompass the aforementioned features of their parent ligand 4,4′-bipy with added benefits of a longer and functionalized backbone. H**L** and **L1** differ by the angle and the distance between the nitrogen atoms of the pyridyl rings, and the functionalities which are for H**L**, the NH group within the pyrazole ring and two triple bonds for **L1**, respectively.

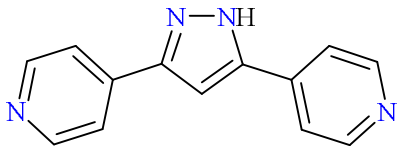

3,5-bis(4-pyridyl)-1*H*-pyrazole

H**L**

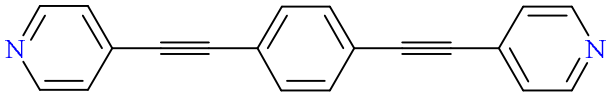

1,4-bis(4'-pyridylethynyl)benzene

L1

Figure 2-1. The functionalised dipyridyl linkers used in this work.

Both H**L** and **L1** have been previously synthesised and characterized but there are no reports of coordination networks with them. The main target of this work was to make MOFs using H**L** and **L1** and further to explore the chemistry of their functionalities. The NH group of H**L** has potential to selectively interact with guests through hydrogen bonding and the triple bonds of **L1** can be exploited as well.

The results obtained during this work are presented in two sections, each for one of the two dipyridyl-based functionalised linkers. Firstly, a more extended section with the results obtained from using H**L** and the last section slightly shorter where the use of **L1** in MOFs chemistry is discussed.

We have employed carboxylate-based ligands as well, in order to balance charges and obtain a neutral MOF, where appropriate.

2.2. MOF synthesis using 3,5-bis(4-pyridyl)-1*H*-pyrazole (HL)

2.2.1. Introduction

The 3,5-bis(4-pyridyl)-1*H*-pyrazole (H**L**) (Figure 1-28, left) known since 1954[15] was synthesised and characterised couple of decades later[10, 11] but its X-ray crystal structure was just reported late in 2006[16] by Li.

The presence of hydrogen bond donors (N-H group in the pyrazole ring) and hydrogen bond acceptors (pyridine nitrogens) resulted in intermolecular contact within the X-ray crystal structure of H**L** which appears to form infinite head-to-tail chains.[16] The tail is represented by the N-H group of the pyrazole ring and the head by the nitrogen atom of one of the pyridine ring. The nitrogen atom of the second pyridine ring is hydrogen bonded

to one of the three water molecules present within the X-ray crystal structure of H**L**. The remaining nitrogen atom of the pyrazole ring acts as a hydrogen bond acceptor for one of the three water molecules. Therefore the H**L** ligand contains both hydrogen bond donors (N-H groups from within pyrazole ring) and acceptors (nitrogen atoms from within the pyrazole or pyridine rings) and is used to promote interactions with a guest molecule which in this case is water molecule (through N-H group) plus has the potential to assist with network formation (formation of infinite head-to-tail chains).

The first two complexes incorporating H**L** have been reported in the same work of Li[16]. These complexes are two isomers of copper(I) with H**L** and thiocyanate which acts as a second ligating spacer where the deprotonated ligand $\mathbf{L}^-$ binds to four Cu atoms acting as a tetradentate ligand.

It is noteworthy that the Cambridge Structural Database (CSD) revealed the existence of just eleven structures containing H**L** including the two examples mentioned above.[17-20] Moreover H**L** linker coordinates through the deprotonated pyrazolyl group in addition to the two pyridyl groups in all these eleven complexes reported all by the same group of Li.

The lack of coordination networks incorporating H**L** and especially that none of the reported complexes contain H**L** linker in its non-deprotonated form motivated the Burrows group to start investigating the use of H**L** as a neutral linker in MOF chemistry. As the H**L** ligand contains both hydrogen bond donors (N-H groups) and acceptors in the pyrazole ring it may be used to promote interactions with a guest molecule (through N-H group) or has the potential to assist with network formation.

The first aim of this work was to see if H**L** can be incorporated into MOFs, in its neutral form. It is believed that this kind of MOF will be able to show interesting chemistry at the NH group, which can act as an excellent site for further chemistry. A reactive site into a MOF is always what researchers are looking for, to further develop its potential.

Results suggest that 3-D MOFs containing only H**L** as a linker cannot be obtained and therefore we have asked ourselves if H**L** can be incorporated into mixed-linker MOFs in conjunction with a dicarboxylate linker, playing the pillaring role. In this respect, various

reactions employing H**L** and aromatic dicarboxylic acids such as those depicted in Figure 2-2 , have been undertaken.

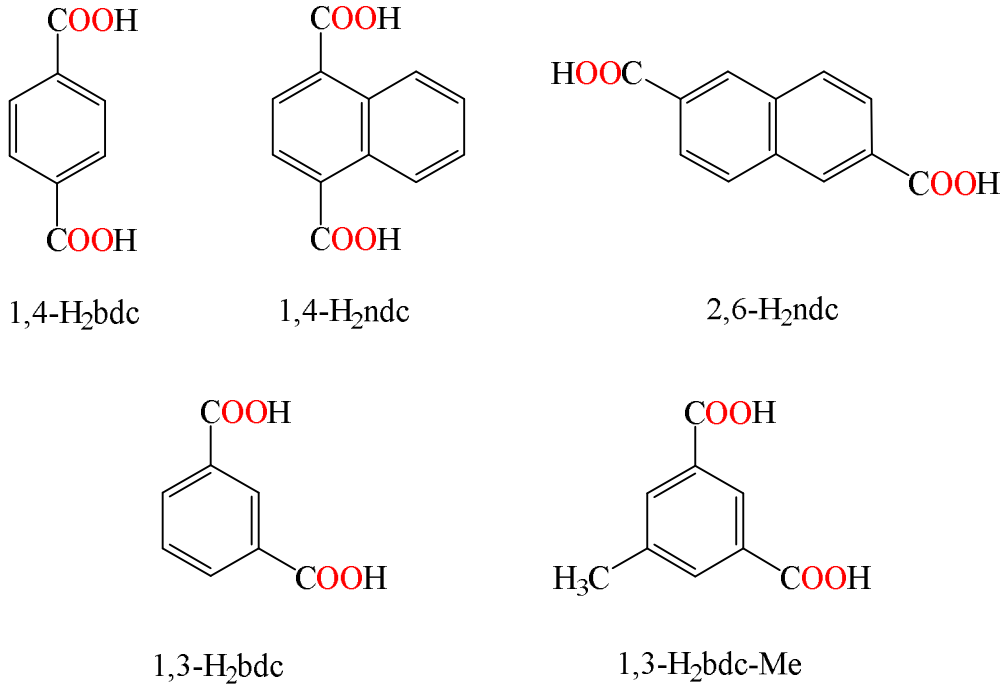

Figure 2-2. The structures of the aromatic dicarboxylic acids used in this study.

The "one-pot" pillaring strategy mentioned in Chapter 1 of this thesis has been used in this work. It is likely that, in conjunction with a dicarboxylate the H**L** to remain in its neutral form when incorporated into a mixed-linker MOF.

The effect of larger substituent or longer linkers on the pores obtained was investigated during this work. The slight degree of flexibility exhibited by H**L** compared with the rigidity of 4,4'-bipy increases the potential of accessing a much larger variety of 3-D MOFs when in combination with a second linker. The difficulty is that adding more than one linker to a reaction changes the variables in a manner whereby the products may not be homogeneous.

The ultimate aim is to assess the properties of the synthesised MOFs, in their activated forms. A potential use of MOFs containing H**L** in its neutral form would be as drug carriers, the NH group attached on MOF being capable of interacting with drugs whose size fits into pores of the carrier MOF.

2.2.2. Results and discussion

The use of 3,5-bis(4-pyridyl)-1*H*-pyrazole (H**L**) has been investigated in reactions with the nitrates of zinc(II), copper(II), cobalt(II), cadmium(II) and nickel(II), the acetates of zinc(II), copper(II), magnesium(II) and nickel(II) and $ZnCl_2$ in DMF, methanol and water.

Compounds formulated as $[Zn_3(OAc)_6(H\mathbf{L})_4]$[21] and $[Zn(OAc)_2(H\mathbf{L})]\cdot 0.5MeOH$[21] were obtained by reacting H**L** with $Zn(OAc)_2$, in DMF and methanol, respectively at room temperature. The hydrothermal conditions used for reactions of H**L** with $Zn(OAc)_2$ and $ZnCl_2$ produced $[Zn(OAc)_2(H\mathbf{L})_2]\cdot H_2O$ **1**[21] and $[ZnCl_2(H\mathbf{L})]$[21] **2**, respectively, discussed later in this chapter. It can be observed that the ratios of Zn:H**L** are different in these compounds but notably this was not influenced by the ratio of starting materials used in the reactions.

One goal was to increase the MOFs dimensionality by employing a second ligand. Further to these investigations, "one-pot" reactions of H**L** with dicarboxylic acids and zinc(II) salts were investigated. The zinc(II) salts used are chlorides and nitrates of zinc(II) and the dicarboxylic acids used (Figure 2-2) are: 1,4-benzenedicarboxylic acid (1,4-H_2bdc), 1,4-naphthalenedicarboxylic acid (1,4-H_2ndc), 2,6-naphthalenedicarboxylic acid (2,6-H_2ndc), 1,3-benzenedicarboxylic acid (1,3-H_2bdc) and 5-methyl-1,3-benzenedicarboxylic acid (1,3-H_2bdc-Me).

H**L** has been reacted with the dicarboxylic acids mentioned above and $ZnCl_2$ and $Zn(NO_3)_2\cdot 6H_2O$ in DMF and DEF at various concentrations and at temperatures of 120°C and 160°C. Therefore the effect of counter-ion, concentration and temperature for each of the dicarboxylic acids involved has been investigated.

Ten new X-ray single crystal structures have been collected from this work, analysed and discussed in this section. Four of the resulted structures have incorporated just one of the two ligands (H**L** or one of the dicarboxylic acids listed above) added to the reaction mixture. This was observed to happen usually at high reaction temperatures such as 160°C. When crystals not suitable for X-ray single crystallography were produced their PXRD analysis helped to a better understanding of the Metal-H**L**-dicarboxylate system.

Similar reactions were also run using microwave radiation, and from those undertaken in DMF, an unidentified product resulted whose PXRD proved identical at different temperatures and concentrations. From reactions undertaken in DEF another unidentified compound resulted at different temperatures and concentrations but this is different from the one resulted in DMF.

2.2.2.1. 3,5-bis(4-pyridyl)-1*H*-pyrazole (HL)

The H**L** ligand was synthesised using a two-step method adapted from literature,[9-11, 15] as shown in Scheme 2-1.

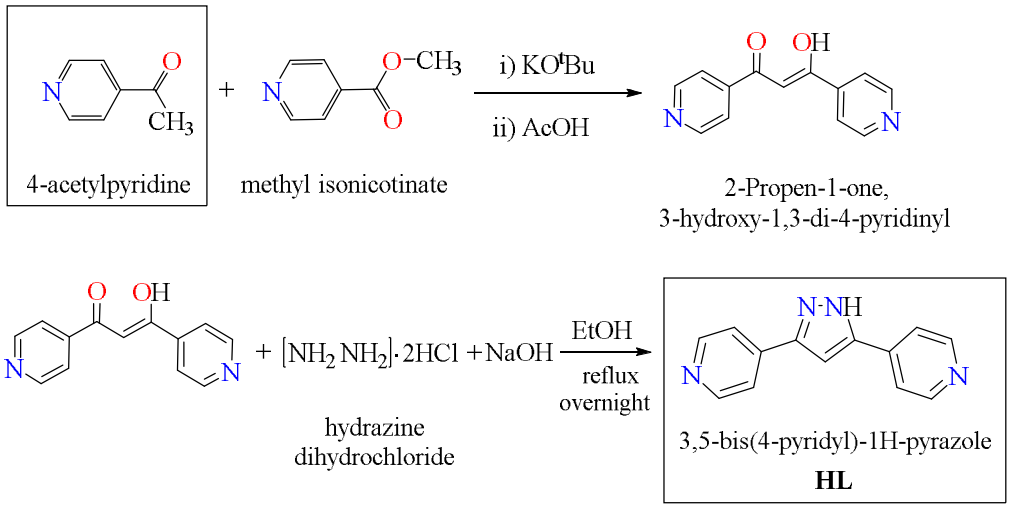

*Scheme 2-1. The two-step synthesis of H**L**.*

Equimolar amounts of 4-acetylpyridine, methyl isonicotinate and KO^{t}Bu (potassium tert-butoxide) were stirred vigorously together. The reaction initiated after about 5 seconds and gave off methanol, while the solution turned dark and began to solidify. The reaction mixture was left to cool down immediately after adding KO^{t}Bu with the aid of a condenser. This formed solid was dissolved in water and addition of acetic acid produced a white solid. The composition of the white solid was confirmed through ^{1}H NMR spectroscopy to be 2-propen-1-one, 3-hydroxy-1,3-di-4-pyridinyl.

2-Propen-1-one, 3-hydroxy-1,3-di-4-pyridinyl was then combined with hydrazine dihydrochloride and sodium hydroxide in ethanol and the resultant suspension heated at reflux overnight. The product was confirmed to be H**L** through ^{1}H NMR spectroscopy. H**L** synthesis and characterisations are detailed in the experimental section of this chapter.

2.2.2.2. $[Zn(OAc)_2(HL)_2]\cdot H_2O$ 1

Crystals of suitable X-ray quality of formula $[Zn(OAc)_2(H\mathbf{L})_2]\cdot H_2O$ **1**, were collected from the hydrothermal reaction of $Zn(OAc)_2\cdot 2H_2O$ with H**L**. The formation of **1** is not influenced by the concentration of the reactants and can be obtained in just 5 min under microware radiation at 120°C in water.

The crystal data and refinement parameters for **1** are shown in Table 2-1.

*Table 2-1. Crystallographic data and refinement parameters for **1**.*

Empirical formula	$C_{30}H_{28}N_8O_5Zn$	
Formula weight	645.97	
Temperature	150(2) K	
Wavelength	0.71073 Å	
Crystal system	Monoclinic	
Space group; Z	C2/*c*, 4	
Unit cell dimensions	a = 20.0990(6) Å	α = 90°
	b = 9.1430(4) Å	β = 115.116(2)°
	c = 17.5490(7) Å	γ = 90°
Volume	2919.98(19) $Å^3$	
Density (calculated)	1.469 g/cm^3	
Crystal size	0.30 x 0.28 x 0.08 mm	
Theta range for data collection	3.77 to 25.05°	
Reflections collected/ observed (>2σ)	16494/ 1860 [R(int) = 0.0902]	
Data Completeness	0.995	
Goodness-of-fit on F^2	1.171	
Final R indices [I>2σ(I)]	$R1$ = 0.0582, w$R2$ = 0.1443	
R indices (all data)	$R1$ = 0.0904, w$R2$ = 0.1696	
Largest diff. peak and hole	0.565 and -0.466 $eÅ^{-3}$	

The asymmetric unit of **1** (Figure 2-3) contains half of a zinc atom, one acetate ligand disordered over two sites in a 60 : 40 ratio, one H**L** ligand and half a molecule of included water. The hydrogen from the half water molecule could not been located crystallographically.

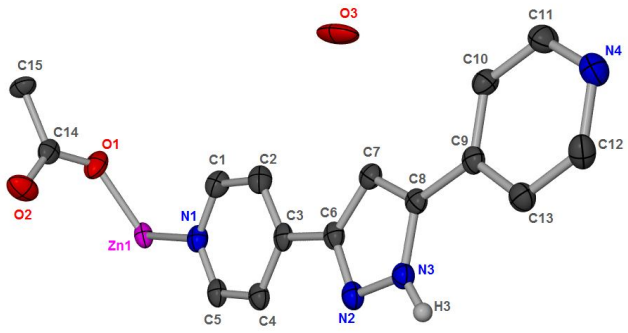

*Figure 2-3. The asymmetric unit of **1** showing thermal ellipsoids at the 30% probability level. The minor disordered acetate and the hydrogen atoms except for H3 have been omitted for clarity.*

The zinc centre is located on a two-fold rotation axis and it is coordinated to two acetates and two pyridyl groups, as shown in Figure 2-4.

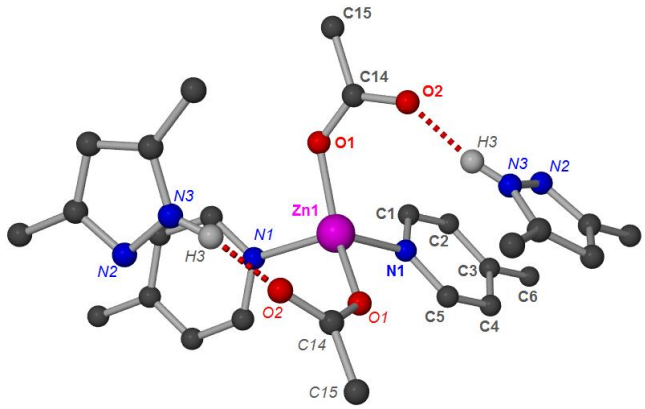

*Figure 2-4. The coordination environment around zinc centre in **1**. Symmetry generated atoms are labelled in italics. Half a water molecule and hydrogen atoms except of H3 have been omitted for clarity.*

The bond angles around the zinc centre range from 95.4(3)° to 140.3(4)° for the major acetate components. Selected bond lengths and angles are given in Table 2-2.

*Table 2-2. Selected bond lengths (Å) and angles (°) for **1**.**

Atoms	Bond length (Å)	Atoms	Angle (°)
Zn1-O1	1.899(6)	O1-Zn1-N1	108.1(2)
Zn1-N1	2.033(4)	O1-Zn1-N1#1	95.4(3)
		N1-Zn1-N1#1	106.7(2)
		O1#1-Zn1-O1	140.3(4)

Symmetry transformations used to generate equivalent atoms: **#1 -x, y, -z-1/2.*

The H**L** ligands are coordinated through only one of the pyridyl groups, giving discrete molecules of **1**. The acetate ligands are coordinated through O1 to zinc atoms and through the other oxygen O2, are hydrogen bonded to H3 (N3···O2#2[1] distance of 2.642Å, H3···O2#2[1] distance of 1.75Å and N3−H3···O2#2[1] angle of 169°) linking the molecules of **1** into double-stranded zig-zag chains, as shown in Figure 2-5.

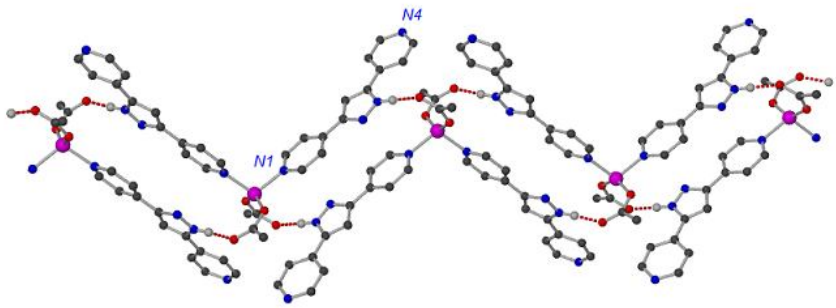

*Figure 2-5. Part of the double-stranded chain structure adopted by **1**. The minor positions of the disordered acetates and carbon-bound hydrogen atoms have been omitted for clarity. Symmetry generated atoms are labelled in italics.*

In addition, a O3···O3 separation of 2.919 Å suggests hydrogen bonding between water molecules is also present.

Overall, these interactions interlink the complex molecules of **1** into a triply-interpenetrated three-dimensional network (Figure 2-6).

[1] Symmetry transformations used to generate equivalent atoms: #2 1/2-x., 1/2-y, -z.

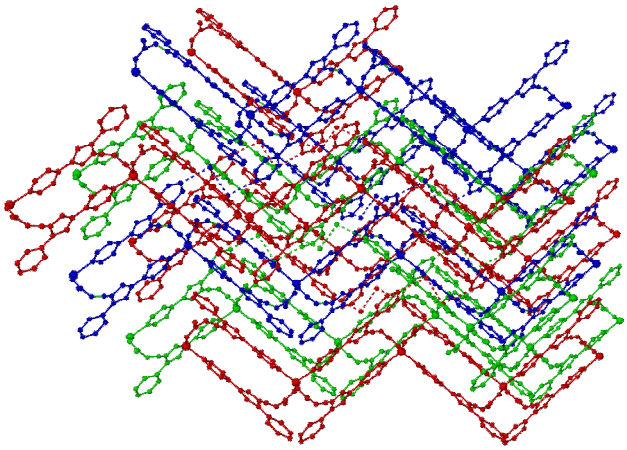

*Figure 2-6. The triply interpenetrated network adopted by **1**. The hydrogen-bonded double-stranded chains are shown in different colours. Hydrogen atoms except of H3 have been omitted for clarity.*

Similar to **1**, in the H**L**-acetate structures reported by Burrows[21] $[Zn_3(OAc)_6(HL)_4]$ (Figure 2-7, left) and $[Zn(OAc)_2(HL)]\cdot 0.5MeOH$ (Figure 2-7, right), N–H···O hydrogen bonds with the pyrazole NH groups acting as donors, and acetate oxygen atoms acting as acceptors link the chains into three-dimensional networks.

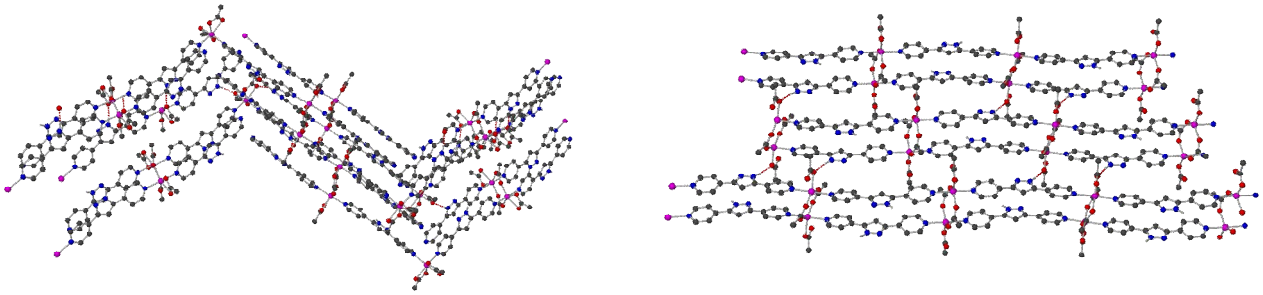

Figure 2-7. The structure of: (left) $[Zn_3(OAc)_6(HL)_4]$ and (right) $[Zn(OAc)_2(HL)]\cdot 0.5MeOH$. Hydrogen atoms except those of pyrazole rings and methanol solvent molecules are omitted for clarity.

The double-stranded chains are present in all of the three H**L**-acetate structures but whilst in both $[Zn_3(OAc)_6(HL)_4]$ and $[Zn(OAc)_2(HL)]\cdot 0.5MeOH$ the strands are linked together through bridging acetate ligands, in **1** the two strands are interconnected by hydrogen bonds. In $[Zn_3(OAc)_6(HL)_4]$ each chain is "broken" after every fourth H**L** ligand whereas in $[Zn(OAc)_2(HL)]\cdot 0.5MeOH$ the double-stranded chains are continuous and much

straighter than in $[Zn_3(OAc)_6(H\mathbf{L})_4]$. The included methanol molecules within $[Zn(OAc)_2(H\mathbf{L})]\cdot 0.5MeOH$ interact with the network in similar manner as water molecules of **1** through O-H···O hydrogen bonds.

The TGA traces of samples of as-made **1** following heating in the oven at 150°C for 3 hours, at 200°C for 2 hours and at 250°C for 2 hours are shown in Figure 2-8 in comparison with that of the as-made **1**. The TGA trace of the as-made **1** (Figure 2-8, red trace) shows a small mass loss of ~3% up to 200°C which can be attributed to the loss of molecule of water (calculated mass loss of a molecule of water for **1** is 2.8%). Another two mass losses are further shown: a first mass loss of ~9% up to 300°C which can be attributed to the loss of one acetate ligand (calculated mass loss of one acetate ligand for **1** is 9.1%) and a second mass loss of ~15% up to 440°C after which **1** is decomposing. The mass loss of ~15% from 300°C to 440°C can be attributed to the loss of the second acetate ligand plus a part of H**L** (calculated mass loss for one H**L** for **1** is 34.4%). This TGA analysis suggests that the removal of both acetate ligands without altering the integrity of H**L** is not been achievable under these conditions.

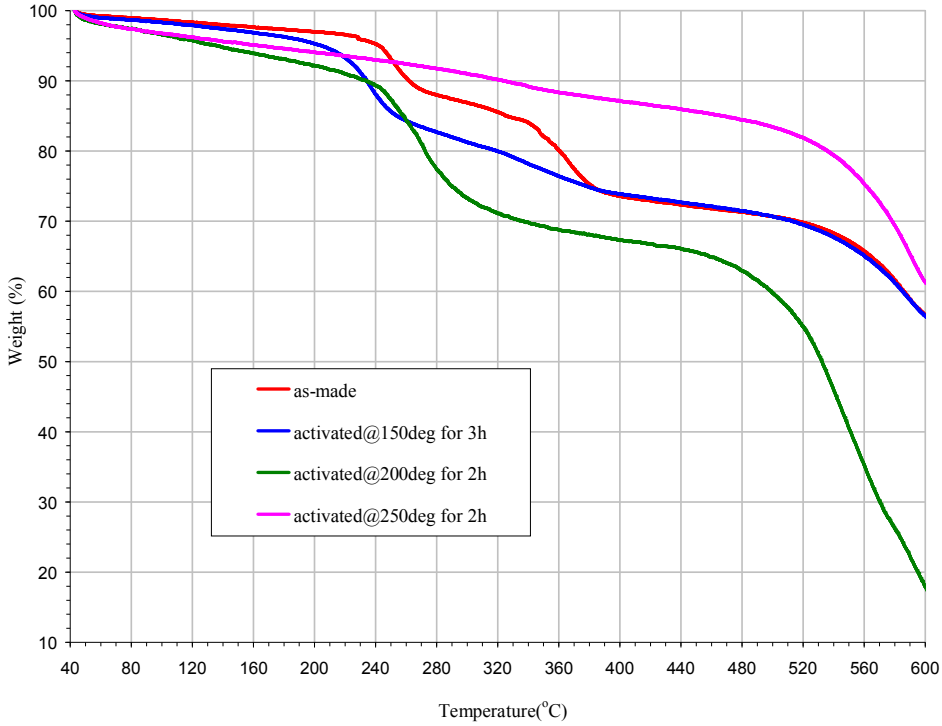

*Figure 2-8. TGA traces of samples of **1** following heating at different temperatures compared with that of the as-made **1**.*

The PXRD patterns of samples of **1** following heating at different temperatures in comparison with that of the as-made **1** are shown in Figure 2-9. The samples of **1** after heating at 150°C and 200°C have similar PXRD patterns showing a new peak at 2-θ ~11° whereas the PXRD pattern of the sample of **1** after heating at 250°C suggests that the framework of **1** is decomposing under these conditions which is in agreement with the information suggested by the TGA trace of the sample of **1** after heating at 250°C (Figure 2-8, pink trace).

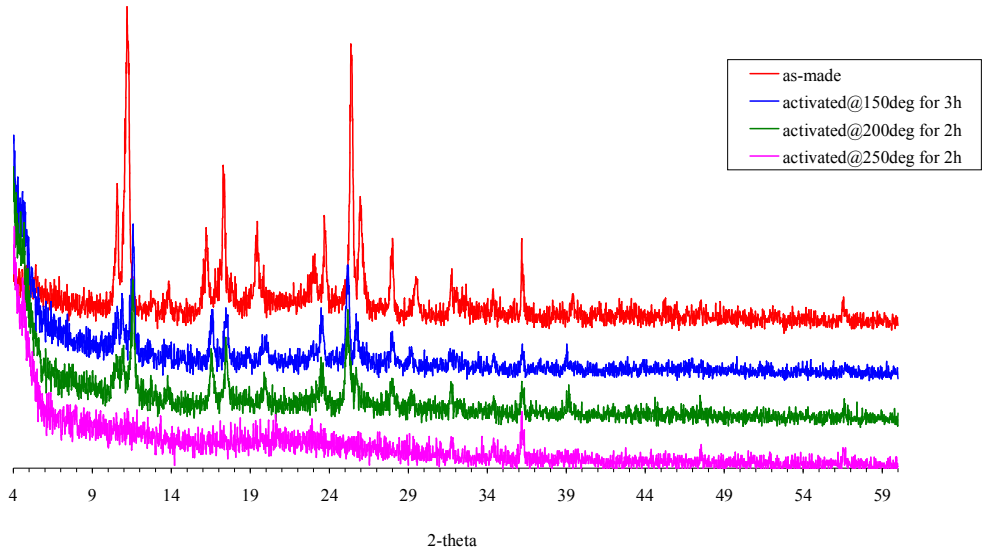

*Figure 2-9. The PXRD patterns of the samples of **1** following heating at different temperatures in comparison with that of the as-made **1**.*

2.2.2.3. $ZnCl_2$(HL) 2

The hydrothermal reaction of H**L** with $ZnCl_2$ produced in 36 hours colourless crystals of suitable size for X-ray single diffraction which were formulated as $ZnCl_2$(H**L**) **2**. The crystal data and refinement parameters for **2** are given in Table 2-3.

*Table 2-3. Crystallographic data and refinement parameters for **2**.*

Empirical formula	$C_{13}H_{10}Cl_2N_4Zn$
Formula weight	358.52

Temperature	150(2) K	
Wavelength	0.71073 Å	
Crystal system	Monoclinic	
Space group; Z	$P2_1/n$, 4	
Unit cell dimensions	a = 5.2750(1) Å	α = 90°
	b = 21.5070(3) Å	β = 101.063(1)°
	c = 12.2530(2) Å	γ = 90°
Volume	1364.26(4) Å^3	
Density (calculated)	1.746 g/cm^3	
Crystal size	0.30 x 0.30 x 0.25 mm	
Theta range for data collection	3.52 to 27.50°	
Reflections collected/ observed (>2σ)	25196/ 2784 [R(int) = 0.0435]	
Data Completeness	0.997	
Goodness-of-fit on F^2	1.050	
Final R indices [I>2σ(I)]	R1 = 0.0263 wR2 = 0.0628	
R indices (all data)	R1 = 0.0317 wR2 = 0.0658	
Largest diff. peak and hole	0.349 and -0.448 eÅ^{-3}	

Microcrystalline powders of **2** can be formed in either MeOH (immediately) or DMF (overnight) and use of a double amount of $ZnCl_2$ produces **2** in better yields. Moreover **2** can be prepared in both DMF and water much faster under microwave radiation, in 5 min either at 120°C in water or at 40°C in DMF. If the H**L**-acetate structure formation is so dependent of the solvent used (DMF, water or MeOH), the structure of **2** is obtained if either of these solvents were used. The concentration of the reactants does not influence the structural output of any of the H**L**-acetate or H**L**-chloride compounds.

The asymmetric unit of **2** (Figure 2-10) contains one zinc atom, two chlorine atoms and one H**L** ligand.

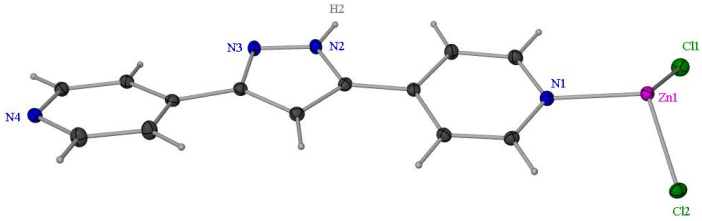

*Figure 2-10. The asymmetric unit of **2** showing thermal ellipsoids at the 30% probability level.*

The zinc centre is coordinated (Figure 2-11) to two chlorides and two pyridyl groups, with bond angles ranging from 103.24(5)° to 124.26(2)° (Table 2-4). The geometry about the zinc centre is distorted tetrahedral.

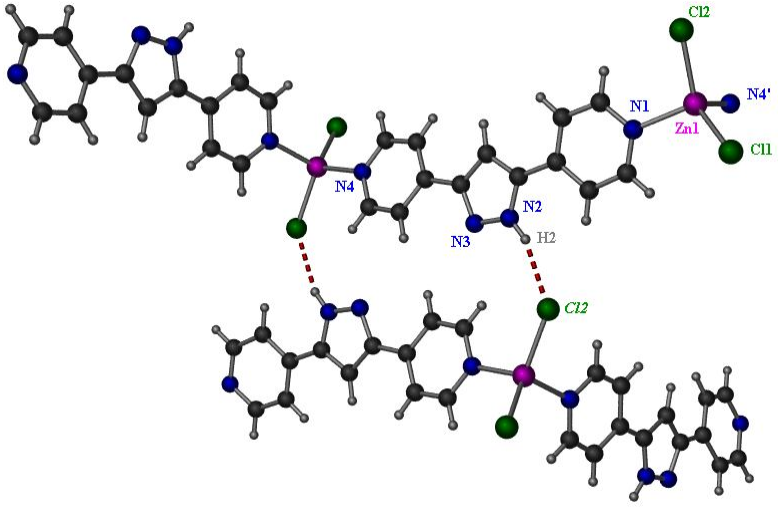

Figure 2-11. The coordination environment around zinc centre showing N-H···Cl hydrogen bonds. Symmetry generated atoms are shown as primed atoms or labelled in italics.

The selected bond lengths and angles for **2** are given in Table 2-4.

*Table 2-4. Selected bond lengths (Å) and angles (°) for **2**.**

Atoms	Bond length (Å)	Atoms	Angle (°)
Zn1-N4’	2.0402(15)	N4’-Zn1-N1	107.40(6)
Zn1-N1	2.0493(15)	N4’-Zn1-Cl1	107.04(5)
Zn1-Cl1	2.2239(5)	N1-Zn1-Cl1	108.21(5)

Zn1-Cl2	2.2528(5)	N4'-Zn1-Cl2	105.72(4)
		N1-Zn1-Cl2	103.24(5)
		Cl1-Zn1-Cl2	124.26(2)
**Symmetry transformation used to generate N4': -x+1/2, y+1/2, -z+3/2*			

The H**L** ligands are coordinated through both their pyridyl groups, and link the $ZnCl_2$ units into zig-zag chains. From the two coordinated chlorides just one is involved in hydrogen bonding (N2···Cl2#2[2] distance of 3.221Å, N2–H2···Cl2#2[1] angle of 162° and H2···Cl2#2[2] distance of 2.37Å). The N–H···Cl hydrogen bonds connect the zig-zag chains into 2-D sheets (Figure 2-12). These sheets contain $R_2^2(20)$ and $R_2^2(42)$ rings. The limiting of dimensionality to 2-D can be attributed to the reduced number of hydrogen bond donors.

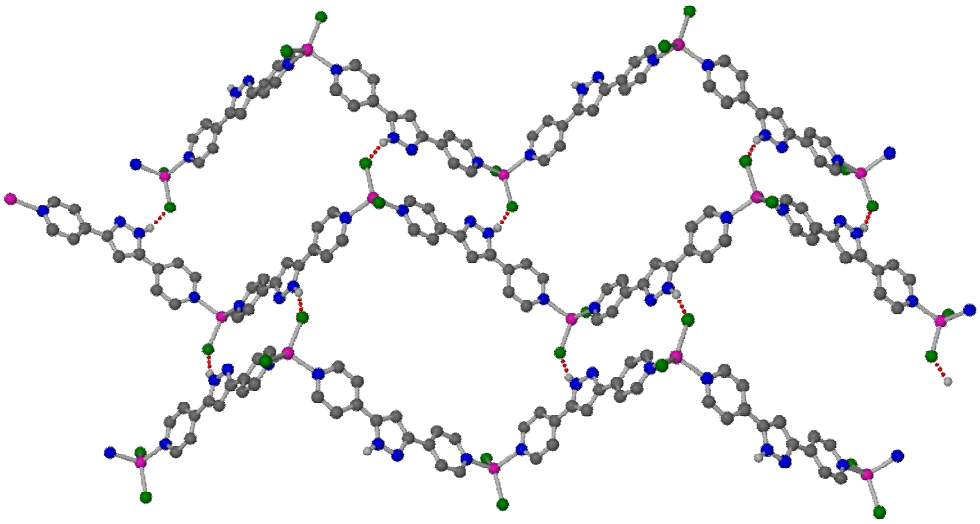

*Figure 2-12. The structure of **2** showing a 2-D sheet.*

The structure of **2** consists of zig-zag chains that are cross-linked into 2-D sheets by N–H···Cl hydrogen bonds whereas the structures with acetates - $Zn_3(OAc)_6(HL)_4$, $[Zn(OAc)_2(HL)]\cdot 0.5MeOH$ and **1** - all contain double-stranded chains, with bridging ligands and hydrogen bonds linking individual chains into pairs.

The TGA trace of **2** (Figure 2-13) shows a steady relatively small mass loss (2.5%) up to 320°C. A further mass loss of 31.5% occurs from 320°C to 495°C after which the TGA

[2] Symmetry transformations used to generate equivalent atoms: #2 x-3/2, -y+5/2, z-1/2.

trace indicates that **2** is decomposing. The TGA indicates that the break down of **2** is not straightforward. The mass loss up to 320°C is too small to be attributed to the loss of chlorides (mass loss calculated for one chloride for **2** is 10%) which is a indication that the chlorides cannot be removed that easily. The loss of 31.5% between 320°C and 495°C can be attributed to the loss of part of H**L** (mass loss calculated for one H**L** for **2** is 62%).

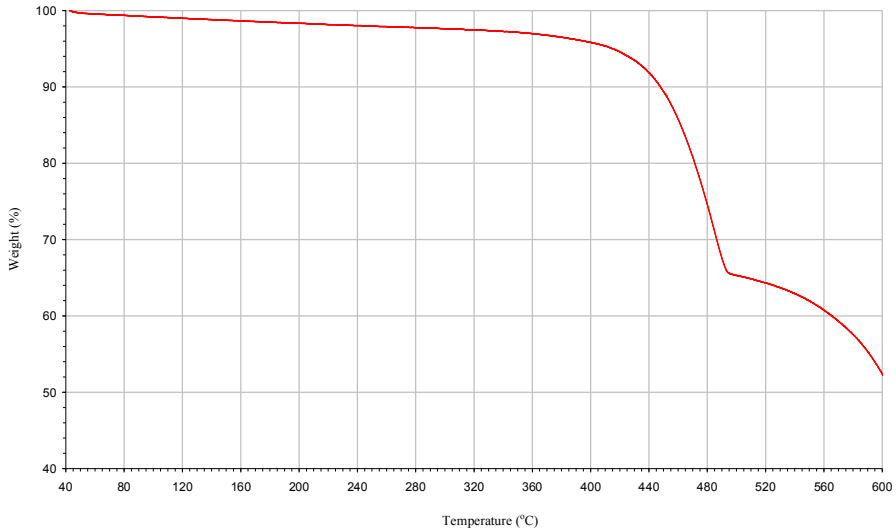

*Figure 2-13. TGA trace for as-made **2**.*

2.2.2.4. [Zn$_4$(HL)$_4$(1,4-bdc)$_4$]·4DMF 3

A reaction mixture of H**L**, 1,4-H$_2$bdc and ZnCl$_2$ (1:2:2 molar ratio) in DMF at 120°C produced in 2 days large block shaped colourless crystals suitable for X-ray analysis. The crystal data analysis (Table 2-5) revealed a MOF with formula [Zn$_4$(H**L**)$_4$(1,4-bdc)$_4$]·4DMF, **3**.

*Table 2-5. Crystallographic data and refinement parameters for **3**.*

Empirical formula	$Zn_4O_{20}N_{20}C_{96}H_{84}$
Formula weight	2099.31
Temperature	150(2) K
Wavelength	0.71073 Å
Crystal system	Orthorhombic
Space group; Z	$P2_12_12_1$, 4

Unit cell dimensions	a = 16.5520(2) Å	α = 90°
	b = 18.8640(2) Å	β = 90°
	c = 29.4330(3) Å	γ = 90°
Volume	9190.07(17) Å^3	
Density (calculated)	1.517 g/cm^3	
Crystal size	0.35 x 0.30 x 0.28 mm	
Theta range for data collection	3.52 to 27.50°	
Reflections collected/ observed (>2σ)	125929/ 16236 [*R*(int) = 0.0638]	
Data Completeness	0.995	
Goodness-of-fit on F^2	1.060	
Final *R* indices [I>2σ(I)]	*R1* = 0.0389 w*R2* = 0.0715	
R indices (all data)	*R1* = 0.0651 w*R2* = 0.0782	
Largest diff. peak and hole	0.275 and -0.323 eÅ^{-3}	

The asymmetric unit of **3** (Figure 2-14) contains four zinc centres, four H**L** linkers, four 1,4-bdc moieties and four DMF lattice solvent molecules. For the DMF based on N19, all atoms except the nitrogen atom are disordered over two sites in a 65:35 ratio.

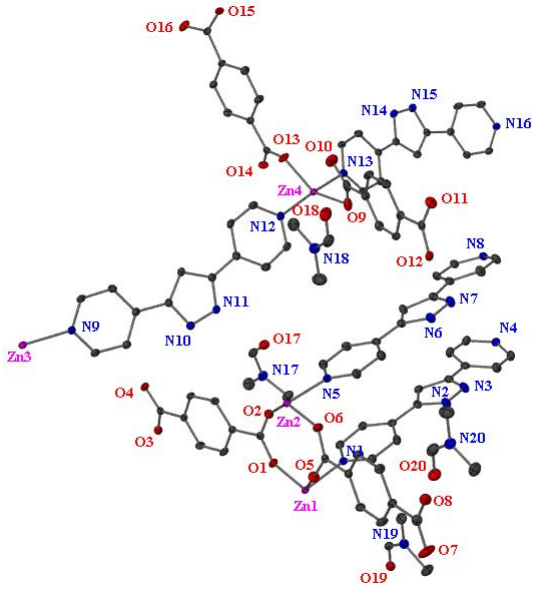

*Figure 2-14. The asymmetric unit of **3** showing thermal ellipsoids at the 30% probability level. The minor disorder of DMF based on N19 and the hydrogen atoms have been omitted for clarity.*

A 1,4-bdc ligand coordinates to Zn1 with one carboxylate end into a chelating fashion and the other carboxylate end bridges Zn1 and Zn2 atoms. A second 1,4-bdc ligand bridges with a carboxylate end Zn1 and Zn2 atoms and through the other carboxylate end is linked into a monodentate fashion to Zn2 as shown in Figure 2-15, left. The $Zn_2(carboxylate)_4$ building blocks are linked into sheets by the benzene rings of 1,4-bdc ligands as shown in Figure 2-15, right.

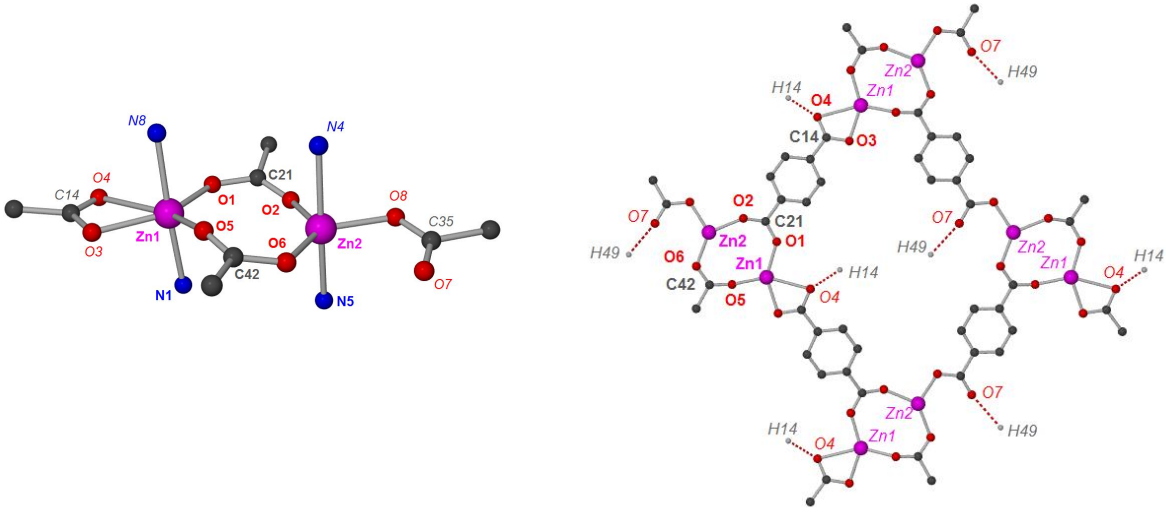

*Figure 2-15. Structure of **3** showing: (left) the $Zn_2(carboxylate)_4N_4$ building block, containing Zn1···Zn2 and (right) [Zn(1,4-bdc)] sheet, containing Zn1···Zn2 units. Symmetry generated atoms are labelled in italics. Hydrogen atoms except those involved in hydrogen bonding have been omitted for clarity.*

The intradinuclear Zn1···Zn2 separation is 3.95Å and the geometry around Zn1 can be best described as distorted octahedral whereas Zn2 atoms show distorted trigonal bipyramidal geometry. The Zn2···O7 distance of 2.980Å and the bond lengths C35-O7 = 1.227(4)Å and C35-O8 = 1.275(4)Å indicate that the carboxylate group bearing O7 and O8 is coordinated to Zn2 just through O8. The bond angles around Zn1 centre range from 57.12(8)° to 116.88(10)° and around Zn2 from 100.74(10)° to 132.61(10)° (Table 2-6).

*Table 2-6. Selected bond lengths (Å) and angles (°) for **3****

Atoms	Bond length (Å)	Atoms	Angle (°)
Zn1-O1	2.014(2)	O5-Zn1-O1	116.88(10)
Zn1-O5	2.004(2)	O3#1-Zn1-O4#1	57.12(8)
Zn1-O3#1	2.063(2)	N1-Zn1-N8#2	175.54(10)
Zn1-O4#1	2.486(2)	O8#3-Zn2-O2	100.74(10)
Zn2-O2	2.035(2)	O8#3-Zn2-O6	126.65(10)
Zn2-O6	1.973(2)	O6-Zn2-O2	132.61(10)
Zn2-O8#3	1.967(2)	N5-Zn2-N4#2	173.97(10)
Zn3-O12#3	2.039(2)	O14#4-Zn3-O12#3	126.99(10)
Zn3-O14#4	2.005(2)	O14#4-Zn3-O15#5	91.55(10)
Zn3-O15#5	2.044(2)	O12#3-Zn3-O15#5	141.45(10)
Zn4-O9	2.000(2)	N9-Zn3-N16#6	175.24(10)
Zn4-O11#7	2.014(2)	O9-Zn4-O11#7	95.96(11)
Zn4-O13	1.981(2)	O13-Zn4-O9	136.53(11)
Zn1-N8#2	2.169(3)	O13-Zn4-O11#7	126.96(10)
Zn1-N1	2.122(3)	N13-Zn4-N12	173.27(10)
Zn2-N5	2.154(3)		
Zn2-N4#2	2.203(3)		
Zn3-N16#6	2.179(3)		
Zn3-N9	2.153(2)		
Zn4-N13	2.170(3)		
Zn4-N12	2.207(3)		

**Symmetry transformations used to generate equivalent atoms: #1 -x+1, y-1/2, -z+1/2; #2 -x+3/2, -y, z+1/2; #3 -x+2, y+1/2, -z+1/2; #4 -x+3/2, -y+1, z+1/2; #5 -x+2, y-1/2, -z+1/2; #6 x, y, z+1; #7 x-1/2, -y+1/2, -z.*

In the Zn3···Zn4 units, one carboxylate end bridges between Zn3 and Zn4 atoms and the other carboxylate end is coordinated through a single oxygen either to Zn3 or Zn 4 (O9 to Zn4 or O15 to Zn3) in an alternating way acting therefore as a monodentate ligand on this end as shown in Figure 2-16, left. The intradinuclear Zn3···Zn4 separation is 3.97Å and

Zn3 and Zn4 atoms show distorted trigonal bipyramidal geometry. The Zn3···O16 distance of 2.604Å and the bond lengths C72-O15 = 1.256(4)Å and C72-O16 = 1.243(4)Å indicate that the carboxylate group bearing O15 and O16 is coordinated to Zn3 just through O15. The Zn4···O10 distance of 2.699Å and the bond lengths C57-O9 = 1.251(5)Å and C57-O10 = 1.239(5)Å indicate that the carboxylate group bearing O9 and O10 is coordinated to Zn4 just through O9. The bond angles around Zn3 centre range from 91.55(10)° to 141.45(10)° and around Zn4 from 95.96(11)° to 136.53(11)° (Table 2-6).

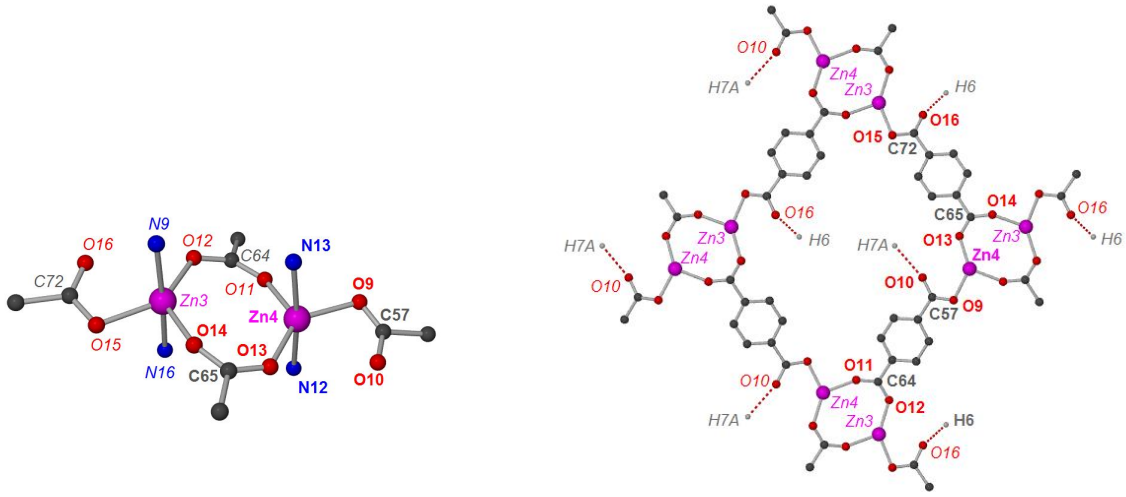

*Figure 2-16. Structure of **3** showing: (left) the $Zn_2(carboxylate)_4N_4$ building block, containing Zn3···Zn4 and (right) [Zn(1,4-bdc)] sheet, containing Zn3···Zn4 units. Symmetry generated atoms are labelled in italics. Hydrogen atoms except those involved in hydrogen bonding have been omitted for clarity.*

All of the pyrazole NH groups are involved in N–H···O hydrogen bonding – two form hydrogen bonds to the carboxylate oxygen atoms (O4 and O16) in the neighbouring framework, and these interactions link the interpenetrated frameworks together (Table 2-7). The other two NH groups based on N3 and N11 form hydrogen bonds with included DMF molecules containing O19/O19A and O17. All four DMF solvent molecules are located in the pores of **3** with the DMFs based on N19 and N17 hydrogen bonded to the framework whereas the DMFs based on N18 and N20 are non-bonded.

*Table 2-7. Hydrogen bond parameters for **3**.**

Atoms	Bond length (Å)	Atoms	Angle (°)
H3···O19A#1	1.79	N3–H3···O19A#1	171.25
N3···O19A#1	2.663	N3–H3···O19#1	168.42
H3···O19#1	2.04	N11-H11···O17	162.28
N3···O19#1	2.910	N6-H6···O16#2	164.28
H11···O17	1.96	N14-H14···O4#3	153.34
N11···O17	2.881	C7-H7A···O10#4	175.79
H6···O16#2	1.83	C49-H49···O7#5	164.08
N6···O16#2	2.687		
H14··O4#3	1.94		
N14···O4#3	2.752		
H7A···O10#4	2.45		
C7···O10#4	3.393		
H49···O7#5	2.42		
C49···O7#5	3.346		

**Symmetry transformations used to generate equivalent atoms: #1 -x+1, y-1/2, -z+1/2; #2 -x+3/2, -y, z+1/2; #3 -x+2, y+1/2, -z+1/2; #4 -x+3/2, -y+1, z+1/2; #5 -x+2, y-1/2, -z+1/2*

Each sheet is pillared by H**L** linkers forming a cube-like cage which is interpenetrated by another identical cube-like cage (Figure 2-17, left). The two interpenetrated cube-like cages of **3** are shown in a space filling representation in Figure 2-17, right.

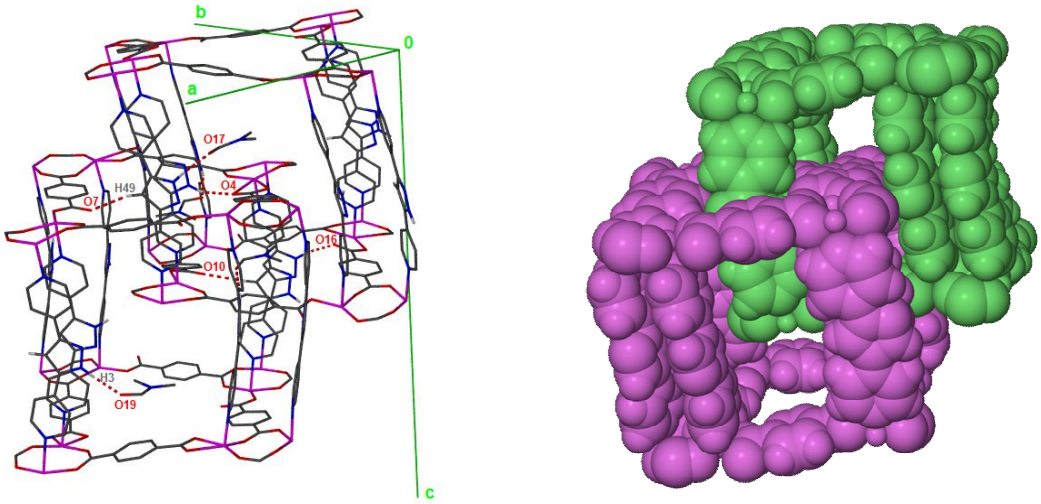

*Figure 2-17. The 3-D structure of **3** showing: (left) 2-fold interpenetrated cube-like cages held together through hydrogen bonds. The hydrogen atoms except those involved in hydrogen bonding and the two non-bonded DMF molecules have been omitted for clarity. The minor disorder of DMF based on N19 has been omitted for clarity; (right) 2-fold interpenetrated cube-like cages in space filling representation showed in different colours. The DMF solvent molecules have been omitted for clarity.*

The effective free volume in **3** is ca. 22.7% of the unit cell as calculated by the program PLATON[22], with the DMF guest molecules removed prior to these calculations.

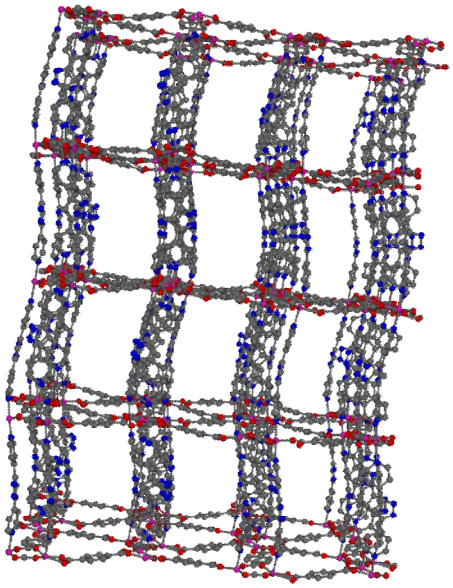

*Figure 2-18. Perspective view of [Zn_4(H**L**)$_4$(1,4-bdc)$_4$] along the c axis. The hydrogen atoms and atoms of one branch were omitted for clarity.*

The presence of hydrogen bonded and non-bonded DMF solvent molecules is confirmed also by the TGA analysis (Figure 2-19, as-made red trace). The mass loss of ~15% is attributed to the loss of four DMF solvent molecules (calculated mass loss of one DMF solvent molecule for **3** is 3.5%). Moreover this mass loss is divided into two equal mass losses shown as two steps in the TGA, a first mass loss of ~7.5% up to 210°C after which a second similar mass loss up to 340°C when the MOF starts to decompose.

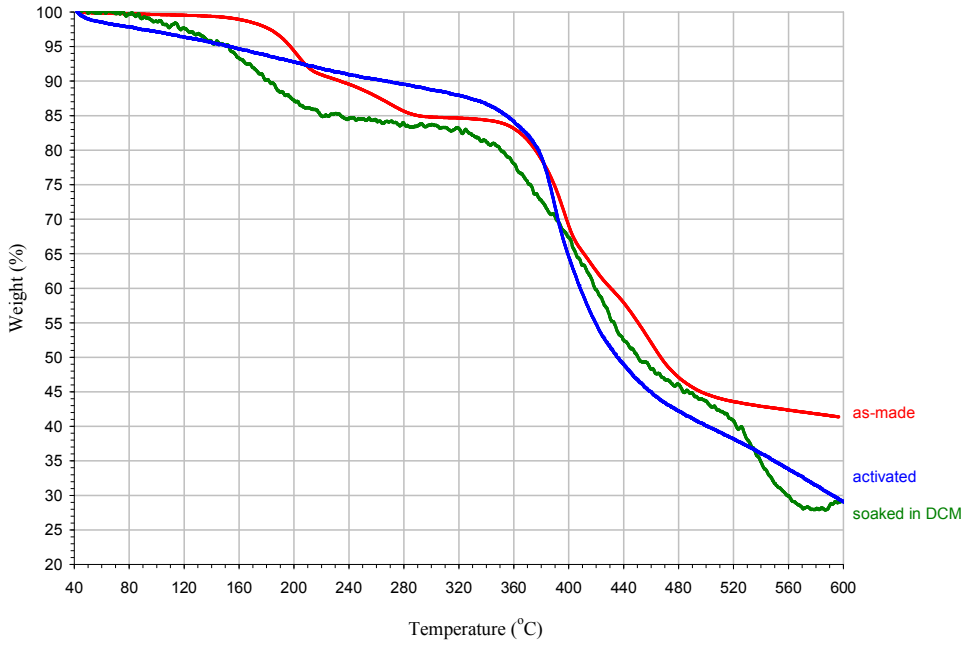

*Figure 2-19. TGA trace of **3** after heating at 155°C for 2 hours (activated blue trace) and of **3** after soaking in DCM for 21 hours (green trace) compared with that of the as-made **3**.*

The TGA analysis suggests that a sample of **3** following heating at 155°C for 2 hours would lose its integrity (Figure 2-19, activated blue trace). Another way of removing the DMF solvent molecules (b.p. = 153°C) is to exchange the DMFs with solvent molecules of a lower boiling point (b.p.) such as DCM (dichloromethane) (b.p. = 39.8°C). In order to do that, a sample of **3** was soaked for 21 hours in DCM. The TGA analysis of the sample soaked in DCM shows a mass loss of ~16% up to 290°C when decomposition occurs (Figure 2-19, soaked in DCM green trace).

2.2.2.5. $Zn_4(1,4\text{-ndc})_4(HL)_4$ 4

The reaction of $Zn(NO_3)_2 \cdot 6H_2O$ with H**L** and 1,4-naphthalenedicarboxylic acid (1,4-H_2ndc) in DMF (1:1:2 molar ratio) at 130°C yielded after 2 days colourless lath like crystals which were analysed by single crystal X-ray diffraction. The structure was refined as $Zn_4(1,4\text{-ndc})_4(HL)_4$, **4**. The crystal data and refinement parameters for **4** are given in Table 2-8. The diffraction of **4** at high angles was of low intensity, resulting in poor resolution data and a high R-value of 15%. Rigid hexagon restraints were applied throughout where possible, augmented by some distance and planarity restraints. The poor

quality of the X-ray data for **4** limits the use of the metric data. However, the data allow for an unambiguous assignment of the framework, and the analysis here is limited to that.

*Table 2-8. Crystallographic data and refinement parameters for **4**.*

Empirical formula	$C_{50}H_{32}N_8O_8Zn_2$	
Formula weight	1003.58	
Temperature	150(2) K	
Wavelength	0.71073 Å	
Crystal system	Triclinic	
Space group; Z	*P*-1, 4	
Unit cell dimensions	a = 18.532(2) Å	α = 116.099(8)°
	b = 20.3541(15) Å	β = 112.218(10)°
	c = 20.561(2) Å	γ = 97.506(7)°
Volume	6022.4(10) Å^3	
Density (calculated)	1.107 g/cm^3	
Crystal size	0.10 x 0.08 x 0.08 mm	
Theta range for data collection	3.00 to 21.97°	
Reflections collected/ observed (>2σ)	24223/ 4496 [R(int) = 0.1069]	
Data Completeness	0.892	
Goodness-of-fit on F^2	0.948	
Final R indices [I>2σ(I)]	$R1$ = 0.1497 $wR2$ = 0.3620	
R indices (all data)	$R1$ = 0.2370 $wR2$ = 0.4239	
Largest diff. peak and hole	1.864 and -0.890 eÅ^{-3}	

The asymmetric unit of **4** (Figure 2-20) consists of four zinc centres, four 1,4-ndc ligands and four H**L** linkers. Only the zinc atoms were treated anisotropically due to the data quality.

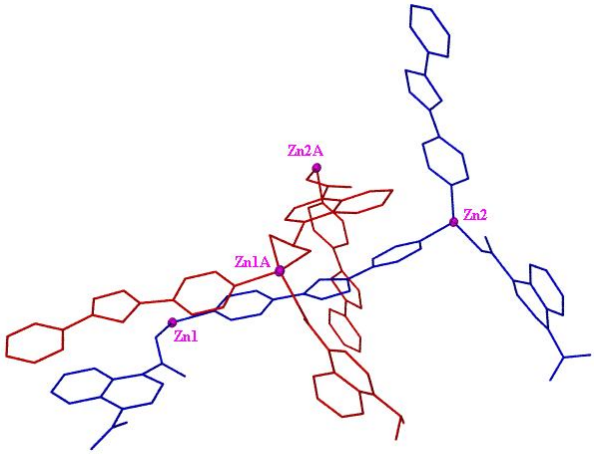

*Figure 2-20. The asymmetric unit of **4** showing the two molecules in different colours. Zinc atoms are represented by thermal ellipsoids at the 30% probability level. The hydrogen atoms have been omitted for clarity.*

Each zinc centre is coordinated to two 1,4-ndc carboxylate groups and two H**L** pyridyl groups. The zinc centres therefore act as tetrahedral nodes, and the bridging ligands interlink them into three-dimensional diamondoid networks (Figure 2-21).

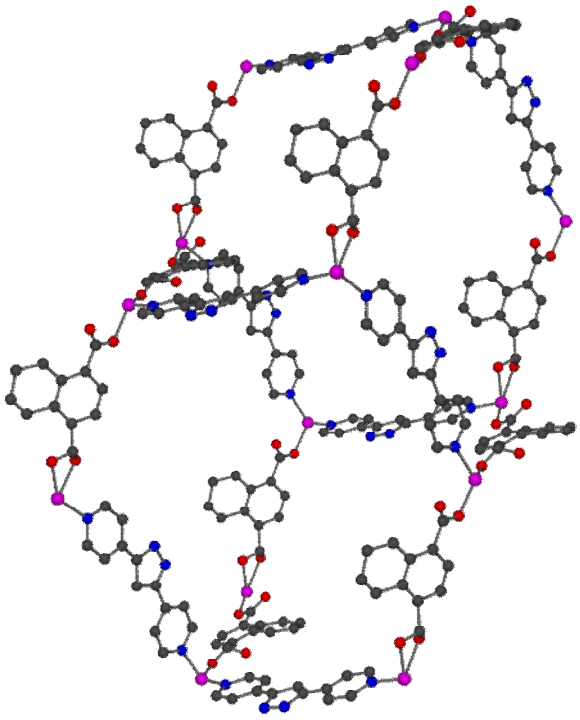

*Figure 2-21. The structure of **4** showing a diamandoid like cage.*

The structure of **4** is four-fold interpenetrated (Figure 2-22). The relative proximity of pyrazole nitrogen atoms and carboxylate oxygen atoms suggests the presence of hydrogen bonding, which interlinks the networks in a pairwise manner.

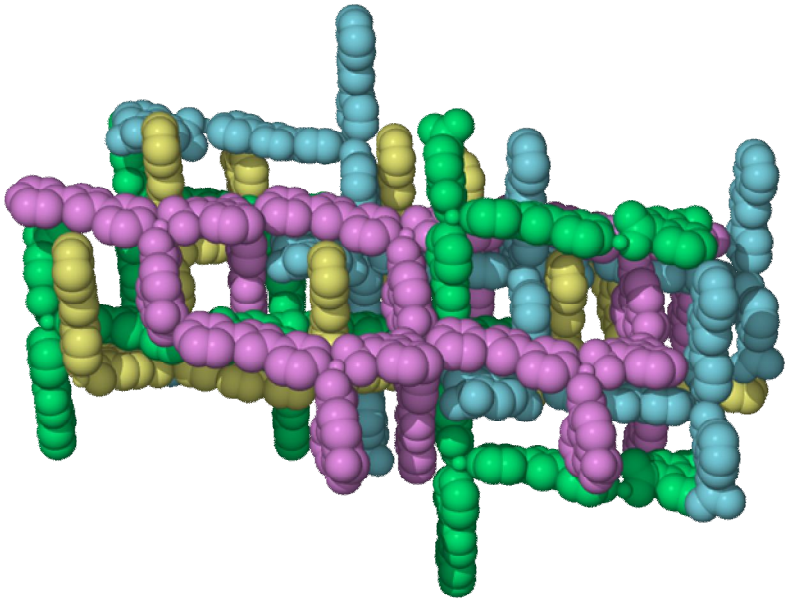

*Figure 2-22. The four-fold interpenetrated structure of **4** shown in different colours.*

2.2.2.6. $[Zn_2(2,6\text{-ndc})_2(HL)]\cdot DMF$, 5

Block-like pale yellow crystals suitable for X-ray diffraction were collected after several weeks being taken from their mother liquor. The crystals resulted from a reaction mixture of H**L**, 2,6-naphthalenedicarboxylic acid (2,6-H_2ndc) and $Zn(NO_3)\cdot 6H_2O$ (1: 2: 1 molar ratio) in DMF at 130°C.

Attempts to collect single X-ray diffraction data straight after crystal formation were made both at low temperature and room temperature but with no success. This was because a certain degree of crystal degradation was observed at low temperature whereas at room temperature the X-ray diffraction gave a poor resolution data. Ultimately successful X-ray data collection was achieved when the crystals were left for several weeks at room temperature, time in which the crystals slightly changed their morphology and gained more well-defined edges.

The X-ray data revealed a compound with formula $[Zn_2(2,6\text{-ndc})_2(H\mathbf{L})]\cdot DMF$ **5**. The crystal data and refinement parameters for **5** are given in Table 2-9.

*Table 2-9. Crystallographic data and refinement parameters for **5**.*

Empirical formula	$C_{40}H_{29}N_5O_9Zn_2$	
Formula weight	854.42	
Temperature	150(2) K	
Wavelength	0.71073 Å	
Crystal system	Triclinic	
Space group; Z	*P*-1, 2	
Unit cell dimensions	a = 8.1920(2) Å	α = 93.714(1)°
	b = 16.4330(4) Å	β = 99.822(1)°
	c = 16.4440(4) Å	γ = 99.807(1)°
Volume	2139.29(9) Å^3	
Density (calculated)	1.326 g/cm3	
Crystal size	0.20 x 0.13 x 0.08 mm	
Theta range for data collection	3.53 to 27.56°	
Reflections collected/ observed (>2σ)	42369/ 6004 [R(int) = 0.0672]	
Data Completeness	0.992	
Goodness-of-fit on F^2	0.956	
Final R indices [I>2σ(I)]	$R1$ = 0.0513 $wR2$ = 0.1324	
R indices (all data)	$R1$ = 0.0922 $wR2$ = 0.1467	
Largest diff. peak and hole	0.376 and -0.407 eÅ^{-3}	

The asymmetric unit of **5** shown in Figure 2-23 consists of two zinc centres, one and two halves of 2,6-ndc ligands, one H**L** ligand and one lattice DMF solvent molecule. The DMF solvent in the lattice of **5** is diffuse and is estimated herein as one DMF per asymmetric unit of **5**. This estimate is based on the pre-SQUEEZE evident electron density, in combination with the SQUEEZE output. The hydrogen attached to either N3 or N4 could not be located with any credibility, and hence is omitted from the refinement. The phenyl carbons in the two crystallographically independent 2,6-ndc ligand halves are subject to

50:50 disorder, which was readily modelled by employing minimal distance restraints to assist convergence.

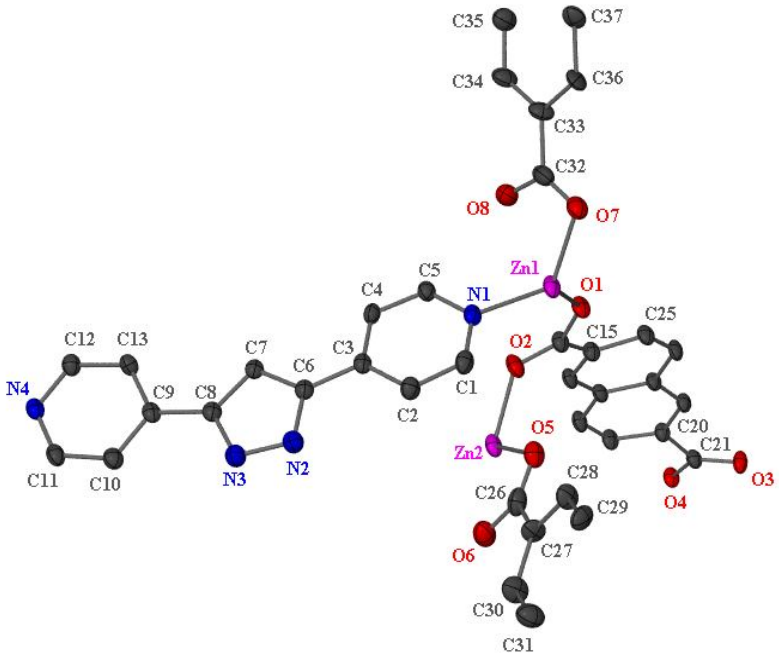

*Figure 2-23. The asymmetric unit of **5** showing thermal ellipsoids at the 30% probability level. The second disordered components from 2,6-ndc phenyl rings and the hydrogen atoms have been omitted for clarity.*

Each zinc centre is coordinated to three carboxylates and one H**L** ligand. The full and partial occupancy 2,6-ndc ligands play very different structural roles.

The two carboxylate groups in the 2,6-ndc linker containing O1–O2 and O3–O4 bridge between zinc centres connecting them into zinc-carboxylate chains, which are linked into pairs by the naphthalene groups (Figure 2-24). π···π interactions are also present between the naphthalene rings.

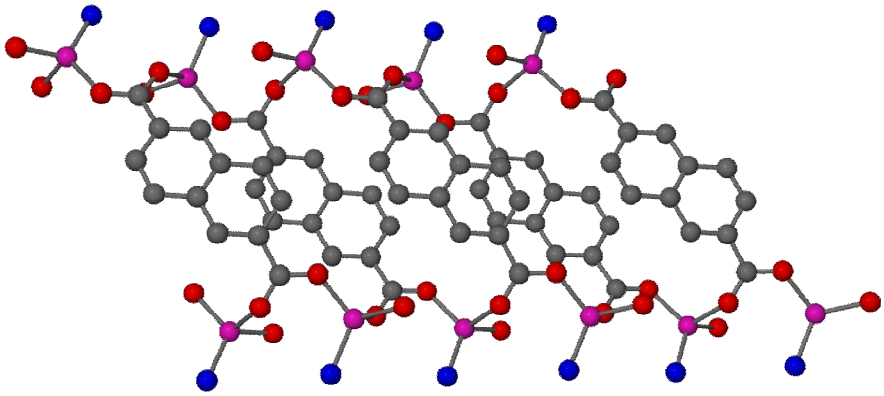

*Figure 2-24. The structure of **5**, showing the tapes formed by linking zinc-carboxylate chains with 2,6-ndc ligands. The second disordered components from 2,6-ndc phenyl rings and the hydrogen atoms have been omitted for clarity.*

The 2,6-ndc linkers containing O5–O6 and O7–O8 connect the pairs of chains into a three-dimensional network, which is further supported by the H**L** ligands, which bridge zinc centres (Figure 2-25).

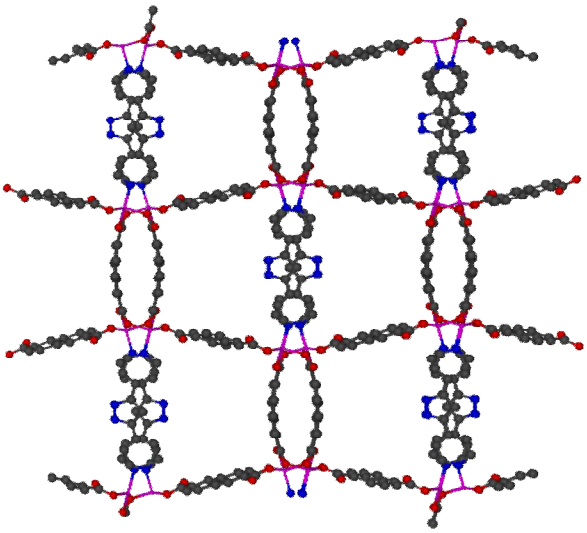

*Figure 2-25. The 3-D network of **5** formed by interlinking the tapes with 2,6-ndc and H**L** ligands. The second disordered components from 2,6-ndc phenyl rings and the hydrogen atoms have been omitted for clarity.*

2.2.2.7. $[Zn_4(1,3\text{-bdc})_4(HL)_4]\cdot 4DMF$ 6

Block colourless crystals suitable for single crystal X-ray diffraction were collected from a reaction mixture of H**L**, 1,3-benzenedicarboxylic acid (1,3-H_2bdc) and $ZnCl_2$ (1:2:2 molar ratio), in DMF, heated at 120°C. Owing to crystal quality, the data are not as complete as desirable, but the structure is unambiguous with the formulae $[Zn_4(1,3\text{-bdc})_4(H\mathbf{L})_4]\cdot 4DMF$ **6**. The crystallographic and refinement data for **6** are shown in Table 2-10.

*Table 2-10. Crystallographic data and refinement parameters for **6**.*

Empirical formula	$C_{96}H_{48}N_{20}O_{20}Zn_4$	
Formula weight	2063.08	
Temperature	150(2) K	
Wavelength	0.71073 Å	
Crystal system	Triclinic	
Space group; Z	*P*-1, 2	
Unit cell dimensions	a = 10.0420(3) Å	α = 81.958(1)°
	b = 16.2980(5) Å	β = 81.349(1)°
	c = 29.5300(9) Å	γ = 77.745(1)°
Volume	4639.90 $Å^3$	
Density (calculated)	1.476 g/cm^3	
Crystal size	0.30 x 0.20 x 0.20 mm	
Theta range for data collection	2.91 to 25.03°	
Reflections collected/ observed (>2σ)	37496/ 8479 [*R*(int) = 0.1075]	
Data Completeness	0.810	
Goodness-of-fit on F^2	1.456	
Final *R* indices [$I>2\sigma(I)$]	*R1* = 0.1161 w*R2* = 0.0715	
R indices (all data)	*R1* = 0.0651 w*R2* = 0.0782	
Largest diff. peak and hole	1.79 and -0.93 $eÅ^{-3}$	

The asymmetric unit of **6** (Figure 2-26) contains four zinc atoms, four H**L** linkers, four 1,3-bdc linkers and four DMF solvent molecules. The DMF solvent molecules containing N19

and N20 are disordered. The hydrogen atoms of the pyrazole rings could not be located from this data either.

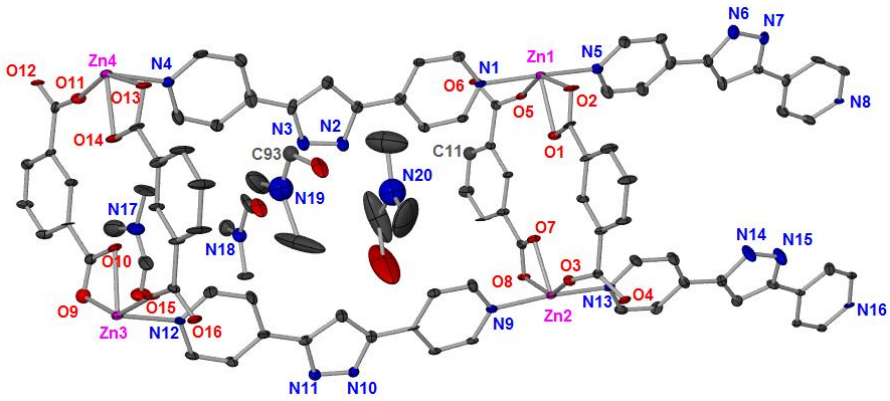

*Figure 2-26. The asymmetric unit of **6** showing thermal ellipsoids at the 30% probability level except for the atoms O9, C93 and C11. Hydrogen atoms have been omitted for clarity.*

The zinc atoms show the same distorted octahedral geometry (Figure 2-27) with 1,3-bdc linker adopting the same coordination mode, one carboxylate bridges between two zinc atoms and the other carboxylate group chelates to zinc atom.

The intradinuclear Zn1···Zn2 separation is 4.043 Å, and Zn3···Zn4 separation is 4.082 Å. The Zn2-O8 bond length (2.483 Å) is substantially longer than Zn2-O7 (2.061 Å) and the Zn4-O13 bond length (2.329 Å) is also longer than Zn4-O14 (2.148 Å). This suggests that the carboxylate groups containing O8 and O13 atoms might adopt a semi-chelating mode[23, 24]. Overall, the geometry around the zinc atoms remains distorted octahedral.

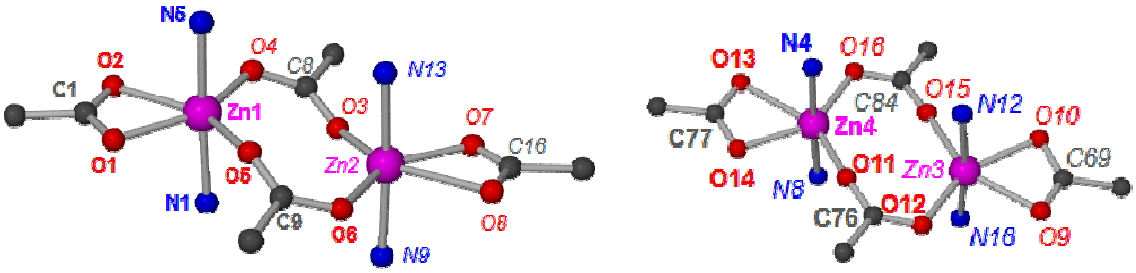

*Figure 2-27. Structure of **6** showing the $Zn_2(carboxylate)_2N_4$ units, containing Zn1···Zn2 (left) and Zn3···Zn4 (right). Symmetry generated atoms are labelled in italics.*

The double chain containing Zn1-Zn2 pair is shown in Figure 2-28. A similar double chain is also formed by the Zn3-Zn4 pair.

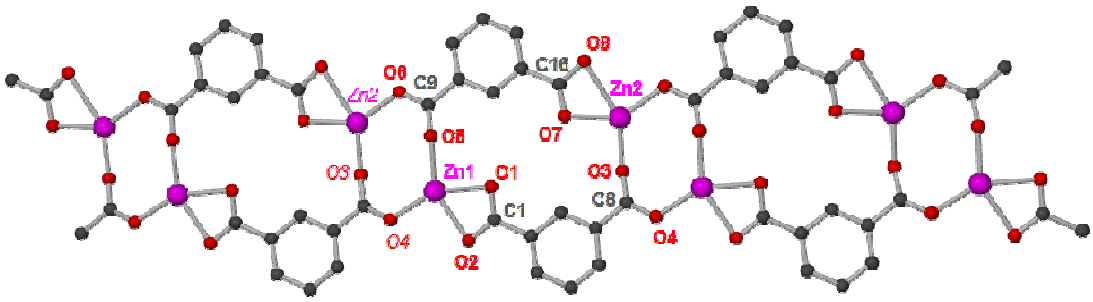

*Figure 2-28. Structure of **6** showing double-chain of [Zn(1,3-bdc)]$_n$. Symmetry generated atoms are labelled in italics. Hydrogen atoms have been omitted for clarity.*

The double chains pillared by H**L** linkers form 2-D sheets as shown in Figure 2-29. Weak interactions as π-π stacking are observed between the aromatic rings of 1,3-bdc ligands from two adjacent 2-D sheets. The location of the DMF molecules suggests the existence of some hydrogen bonding between the NH groups of the H**L** linker and the solvent. The distance between the centroids of aromatic rings of 1,3-bdc linkers was calculated at approximately 3.581 Å and 3.689 Å, consistent with the presence of a π-π interaction.

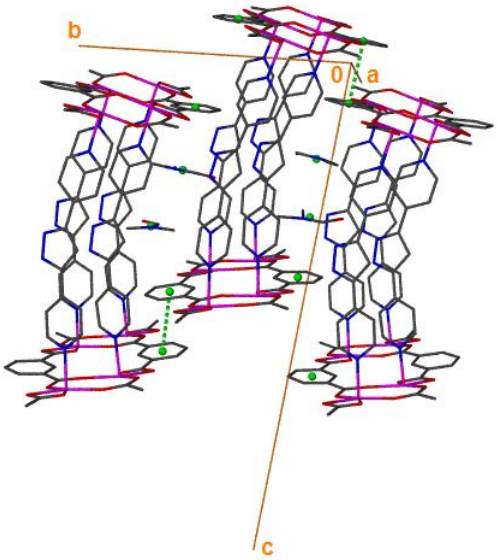

*Figure 2-29. Structure of **6** showing π-π stacking between aromatic rings of 1,3-bdc ligands. The hydrogen atoms have been omitted for clarity. The centroids of the phenyl rings of 1,3-bdc ligands are shown in green.*

The 3-D framework of **6** is shown in Figure 2-30.

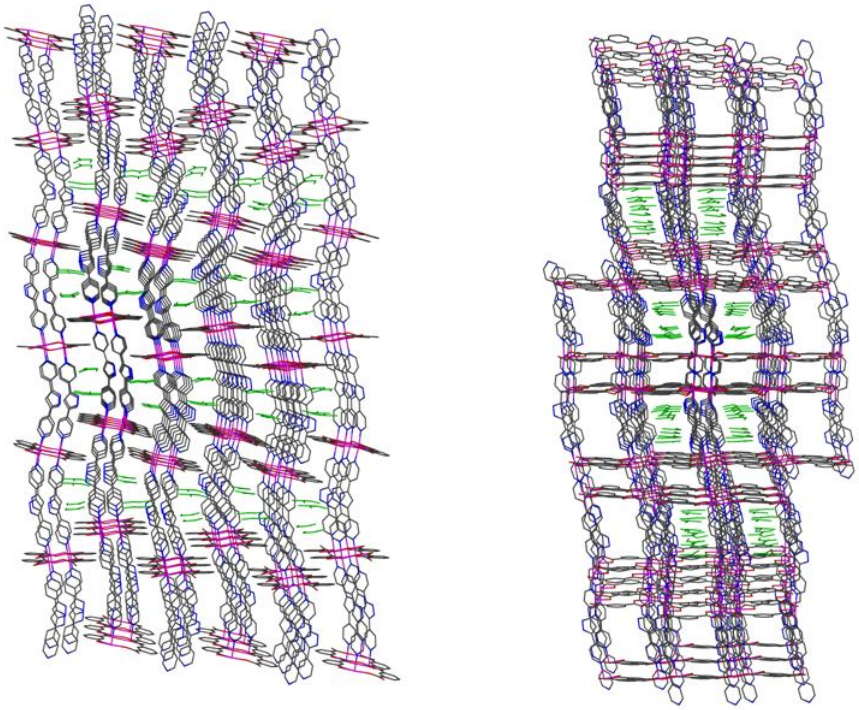

*Figure 2-30. The 3-D framework of **6** viewed along: (left) a axis and (right) b axis. The DMF solvent molecules are shown in green. The hydrogen atoms have been omitted for clarity.*

Total potential solvent area volume for **6** per unit cell volume is 27.0% as calculated by the program PLATON[22] with DMF guest molecules being removed prior to these calculations.

2.2.2.8. [Zn(1,3-bdc)(HL)]·DMF 7

The reaction of $Zn(NO_3)_2 \cdot 6H_2O$ with H**L** and 1,3-benzenedicarboxylic acid (1,3-H_2bdc) in DMF (2:1:2 molar ratio) yielded colourless block-shaped crystals which were analysed by single crystal X-ray diffraction. The structure was refined as [Zn(1,3-bdc)(H**L**)]·DMF **7** and its crystallographic and refinement data are shown in Table 2-11.

*Table 2-11. Crystallographic data and refinement parameters for **7**.*

Empirical formula	$ZnC_{24}H_{21}N_5O_5$
Formula weight	524.83

Temperature	150(2) K	
Wavelength	0.71073 Å	
Crystal system	Orthorhombic	
Space group; Z	$P2_12_12_1$, 4	
Unit cell dimensions	a = 10.1440(1) Å	α = 90°
	b = 13.9760(1) Å	β = 90°
	c = 16.1920(2) Å	γ = 90°
Volume	2295.58(4) Å^3	
Density (calculated)	1.519 g/cm^3	
Crystal size	0.50 x 0.35 x 0.10 mm	
Theta range for data collection	3.53 to 27.50°	
Reflections collected/ observed (>2σ)	44382/ 4954 [R(int) = 0.0685]	
Data Completeness	0.996	
Goodness-of-fit on F^2	1.052	
Final R indices [I>2σ(I)]	$R1$ = 0.0282 w$R2$ = 0.0665	
R indices (all data)	$R1$ = 0.0317 w$R2$ = 0.0681	
Largest diff. peak and hole	0.259 and -0.439 eÅ^{-3}	

Figure 2-31 shows the asymmetric unit of **7**, which contains one zinc atom, one H**L** ligand, one 1,3-bdc ligand and one DMF solvent molecule. C22, C23 and O5 from DMF molecule are disordered over two sites in a 60 : 40 ratio.

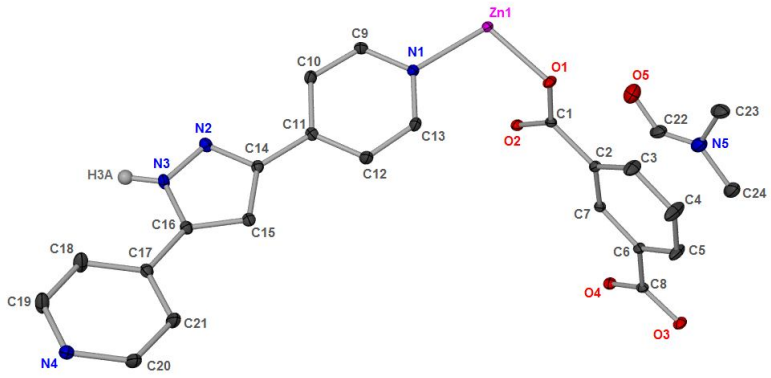

*Figure 2-31. The asymmetric unit of **7** showing thermal ellipsoids at the 30% probability level. The hydrogen atoms except that from the pyrazole ring of H**L** have been omitted for clarity. Minor disordered atoms from the DMF molecule have been omitted for clarity.*

The zinc centre has distorted tetrahedral geometry coordinating to two 1,3-bdc ligands and two H**L** ligands, which are located into axial positions. Selected bond lengths and angles are given in Table 2-12.

*Table 2-12. Selected bond lengths (Å) and angles (°) for **7**.**

Atoms	Bond length (Å)	Atoms	Angle (°)
Zn1-O1	1.9922(13)	O1-Zn1-N1	105.03(7)
Zn1-O3#1	2.0088(14)	O3#1-Zn1-N1	108.09(7)
Zn1-N1	2.0422(15)	N4#2-Zn1-N1	128.01(6)
Zn1-N4#2	2.0387(17)	O1-Zn1-O3#1	97.22(5)
		O3#1-Zn1-N4#2	110.91(7)
		O1-Zn1-N4#2	102.74(7)
Symmetry transformations used to generate equivalent atoms: #1 x+1, y, z; #2 x, y-1, z			

The 1,3-bdc ligands are both coordinated into a monodentate fashion linking the zinc centres into a $[Zn(1,3\text{-bdc})]_n$ single chain which is then pillared by H**L** into a wave like sheet (Figure 2-32). These sheets are hydrogen bonded through the NH groups from the pyrazole rings and oxygens from a carboxylate group within the 1,3-bdc ligand (N3···O2 distance of 2.710Å, H3A···O2 distance of 1.83 Å and N3–H3A···O2 angle of 174.11°).

The H**L** linker shows a high curvature with an angle between the planes containing the pyridine rings of approximately 30.98°.

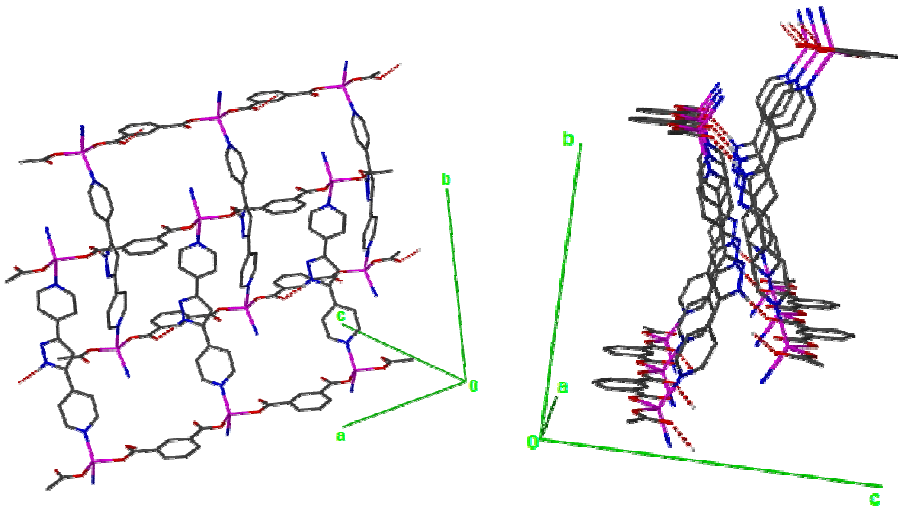

*Figure 2-32. The structure of **7** from two perspectives showing the hydrogen bonding present between the sheets.*

The hydrogen bonded sheets (ladder like) are interdigitated forming a 3-D MOF, with the DMF solvent molecules housed within some of the rectangular-shaped infinite channels (Figure 2-33). These channels have been measured to be approximately 2.5 Å x 7 Å.

Unit cell of **7** contains no residual solvent accessible void as calculated by program Platon[22].

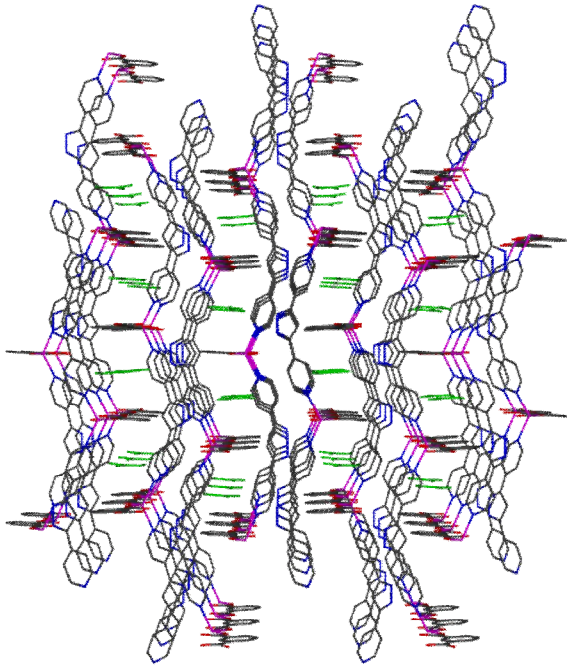

*Figure 2-33. The 3-D structure of **7** viewed down the a axis. The DMF solvent molecules are shown in green. The hydrogen atoms and minor disordered atoms from DMF have been omitted for clarity.*

The DMF molecules are involved in π-interaction with the aromatic groups present within 1,3-bdc linkers. The DMF molecules are housed between interdigitated chains containing 1,3-bdc linkers through π-π stacking [$centroid_{DMF}\cdots centroid_{1,3\text{-}bdc}$ = 3.599-3.736 Å, $plane_{DMF}$<$plane_{1,3\text{-}bdc}$ < 7°] (Figure 2-34). Values of 3.3 - 3.8 Å have previously been reported for similar π-stacking interactions.[25]

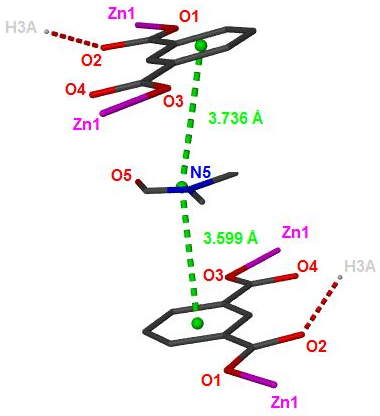

*Figure 2-34. Structure of **7** showing π-π stacking between DMF and aromatic rings of 1,3-bdc ligands. The minor disordered atoms from DMF and the hydrogen atoms except those from the pyrazole rings of H**L** have been omitted for clarity. The centroids of the phenyl rings of 1,3-bdc ligands are shown in green.*

A. Warren[26] found that just approximately 10% of the structures present on CSD contain DMF molecules that are involved in a π-interaction with the aromatic groups present within the organic linkers of the MOF framework. In this respect, structure **7** might be a unique example of an interdigitated 3-D MOF with DMF solvent molecules π-π stacked into the channels.

2.2.2.9. $[Zn_2(1,3\text{-bdc-Me})_2(HL)_2]\cdot DMF$ 8

The solvothermal reaction of H**L**, 5-methyl-1,3-benzenedicarboxylic acid (1,3-H_2bdc-Me) and $Zn(NO_3)_2\cdot 6H_2O$ in a 1:2:2 molar ratio, in DMF at 120°C afforded colourless block crystals of formula $[Zn_2(1,3\text{-bdc-Me})_2(HL)_2]\cdot DMF$ **8**. The crystallographic data and refinement parameters for **8** are shown in Table 2-13.

*Table 2-13. Crystallographic data and refinement parameters for **8**.*

Empirical formula	$Zn_2C_{47}H_{39}N_9O_9$
Formula weight	1004.61
Temperature	123(2) K
Wavelength	0.68890 Å

Crystal system	Monoclinic	
Space group; Z	$P2_1/c$, 4	
Unit cell dimensions	a = 10.040(6) Å	α = 90°
	b = 29.598(17) Å	β = 102.762(5)°
	c = 17.153(11) Å	γ = 90°
Volume	4971(5) Å^3	
Density (calculated)	1.342 g/cm^3	
Crystal size	0.04 x 0.03 x 0.02 mm	
Theta range for data collection	1.36 to 25.00°	
Reflections collected/ observed (>2σ)	29676/ 7087 [*R*(int) = 0.0928]	
Data Completeness	0.902	
Goodness-of-fit on F^2	1.073	
Final *R* indices [I>2σ(I)]	*R1* = 0.0748 w*R2* = 0.2089	
R indices (all data)	*R1* = 0.0851 w*R2* = 0.2191	
Largest diff. peak and hole	0.689 and -0.915 eÅ^{-3}	

The asymmetric unit of **8** (Figure 2-35) contains two zinc atoms, two 1,3-bdc-Me ligands, two H**L** ligands and one DMF solvent molecule. The carbon atoms C11 to C14 and C16 from one of the 1,3-bdc-Me ligands are disordered in 75:25 ratio, the suffix 'A' in atom labels being attributed to the highest occupancy. The DMF molecule included in the asymmetric unit is formed from an ordered half DMF molecule containing N9 and a diffuse half DMF molecule which was calculated by treating the residual electron density with PLATON SQUEEZE.

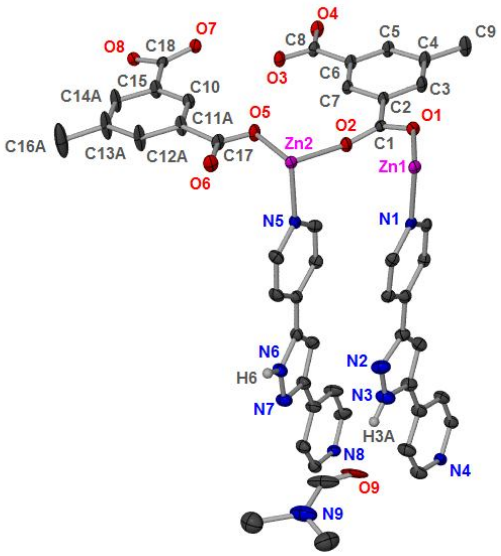

*Figure 2-35. The asymmetric unit of **8** showing thermal ellipsoids at the 30% probability level. The minor disordered component from 1,3-bdc-Me has been omitted for clarity. Hydrogen atoms except those from the pyrazole ring of the HL linkers have also been omitted for clarity.*

The framework of **8** is sustained by dinuclear $Zn_2(carboxylate)_2N_4$ molecular building blocks (Figure 2-36).

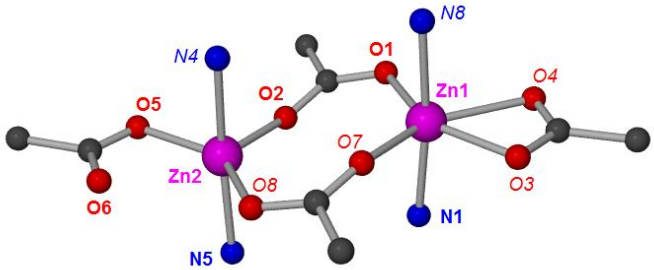

*Figure 2-36. Structure of **8** showing the $Zn_2(carboxylate)_2N_4$ building block. Symmetry generated atoms are labelled in italics.*

The intradinuclear Zn1···Zn2 separation is 4.006 Å. The local co-ordination environment around Zn1 can best be described as distorted octahedral geometry and around Zn2 as distorted trigonal bipyramidal geometry since O6 from the carboxylate group is hydrogen bonded to the NH from the pyrazole ring of H**L**. The Zn2···O6 distance of 2.496 Å suggests a non-negligible interaction, which may be described as a semi-chelating coordination mode[23, 24]. Hence, Zn2 atom may be also regarded as in a distorted

octahedral geometry. The O-Zn1-N angle is around 90° ranging from 85.17(15)° to 93.82(14)° similar with that around Zn2 centre [85.92(13)° to 94.85(14)°]. The selected bond lengths (Å) and angles (°) are given in Table 2-14.

*Table 2-14 Selected bond lengths (Å) and angles (°) for **8**.**

Atoms	Bond length (Å)	Atoms	Angle (°)
Zn1-O3#1	2.125(3)	O1-Zn1-O7#1	121.15(12)
Zn1-O4#1	2.285(4)	O3#1-Zn1-O4#1	59.34(12)
Zn1-O1	2.027(3)	O7#1-Zn1-O3#1	88.76(12)
Zn1-O7#1	2.091(3)	O1-Zn1-O4#1	90.63(12)
Zn2-O2	2.014(3)	O2-Zn2-O5	93.07(12)
Zn2-O8#1	2.042(3)	O2-Zn2-O8#1	125.50(12)
Zn2-O5	2.093(3)	O8#1-Zn2-O5	141.43(13)
Zn1-N1	2.140(4)	O7#1-Zn1-N8#2	85.17(15)
Zn1-N8#2	2.183(4)	N1-Zn1-O4#1	93.82(14)
Zn2-N5	2.167(4)	O8#1-Zn2-N5	85.92(13)
Zn2-N4#2	2.167(4)	O5-Zn2-N5	94.85(14)

**Symmetry transformations used to generate equivalent atoms: #1 x+1, y, z; #2 -x, y+1/2, -z+3/2*

The dinuclear $Zn_2(carboxylate)_2N_4$ molecular building blocks are further linked by 1,3-bdc-Me ligands into double chains as shown in Figure 2-37.

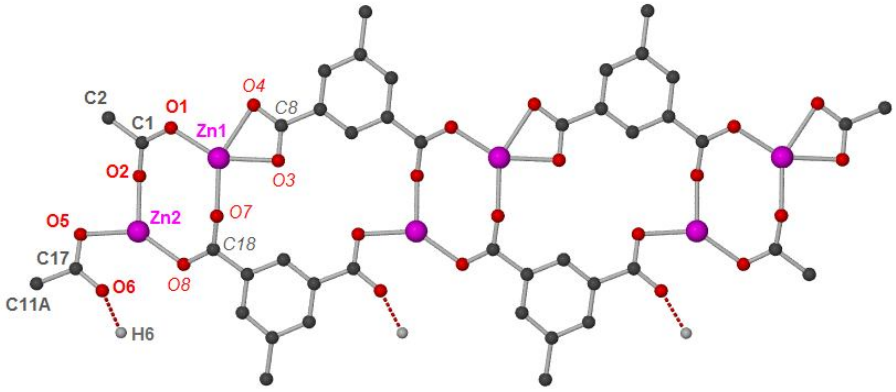

*Figure 2-37. Structure of **8** showing [Zn(1,3-bdc-Me)]$_n$ double chain. Symmetry generated atoms are labelled in italics. Hydrogen atoms except those from the pyrazole rings of H**L** linkers have been omitted for clarity.*

The angles formed by the planes containing the pyridine rings of H**L** in **8** are approximately 3.46° and 11.27°, respectively. The double chains of [Zn(1,3-bdc-Me)]$_n$ are pillared by H**L** linkers forming sheets which are held together by π-π interactions between the aromatic groups within 1,3-bdc-Me linkers and also by hydrogen bonds between these sheets (Figure 2-38).

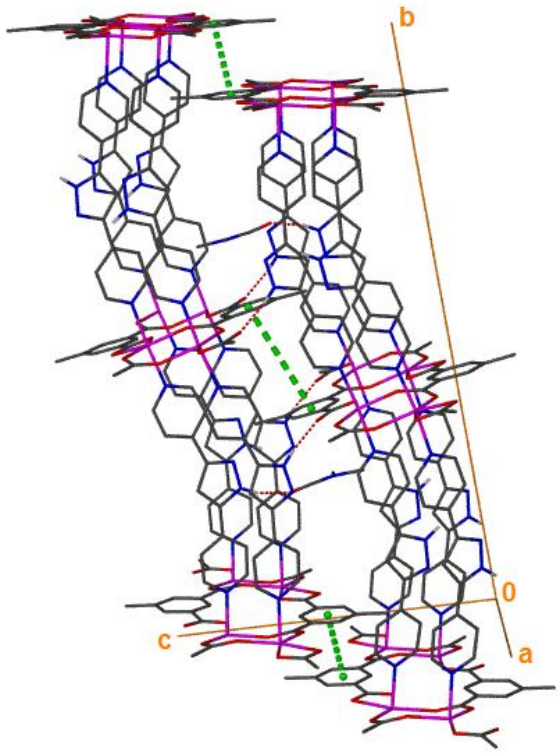

*Figure 2-38. Structure of **8** showing the hydrogen bonding present between two adjacent sheets and between DMFs and the framework. The centroids of the phenyl rings of 1,3-bdc-Me linker are shown in green. The minor disordered components of the DMFs and hydrogen atoms except those from the pyrazole rings of H**L** linkers have been omitted for clarity.*

The oxygen of the DMF solvent is hydrogen bonded with the N-H group of the pyrazole ring from the H**L** linker (N3···O9 distance of 2.736 Å, H3A···O9 distance of 1.89 Å, N3–H3A···O9 angle of 161.39°; N6···O6#1[3] distance of 2.779 Å, H6···O6#1[3] distance of 1.90 Å and N6–H6···O6#1[3] angle of 172.30°).

The distance between the centroids of aromatic rings of 1,3-bdc-Me linkers in **8** was calculated to be 3.644 Å, consistent with the presence of a π-π interaction. The distance between the other two adjacent aromatic groups of 1,3-bdc-Me linkers was calculated at approximately 6.100 Å being out of the range required for a π-π interaction. The distance

[3] Symmetry transformations used to generate equivalent atoms: #1 -x, -y, 2-z.

between DMF solvent molecule and the nearest aromatic rings is 6.884 Å, also not consistent with presence of a π-π interaction.

The 3-D interdigitated framework of $[Zn_2(1,3\text{-bdc-Me})_2(H\mathbf{L})_2]\cdot$DMF **8** (Figure 2-39) can be seen to have some similarity to that of [Zn(1,3-bdc)(H**L**)] DMF **7**. The sheets in **7** are formed through non-covalent interactions whereas in **8** are formed through covalent interactions. Both **7** and **8** can be finally described as 3-D interdigitated MOFs where there is π-π stacking present between DMF solvent molecules and the aromatic rings of the 1,3-bdc ligands in **7** or π-π stacking between aromatics rings of the 1,3-bdc-Me in **8**. These structures may be viewed as showing a degree of flexibility. Additionally by comparing the two structures, **7** may be viewed as showing a higher degree of flexibility than **8**.

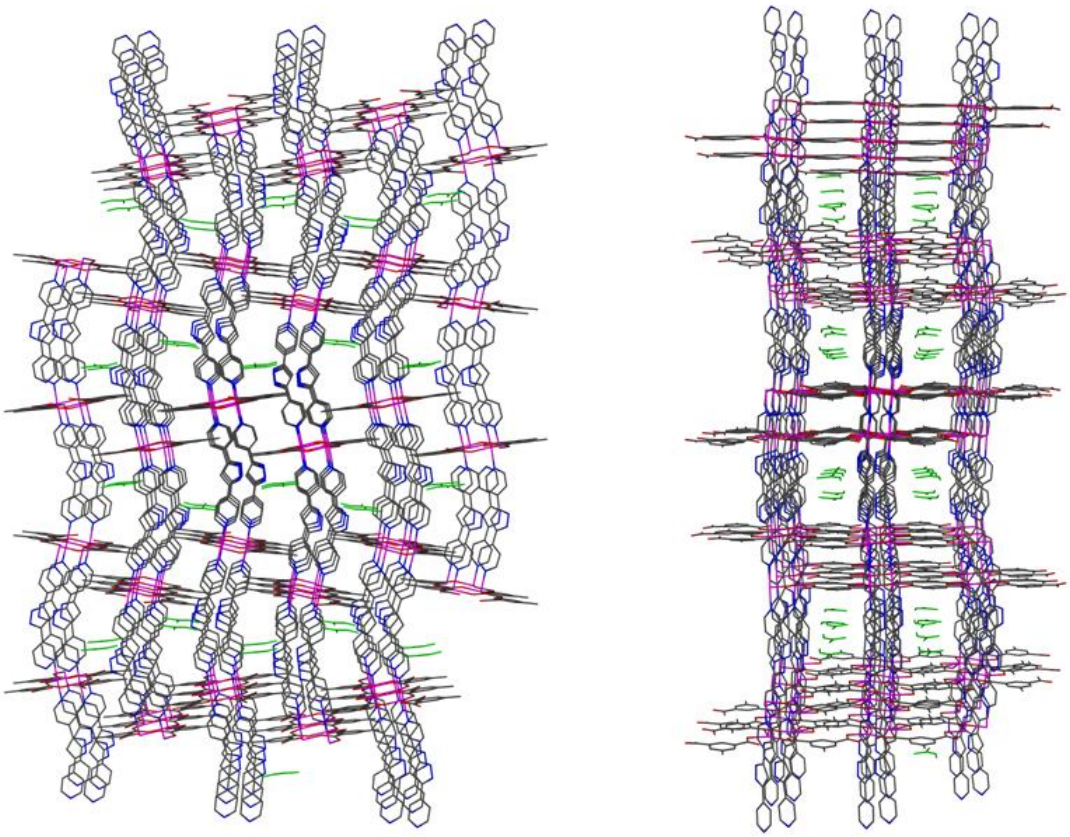

*Figure 2-39. The 3-D framework of **8** viewed down the: (left) a axis and (right) c axis. The DMFs are shown in green. The hydrogen atoms and minor disordered components have been omitted for clarity.*

The effective free volume in **8** is ca. 15.5% of the unit cell as calculated by the program Platon[22]. The square channels have approximate dimensions of 10 Å x 10 Å.

2.2.2.10. $(Me_2NH_2)_2[Zn(1,4\text{-bdc})_2]\cdot 2DMF$ 9

Block colourless crystals suitable for X-ray diffraction were collected from the reaction mixture of H**L**, $ZnCl_2$ and 1,4-H_2bdc (1 : 2: 2 molar ratio) in DMF after 2 days at 160°C. The X-ray data indicated that the H**L** linker was not present in the overall structure, and that a product formulated as $(Me_2NH_2)_2[Zn(1,4\text{-bdc})_2]\cdot 2DMF$ **9** has been obtained. The crystallographic data and refinement parameters for **9** are shown in Table 2-15.

*Table 2-15. Crystallographic data and refinement parameters for **9**.*

Empirical formula	$C_{26}H_{38}N_4O_{10}Zn$	
Formula weight	631.97	
Temperature	150(2) K	
Wavelength	0.71073 Å	
Crystal system	Orthorhombic	
Space group; Z	Fddd, 16	
Unit cell dimensions	a = 21.4990(3) Å	α = 90°
	b = 27.0040(5) Å	β = 90°
	c = 27.7670(5) Å	γ = 90°
Volume	16120.4(5) Å^3	
Density (calculated)	1.042 g/cm^3	
Crystal size	0.28 x 0.20 x 0.10 mm	
Theta range for data collection	3.30 to 25.04°	
Reflections collected/ observed (>2σ)	70009/ 3549 [R(int) = 0.1582]	
Data Completeness	0.994	
Goodness-of-fit on F^2	1.214	
Final R indices [I>2σ(I)]	R1 = 0.0842, wR2 = 0.1800	
R indices (all data)	R1 = 0.1176, wR2 = 0.1952	
Largest diff. peak and hole	0.582 and -0.396 eÅ^{-3}	

The asymmetric unit of **9** (Figure 2-40) consists of half a zinc atom, one 1,4-bdc ligand, one DMF molecule and one dimethylammonium cation ($Me_2NH_2^+$).

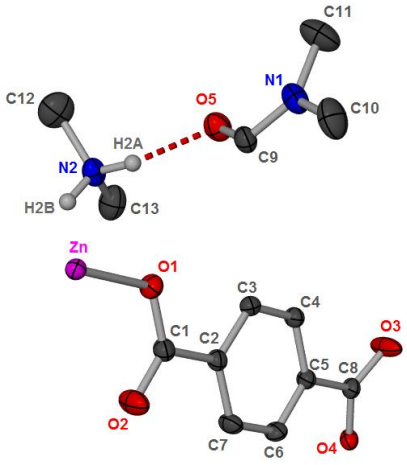

*Figure 2-40. The asymmetric unit of **9** showing thermal ellipsoids at the 30% probability level. Hydrogen atoms except those of cation have been omitted for clarity.*

The zinc atom is coordinated (Figure 2-41) to four 1,4-bdc ligands with bond lengths of Zn-O1 = 1.967(3) Å, Zn-O4#1[4] = 1.953(3) Å and angles ranging from O1-Zn-O4#1[4] = 99.13(15)° to O4#1[4]-Zn-O4#2[4] = 122.8(2)°. The geometry about the zinc centre is distorted tetrahedral. The 1,4-bdc ligand acts as a monodentate linker being covalently bond to zinc centres through O1 and O4. The other oxygen atoms are involved in hydrogen bonding to either a dimethylammonium cation or to a DMF molecule.

[4] Symmetry transformations: #1: -x+3/2, y+1/4, z-1/4; #2: x+1/4, -y+1/2, z-1/4

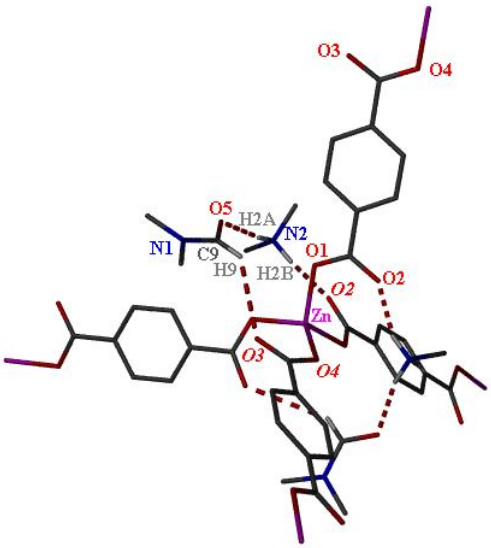

*Figure 2-41. The coordination environment around zinc and H-bonding present in **9**. Hydrogen atoms except those involved in H-bonding have been omitted for clarity. Symmetry related atoms have been labelled in italics.*

The hydrogen bonding parameters for **9** are given in Table 2-16.

*Table 2-16. Hydrogen bonding parameters for **9**.**

Atoms	Distance N/C···O (Å)	Distance H···O (Å)	Angle (°)
N2−H2A···O5	2.789	1.89	165
N2−H2B···O2#3	2.734	1.87	155
C9−H9···O3#2	3.694	2.93	139

**Symmetry transformations used to generate equivalent atoms: #1: -x+3/2,y+1/4,z-1/4; #2: x+1/4,-y+1/2,z-1/4; #3: -x+7/4,-y+3/4,z*

The linear 1,4-bdc ligands then link zinc centres forming a three dimensional double interpenetrated diamondoid framework (Figure 2-42). The Zn···Zn distances of approximately 11Å create diamondoid-shaped voids with approximate 7 Å diameter. These pores are occupied by DMF molecules and $Me_2NH_2^+$ ions.

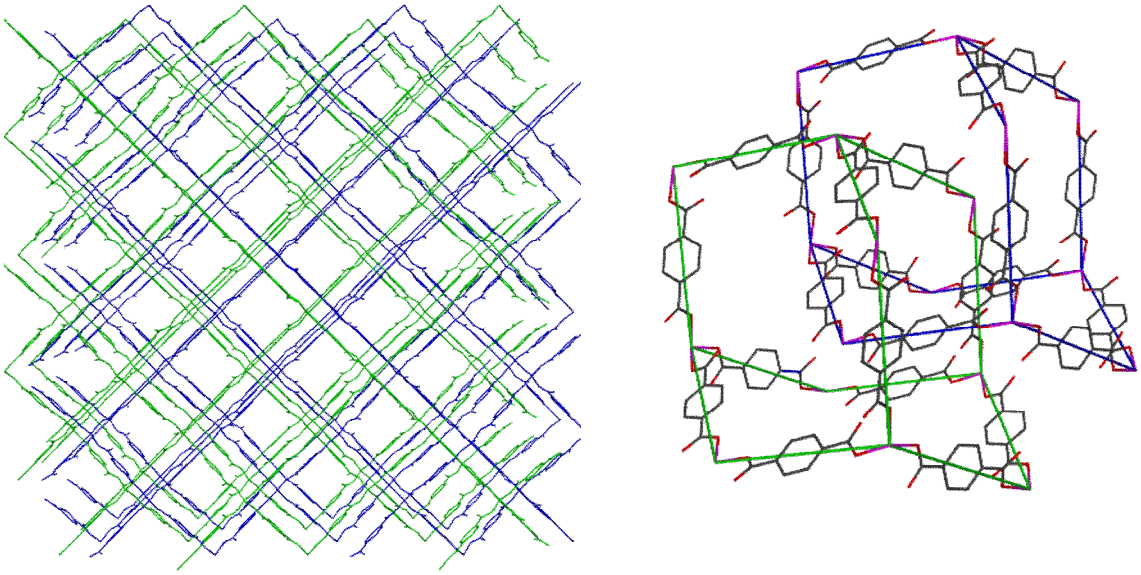

*Figure 2-42. The 3-D double interpenetrated diamondoid structure of **9**: (left) viewed down the a axis and (right) showing the two interpenetrated diamandoid cages in different colours. The DMF, $Me_2NH_2^+$ and the hydrogen atoms have been omitted for clarity.*

The dimethylammonium cations ($Me_2NH_2^+$) present in **9** may arise from DMF hydrolysis[27] or decarbonylation of DMF upon heating in the presence of base[28, 29]. The $Me_2NH_2^+$ in **9** are believed to derive from the decarbonylation of DMF, rather than solvent hydrolysis explained below.

In the presence of water, DMF hydrolyses to form dimethylamine and formic acid (Scheme 2-2) and this process can be observed to occur in aged DMF as previously reported by Burrows[30].

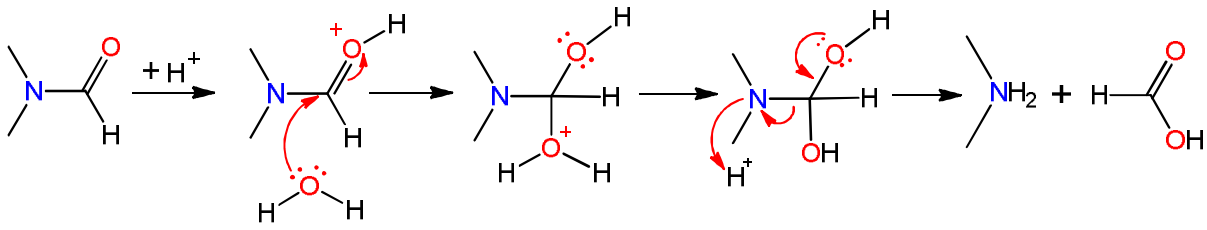

Scheme 2-2. The hydrolysis of DMF.

It is known that the DMF hydrolysis phenomenon is not specific to the $Zn(NO_3)_2 \cdot 6H_2O$ reactions[30] or other metal nitrates [31] and moreover our results suggest that the DMF hydrolysis is not specific to metal nitrate salts either.

The reaction mixture of H**L**, 1,4-H_2bdc and $ZnCl_2$ (1:2:2 molar ratio) in DMF at 120°C produced $[Zn_4(H\mathbf{L})_4(1,4\text{-bdc})_4] \cdot 4DMF$, **3**. The same reaction mixture heated at 160ºC produced crystals of $(Me_2NH_2)_2[Zn_3(1,4\text{-bdc})_4] \cdot DMF \cdot H_2O$[32] as revealed by the unit cell check and simulated PXRDs match. Therefore both compounds $(Me_2NH_2)_2[Zn(1,4\text{-bdc})_2] \cdot 2DMF$ **9** and $(Me_2NH_2)_2[Zn_3(1,4\text{-bdc})_4] \cdot DMF \cdot H_2O$[32] were obtained from similar reaction mixtures at the same temperature of 160ºC but the former was obtained when the reaction mixture was twice as concentrated as the one producing the latter compound. $(Me_2NH_2)_2[Zn_3(1,4\text{-bdc})_4] \cdot DMF \cdot H_2O$[32] has been previously obtained by heating a mixture of $Zn(NO_3)_2 \cdot 6H_2O$, 1,4-H_2bdc and $[Me_2NH_2]Cl$ in DMF at 95°C for 3 hours[30]. This compound was also prepared in the absence of added $[Me_2NH_2]Cl$ using DMF in which a degree of hydrolysis had occurred[30]. Cassar reported $(Me_2NH_2)_2[Zn(DMF)_4(OH)_2][Zn_6(1,4\text{-bdc})_8] \cdot 6DMF$[32] which formed alongside $(Me_2NH_2)_2[Zn_3(1,4\text{-bdc})_4] \cdot DMF \cdot H_2O$[32] when a reaction mixture of $Zn(NO_3)_2 \cdot 6H_2O$, 1,4-H_2bdc in aged DMF was heated at 115°C.

The incorporation of $NH_2Me_2^+$ as a counter-cation in an anionic coordination network has previously been reported for $[NH_2Me_2]_2[Zn_3(1,4\text{-bdc})(btc)_2] \cdot 2NHMe_2$[33], for other btc compounds[34] or for a cadmium 1,3-bdc[35] but the hydrolysis effect of the resulting $NH_2Me_2^+$ on influencing the products of metallosupramolecular assemblies is quite scarce and was reported for the first time in 2005 by Burrows *et al.*[30].

2.2.2.11. $(Me_2NH_2)_2[Zn(2,6\text{-ndc})_2] \cdot 3DMF$ 10

Colourless crystals of suitable size for X-ray single diffraction were collected from a reaction mixture of H**L,** 2,6-H_2ndc and $ZnCl_2$ (1:2:2 molar ratio) in DMF after one day at 120°C. The X-ray data indicated that the H**L** linker was not present in the overall structure, and that a product formulated as $(Me_2NH_2)_2[Zn(2,6\text{-ndc})_2] \cdot 3DMF$ **10** has been obtained. The crystallographic data and refinement parameters for **10** are given in Table 2-17.

*Table 2-17. Crystallographic data and refinement parameters for **10**.*

Empirical formula	$C_{37}H_{49}N_{4.5}O_{11}Zn$	
Formula weight	798.18	
Temperature	150(2) K	
Wavelength	0.71073 Å	
Crystal system	Triclinic	
Space group; Z	*P*-1, 2	
Unit cell dimensions	a = 11.8760(4) Å	α = 72.940(2)°
	b = 12.2730(4) Å	β = 77.772(2)°
	c = 15.7920(5) Å	γ = 68.122(2)°
Volume	2028.32(11) Å^3	
Density (calculated)	1.307 g/cm^3	
Crystal size	0.25 x 0.20 x 0.10 mm	
Theta range for data collection	3.53 to 25.09°	
Reflections collected/ observed (>2σ)	27554/ 4971 [R(int) = 0.0703]	
Data Completeness	0.981	
Goodness-of-fit on F^2	1.046	
Final R indices [I>2σ(I)]	R1 = 0.0614, wR2 = 0.1560	
R indices (all data)	R1 = 0.0938, wR2 = 0.1705	
Largest diff. peak and hole	1.800 and -0.422 eÅ^{-3}	

The asymmetric unit of **10** (Figure 2-43) consists of one zinc centre, four crystallographically independent 2,6-ndc halves, one full occupancy DMF (contains N1), one half occupancy DMF (contains N2), and additional DMF split over two overlapping sites (bearing N3 and N3A), one full occupancy dimethylammonium anion (based on N6), one half of a dimethylammonium anion proximate to an inversion centre (based on N5), and a diffuse region of electron density which resisted modeling followed by satisfactory convergence. The latter also straddles an inversion centre, which increased the modeling difficulties.

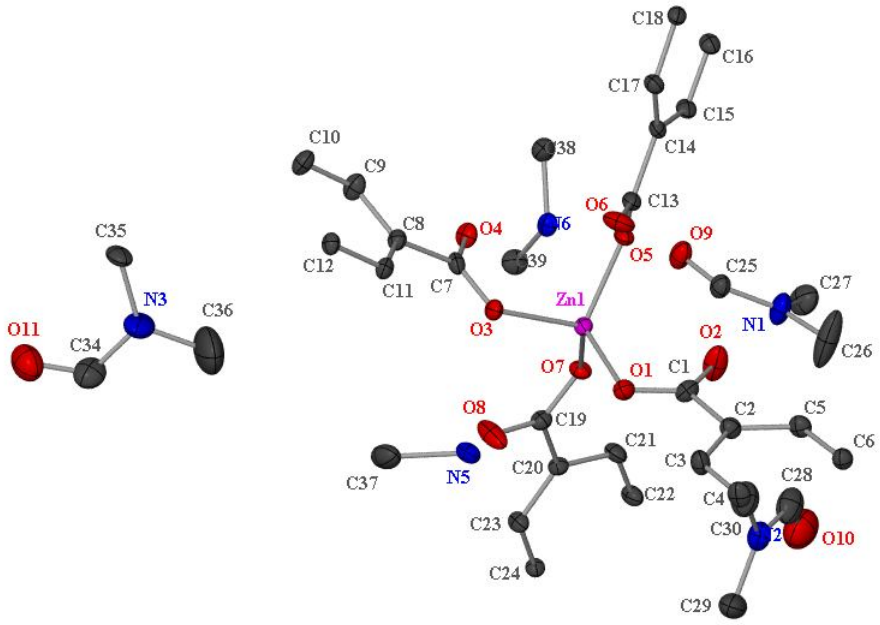

*Figure 2-43. The asymmetric unit of **10** showing thermal ellipsoids at the 30% probability level. Hydrogen atoms and minor disordered components from the DMF containing N3 have been omitted for clarity.*

The hydrogen bonding parameters for **10** are given in Table 2-18.

*Table 2-18. Hydrogen bonding parameters for **10**.*

Atoms	Distance N···O (Å)	Distance H···O (Å)	Angle (°)
N5−H5A···O3	2.939	2.25	132
N5−H5A···O8	2.874	2.25	125
N6−H6A···O9	2.752	1.88	156
N6−H6B···O4	2.736	1.85	160

The 3-D network of **10** is shown in Figure 2-44. There is a similarity with structure **5**.

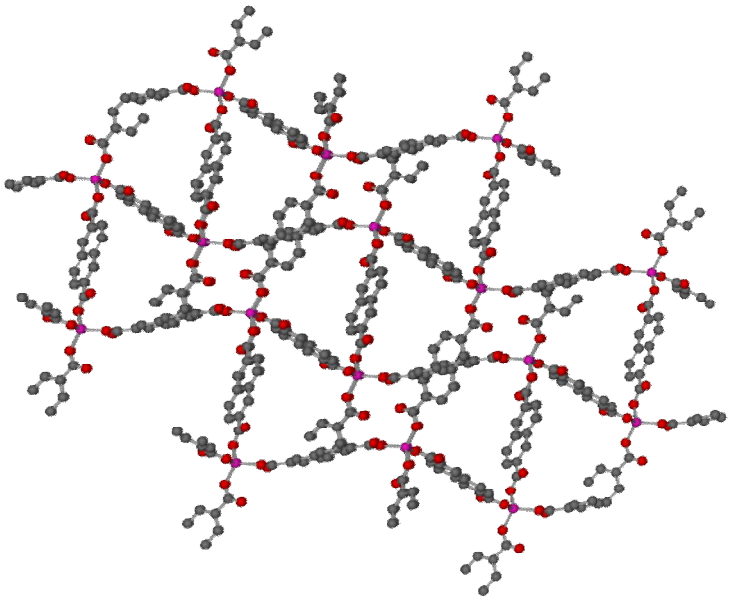

*Figure 2-44. The 3-D network of **10**. The DMFs, cations and hydrogen atoms have been omitted for clarity.*

2.3. A zinc containing 1,4-bis(4'-pyridylethynyl)benzene (L1) MOF

2.3.1. Introduction

The dipyridyl-based functionalised linker chosen is 1,4-bis(4'-pyridylethynyl)benzene (**L1**) depicted in Figure 2-45, which contains two peripheral pyridines symmetrically connected to a central benzene by two ethynes, giving the rigidity along the long axis, though rotation of the pyridine rings is possible.

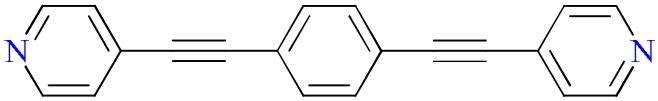

*Figure 2-45. 1,4-bis(4'-pyridylethynyl)benzene (**L1**).*

The distance of approximately 16.5Å between the nitrogens of the pyridyl rings in **L1** is in the region of 6Å longer than the equivalent distance in H**L** and 9Å longer than that in the shortest representative of the coplanar dipyridyl-based functionalised linker series, namely 4,4′-bipyridine (4,4′-bipy).

The synthesis of **L1** has been reported [36-40] and Zaman *et al.* [41] first reported the single crystal X-ray data of **L1** including a recrystallization solvent benzene. **L1** has been

reported to form MOFs [37, 41-46] and a search of Cambridge Structural Database (CSD)[17-20] has revealed the existence of eleven MOFs containing **L1** but none of them are 3-D porous MOFs. Being a fairly soft donor, **L1** is seen bound to soft metals such as silver[45].

The alkyne entity of **L1** can be readily ligated to $Cp_2Mo_2(CO)_4$ and $Co_2(CO)_6$, derived from $Co_2(CO)_8$, as was reported by Lin *et al.*[43]. Furthermore they show that both alkyne and pyridine entities of **L1** can be ligated to metal carbonyls. In this respect Burrows *et al.*[47] have reacted $[Zn_4O(edb)_3(H_2O)_2]\cdot 6DMF$, where H_2edb is 4,4′-ethynylenedibenzoic acid (Figure 2-46) with $[Co_2(CO)_8]$. $Co_2(CO)_6$ coordinates to the alkyne groups but a partial framework collapse occurs. This is attributed to a strain introduced into the network by coordination of $Co_2(CO)_6$, which it is believed to change the preferred angle between carboxylate groups in the edb ligands.

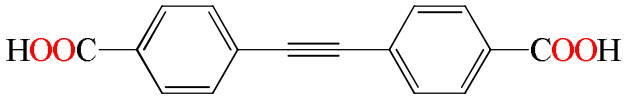

Figure 2-46. 4,4′-ethynylenedibenzoic acid (H_2edb).

Yamauchi *et al.* [48] mentioned in 2008 the first MOF where **L1** plays a pillaring role. In the presence of excess aromatic guest (pyrene), the pillar **L1** was combined with the triazine plate (tris(4-pyridyl)-2,4,6-triazine) and the metal hinge ($(en)Pd(NO_3)_2$) in a 6:4:12 ratio in D_2O. After 3h at 60°C, they observed the formation of a single product which was assigned as the expected compound by NMR analysis and the structure of this MOF was optimized by a force-field calculation. They also obtained the single X-ray crystal structure for the analogous MOF with 1,4-bis-(4-pyridyl)butadiyne, and suggest that both structures are potential elements for nanofabrication applications involving electroconductive and photophysical devices.

Nguyen *et al.* [49] reported very recently a zinc-based pillared paddlewheel MOF containing a protected catechol-functionalized **L1** in combination with a dibromotetratopic ligand (Scheme 2-3). This MOF, which has large pores, showed catalytic activity in the benzylic oxidation of tetralin in the presence of tert-butylhydroperoxide.

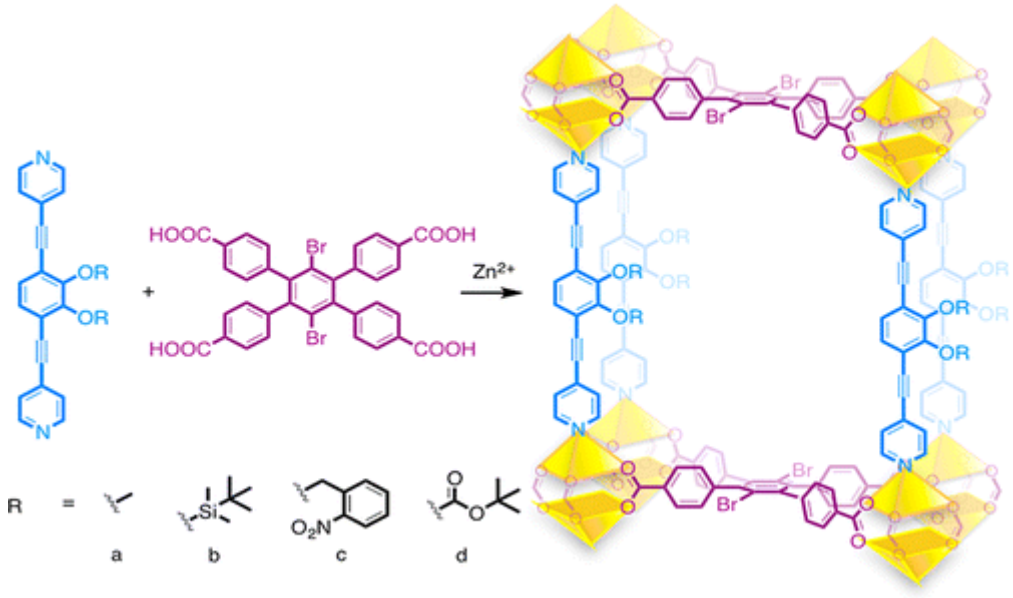

*Scheme 2-3. Solvothermal synthesis of Zn-Pillared Paddlewheel MOF containing a protected catechol-functionalized **L1**.*[49]

The present work stems from previously reported one-pot synthesis approach used to prepare mixed-linker MOFs of H**L** with dicarboxylates. We aimed to introduce a highly rigid long bipyridine ligand **L1** with zinc dicarboxylates in order to understand the effect of interpenetration and pore generation.

2.3.2. Results and discussion

Reactions of **L1** with 1,4-H_2bdc and either $ZnCl_2$ or $Zn(NO_3)_2 \cdot 6H_2O$ have been performed at 120°C. The molar ratio was altered from 1:1:1 (**L1**: 1,4-H_2bdc: Zn(II) salt) to 1:2:2. All these reactions produced a mix of crystals which have been checked by means of unit cell and powder X-ray diffraction measurements. These resultant materials were identified as known compounds such as MOF-2, $[Zn_3(1,4\text{-bdc})_4(Me_2NH_2)_2] \cdot DMF \cdot H_2O$[32], $[Zn_3(1,4\text{-bdc})_3 \cdot 2H_2O] \cdot 4DMF$ (known as IFACAT). The reaction mixtures with $ZnCl_2$ produced better crystals for single X-ray analysis than those with $Zn(NO_3)_2 \cdot 6H_2O$, hence the metal-chloride salt seems to be a better candidate for producing crystals than the nitrate in this particular case.

L1 reacted with 1,4-H_2bdc at 80°C in DMF with either $ZnCl_2$ or $Zn(NO_3) \cdot 6H_2O$, in 1:1:1 or 1:2:2 molar ratio produces a new material which has been formulated as $[Zn_2$(1,4-

bdc)$_2$(**L1**)$_2$]·2.7DMF **11** but better crystals were obtained from **L1**: 1,4-H_2bdc:$ZnCl_2$= 1:2:2.

All these results suggest that **L1** can be incorporated into a mixed-linker MOF but is still place for establishing the reaction conditions which give a single-phased bulk sample of [Zn_2(1,4-bdc)$_2$(**L1**)$_2$]·2.7DMF **11**. A whole range of compounds which does not have **L1** incorporated, as [Zn_3(1,4-bdc)$_3$·2H_2O]·4DMF (IFACAT) and **9**, have been found in the resulting reaction mixtures. This is suggesting that one-pot synthesis results can be quite messy sometimes as was for this system and a controlled stepwise synthesis might be a better approach in this instance.

In summary reaction mixtures of **L1** : 1,4-H_2bdc and either $ZnCl_2$ or $Zn(NO_3)_2$·6H_2O in either 1:1:1: or 1:2:2 molar ratio at or above 120^{0}C give mixtures containing known compounds and generally not including L1.

2.3.2.1. 1,4-bis(4'-pyridylethynyl)benzene (L1)

The 1,4-bis(4'-pyridylethynyl)benzene (**L1**) ligand was synthesised using a three-step procedure as shown in Scheme 2-4.

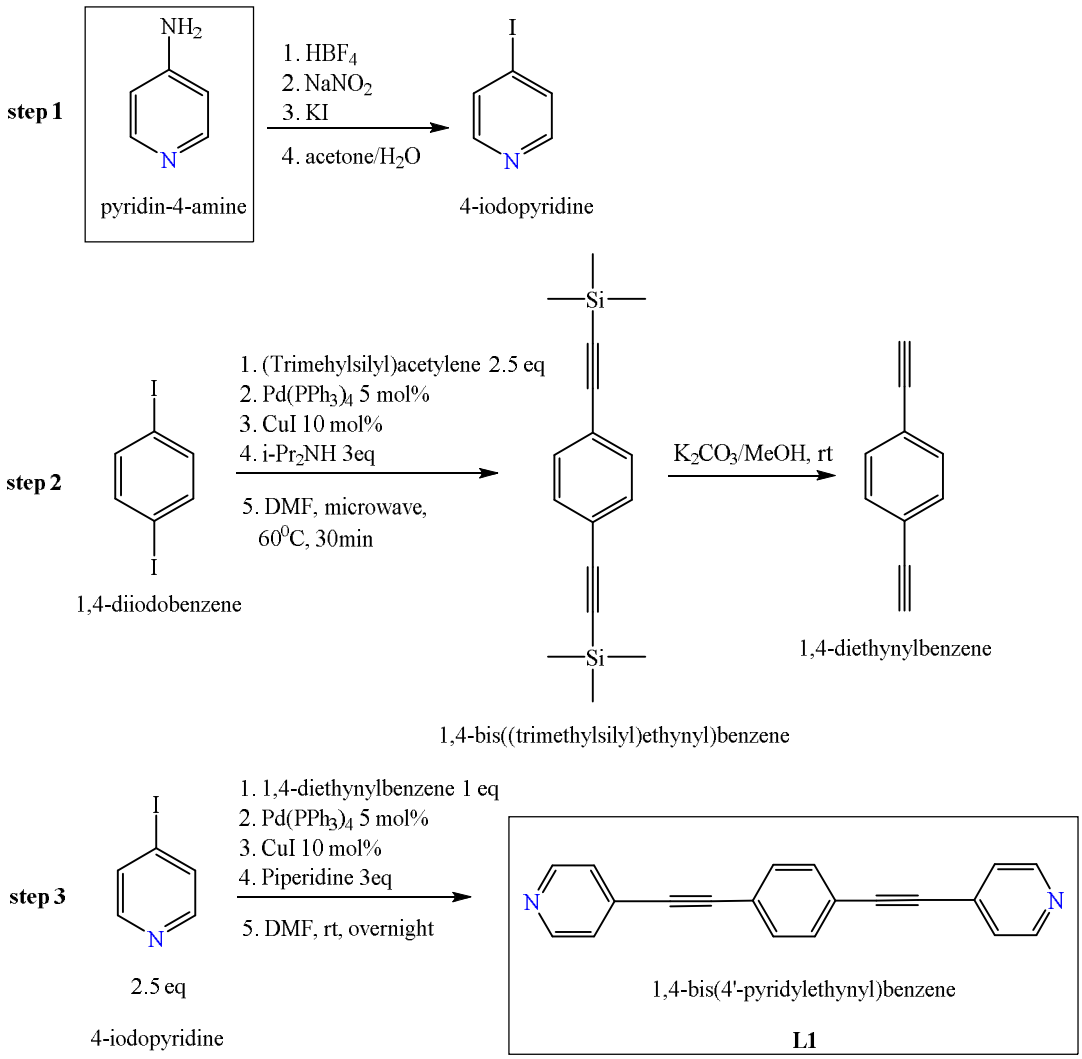

*Scheme 2-4. The three-step synthesis of **L1**.*

To a solution of purchased pyridin-4-amine in aqueous tetrafluoroboric acid, sodium nitrite was added portion-wise ensuring that no gas evolution could be detected. The resultant slurry was stirred for 30 min. The reaction mixture was filtered to give a white solid. The solid was quickly transferred portion-wise to a stirring saturated solution of potassium iodide in acetone/H_2O. The brown slurry was decolorised with saturated sodium thiosulphate, carefully neutralized with saturated $NaHCO_3$ and extracted with diethyl ether. The organic layers were washed with water, brine, dried over $MgSO_4$, filtered and concentrated. The 4-iodopyridine obtained is used in the 3rd step. In **step 2**, to a solution of purchased 1,4-diiodobenzene, $Pd(PPh_3)_4$ and CuI in dry DMF, (trimethylsilyl)acetylene was added and the solution stirred for 30 min at room temperature in degassed conditions. Next *i*-Pr_2NH was added and the reaction mixture heated in the microwave at 60^{o}C for 30 min. The mixture was quenched with water and extracted with ethyl acetate. The organic

layers were washed with water, brine, saturated $NaHCO_3$, dried over $MgSO_4$, filtered and concentrated. The solid obtained was dissolved in MeOH and K_2CO_3 added. The mixture was stirred for 20 min at room temperature, solvent evaporated and the product purified on chromatography column (diethyl ether : petrol; 1:9). The 1,4-diethynylbenzene obtained is used in the 3rd step together with 4-iodopyridine obtained in the 1st step. In **step 3**, to a solution of 4-iodopyridine, $Pd(PPh_3)_4$ and CuI in dry DMF, 1,4-diethynylbenzene was added and the mixture was stirred for 30 min at room temperature in degassed conditions. Next piperidine was added and the reaction stirred overnight. The mixture was quenched with water and extracted with ethyl acetate. The organic layers were washed with water, brine and saturated $NaHCO_3$, dried over $MgSO_4$, filtered and concentrated. The product 1,4-bis(4'-pyridylethynyl)benzene (**L1**) was purified on a chromatography column (DCM : ethyl acetate; 3:7, with a drop of triethylamine for each 100ml of eluent). The synthesis steps for **L1** are detailed in the experimental section of this chapter.

2.3.2.2. $[Zn_2(1,4\text{-bdc})_2(L1)_2]\cdot 2.7DMF$ 11

The solvothermal reaction of **L1** with 1,4-H_2bdc and $ZnCl_2$ (1:2:2 molar ratio) in DMF at 80°C yielded in 3 days colourless plate-like crystals which subsequently were formulated as $[Zn_2(1,4\text{-bdc})_2(\mathbf{L1})_2]\cdot 2.7DMF$ **11**. The crystal data and refinement parameters for **11** are shown in Table 2-19.

*Table 2-19. Crystallographic data and refinement parameters for **11**.*

Empirical formula	$Zn_2C_{64.1}O_{10.7}N_{6.70}H_{50.9}$	
Formula weight	1216.96	
Temperature	150(2) K	
Wavelength	0.71073 Å	
Crystal system	Triclinic	
Space group; Z	*P*-1, 2	
Unit cell dimensions	a = 10.0660(3) Å	α = 101.468(2)°
	b = 15.0730(5) Å	β = 93.773(2)°
	c = 20.7290(5) Å	γ = 105.213(1)°
Volume	2951.06(15) Å^3	

Density (calculated)	1.370 g/cm^3
Crystal size	0.40 x 0.25 x 0.25 mm
Theta range for data collection	3.68 to 25.03°
Reflections collected/ observed (>2σ)	42004/ 30232 [*R*(int) = 0.0284]
Data Completeness	0.989
Goodness-of-fit on F^2	1.446
Final *R* indices [$I>2\sigma(I)$]	*R*1 = 0.1277 *wR*2 = 0.3612
R indices (all data)	*R*1 = 0.1538 *wR*2 = 0.3799
Largest diff. peak and hole	1.983 and -1.117 eÅ^{-3}

The asymmetric unit of **11** shown in Figure 2-47 consists of two zinc centres, two 1,4-bdc ligands, two **L1** ligands, 0.7 of a modelled DMF solvent fragment containing N5 and some diffuse solvent. The diffuse solvent was treated using the SQUEEZE subroutine of PLATON[22], and it approximately accrues to two DMF molecules per asymmetric unit. Data presented here take account of the presence of this lattice solvent in the MOF.

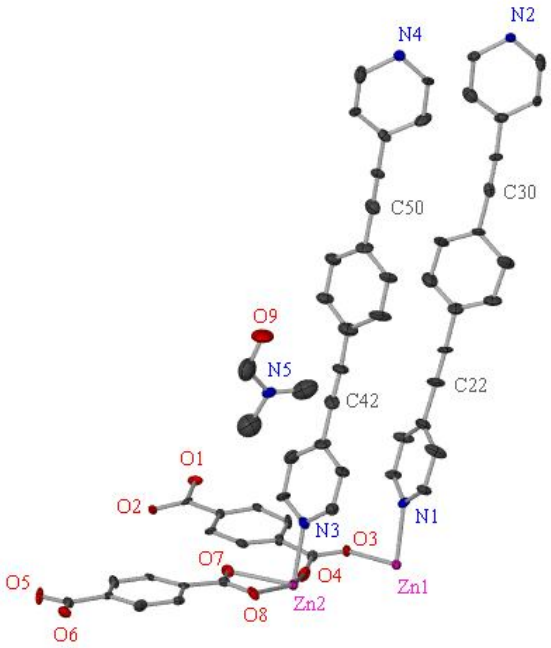

*Figure 2-47. The asymmetric unit of **11** showing thermal ellipsoids at the 30% probability level. The minor disordered carbon atoms and the hydrogen atoms have been omitted for clarity.*

The SBU node consists of a zinc dimer in distorted octahedral geometry formed by two bidentate bridging carboxylates from two 1,4-bdc ligands, two chelating 1,4-bdc ligands, and two pairs of **L1** ligands in *trans*-positions.

The layers are coplanar in **11** compared with those in **3** which are undulated. This may be attributed to the same coordination mode adopted by both carboxylate groups of the 1,4-bdc linker compared with a different coordination mode for the carboxylate groups attached to the same 1,4-bdc linker in **3**.

Two **L1** pillars at each metallic node connect the layers to generate one of the two identical 3-D frameworks shown in Figure 2-48. The 3-D framework of **11** shows two types of channels: longer parallelogram-like ones of approximately 13.8 x 4.7 Å filled with DMF solvent molecules and smaller square-like empty channels of approximately 6.9 x 4.7 Å.

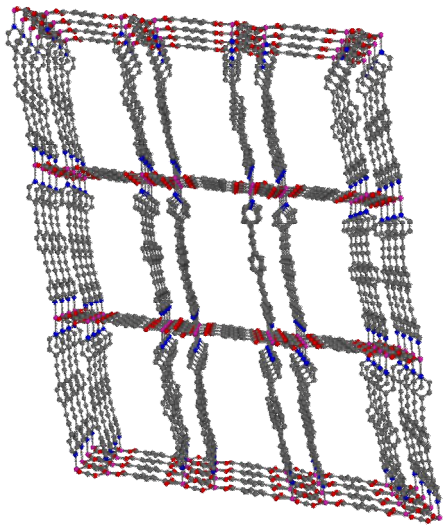

*Figure 2-48. Perspective view of **11** along the c axis. The DMF solvent molecules, minor disordered carbon atoms and hydrogen atoms have been omitted for clarity.*

There are two interpenetrating 3-D frameworks in the structure shown in a space filling representation in Figure 2-49. In **11** there is no hydrogen bonding present which contrast with **3** where doubly-interpenetrated frameworks are held together through hydrogen bonding.

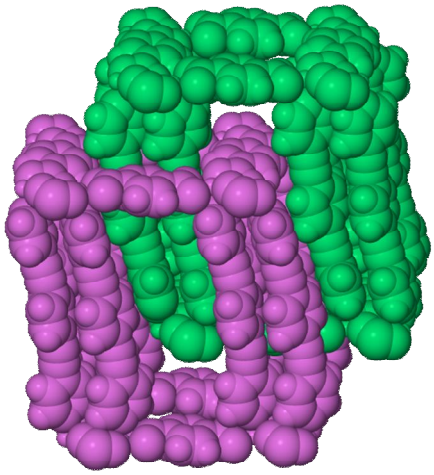

*Figure 2-49. Space filling representation of **11** showing the 2-fold interpenetrated cube-like cages in different colours. DMF solvent molecules and minor disordered carbon atoms have been omitted for clarity.*

The total potential solvent area volume per unit cell volume of **11** was calculated using program PLATON[22] as ca. 28.7%. The larger free volume for **11** compared with **3** is consistent with the linker lengths. The N···N distance in **L1** is 16.5 Å, which is about 6 Å longer than in H**L**.

Further work for this MOF will be needed in order to optimise the reaction conditions and obtain sufficient of this material to assess its porosity by running nitrogen adsorption measurements. The presence of the alkyne group on the **L1** ligand means that **11** might be useful for post-synthetic modification (PSM). The alkyne group as mentioned earlier could be coordinated to a metal centre to create additional functionality within the MOF. Moreover, it is hoped that coordination to the alkyne groups of **11** will not affect the integrity of framework due to the presence of two triple bonds into the **L1** linker, which will compensate each other changes imposed by the attachment.

It seems that a similar work has been undertaken in the same time to our work on making MOFs with **L1,** by Kitagawa's group. They reported the synthesis, structure and gas sorption properties of Zn(1,4-bdc)**L1.** [50] TGA suggested the presence of six DMF molecules for each formula unit of Zn(1,4-bdc)**L1** and the MOF did not show any nitrogen gas adsorption properties. However, we got superior crystals for the single crystal X-ray

analysis by using zinc chloride instead of zinc nitrate and a reaction temperature of 80° rather than 120°.

2.4. Experimental

2.4.1. General

L1 was synthesised by Dominika Bachera from Dr. Sean Bew's group, our collaborators from University of East Anglia. All other reagents were purchased commercially and used without further purification.

The MOF syntheses were carried out in vials, tubes or vessels dependent upon the reaction temperature and the solvothermal reactions were heated in a Sanyo MOV-112 temperature-control programmable oven. The reactions run at room temperature were carried out in simple vials while the solvothermal ones in 10 – 30 cm^3 thick-walled vials, 15- 40 cm^3 Ace pressure tubes purchased from Sigma Aldrich or in 23 cm^3 Parr Teflon lined stainless steel vessels when the reaction temperature was higher than the boiling point of the solvent used in reaction.

Powder X-ray diffractions (PXRDs) were recorded on a Bruker AXS D8 Advance diffractometer with copper Kα radiation of wavelength 1.5406 Å at 298 K. Samples were placed in 0.3- 0.7 mm diameter Lindemann capillaries, and measured with a 2θ range of 3 - 60°. The step size was 0.02° with time per step of 1.00s. Simulated X-ray powder patterns were generated from single crystal data that were imported into PowderCell[51].

Microanalysis (Carbon, Hydrogen and Nitrogen = CHN) data was recorded on a CE-440 Elemental Analyser by Mr. Alan Carver at the University of Bath. Where microanalysis data is missing this is due to the inability to get a satisfactory match after multiple attempts.

TGA experiments were performed on a Perkin Elmer TGA 4000 Thermogravimetric Analyser. The samples were usually heated if not mentioned otherwise from 25°C to 600°C at 10°C/min under a flow of nitrogen (20 mL/min).

^{1}H NMR spectra were recorded at 298 K on a Bruker Ultrashield 300 MHz spectrometer.

2.4.2. Single-Crystal X-Ray Crystallography

X-ray data on $Zn_4(1,4\text{-ndc})_4(H\mathbf{L})_4$ **4** were collected by Dr. Mary Mahon on an Oxford Diffraction Gemini diffractometer fitted with an Atlas CCD (charge-coupled device) detector, and on a Nonius Kappa CCD diffractometer respectively, using in both cases X-rays with Mo-Kα radiation wavelength of 0.71073 Å at 150 K.

X-ray data on $[Zn_4(1,3\text{-bdc})_4(H\mathbf{L})_4]\cdot 4DMF$ **8** were collected by Dr. Mary Mahon on a Beamline I19 of Diamond Light Source using a Crystal Logic 4-circle kappa goniometer fitted with a Rigaku Saturn 724 CCD detector employing synchrotron radiation (λ = 0.6889 Å) at 123(2) K.

X-ray data on $[Zn(OAc)_2(H\mathbf{L})_2]\cdot H_2O$ **1** and $(Me_2NH_2)_2[Zn(2,6\text{-ndc})_2]\cdot 3DMF$ **10** were collected by Dr. Anna Warren on a Nonius Kappa CCD diffractometer using X-rays with Mo-Kα radiation wavelength of 0.71073 Å at 150 K.
X-ray data for the remaining compounds were collected by myself on a Nonius Kappa CCD diffractometer using X-rays with Mo-Kα radiation wavelength of 0.71073 Å at 150 K.

The structures were solved using SHELXS-97[52] and refined using full-matrix least squares in SHELXL-97[52]. The final refinement for $(Me_2NH_2)_2[Zn(1,4\text{-bdc})_2]\cdot 2DMF$, **9** was run by Dr. Gabriele Kociok-Köhn. The final refinements for all of the remaining structures were run by Dr. Mary Mahon and were generally straightforward with the following exceptions and points of note. Unless noted below, all non-hydrogen atoms were refined anisotropically in the final least squares run, and hydrogen atoms were included at calculated positions. Siobhan Chan has been involved as part of her final year MChem project with structure determination of $[Zn_4(1,4\text{-ndc})_4(H\mathbf{L})_4]$ **4** and $[Zn_2(2,6\text{-ndc})_2(H\mathbf{L})_2]\cdot DMF$ **5**.[53]

Search for and analysis of solvent accessible voids in the structures was performed using the SQUEEZE subroutine of PLATON [22]. Solvent accessible voids are defined as regions in the structure that can accommodate at least a sphere with radius 1.2 Å without intersecting with any of the van der Waals spheres assigned to each atom in the structure.

The free solvent molecules from within the structure and the minor disordered atoms have been removed prior to these calculations.

For $[Zn_4(1,4\text{-bdc})_4(H\mathbf{L})_4]\cdot 4DMF$ **3** some distance restraints were added to aid refinement in the final least squares. The nitrogen bound hydrogens in the H**L** ligands were located but ultimately included at calculated positions, although the atomic isotropic thermal parameter U_{iso} values were refined. The diffraction data suggested racemic twinning which was accounted for in the refinement.

Regarding $Zn_4(1,4\text{-ndc})_4(H\mathbf{L})_4$ **4** while the refinement converged well in terms of shift/esd value, there are clear shortcomings in the model. These are largely due to the fall off in diffraction intensity of this material at early Bragg angles. The worst affected regions concern the carboxylate ligands, largely perhaps, because the resolution of the data is not good. The high angle data were diffuse at best. Rigid hexagons restraints were applied throughout where possible, augmented by some distance and planarity restraints. Only the zinc atoms were treated anisotropically due to the data quality. Nonetheless, what we have here is an unambiguous assignment of the interpenetrated framework in this compound. We do not intend to make any claims about the individual metric data presented herein.

The solvent in the lattice of $[Zn_2(2,6\text{-ndc})_2(H\mathbf{L})_2]\cdot DMF$ **5** is diffuse and is estimated herein as one DMF per asymmetric unit. This estimate is based on the pre-SQUEEZE evident electron density, in combination with the SQUEEZE output. The hydrogen attached to either N3 or N4 could not be located with any credibility, and hence is omitted from the refinement. The phenyl carbons in the two crystallographically independent 2,6-ndc ligand halves are subject to 50:50 disorder, which was readily modelled by employing minimal distance restraints to assist convergence.

In $[Zn_4(1,3\text{-bdc})_4(H\mathbf{L})_4]\cdot 4DMF$ **6** restraints were placed on the atomic displacement parameters of atoms with less than 100% occupancy. This includes the ordered half molecule of guest DMF which could be modelled with some confidence.

Two attempts have been made to collect X-ray data for $[Zn(1,3\text{-bdc})(H\mathbf{L})]\cdot DMF$ **7** but the highest completeness for this data has reached 81% due to a poor quality/size of this crystal but overall this data is an unambiguous result.

For $(Me_2NH_2)_2[Zn(2,6\text{-ndc})_2]\cdot 3DMF$ **10** it was moderately clear that the diffuse region (treated with PLATON SQUEEZE) consisted of two overlapping elements, one of which was a DMF fragment - the oxygen therein positioned to hydrogen bond to H5B. The second component of electron density is attributed to half of an additional anion – which is needed to balance the charge on the framework. The data presented here take account of the SQUEEZED electron density, and also of the three hydrogen atoms that could not be included at calculated positions (because of disorder) on C37. Some distance restraints applied in non-SQUEEZED disordered solvent region, and ADP restraint applied to two atoms.

Refinement of $[Zn_2(1,4\text{-bdc})_2(\mathbf{L1})_2]\cdot 2.7DMF$ **11** was hampered by two factors: 20% twinning about the [0 0 1] reciprocal lattice direction and disorder. The final residuals are partially due to the residual density maximum, which manifests itself close to one of the solvent accessible regions in the lattice. Atomic displacement parameter restraints were applied to some atoms to assist convergence.

2.4.3. Synthesis of 3,5-bis(4-pyridyl)-1H-pyrazole (HL)

4-acetylpyridine (11.9 mL, 107.31 mmol) and methylisonicotinate (14.72 g, 107.31 mmol) were both placed in a 500 mL round bottomed flask and stirred vigorously with a large stirrer bar. KO^tBu (12.04 g, 107.31 mmol) was added and a reflux condenser immediately attached to aid cooling down the reaction mixture. The reaction initiated after approximately five seconds and the solution began to turn into a brown solid, hence grinding of KO^tBu is required. Once cooled the solid was dissolved in water (300 mL) and the product was then precipitated out on the addition of acetic acid (acetic acid dropwise added to pH = 4-5). The solid was then filtered and washed with water (2 x 50 mL). The product was then purified through recrystallization in the minimum amount of ethanol and water (1: 1 mixture) yielding a white material which was dried in oven at 85°C for 3 hours. Yield 8.49 g (35%). The product was identified as 2-Propen-1-one, 3-hydroxy-1,3-di-4-pyridinyl through ^1H NMR (300 MHz, $CDCl_3$): δ = 16.10 (s, 1 H, OH), δ = 8.77 (d, J = 1.66 Hz, 2 H), δ = 8.76 (d, J = 1.66 Hz, 2 H), 7.73 (d, J = 1.68 Hz, 2 H), 7.72 (d, J = 1.68 Hz, 2 H), δ = 6.82 (s, 1 H).

2-Propen-1-one, 3-hydroxy-1, 3-di-4-pyridinyl (5.5 g, 24.4 mmol), hydrazine dihydrochloride (2.92 g, 27.8 mmol), NaOH (1.6 g, 40 mmol) were placed in a 500 mL round bottom flask and ethanol (80 mL) added. The reaction mixture was then stirred vigorously for 5 min until a suspension was formed which was heated at reflux overnight. The solvent was then removed with a rotavapour and to the wet solid 300 mL of water was added before neutralisation with $NaHCO_3$ (5 g). The formed white solid was then separated by filtration, washed with water (2 x 50 mL) and air dried. Yield 5.32 g (98%). The product was identified through ^1H NMR (300 MHz, DMSO-d_6): δ = 13.99 (broad s, 1 H, NH), δ = 8.64 (d, J = 6.01 Hz, 4 H), δ = 7.79 (d, J = 6.12 Hz, 4 H), 7.61 (s, 1 H).

2.4.4. Synthesis of 1,4-bis(4'-pyridylethynyl)benzene (L1)

The synthesis of 1,4-bis(4'-pyridylethynyl)benzene (**L1**) was performed over three-step method as previously depicted in Scheme 2-4:

Step 1:

To a cooled (-10^{o}C) solution of pyridin-4-amine (2 g, 0.021 mmol) in 48% aqueous tetrafluoroboric acid (17 mL, 267 mmol) sodium nitrite (1.58 g, 0.023 mmol) was added portion-wise ensuring that no gas evolution could be detected. The resultant slurry was stirred at that temperature for 30 min. The reaction mixture was filtered to give a white solid (keep damp: potentially explosive). The solid was quickly transferred portion-wise to a stirring saturated solution of potassium iodide (5.6 g, 33 mL) in acetone/H_2O (4 : 6). The brown slurry was decolorised with sat. sodium thiosulphate (10 mL), carefully neutralized with sodium carbonate (20 mL) and extracted with diethyl ether (3 x 50 mL). The organic layers were washed with water (3 x 50 mL), brine (100 mL), dried over $MgSO_4$, filtered and concentrated. The obtained product was used in the 3rd step.

Step 2:

To a solution of 1,4-diiodobenzene (0.1 g, 0.303 mmol), $Pd(PPh_3)_4$ (0.018 g, 0.015 mmol) and CuI (0.0058 g, 0.03 mmol) in dry DMF (5 mL) (trimethylsilyl)acetylene (0.11 mL, 0.758 mmol) was added and the solution stirred for 30 min at room temperature in degassed conditions. Next i-Pr_2NH (0.13 mL, 0.909 mmol) was added and the reaction mixture heated in the microwave at 60^{o}C for 30 min. The mixture was quenched with water (10 mL) and extracted with ethyl acetate (3 x 15 mL). The organic layers were

washed with water, brine, sat. $NaHCO_3$, dried over $MgSO_4$, filtered and concentrated. Thus received solid was dissolved in MeOH (10 mL) and potassium carbonate (0.1 g, 0.724 mmol) added. The mixture was stirred for 20 min at room temperature, solvent evaporated and the product purified on chromatography column (diethyl ether : petrol; 1 : 9). Product mass = 0.0182 g. Reaction yield = 48 %.

Step 3:

To a solution of 4-iodopyridine (0.073 g, 0.357 mmol), $Pd(PPh_3)_4$ (0.021 g, 0.018 mmol) and CuI (0.0068 g, 0.0357 mmol) in dry DMF (5 mL) 1,4-diethynylbenzene (0.018 g, 0.143 mmol) was added and the mixture was stirred for 30 min at room temperature in degassed conditions. Next piperidine (0.1 mL, 1.07 mmol) was added and the reaction stirred overnight in the same conditions. The mixture was quenched with water (10 mL) and extracted with ethyl acetate (3 x 15 mL). The organic layers were washed with water, brine and sat. $NaHCO_3$, dried over MgSO4, filtered and concentrated. Product was purified on chromatography column (DCM : ethyl acetate; 3:7, with a drop of triethylamine for each 100ml of eluent). Product mass= 0.0296g. Reaction yield= 74%. The product was identified as **L1** through ^{1}H NMR (Figure 2-50) and IR (Figure 2-51).

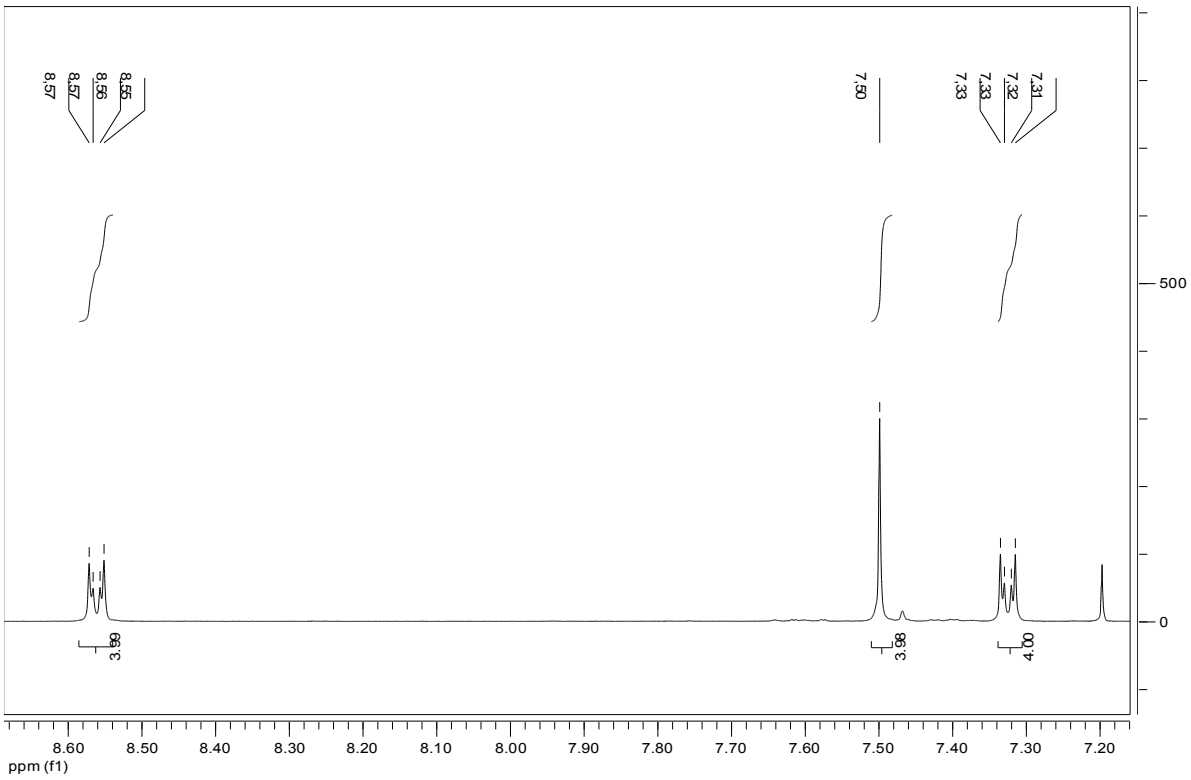

*Figure 2-50. ^{1}H-NMR of **L1** in $CDCl_3$.*

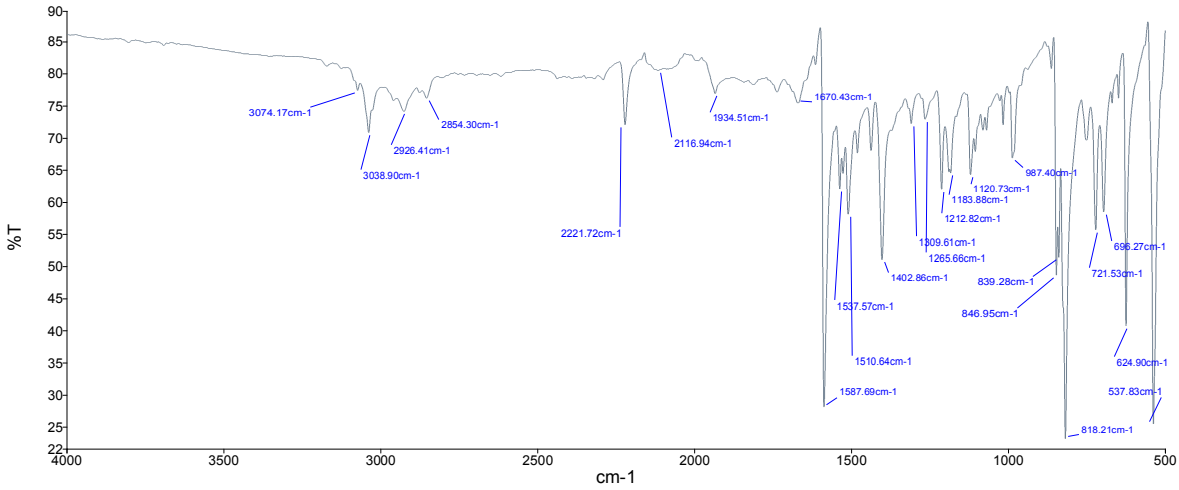

*Figure 2-51. IR of **L1**.*

2.4.5. Synthesis of $[Zn(OAc)_2(HL)_2]\cdot H_2O$ 1

A mixture of H**L** (0.112 g, 0.5 mmol), $Zn(OAc)_2\cdot 2H_2O$ (0.111 g, 0.5 mmol) and water (8 cm^3) was added to a 23 cm^3 Parr Teflon-lined stainless steel vessel. The vessel was sealed and heated at 140°C for 36 hours and then cooled to room temperature. Colourless crystals of **1** were separated by filtration. Yield 0.100 g (31%). The PXRD pattern of the sample matches that of the simulated X-ray single crystal structure (Figure 2-52).

Found (calculated for $C_{30}H_{28}N_8O_5Zn$): C, 55.5 (55.8); H, 3.95 (4.37); N, 17.4 (17.4) %.

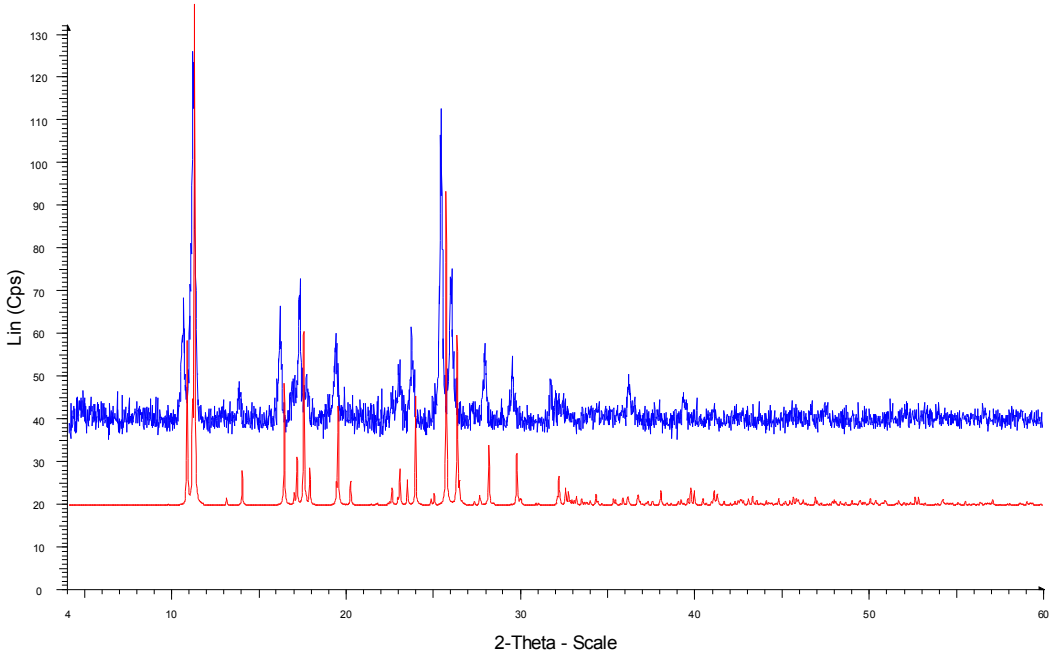

*Figure 2-52. The PXRD pattern for **1**: top) as-synthesised and bottom) simulated from the X-ray crystal structure.*

2.4.6. Synthesis of $ZnCl_2$(HL) 2

A mixture of H**L** (0.112 g, 0.5 mmol), $ZnCl_2$ (0.070 g, 0.5 mmol) and water (8 cm^3) was added to a 23 cm^3 Parr Teflon-lined stainless steel vessel. The vessel was sealed and heated at 140°C for 36 hours and then cooled to room temperature. Colourless crystals of **2** were separated by filtration. Yield 0.140 g (78%). The PXRD pattern of the sample matches that of the simulated X-ray single crystal structure (Figure *2-53*).

Found (calculated for $C_{13}H_{10}Cl_2N_4Zn$): C, 43.4 (43.5); H, 2.81 (2.81); N, 15.5 (15.6) %.

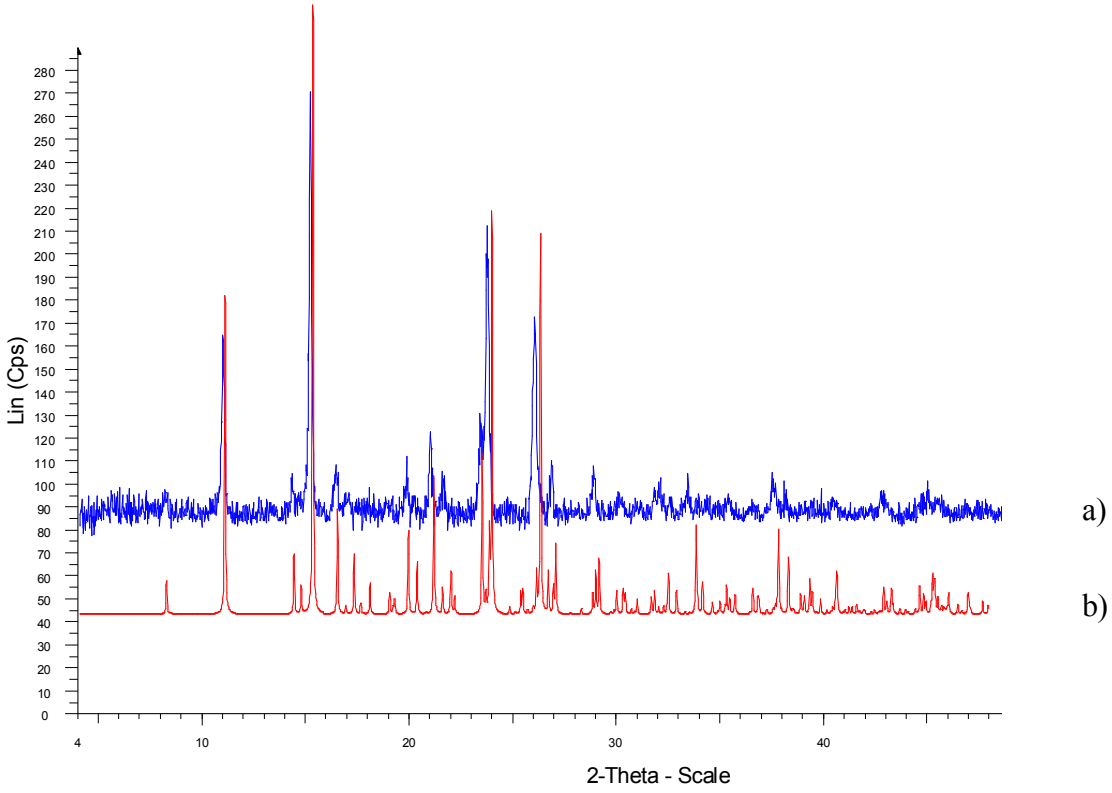

*Figure 2-53. The PXRD pattern for **2**: a) as-synthesised and b) simulated from the X-ray crystal structure.*

2.4.7. Synthesis of $[Zn_4(1,4\text{-bdc})_4(HL)_4]\cdot 4DMF$ 3

H**L** (0.044g, 0.2 mmol), $ZnCl_2$ (0.060 g, 0.4 mmol) and terephthalic acid (0.066 g, 0.4 mmol) were dissolved in 20 cm^3 of anhydrous DMF with gentle heating and stirring. The clear solution was placed in a 40 mL Ace Pressure tube, sealed and heated at 120°C for 2 days in an oven. The resulted colourless hexagonal crystals were then separated by filtration and washed with fresh DMF (0.05 g, 12%). The PXRD pattern of the sample matches that of the simulated X-ray single crystal structure (Figure 2-54).

Found (calculated for $[Zn_4(H\mathbf{L})_4(1,4\text{-bdc})_4]\cdot 4DMF$): C, 54.0 (54.92); H, 3.99 (4.03); N, 13.1 (13.34) %.

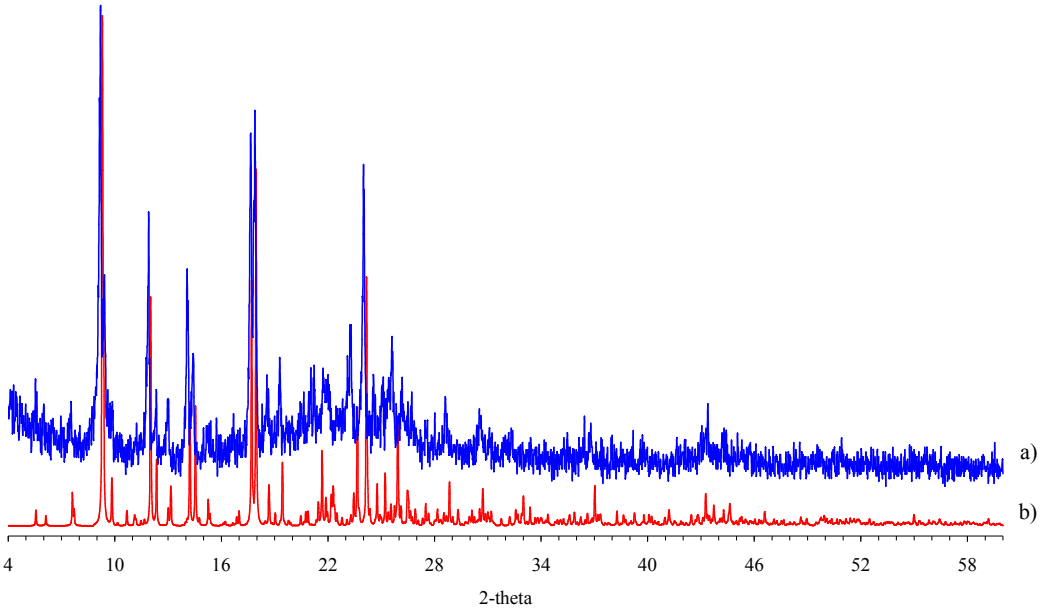

*Figure 2-54. The PXRD pattern for **3**: a) as-synthesised and b) simulated from the X-ray crystal structure.*

2.4.8. Synthesis of $Zn_4(1,4\text{-ndc})_4(HL)_4$ 4

HL (0.022 g, 0.1 mmol), 1,4-H_2ndc (0.043 g, 0.2 mmol) and $Zn(NO_3)\cdot 6H_2O$ (0.027 g, 0.1 mmol) were dissolved in 6 cm^3 of anhydrous DMF with gentle stirring. The colourless solution was placed in a vial, capped and heated at 130°C for 2 days in an oven. The resulted colourless lath like crystals were observed to undergo visible morphological changes if taken out from their reaction medium, in air as can be seen from Figure 2-55.

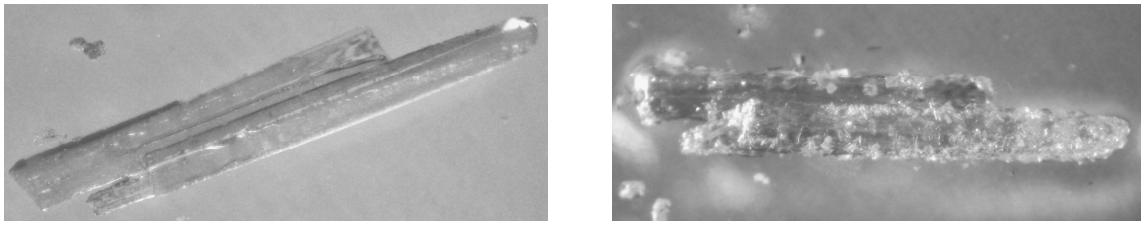

*Figure 2-55. The colourless crystals of **4**: (left) as-synthesised and (right) after 10 min taken out of its mother liquor.*

The as-synthesised crystals were analysed immediately through single crystal X-ray diffraction and the structure was determined to be **4**. However, a matching PXRD pattern of this sample to that of the simulated X-ray single crystal structure of **4** has not been obtained due to its moisture sensitivity.

2.4.9. Synthesis of $[Zn_2(2,6\text{-ndc})_2(HL)_2]\cdot DMF$ 5

H**L** (0.022g, 0.1 mmol), 2,6-H_2ndc (0.043 g, 0.2 mmol) and $Zn(NO_3)\cdot 6H_2O$ (0.027 g, 0.1 mmol) were dissolved in 6 cm^3 of anhydrous DMF with gentle stirring. The clear solution was placed in a pressure vial, capped and heated at 130°C for 2 days in an oven. The resulted block-like pale yellow crystals with rounded edges showed signs of degradation at low temperatures whilst trying to collect single crystal X-ray data and room temperature collection only gave poor resolution X-ray data. However, when the DMF solvent was removed from the reaction vial and the crystals were left at room temperature for several weeks, a change in morphology was observed, resulting in crystals with much more well-defined edges. Single crystal X-ray diffraction of one of these crystals produced good data from which $[Zn_2(2,6\text{-ndc})_2(H\mathbf{L})_2]\cdot DMF$ was formulated. The PXRD pattern of the sample matches that of the simulated X-ray single crystal structure of **5** (Figure 2-56).

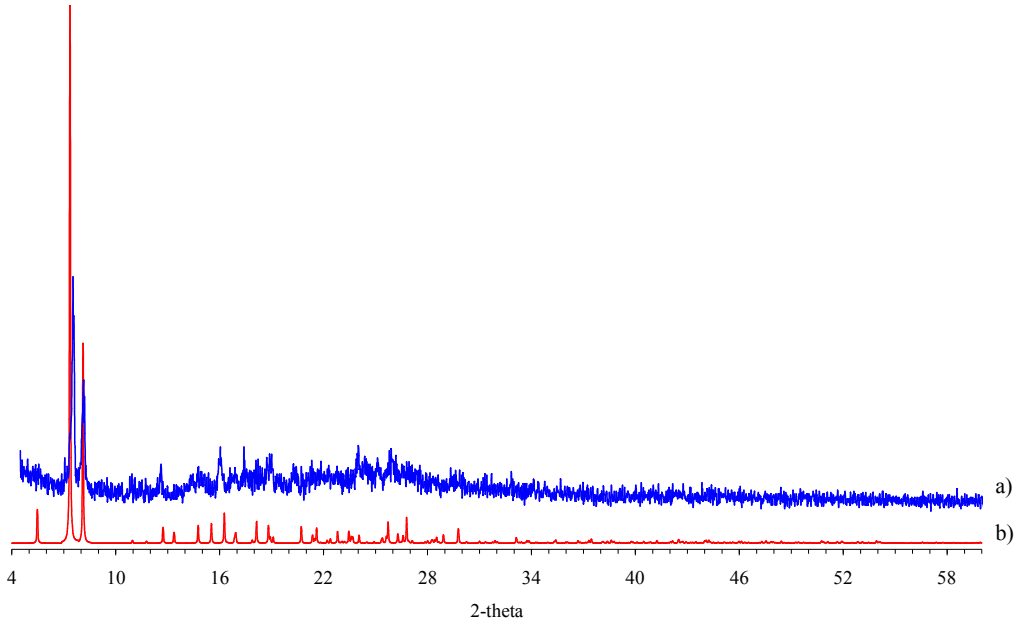

*Figure 2-56. The PXRD pattern for **5**: a) as-made and b) simulated from the X-ray crystal structure.*

Crystals of **5** produce better single crystal X-ray data if collected after several weeks kept out of their mother liquor. This is in contrast with the crystals of **4** which seem to degrade quite rapidly when taken out of their reaction medium.

2.4.10. Synthesis of $[Zn_4(1,3\text{-bdc})_4(HL)_4]\cdot 4DMF$ 6

H**L** (0.022g, 0.1 mmol), $ZnCl_2$ (0.030 g, 0.2 mmol) and 1,3-H_2bdc (0.033 g, 0.2 mmol) were dissolved in 5 mL of anhydrous DMF with gentle heating and stirring. The colourless solution was placed in a vial, sealed and heated up to 120°C for 2 days in an oven. The colourless crystals were then separated by filtration and washed with DMF.

2.4.11. Synthesis of $[Zn(1,3\text{-bdc})(HL)]\cdot DMF$ 7

H**L** (0.111 g, 0.5 mmol), $Zn(NO_3)_2\cdot 6H_2O$ (0.297 g, 1 mmol) and 1,3-H_2bdc (0.166 g, 1 mmol) were dissolved in 10 mL of anhydrous DMF with gentle heating and stirring. The colourless solution was placed in a 20 mL Ace Pressure tube, sealed and heated up to 120°C for 2 days in an oven. Colourless big plate like crystals were then separated by filtration and washed with DMF.

2.4.12. Synthesis of $[Zn_2(1,3\text{-bdc-Me})_2(HL)_2]\cdot DMF$ 8

H**L** (0.111 g, 0.5 mmol), $Zn(NO_3)_2\cdot 6H_2O$ (0.297 g, 1 mmol) and 1,3-H_2bdc-Me (0.166 g, 1 mmol) were dissolved in 10 mL of anhydrous DMF with gentle heating and stirring. The resulted colourless solution was placed in a 20 mL Ace Pressure tube, sealed and heated up to 120°C for a day in an oven. The colourless crystals were separated by filtration and washed with DMF.

2.4.13. Synthesis of $(Me_2NH_2)_2[Zn(1,4\text{-bdc})_2]\cdot 2DMF$ 9

H**L** (0.022 g, 0.1 mmol), $ZnCl_2$ (0.030 g, 0.2 mmol) and 1,4-H_2bdc (0.033 g, 0.2 mmol) were dissolved in 5 cm^3 of anhydrous DMF with gentle heating and stirring. The clear solution was placed in a 20 mL Ace Pressure tube, sealed and heated at 160°C for 2 days in an oven. The resulted colourless block like crystals were then separated by filtration and washed with fresh DMF. The PXRD pattern of the sample suggests that some sort of changes might had taken place during work-up and further investigation such as running a PXRD of a wet sample could help explaining the difference between the PXRD patterns of the sample and simulated X-ray single crystal structure of $(Me_2NH_2)_2[Zn(1,4\text{-bdc})_2]\cdot 2DMF$ **9**.

2.4.14. Synthesis of $(Me_2NH_2)_2$ $[Zn(2,6\text{-ndc})_2]\cdot 3DMF$ 10

H**L** (0.022 g, 0.1 mmol), $ZnCl_2$ (0.030 g, 0.2 mmol) and 2,6-H_2ndc (0.043g, 0.2 mmol) were dissolved in 10 cm^3 of anhydrous DMF with gentle heating and stirring. The clear solution was placed in a 20 mL Ace Pressure tube, sealed and heated at 120°C for 24 hours in an oven. Colourless crystals of suitable size for X-ray single diffraction were collected and formulated as $(Me_2NH_2)_2[Zn(2,6\text{-ndc})_2]\cdot 3DMF$, **10**. Further investigation is needed in order to establish the reaction mixture and conditions which enables to obtain a phase pure **10**.

2.4.15. Synthesis of $[Zn_2(1,4\text{-bdc})_2(L1)_2]\cdot 2.7DMF$ 11

L1 (0.028 g, 0.10 mmol), 1,4-H_2bdc (0.033 g, 0.20 mmol) and $ZnCl_2$ (0.030 g, 0.20 mmol) were dissolved in 13 mL of anhydrous DMF with gentle heating and stirring. This solution (4 mL) was sealed in a 10 mL Biotage vial which was then heated in a temperature-controlled oven at 80°C. Colourless plate-like crystals (Figure 2-57) were collected after 3 days and their single crystal X-ray analysis revealed a new MOF formulated $[Zn_2(1,4\text{-bdc})_2(\mathbf{L1})_2]\cdot 2.7DMF$ **11** to be obtained.

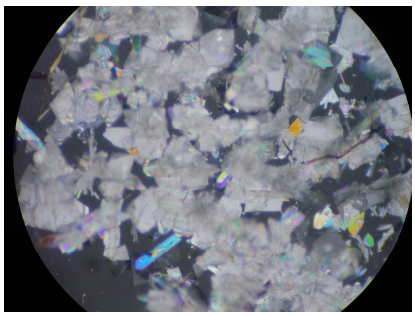

*Figure 2-57. Crystals of **11** viewed down the microscope.*

The crystals were separated by filtration and washed with DMF. The PXRD pattern of the sample matches that of the simulated X-ray single crystal structure (Figure 2-58).

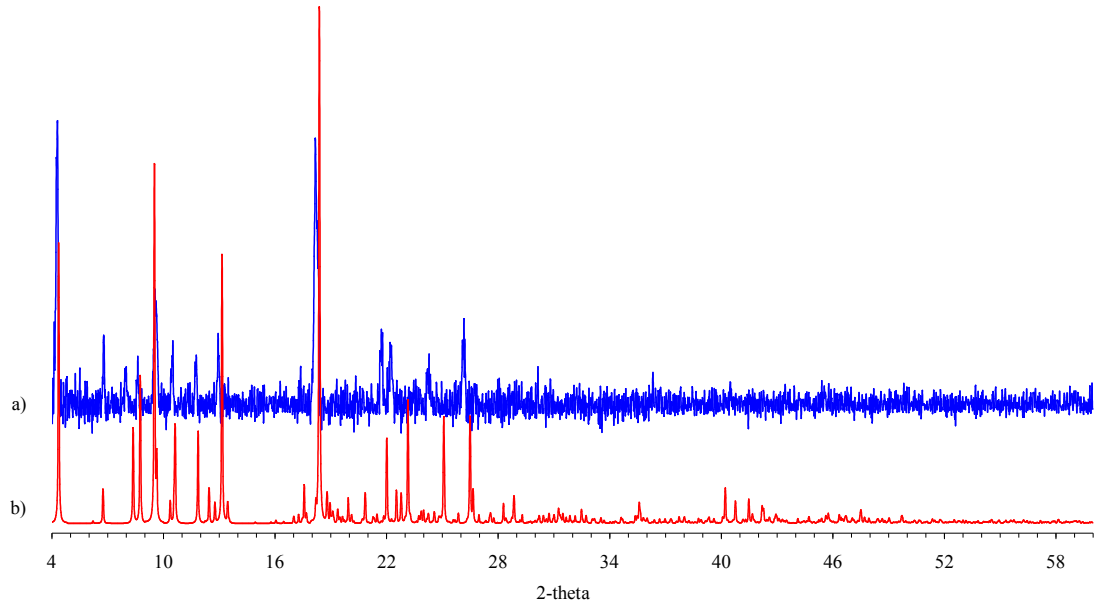

*Figure 2-58. The PXRD pattern for **11**: a) as-made and b) simulated from the X-ray crystal structure.*

2.5. Summary and Future work

H**L** has been mixed with a large variety of metal salts in different solvents at temperature ranging from room temperature to 180°C. Factors as molar ratio and reaction time were altered as well but in the end all these reactions produce just discrete complexes. The synthesis of a discrete MOF with formula $ZnCl_2$(H**L**) **2** collected serendipitously from a previous work done in Burrows group, has been elucidated. As an addition to the discrete structures containing H**L** previously obtained by members of Burrows group, $[Zn(OAc)_2(HL)_2]\cdot H_2O$ **1** has been synthesised and analysed by means of single X-ray diffraction, powder X-ray diffraction and elemental analysis. **1** has been obtained using the microwave route as well. It was believed that the acetate (OAc) linkers can be removed by heating **1** and replaced lately with a linker which would increase the dimensionality of this MOF. Thermogravimetric analysis also revealed that removal of the acetate linkers is not an easy task.

In order to increase the dimensionality of MOFs containing H**L**, pillaring approach has been used and H**L** mixed with a large variety of dicarboxylic acids.

Six new 3-D mixed-linker MOFs containing H**L** and aromatic dicarboxylates: $[Zn_4(1,4\text{-bdc})_4(H\mathbf{L})_4]\cdot 4DMF$ **3**, $Zn_4(1,4\text{-ndc})_4(H\mathbf{L})_4$ **4**, $[Zn_2(2,6\text{-ndc})_2(H\mathbf{L})_2]\cdot DMF$ **5**, $[Zn_4(1,3\text{-bdc})_4(H\mathbf{L})_4]\cdot 4DMF$ **6**, $[Zn(1,3\text{-bdc})(H\mathbf{L})]\cdot DMF$ **7** and $[Zn_2(1,3\text{-bdc-Me})_2(H\mathbf{L})_2]\cdot DMF$) **8** have been synthesised and characterized by means of single X-ray diffraction, powder X-ray diffraction (PXRD), thermal analysis (TGA) and microanalysis (CHN).

Two new compounds which does not have H**L** incorporated: $(Me_2NH_2)_2[Zn(1,4\text{-bdc})_2]\cdot 2DMF$ **9** and $(Me_2NH_2)_2[Zn(2,6\text{-ndc})_2]$ 2DMF **10** , have been obtained and identified by means of single X-ray diffraction and powder X-ray diffraction (PXRD).

All the structures collected from the work done with H**L** have the NH group from the pyrazole ring involved in hydrogen bonding, either with oxygen atoms from the carboxylate group of the dicarboxylic acid or from the DMF solvent molecule. Thus, the 3-D mixed-linker MOFs containing H**L** posses NH groups which are not involved in strong bonding, being therefore capable to act as excellent sites for further chemistry.

Trials to obtain 3-D MOFs with **L1** have been made and successfully turn into a new MOF with formula $[Zn_2(1,4\text{-bdc})_2(\mathbf{L1})_2]\cdot 2.7DMF$, **11**. The structure of this MOF is very similar with that of **3**, but slight different conditions were used.

It was believed that bringing both H**L** and **L1** into the same MOF will give a very exciting result with the final MOF bearing two functional sites: NH groups (within H**L**) and triple bonds (within **L1**). These two interesting sites both present simultaneously in a MOF offer considerable potential for postsynthetic modification. Attempts to synthesise mixed-linker MOFs containing both H**L** and **L1** have been made but none of them produced suitable crystals for X-ray analysis.

The general key feature of the new compounds obtained in this work is their pillared layered structures where the layers are formed of zinc atoms bridged by the dicarboxylate (1.4-bdc) while the pillar is the bipyridine (H**L** or **L1**). They differ in the symmetry of the zinc-carboxylate layer network.

The results suggest that mixed-linker MOFs of H**L** and **L1** with dicarboxylates can be obtained but most of the time it is not straightforward. Each system needs carefully tuning

of factors as temperature, counter ion, molar ratio and concentration and as we expected the complexity increases with the number of linkers used in reaction.

Investigation into getting mixed-linker MOF with the dicarboxylate linkers which have been unsuccessful in this work is worth trying in future. Very interesting results may come from using 5-acetamidoisophthalic acid (Figure 2-59) which has produced mixed-linker MOFs with 4,4′-bipyridine from a very recent work done in Burrows group.

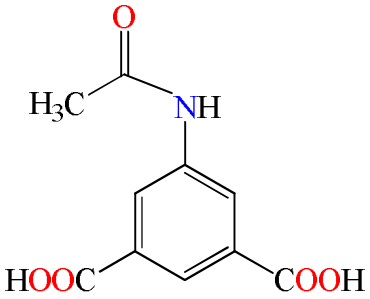

Figure 2-59. 5-acetamidoisophthalic acid.

Further studies into removing DMF solvent from MOFs synthesised in here are requested in order to asses their porosity by means of nitrogen adsorption measurements.

H**L** derivatives where the hydrogen from the NH group is substituted by a bulkier R group (Figure 2-60, left) are reported but they have not been used in MOF chemistry. It will be interesting to explore how the R group attached to the pyrazole ring might assist in the formation of non-interpenetrated 3-D MOFs. Moreover, an unreported longer H**L** derivative but already prepared within Burrows group (Figure 2-60, right) it will be a great candidate for future work. It is hoped to produce 3-D mixed-linker MOFs similar with H**L** but showing a higher porosity, making of them better candidates as "drug carriers" or "gas containers".

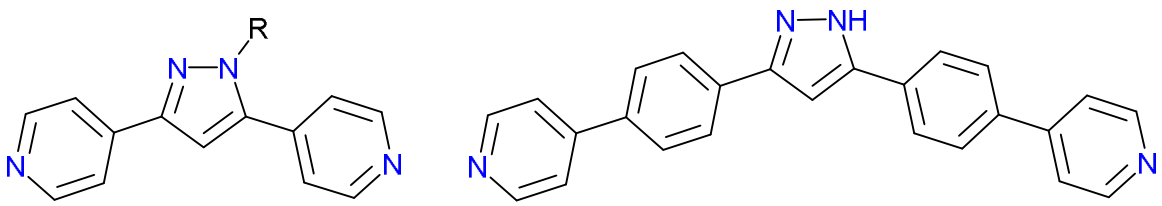

3,5-bis(4-pyridyl)-1R-pyrazole 3,5-bis(4-phenylpyridyl)-1 *H*-pyrazole

*Figure 2-60. H**L** derivatives scope for further work.*

In order to obtain MOFs featuring both NH groups and triple bonds the reaction conditions which have been used to get mixed-linker MOFs containing both H**L** and **L1** linkers are recommended to be altered in future.

The use of **L1** in MOF chemistry can be further explored, especially in conjunction with other linkers to form mixed- linker MOFs and the chemistry of its triple bonds further investigated as well. Mixing **L1** with other dicarboxylate linkers it is worth trying in future, it will tell us whether or not **L1** is going to form similar structures as H**L**, as was the case when 1,4-H_2bdc linker had been used.

2.6. References

[1] T. R. Cook, Y.-R. Zheng, P. J. Stang, *Chemical Reviews* **2013**, *113*, 734.

[2] C. Pettinari, N. Masciocchi, L. Pandolfo, D. Pucci, *Chemistry – A European Journal* **2010**, *16*, 1106.

[3] J.-P. Zhang, Y.-B. Zhang, J.-B. Lin, X.-M. Chen, *Chemical Reviews* **2012**, *112*, 1001.

[4] S. M. F. Lo, S. S. Y. Chui, L.-Y. Shek, Z. Lin, X. X. Zhang, G.-h. Wen, I. D. Williams, *Journal of the American Chemical Society* **2000**, *122*, 6293.

[5] B.-Q. Ma, K. L. Mulfort, J. T. Hupp, *Inorganic Chemistry* **2005**, *44*, 4912.

[6] C. Gao, S. Liu, L. Xie, Y. Ren, J. Cao, C. Sun, *CrystEngComm* **2007**, *9*, 545.

[7] M. Du, C.-P. Li, C.-S. Liu, S.-M. Fang, *Coordination Chemistry Reviews* **2013**, *257*, 1282.

[8] S.-Z. Zhan, M. Li, J.-Z. Hou, J. Ni, D. Li, X.-C. Huang, *Chemistry – A European Journal* **2008**, *14*, 8916.

[9] S. Vatsadze, V. Nuriev, N. Zyk, *Chemistry of Heterocyclic Compounds* **2005**, *41*, 1091.

[10] R. L. a. P. T. Miroslav Ferles, *Collect. Czech. Chem. Commun.* **1990**, *55*, 1228.

[11] Vyatsheslav N. Nuriev, N. V. Zyk, S. Z. Vatsadze, *ARKIVOC* **2005**, 208

[12] J. S. Lucas, L. D. Bell, C. M. Gandolfo, R. L. LaDuca, *Inorganica Chimica Acta* **2011**, *378*, 269.

[13] N. N. Adarsh, P. Dastidar, *Chemical Society Reviews* **2012**, *41*, 3039.

[14] D. N. Bunck, W. R. Dichtel, *Chemistry – A European Journal* **2013**, *19*, 818.

[15] L. Fabbrini, *Farmaco. Ed. Sci.* **1954**, *9*, 603.

[16] S.-Z. Zhan, D. Li, X.-P. Zhou, X.-H. Zhou, *Inorganic Chemistry* **2006**, *45*, 9163.

[17] F. Allen, *Acta Cryst. B* **2002**, *58*, 380.

[18] I. J. Bruno, J. C. Cole, P. R. Edgington, M. Kessler, C. F. Macrae, P. McCabe, J. Pearson, R. Taylor, *Acta Cryst. B* **2002**, *58*, 389.

[19] D. A. Fletcher, R. F. McMeeking, D. Parkin, *Journal of Chemical Information and Computer Sciences* **1996**, *36*, 746.

[20] *CSD version 5.31 plus 1 update, accessed on 06/10/2009*.

[21] A. D. Burrows, D. J. Kelly, M. I. Haja Mohideen, M. F. Mahon, V. M. Pop, C. Richardson, *CrystEngComm* **2011**, *13*, 1676.

[22] A. L. Spek, University of Utrecht, **1999**.

[23] G. Guilera, J. W. Steed, *Chemical Communications* **1999**, 1563.

[24] C. C. Addison, N. Logan, S. C. Wallwork, C. D. Garner, *Quarterly Reviews, Chemical Society* **1971**, *25*, 289.

[25] M.-P. Teulade-fichou, J.-P. Vigneron, J.-M. Lehn, *Supramolecular Chemistry* **1995**, *5*, 139.

[26] A. J. Warren, PhD thesis, University of Bath **2011**.

[27] J. F. Coetzee, *Recommended Methods for Purification of Solvents and Tests for Impurities*, Pergamon Press Ltd., Oxford, UK, **1982**.

[28] Y. Wan, M. Alterman, M. Larhed, A. Hallberg, *J. Org. Chem.* **2002**, *67*, 6232.

[29] D. D. Perrin, W. L. F. Armarego, *Purification of Laboratory Chemicals*, Pergamon, Oxford, **1988**.

[30] A. D. Burrows, K. Cassar, R. M. W. Friend, M. F. Mahon, S. P. Rigby, J. E. Warren, *CrystEngComm* **2005**, *7*, 548.

[31] S. M. Hawxwell, L. Brammer, *CrystEngComm* **2006**, *8*, 473.

[32] K. Cassar, PhD thesis, University of Bath **2007**.

[33] W. Chen, J.-Y. Wang, C. Chen, Q. Yue, H.-M. Yuan, J.-S. Chen, S.-N. Wang, *Inorganic Chemistry* **2003**, *42*, 944.

[34] L. Xie, S. Liu, B. Gao, C. Zhang, C. Sun, D. Li, Z. Su, *Chemical Communications* **2005**, 2402.

[35] N. L. Rosi, J. Kim, M. Eddaoudi, B. Chen, M. O'Keeffe, O. M. Yaghi, *Journal of the American Chemical Society* **2005**, *127*, 1504.

[36] T. M. Fasina, J. C. Collings, D. P. Lydon, D. Albesa-Jove, A. S. Batsanov, J. A. K. Howard, P. Nguyen, M. Bruce, A. J. Scott, W. Clegg, S. W. Watt, C. Viney, T. B. Marder, *Journal of Materials Chemistry* **2004**, *14*, 2395.

[37] J. T. Lin, S.-S. Sun, J. J. Wu, L. Lee, K.-J. Lin, Y. F. Huang, *Inorganic Chemistry* **1995**, *34*, 2323.

[38] N. R. Champness, A. N. Khlobystov, A. G. Majuga, M. SchrÃ¶der, N. V. Zyk, *Tetrahedron Letters* **1999**, *40*, 5413.

[39] P. Nguyen, Z. Yuan, L. Agocs, G. Lesley, T. B. Marder, *Inorganica Chimica Acta* **1994**, *220*, 289.

[40] A. J. Amoroso, A. M. W. C. Thompson, J. P. Maher, J. A. McCleverty, M. D. Ward, *Inorganic Chemistry* **1995**, *34*, 4828.

[41] M. B. Zaman, K. Udachin, J. A. Ripmeester, M. D. Smith, H.-C. zur Loye, *Inorganic Chemistry* **2005**, *44*, 5047.

[42] B. J. Coe, J. L. Harries, M. Helliwell, B. S. Brunschwig, J. A. Harris, I. Asselberghs, S.-T. Hung, K. Clays, P. N. Horton, M. B. Hursthouse, *Inorganic Chemistry* **2006**, *45*, 1215.

[43] J. T. Lin, M.-F. Yang, C. Tsai, Y. S. Wen, *Journal of Organometallic Chemistry* **1998**, *564*, 257.

[44] M. B. Zaman, M. D. Smith, H.-C. zur Loye, *Chemical Communications* **2001**, 2256.

[45] A. J. Blake, G. Baum, N. R. Champness, S. S. M. Chung, P. A. Cooke, D. Fenske, A. N. Khlobystov, D. A. Lemenovskii, W.-S. Li, M. Schroder, *Journal of the Chemical Society, Dalton Transactions* **2000**, 4285.

[46] C. J. Kuehl, S. D. Huang, P. J. Stang, *Journal of the American Chemical Society* **2001**, *123*, 9634.

[47] A. D. Burrows, L. C. Fisher, D. Hodgson, M. F. Mahon, N. F. Cessford, T. Duren, C. Richardson, S. P. Rigby, *CrystEngComm* **2011**, *14*, 188.

[48] Y. Yamauchi, M. Yoshizawa, M. Fujita, *Journal of the American Chemical Society* **2008**, *130*, 5832.

[49] H. G. T. Nguyen, M. H. Weston, A. A. Sarjeant, D. M. Gardner, Z. An, R. Carmieli, M. R. Wasielewski, O. K. Farha, J. T. Hupp, S. T. Nguyen, *Crystal Growth & Design* **2013**, *13*, 3528.

[50] T. Yamada, S. Iwakiri, T. Hara, K. Kanaizuka, M. Kurmoo, H. Kitagawa, *Crystal Growth & Design* **2011**, *11*, 1798.

[51] W. Kraus, G. Nolze, Federal Institute for Materials Research and Testing Rudower Chaussee 5, Berlin, Germany, **1999**.

[52] G. Sheldrick, *Acta Cryst. A* **2008**, *64*, 112.

[53] S. Chan, University of Bath, **2011**.

Chapter 3. MOF synthesis using an upper-rim functionalised calix[4]arene dicarboxylic acid

3.1. Introduction

Calixarenes (Figure 3-1) belong to a family of macrocyclic compounds consisting of cyclic arrays of phenol moieties linked by methylene groups. The commonly accepted nomenclature for calixarenes is *p*-R-calix[n]arene where R is the group *para* to the OR group of the phenol and n is the number of phenolic units present.[1]

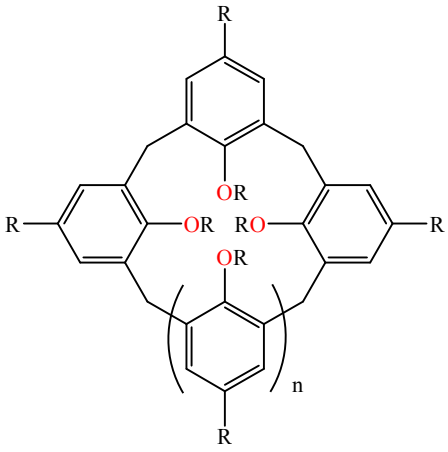

Figure 3-1. Representation of a calix[n]arene.

The name "calixarene" was introduced in 1978 by the American chemist Gutsche as he observed that the phenol-derived cyclic tetramer resembled the shape of a Greek vase called a calyx krater (Figure 3-2, left), hence the name "calix", and "arene" for the presence of aryl groups in the cyclic array. The three-dimensional bucket-like shape of the smallest members of the series, the calix[4]arenes, represented in Figure 3-2 (right) is characterised by a wide upper rim and a narrow lower rim and this is how their rims will be referred to throughout this thesis.

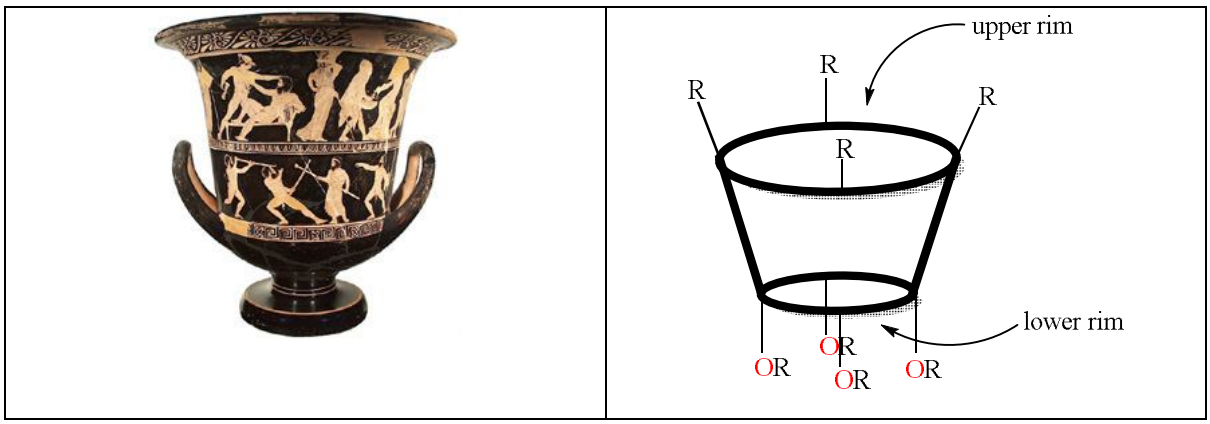

Figure 3-2. Calyx krater (left) and designation of the rims for a calix[4]arene (right).

However, especially when applied to larger calixarenes (n > 4) the "wide or upper" rim can be found in literature designated as the "exo rim" and the "narrow or lower" rim as the "endo rim". The exo and endo abbreviation does not recourse to either the orientation or shape of the calixarene structure and is based on the cyclic structure in itself.

Due to extensive work carried out by researchers like Gutsche[2], the structure, synthesis, and properties of calixarenes are well understood. Cornforth and co-workers[3] pointed out that calix[4]arenes can exist in four discrete forms which were later designated by Gutsche[4] as the "cone", "partial cone", "1,2-alternate" and "1,3-alternate" conformations as shown in Figure 3-3.

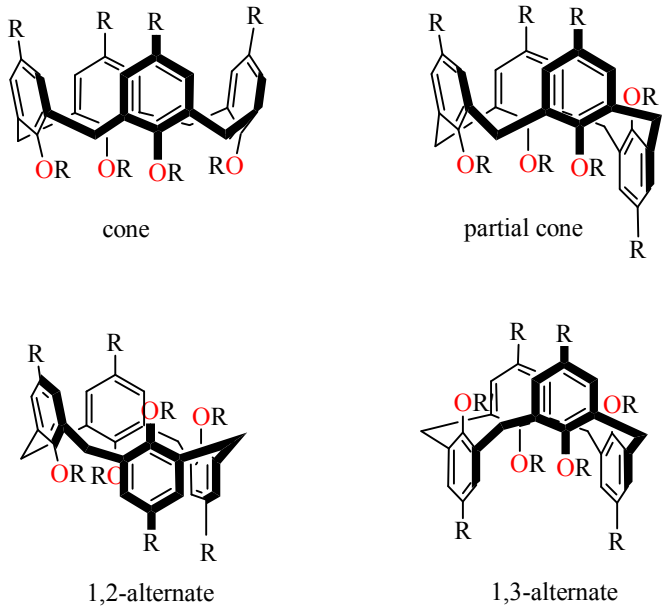

Figure 3-3. Possible conformations of a calix[4]arene.

In the solid state, calix[4]arenes (with hydroxyl groups at the lower rim) have been proven by X-ray crystallographic studies[5, 6] to exist in the cone conformation with C_4 symmetry due to favourable hydrogen bond interactions between the hydroxyl groups from the lower rim. However, in non-polar solutions at temperatures above room temperature, the hydroxyl groups of the arene units may pass back and forth through the central cavity of the molecule leading to any one of the four conformers at a given moment in time. Analogous calix[n]arenes lacking OH groups at their lower rim[7] have been shown to prefer 1,3-alternate conformations.

Calix[4]arene can be frozen into its basket-like shape (the "cone" conformation) by the introduction of sufficiently large substituents on the lower rim. Any alkyl ether sterically bulkier than ethyl ether prevents the lower rim of the arene unit from passing through the central cavity of the molecule, effectively "locking" that arene unit into cone conformation.[8, 9]

Calixarenes can be obtained in multigram amounts on a laboratory scale in a relatively simple procedure starting from cheap starting materials which makes them more attractive than many other synthetic macrocycles. Moreover, calixarenes are versatile ligands as they can be functionalised at various parts of the structure. For example the number of phenolic residues can be changed, n = 4, 5, 6, 7, 8…etc, the *p*-substituent at the upper rim can be functionalised as can the groups bonded to the phenolic oxygens at the lower rim.

Extended structures containing calixarenes have started to attract attention, calixarenes being referred by researchers as "the third generation of supramolecules", the first being cyclodextrins and the second being crown ethers.[10] Networks with upper-rim *p*-sulfonated calix[4]arenes[11, 12] and calix[6]arenes[13, 14] were reported, as have lower-rim appended calix[4]arenes containing pyridine groups.[15] Similar, calixarene analogues with sulfur-bridged aryl groups were also reported to form coordination networks.[16]

Calix[4]arenes were shown to act as macrocyclic structures capable of forming hydrophobic cavities that bind apolar guests[17] and in the solid-state, calix[4]arenes were reported to act as porous entities allowing gases[18, 19] or solvents[20] to be adsorbed. In calix[4]arenes the internal volume is around 10 $Å^3$. Calixarenes can act as hosts for cations, anions and neutral molecules depending on their functionalisation.

The formation of MOFs with calixarene-based ligands opens up the possibility of forming hierarchically-porous materials, with porosity due to both the ligand and framework structures. The most commonly used functional groups in constructing MOFs are carboxylates, but despite this there have been relatively few reports of metal complexes of calixarene-based polycarboxylates. Dimeric upper-rim *p*-carboxylatocalix[4]arenes were reported to self-assemble into infinite hydrogen-bonded nanotubes or bilayers, depending on the metal,[21] whereas *p*-carboxylatocalix[4]arene-O-methyl ethers were shown to generate nanocapsules.[22] Lower-rim functionalised calix[4]arenes were reported to form 3-D networks with Co(II), with the metal centres linking the ligands into a non-interpenetrated (10,3)a net.[23] More recently, Redshaw *et al.*[24] reported three compounds prepared by reacting a lower-rim appended 1,3-diacid calix[4]arene with lithium carbonate, t-butyl-lithium and zinc acetate.

A ladder-type 1-D coordination network using the anionic form of the calix[4]arene tetracarboxylic acid and a macrocyclic nickel-containing cation were reported by Lampeka *et al.*[25].

25,26,27,28-tetrapropoxycalix[4]arene-5,17-dicarboxylic acid (H_2caldc) (Figure 2) is a calix[4]arene featuring two carboxylic groups at the 5 and 17 positions on the upper rim. The substituents (R) at the lower rim are all the same, namely the *n*-propyl group (Pr).

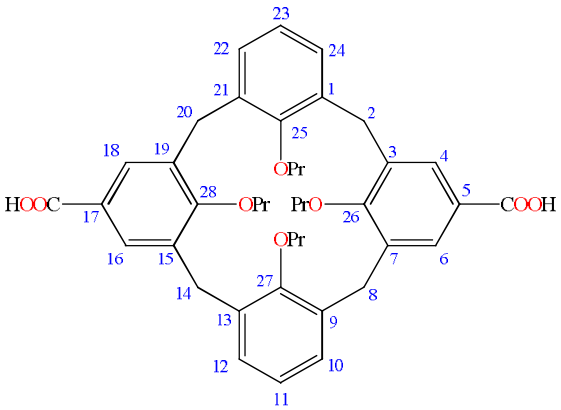

Figure 3-4. Representation of H_2caldc showing the numbering of carbon atoms (Pr = n-propyl).

H_2caldc is stabilised into a cone conformation by the steric constraints of the "locking" propoxy groups but some conformational flexibility still exists and in solution the C_{4v}

symmetry, usually observed in the ^{1}H NMR spectrums of these compounds, are considered to be a transition state for the interconversion (Figure 3-5) between two C_{2v} structures named the closed pinched and open pinched cone conformers.

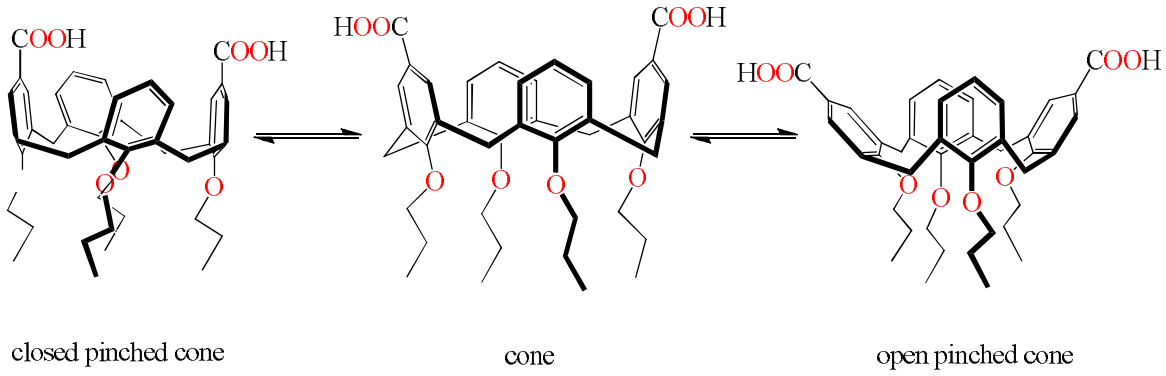

Figure 3-5. Interconversion of H_2caldc cone conformers.

The pinched cone conformations adopted by most of the symmetrically substituted calix[4]arene in the solid state, showing a C_{2v} symmetry, has been also shown to be the most stable by molecular modelling.[26, 27]

Crystals of H_2caldc suitable for X-ray diffraction were grown from methanol by Tucker *et al.*,[28] and revealed the formation of a symmetrical dimer shown in Figure 3-6, as a result of hydrogen bonds between the carboxylic acid groups.

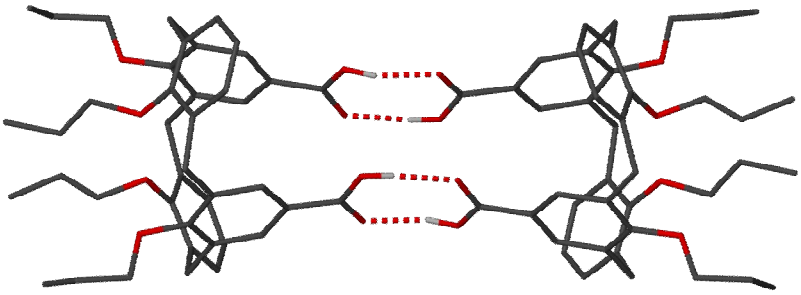

Figure 3-6. Structure of the $(H_2caldc)_2$ dimer.

H_2caldc adopts a closed pinched cone conformation, where two of the carboxy-substituted phenyl rings are turned in towards one another (dihedral angle = 21°), whereas the unsubstituted phenyl rings point away from one another (dihedral angle = 73°).

With this in mind, we aimed to synthesise MOFs using an upper-rim functionalised calix[4]arene dicarboxylic acid, such as H_2caldc (25,26,27,28-tetrapropoxycalix[4]arene-5,17-dicarboxylic acid).

3.2. Results and discussion

H_2caldc has been synthesised and used in solvothermal reactions with Zn(II), Cu(II), Cd(II) and Co(II) salts. Six new compounds containing caldc^{2-} anion were obtained: a $(NMe_2H_2)_2$caldc dimer and five MOFs formulated as $[M_2(caldc)_2(DMF)_2]$ (M= Cu, Zn and Co), $[Cd_2(caldc)_2(DMF)_2]\cdot 3DMF$ and $[Co_5(caldc)_4(OH)_2(H_2O)_4]\cdot 8DMF$. Their synthesis and characterisations are presented herein. Three of these calix[4] MOFs have been structurally characterised and shown to form two- or three-dimensional network structures. The ability of these calix[4] MOFs to act as nitrogen adsorbents has also been investigated and compared with the results obtained from molecular simulations.

3.2.1. 25,26,27,28-tetrapropoxycalix[4]arene-5,17-dicarboxylic acid (H_2caldc)

H_2caldc was prepared according to literature procedures [29-31] with the overall reaction pathway summarised in Scheme 3-1. The synthesis of H_2caldc is comprised of seven reactions or steps using *p-tert*-butylphenol as the starting material for **step 1**.

Step 1 consists of two steps: the condensation method which involved heating p-*tert*-butylphenol with formaldehyde in the presence of sodium hydroxide followed by pyrolysis to convert any octamer formed into *p-tert*-butylcalix[4]arene. An excess of $AlCl_3$ was then used as a Lewis acid, to remove the *tert*-butyl moieties from *p-tert*-butylcalix[4]arene in the presence of phenol (**step 2**) to give 25,26,27,28-tetrahydroxycalix[4]arene (**1**). In order to selectively functionalise the 5 and 17 positions of the upper rim of **1** it was necessary to alkylate the molecule in a distal fashion to deactivate the carbon atoms at the 11 and 23 positions. This was achieved firstly by using K_2CO_3 to successively and selectively deprotonate opposing hydroxyl groups followed by the addition of *n*-propyl iodide (PrI) (**step 3**). The formylation of the 5 and 17 positions, was achieved by treating the 25,27-dipropoxy-26,28-dihydroxycalix[4]arene (**2**) with 1,1-dichloromethyl methyl ether (Cl_2CHOCH_3) in the presence of a catalyst such as tin(IV) chloride (**step 4**). In **step 5**, the 5,17-diformyl-25,27-dipropoxy-26,28-dihydroxycalix[4]arene (**3**) was reacted with trimethyl orthoformate ($HO(OCH_3)_3$) in the presence of *p*-toluene sulfonic acid (PTSA) to protect the formyl group. The 5,17-dimethoxy-25,27-dipropoxy-26,28-dihydroxycalix[4]arene (**4**) was further reacted with PrI in the presence of NaH to alkylate the remaining hydroxyl groups (**step 6**). The oxidation of 5,17-diformyl-25,26,27,28-

tetrapropoxycalix[4]arene (**5**) with sodium chlorite ($NaClO_2$) and sulfamic acid (NH_2SO_3H) in a 1:1 chloroform : acetone mixture (**step 7**) produces H_2caldc.

The seven steps to synthesis H_2caldc are detailed in the experimental section of this chapter together with the characterisations of the intermediate products.

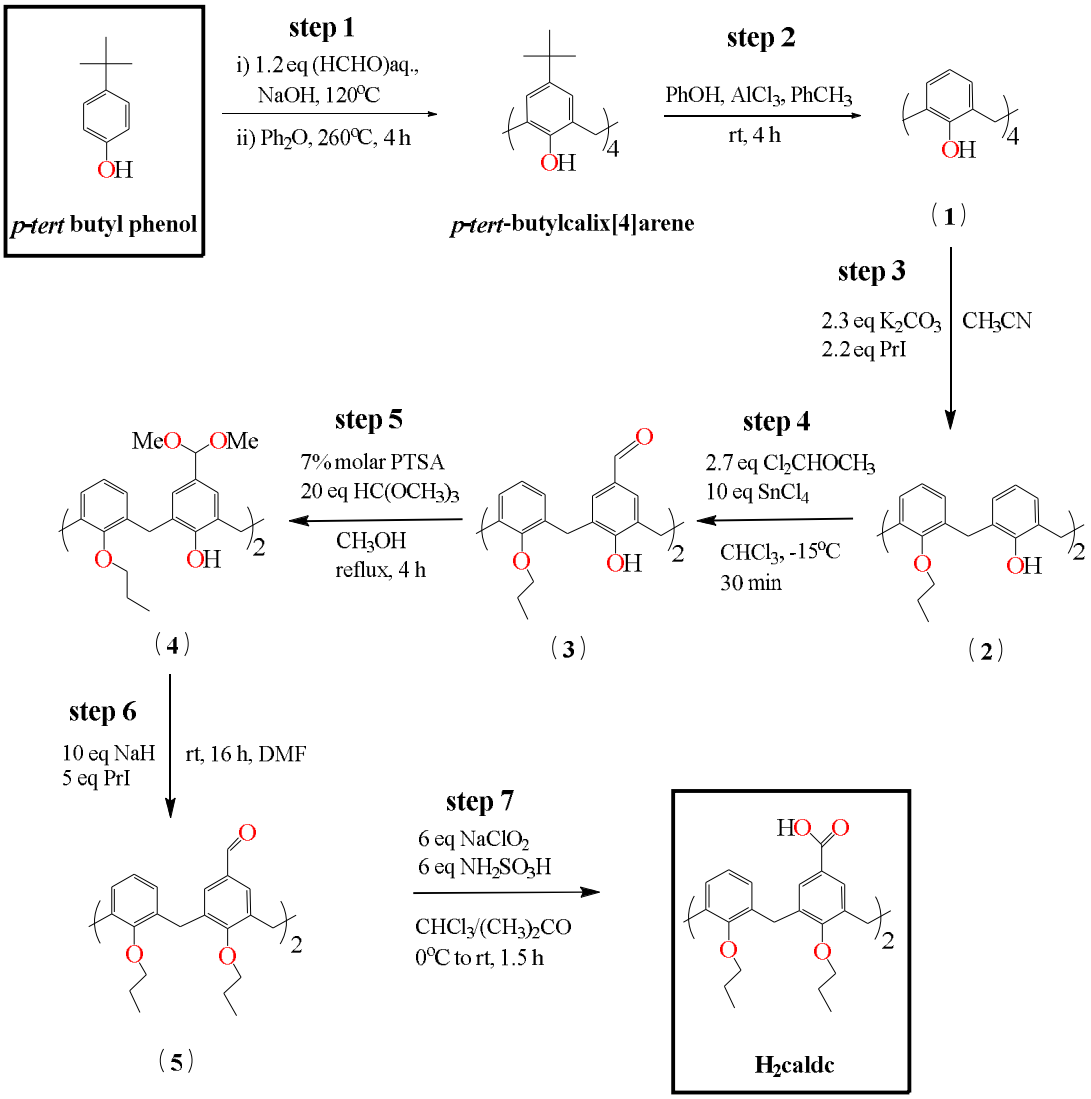

Scheme 3-1. Pathway for the synthesis of H_2caldc.

3.2.2. $(NMe_2H_2)_2$caldc

Needle-shaped colourless crystals of suitable X-ray quality of formula $(NMe_2H_2)_2$caldc, were collected from a mixture of $Co(NO_3)_2 \cdot 6H_2O$ and H_2caldc (1:2 molar ratio) in DMF which has been heated at 120°C for 2 days. The crystal data and refinement parameters for $(NMe_2H_2)_2$caldc are given in Table 3-1.

Table 3-1. Crystallographic data and refinement parameters for $(NMe_2H_2)_2$caldc.

Empirical formula	$C_{46}H_{62}N_2O_8$	
Formula weight	770.98	
Temperature	150(2) K	
Wavelength	0.71073 Å	
Crystal system	Tetragonal	
Space group, Z	$I4_1/a$, 8	
Unit cell dimensions	a = 18.6720(4) Å	α = 90°
	b = 18.6720(4) Å	β = 90°
	c = 24.3930(7) Å	γ = 90°
Volume	8504.5(4) Å^3	
Density (calculated)	1.204 g/cm^3	
Crystal size	0.33 x 0.33 x 0.15 mm	
Theta range for data collection	3.68 to 25.03°	
Reflections collected/ observed (>2σ)	52093/ 2400 [R(int) = 0.0799]	
Data Completeness	0.995	
Goodness-of-fit on F^2	1.054	
Final R indices [I>2σ(I)]	$R1$ = 0.0830 $wR2$ = 0.2267	
R indices (all data)	$R1$ = 0.1256 $wR2$ = 0.2713	
Largest diff. peak and hole	0.828 and -0.352 eÅ^{-3}	

The crystal structure of $(NMe_2H_2)_2$caldc (Figure 3-7) is comprised of a caldc anion and two dimethylammonium cations. The carbon atoms of the propoxy groups were disordered over two sites in a 60:40 ratio.

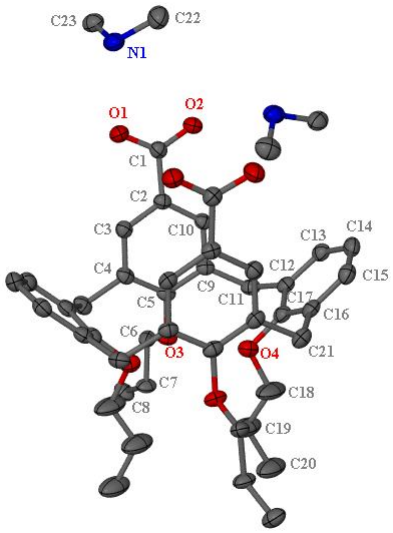

Figure 3-7. Crystal structure of $(NMe_2H_2)_2$caldc showing thermal ellipsoids at the 30% probability level. Only the atoms in the asymmetric unit are labelled. The minor disordered fragments and the hydrogen atoms have been omitted for clarity.

In the presence of water, DMF hydrolyses to form dimethylamine (Me_2NH) and formic acid[32] and the templating effects of dimethylammonium cations ($NMe_2H_2^+$) in the synthesis of MOFs it is well known.[33] In the formation of $(NMe_2H_2)_2$caldc it seems that $NMe_2H_2^+$ cations were generated by the presence of Co(II) in the mixture. Similar reactions to those producing $(NMe_2H_2)_2$caldc but in absence of $Co(NO_3)_2 \cdot 6H_2O$ were carried out in aged DMF and even using an excess of dimethylammonium chloride ($Me_2NH_2Cl_2$) but they all produced H_2caldc only and not the $(NMe_2H_2)_2$caldc.

The caldc anions are hydrogen bonded to the dimethylammonium cations forming $[(NMe_2H_2)_2caldc]_2$ dimers as shown in Figure 3-8. The carboxylic acid groups of the caldc bowls within the dimer are not directed towards each other as in the dimer of the free acid of H_2caldc shown in Figure 3-6. Instead the caldc bowls within the $[(NMe_2H_2)_2caldc]_2$ dimer are rotated by approximately 90° to each other.

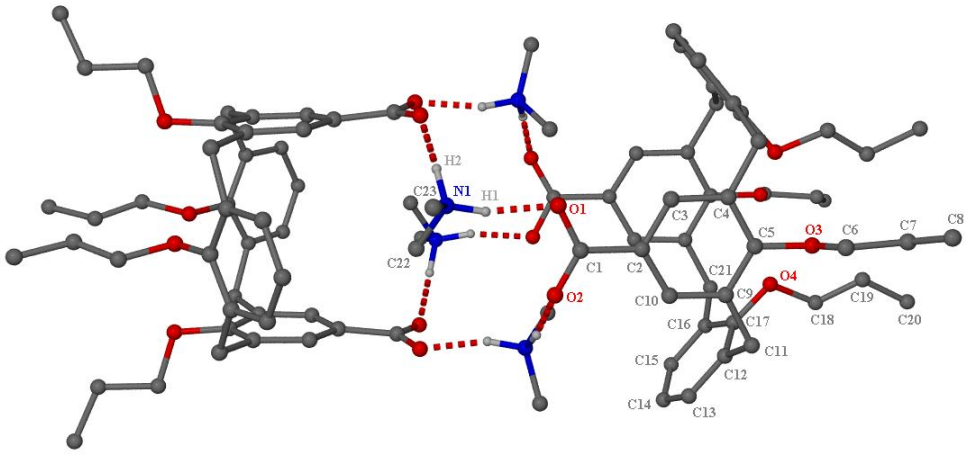

Figure 3-8. Structure of [(NMe$_2$H$_2$)$_2$caldc]$_2$ dimer. The minor disordered fragments and hydrogen atoms except those within NMe$_2$H$_2^+$ have been omitted for clarity.

The caldc dianions within the structure of (NMe$_2$H$_2$)$_2$caldc adopt a closed pinched cone conformation similar to those within the free acid H$_2$caldc, but the carboxy-substituted phenyl rings herein are almost parallel one to the other (dihedral angle = 3°) and the angle between the unsubstituted phenyl rings is 81°.

The gross structure is dominated by these hydrogen-bonded dimers which stack along the *c* axis to form channels as shown in Figure 3-9.

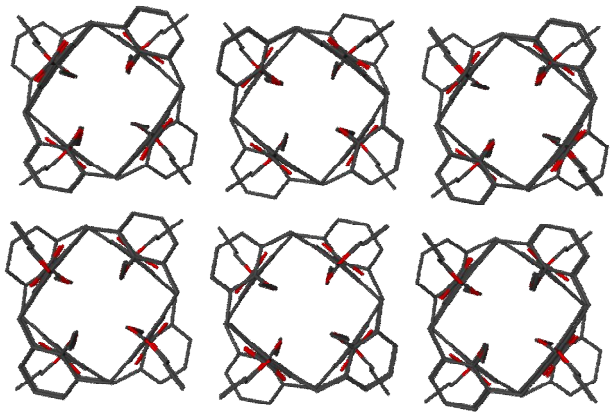

Figure 3-9. Structure of (NMe$_2$H$_2$)$_2$caldc showing channels along c axis. The NMe$_2$H$_2^+$, disordered fragments and hydrogen atoms have been omitted for clarity.

3.2.3. $M_2(caldc)_2(DMF)_2$ (M = Cu, Zn and Co)

Small blue plate-like crystals of suitable size for X-ray single diffraction were collected from the solvothermal reaction of $CuCl_2$ with H_2caldc (1 : 2 molar ratio) in DMF/water. The crystal data and refinement parameters for $Cu_2(caldc)_2(DMF)_2$ are given in Table 3-2.

Table 3-2. Crystallographic data and refinement parameters for $Cu_2(caldc)_2(DMF)_2$.

Empirical formula	$C_{90}H_{106}Cu_2N_2O_{18}$	
Formula weight	1630.85	
Temperature	150(2) K	
Wavelength	0.71073 Å	
Crystal system	Monoclinic	
Space group, Z	$P2_1/c$, 2	
Unit cell dimensions	a = 9.4670(2) Å	α = 90°
	b = 26.3310(5) Å	β =
	c = 17.6480(5) Å	γ = 90°
Volume	4290.08(17) $Å^3$	
Density (calculated)	1.262 g/cm^3	
Crystal size	0.30 x 0.20 x 0.20mm	
Theta range for data collection	3.58 to 24.93°	
Reflections collected/ observed (>2σ)	47644/ 4673 [R(int) = 0.1632]	
Data Completeness	0.986	
Goodness-of-fit on F^2	1.018	
Final R indices [I>2σ(I)]	$R1$ = 0.0700 $wR2$ = 0.1644	
R indices (all data)	$R1$ = 0.1265 $wR2$ = 0.1955	
Largest diff. peak and hole	2.114 and -0.678 $eÅ^{-3}$	

The asymmetric unit of $Cu_2(caldc)_2(DMF)_2$ (Figure 3-10) consists of one copper centre, one DMF and one caldc. C6, C7 and C8 of the propoxy group are modelled as equally disordered over two sites.

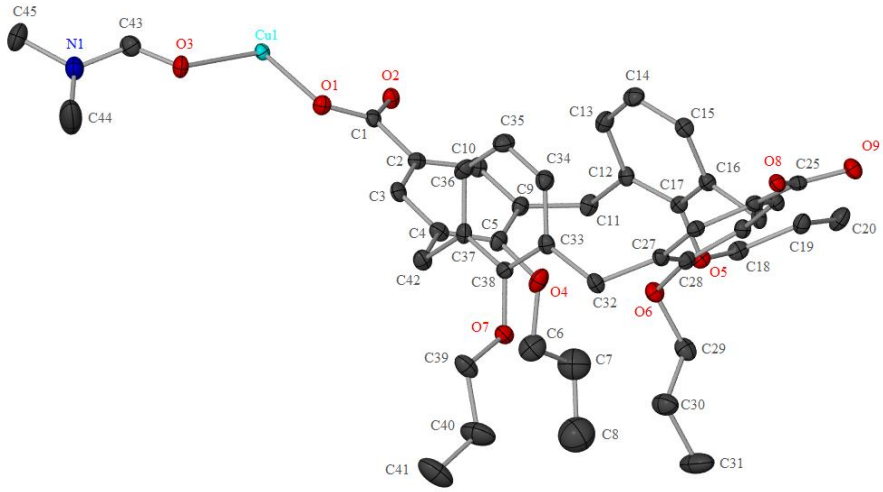

Figure 3-10. The asymmetric unit of $Cu_2(caldc)_2(DMF)_2$ showing thermal ellipsoids at the 30% probability level. The minor disordered fragments and hydrogen atoms have been omitted for clarity.

The copper atoms are linked together by four carboxylic groups from four different caldc ligands forming a paddle-wheel type $Cu_2(O_2CR)_4$ secondary building unit (SBU). The copper paddle-wheel dimers coordinated to DMF molecules are shown in Figure 3-11.

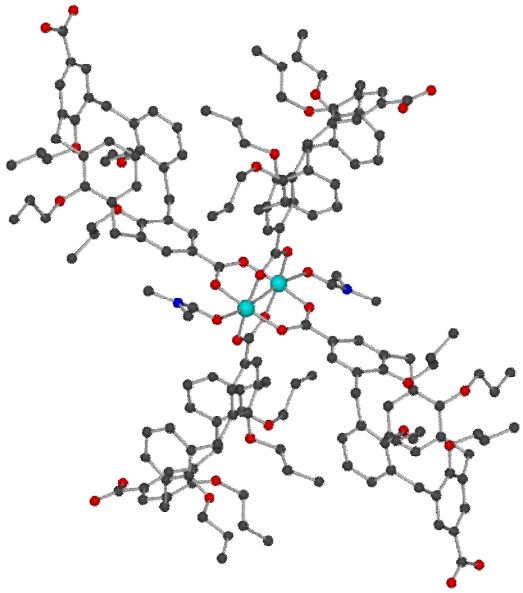

Figure 3-11. The copper paddle-wheel dimers coordinated to DMF molecules.

These copper paddle-wheel dimers are linked by the caldc anions into sheets as shown in Figure 3-12. The sheets have a (4, 4) topology, though the curvature present within the caldc dianion gives each pore an hourglass shape.

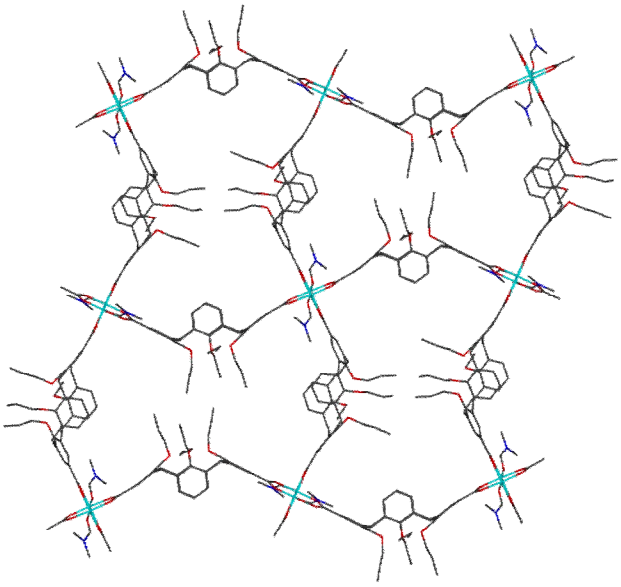

Figure 3-12. The structure of $Cu_2(caldc)_2(DMF)_2$ showing part of one of the (4,4) sheets.

The copper paddle-wheel dimers are also coordinated to DMF molecules, so there are no strong interactions between the sheets, which stack in a staggered manner, as shown in Figure 3-13. This means that the structure does not contain significant channels.

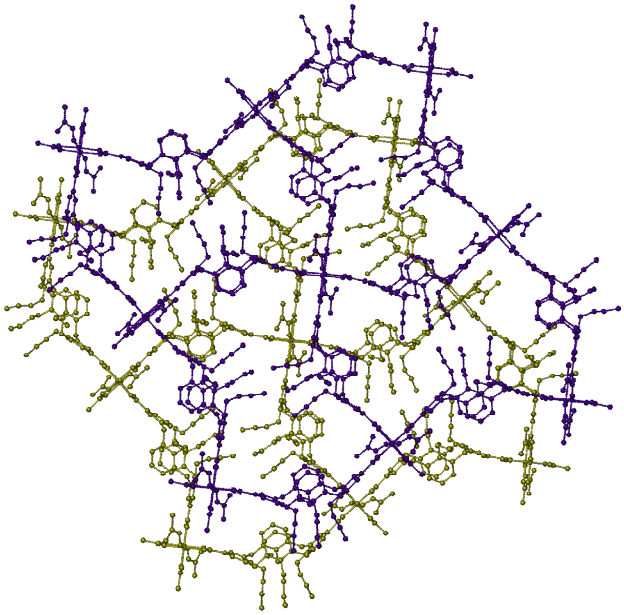

Figure 3-13. The structure of $Cu_2(caldc)_2(DMF)_2$ showing the manner in which the (4, 4) sheets (shown in different colours) stack together.

In $Cu_2(caldc)_2(DMF)_2$, the caldc bowls adopt an open pinched conformation with an angle between the unsubstituted phenyl rings of approximately 26° and between the carboxy substituted phenyl rings of 120°.

Taking in consideration the orientation of the carboxy substituted phenyl rings, the caldc ligand is represented in a simplified manner as in Scheme 3-2.

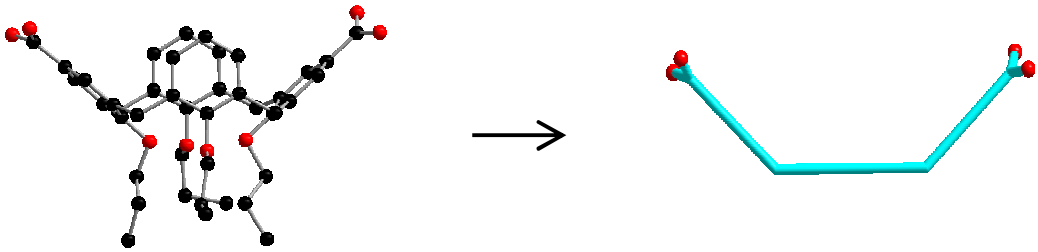

Scheme 3-2. The simplified representation of the caldc ligand.

Using the simplified representation of the caldc ligand (Scheme 3-2) and showing the coordination environments around Cu centres as orange polyhedra, the layers present within $Cu_2(caldc)_2(DMF)_2$ are depicted in Figure 3-22, left. These layers viewed from the top are pictured in Figure 3-14, right.

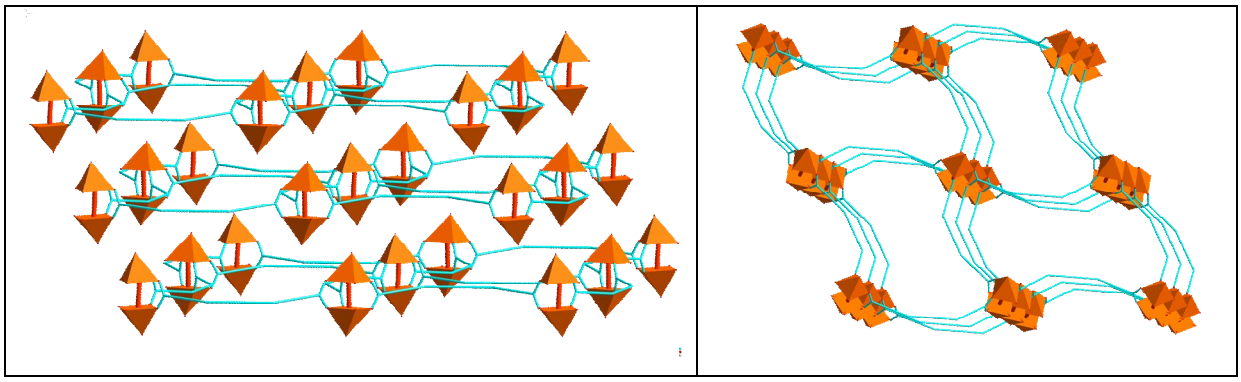

Figure 3-14. (Left) The structure of $Cu_2(caldc)_2(DMF)_2$ showing the manner in which the (4, 4) sheets stack together using the simplified representation for the caldc ligand and showing the coordination environments around Cu centres as orange polyhedra. (Right) The layers viewed from the top.

The (4,4) sheets present in the structure of $Cu_2(caldc)_2(DMF)_2$ with hourglass-shaped pores are reminiscent of those in the structures of MOFs containing the camphorate (cam) linker, such as $Cd_2(cam)_2$[34] and $Zn_2(cam)_2(dabco)$[35] (dabco = 1,4-diazabicyclo[2.2.2]octane). This can be explained on the basis of the similar angles between the carboxylate groups in the two ligands – approximately 120° for both camphorate and the conformation adopted by caldc in $Cu_2(caldc)_2(DMF)_2$.

The potentially accessible volume in the framework was calculated using PLATON SQUEEZE.[36] For $Cu_2(caldc)_2(DMF)_2$ the potentially accessible volume is 21.2% of the unit cell volume when the minor disordered fragments and all the solvent molecules were removed prior to these calculations.

Prior to assessing the porosity of a MOF it is necessary to remove the solvent molecules with retaining of MOF's framework. In order to achieve that, first step is usually to run a thermogravimetric analysis (TGA) of the MOF.

Figure 3-15 shows the TGA traces for the desolvated $Cu_2(caldc)_2(DMF)_2$ compared with that of the as-made $Cu_2(caldc)_2(DMF)_2$. The TGA trace for the as-made $Cu_2(caldc)_2(DMF)_2$ (Figure 3-15, red) shows a slow mass loss of approx. 13% (calculated 9% based on MOFs formula) up to 330°C. The difference of 4% could be attributed to the presence of an extra DMF solvent molecule per unit cell of MOF such as the MOF could be formulated as $Cu_2(caldc)_2(DMF)_3$. Above 330°C the TGA trace suggests that MOF starts to decompose. When $Cu_2(caldc)_2(DMF)_2$ was evacuated for 1 hour at 200°C its colour changed from turquoise to petrol but its TGA trace (Figure 3-15, blue) indicated that not all the solvent had been removed. The colour of this sample changes from petrol to dark-violet after it was evacuated for a further 2 hours which is consistent with removal of all the DMF solvent molecules. The TGA trace (Figure 3-15, black) of the fully desolvated MOF suggested that a small amount of water was picked up during handling for TGA measurements. It is known from literature that $Cu_3(btc)_2(H_2O)_3$ (HKUST-1, btc = 1,3,5-benzenetricarboxylate) changes its colour from blue-turquoise to dark-violet when it is fully dehydrated.[37]

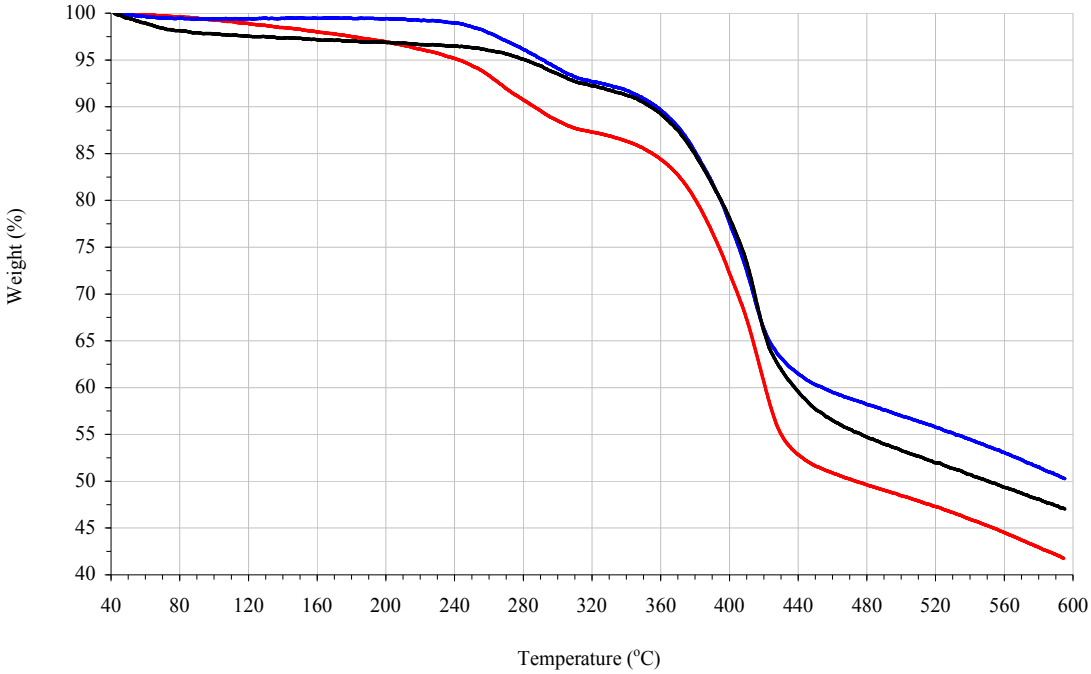

Figure 3-15. TGA traces of $Cu_2(caldc)_2(DMF)_2$: as-made (red), activated for 1h at 200°C (blue) and further activated for 2h at 200°C (black).

Exchanging the DMF solvent within $Cu_2(caldc)_2(DMF)_2$ with a solvent with a lower boiling point was also investigated herein. MeOH was the solvent chose to exchange the DMF solvent within $Cu_2(caldc)_2(DMF)_2$. To do that the MOF was soaked in MeOH for three days, each day MeOH being replaced with fresh MeOH. PXRD analysis suggests that the MOF framework was unaltered after 3 days in MeOH and the TGA analysis (Figure 3-16) suggests that two DMF solvent molecules were replaced by two molecules of MeOH. The TGA shows a mass loss of approx. 4.5 % up to 100°C which is consistent with the calculated mass loss (4.2%) if two MeOH molecules were lost by $Cu_2(caldc)_2(MeOH)_2$.

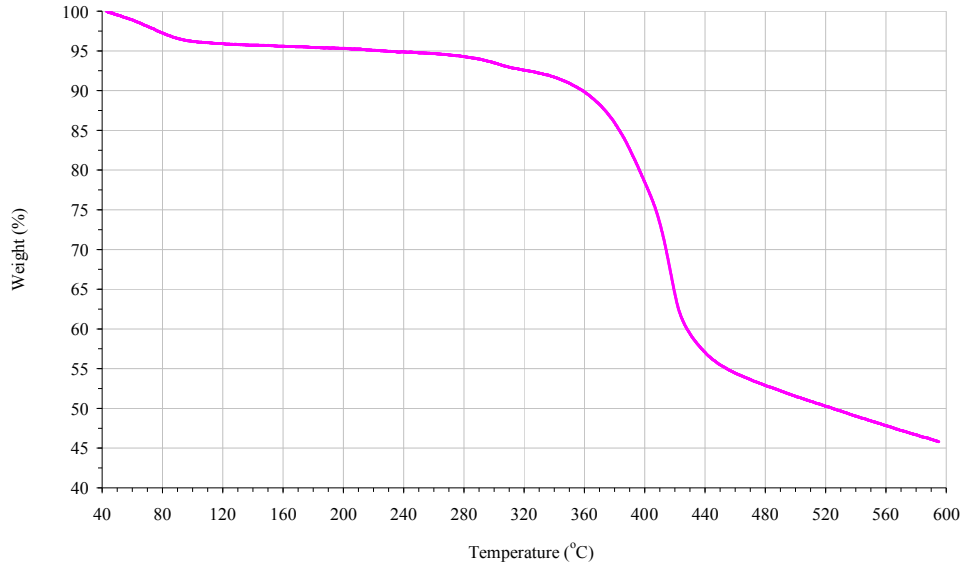

Figure 3-16. TGA trace of $Cu_2(caldc)_2(DMF)_2$ after soaking in MeOH for 3 days.

Figure 3-17 shows the N_2 isotherm for $Cu_2(caldc)_2(DMF)_2$ measured at 77 K and 101.33 KPa. The MOF was evacuated for 3 hours at 200°C prior to N_2 sorption measurement. The isotherm is a Type III isotherm which usually indicates weak adsorbent-adsorbate interactions. The BET surface area value of 5.15 m^2/g calculated from the N_2 isotherm suggests an insignificant porosity for this MOF.

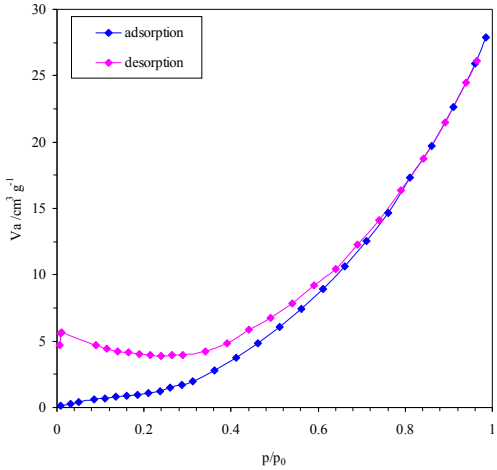

Figure 3-17. N_2 isotherm for $Cu_2(caldc)_2(DMF)_2$ measured at 77K and 101.33KPa.

The experiments suggest that the DMF solvent molecules within $Cu_2(caldc)_2(DMF)_2$ can be exchanged by MeOH and would be interesting to run a N_2 sorption measurement for the MeOH exchanged MOF, to assess MOF's porosity.

It has also been observed that the fine turquoise powder of $Cu_2(caldc)_2(DMF)_2$ with a density of 1.262 g/cm^3 floated if added to water. This suggests a hydrophobic nature of the MOF which can be explained by the presence of non-polar propyl groups, with potential for exhibiting surfactant-like properties.

The solvothermal reactions of H_2caldc (2 : 1 molar ratio) with $Zn(OAc)_2 \cdot 2H_2O$ and of H_2caldc (2 : 1 molar ratio) with $Co(NO_3)_2 \cdot 6H_2O$, in DMF/water produced $Zn_2(caldc)_2(DMF)_2$ and $Co_2(caldc)_2(DMF)_2$, respectively. These MOFs have proved by powder X-ray diffraction to be isomorphous with $Cu_2(caldc)_2(DMF)_2$ as shown in the experimental section.

The $M_2(caldc)_2(DMF)_2$ (M = Cu, Zn and Co) isostructural series is among other few isostructural paddle-wheel based MOFs series containing different metals such as $M_2(1,4\text{-}bdc)_2(dabco)$ (M = Zn[38], Cu[39] and Co[40]).

3.2.4. $[Cd_2(caldc)_2(DMF)_2]\cdot 3DMF$

The equimolar mixture of $Cd(NO_3)_2\cdot 4H_2O$ and H_2caldc in DMF/water yielded in three days at 80°C colourless needle-shaped crystals of formula $[Cd_2(caldc)_2(DMF)_2]\cdot 3DMF$. The crystal data and refinement parameters for $[Cd_2(caldc)_2(DMF)_2]\cdot 3DMF$ are shown in Table 3-3.

Table 3-3. Crystallographic data and refinement parameters for $[Cd_2(caldc)_2(DMF)_2]\cdot 3DMF$.

Empirical formula	$C_{99}H_{127}Cd_2N_5O_{21}$	
Formula weight	1947.86	
Temperature	150(2) K	
Wavelength	0.71073 Å	
Crystal system	Monoclinic	
Space group, Z	$P2_1/n$, 4	
Unit cell dimensions	a = 15.5500(3) Å	α = 90°
	b = 24.9210(2) Å	β = 90.005(1)°
	c = 25.2820(4) Å	γ = 90°
Volume	9797.3(3) Å^3	
Density (calculated)	1.321 g/cm^3	
Crystal size	0.50 x 0.13 x 0.13 mm	
Theta range for data collection	3.59 to 25.03°	
Reflections collected/ observed (>2σ)	74270/ 12798 [R(int) = 0.1147]	
Data Completeness	0.991	
Goodness-of-fit on F^2	1.083	
Final R indices [I>2σ(I)]	$R1$ = 0.0693 $wR2$ = 0.1999	
R indices (all data)	$R1$ = 0.0885 $wR2$ = 0.2163	
Largest diff. peak and hole	2.163 and -1.077 eÅ^{-3}	

The asymmetric unit of $[Cd_2(caldc)_2(DMF)_2]\cdot 3DMF$ contains two cadmium centres, two caldc dianions, two DMF solvent molecules each coordinated to one Cd atom and one well defined free DMF solvent molecule. There were also two solvent diffuse regions which were approximated each to one molecule of free DMF per asymmetric unit using PLATON SQUEEZE. Several of the propyl groups appended to the caldc exhibit 60:40 disorder, as did the DMF moiety ligated to Cd1.

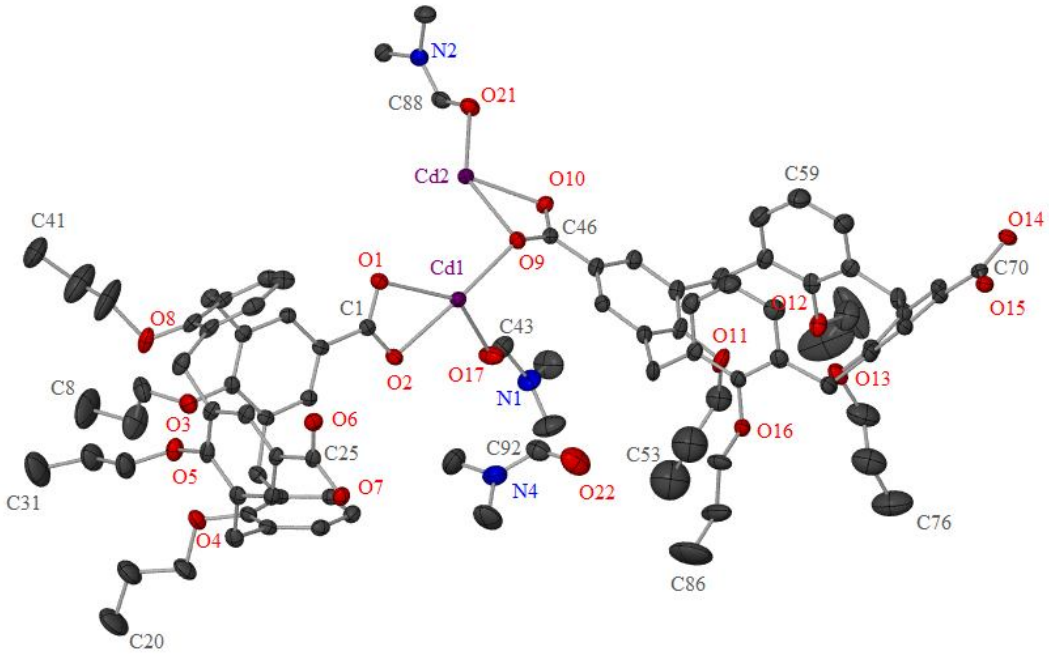

Figure 3-18. The asymmetric unit of $[Cd_2(caldc)_2(DMF)_2]\cdot 3DMF$ showing thermal ellipsoids at the 30% probability level. The minor disordered fragments and hydrogen atoms have been omitted for clarity.

The structure of $[Cd_2(caldc)_2(DMF)_2]\cdot 3DMF$ contains square $Cd_4(O_2CR)_8$ SBUs, in which two carboxylates bridge each edge of the square in a bridging chelating (κ^1O,κ^2O,O'-) coordination mode, as shown in Figure 3-19.

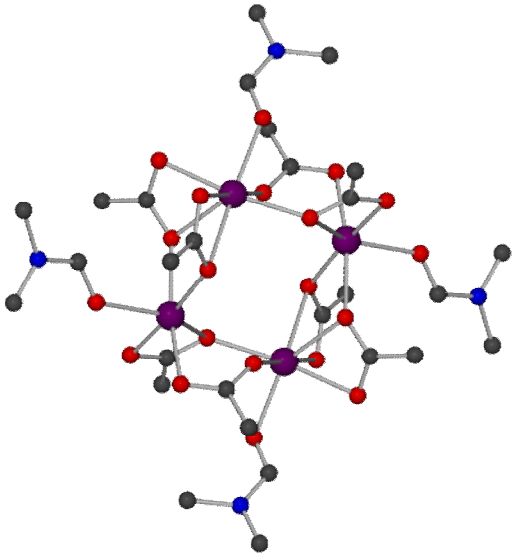

Figure 3-19. The $Cd_4(O_2CR)_8$ SBU with the coordinated DMFs. The minor disordered fragments and hydrogen atoms have been omitted for clarity.

The $Cd_4(O_2CR)_8$ SBUs showing the coordination environments around Cd centres as orange polyhedra (Figure 3-20) are connected by caldc ligands into (4,4) sheets in the *bc* plane. Similar to $Cu_2(caldc)_2(DMF)_2$ the curvature present within these caldc dianions gives each pore an hourglass shape.

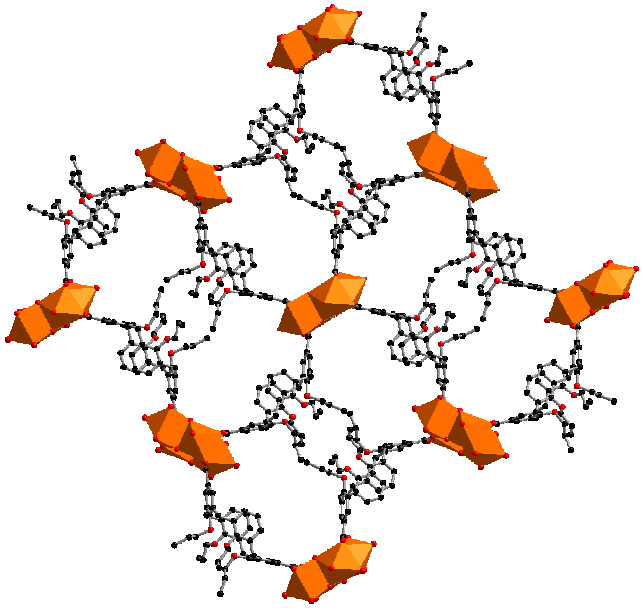

Figure 3-20. The (4,4) sheets of $[Cd_2(caldc)_2(DMF)_2]\cdot 3DMF$ present in the bc plane. The minor disordered fragments and hydrogen atoms have been omitted for clarity.

However, unlike in the structure of $Cu_2(caldc)_2(DMF)_2$, the (4,4) sheets present in $[Cd_2(caldc)_2(DMF)_2]\cdot 3DMF$ are further connected into a three-dimensional network by caldc dianions. These caldc ligands pair-wise forming "calixarene cages" and linking the SBUs into chains along *a* axis, as shown in Figure 3-21.

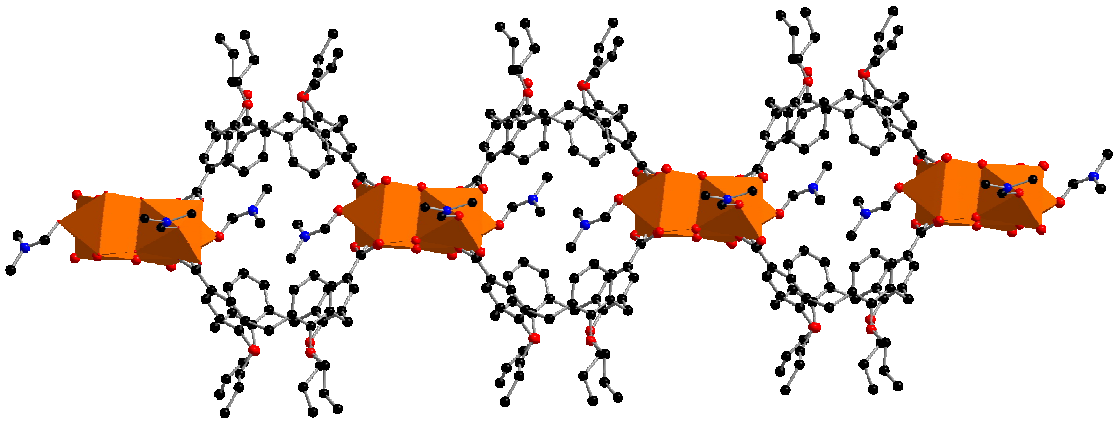

Figure 3-21. The "calixarene cages" linking the SBUs into chains along a axis. The minor disordered fragments and hydrogen atoms have been omitted for clarity.

In $[Cd_2(caldc)_2(DMF)_2]\cdot 3DMF$, there are two crystallographically independent caldc ligands. For the caldc ligands connecting the SBUs into the (4,4) sheets, the angle between the unsubstituted phenyl rings is 13°, whereas that between the carboxyphenyl rings is 105°. For the caldc ligands connecting the (4,4) sheets into a three-dimensional structure, the conformation is closer to that of a regular cone, with the angle between the unsubstituted phenyl rings of 26°, and the angle between the carboxyphenyl rings of 76°.

Using the simplified representation of the caldc ligand (Scheme 3-2) and showing the coordination environments around Cd centres as orange polyhedra, the 3-D network of $[Cd_2(caldc)_2(DMF)_2]\cdot 3DMF$ is pictured in Figure 3-22, left. The pink truncated hexagons represent the "calixarene cages" formed by the almost regular cone caldc ligands. The "simplified representation" of $[Cd_2(caldc)_2(DMF)_2]\cdot 3DMF$ viewed from the top is pictured in Figure 3-22, right.

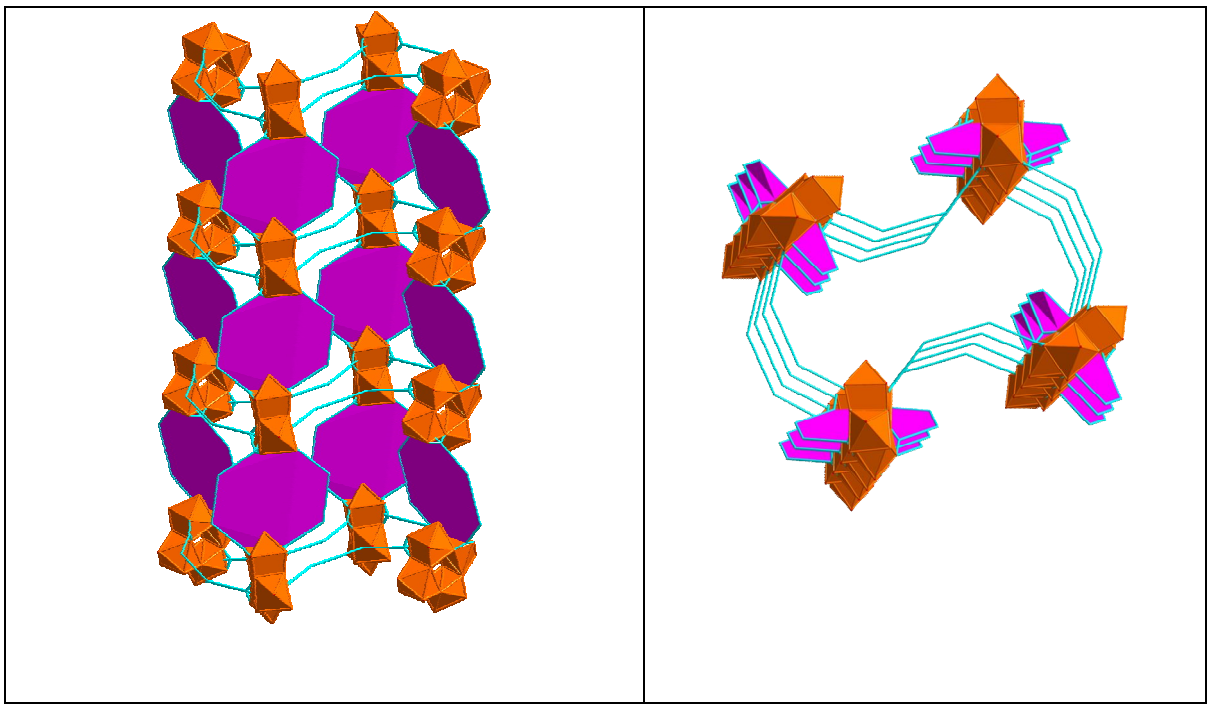

Figure 3-22. (Left) The 3-D network of [$Cd_2(caldc)_2(DMF)_2$]·3DMF using the simplified representation for the caldc ligand and showing the coordination environments around Cd centres as orange polyhedra and "calixarene cages" as pink truncated hexagons. (Right) view from the top of the network from the left.

The potentially accessible volume in the framework of [$Cd_2(caldc)_2(DMF)_2$]·3DMF is ca. 30.6% of the unit cell volume as calculated by PLATON SQUEEZE.[36] The minor disordered fragments and all DMF solvent molecules were removed prior to these calculations.

Figure 3-23 shows the TGA traces for the desolvated $Cd_2(caldc)_2$ (Figure 3-23, blue and black traces) compared with that of the as-made [$Cd_2(caldc)_2(DMF)_2$]·3DMF (Figure 3-23, red trace). The observed mass loss up to 280°C for the as-made [$Cd_2(caldc)_2(DMF)_2$]·3DMF (Figure 3-23, red trace) corresponds to the loss of two coordinated DMF solvent molecules (calculated 11%) plus three free DMF solvent molecules (calculated 6%). Figure 3-23, blue trace suggests that the MOF was only partially desolvated after 3 hours at 150°C. The black trace instead suggests that MOF has lost all the DMF solvent molecules when MOF was further evacuated for 3 hours at 170°C. However the sample evacuated at 170°C has suffered some structural changes as suggested by PXRD analysis.

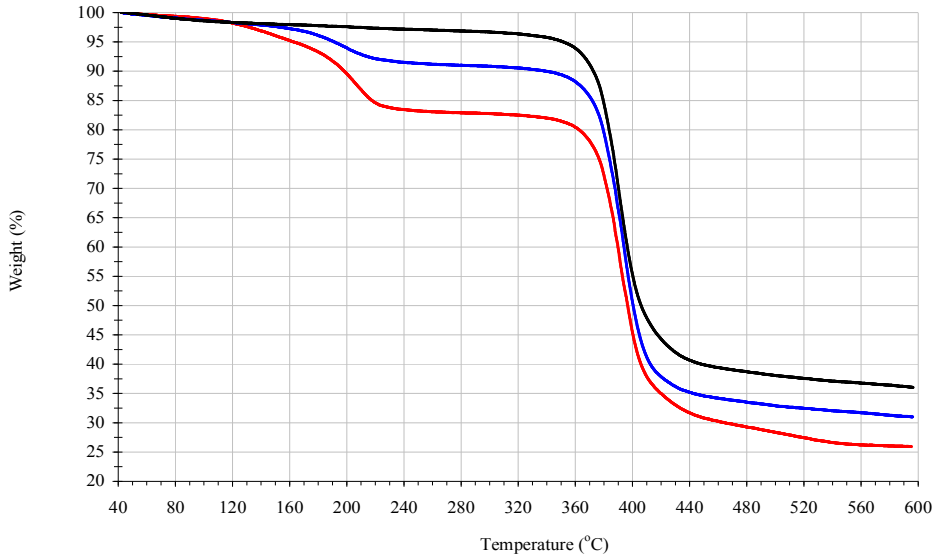

Figure 3-23. TGA traces of $[Cd_2(caldc)_2(DMF)_2]\cdot 3DMF$: as-made (red), activated 3 hours at 150°C (blue) and further activated 3 hours at 170°C (black).

In order to expel the DMF solvent molecules within MOF, less harsh activation conditions were required and attempts to exchange the DMF solvent molecules with MeOH (b.p. 64.7°C) have been made. It was observed that at the addition of MeOH the big needle-shaped crystals of $[Cd_2(caldc)_2(DMF)_2]\cdot 3DMF$ break down immediately and after three days in MeOH the resultant sample shows a PXRD pattern similar to that of the $[Cd_2(caldc)_2(DMF)_2]\cdot 3DMF$ activated at 170°C. A solvent with a much lower boiling point (39.6°C) was chosen instead, the dichloromethane. PXRD analysis suggests that the MOF framework was unaltered after 3 days in CH_2Cl_2 and the TGA analysis (Figure 3-24) suggests that all the free DMF solvent molecules were replaced by CH_2Cl_2 solvent molecules.

The experiments suggest that the DMF solvent molecules within $[Cd_2(caldc)_2(DMF)_2]\cdot 3DMF$ can be exchanged by CH_2Cl_2 and would be interesting to run the N_2 sorption measurement for the CH_2Cl_2 exchanged MOF, in order to assess MOF's porosity.

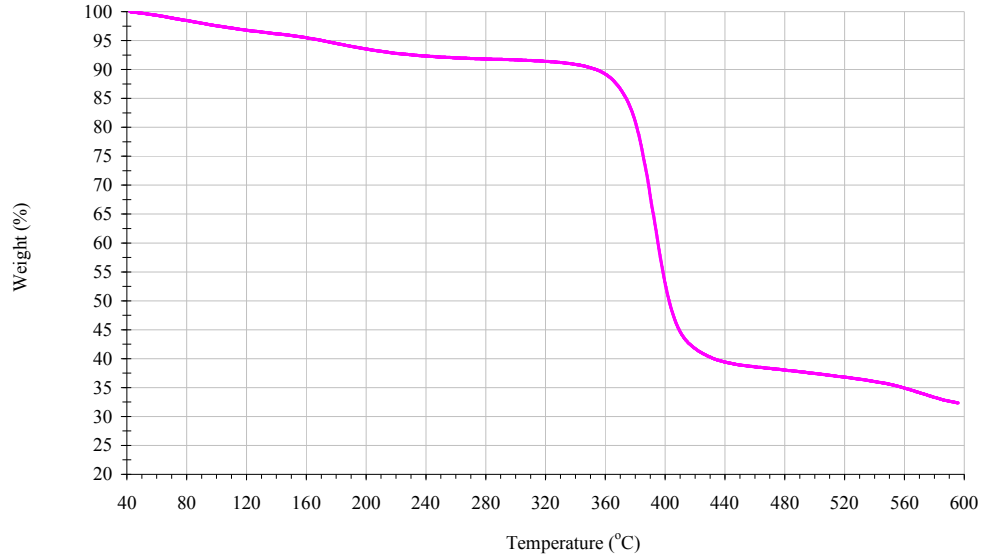

Figure 3-24. TGA trace of $[Cd_2(caldc)_2(DMF)_2]\cdot 3DMF$ after soaking in CH_2Cl_2 for 3 days.

Figure 3-25 shows the N_2 isotherm for $[Cd_2(caldc)_2(DMF)_2]\cdot 3DMF$ measured at 77 K and 101.33 KPa. The MOF was evacuated for 3h at 150°C prior to N_2 sorption measurement. The isotherm is a Type III isotherm as the one obtained for $Cu_2(caldc)_2(DMF)_2$. The BET surface area value calculated from N_2 isotherm is 0.9 m^2/g, suggesting the MOF is essentially nonporous.

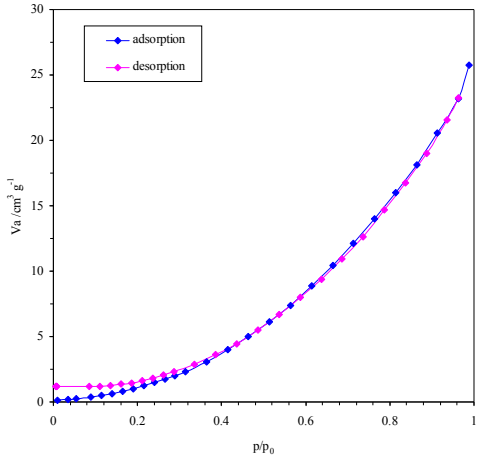

Figure 3-25. N_2 isotherm for $[Cd_2(caldc)_2(DMF)_2]\cdot 3DMF$ measured at 77K and 101.33KPa.

3.2.5. $[Co_5(caldc)_4(OH)_2(H_2O)_4]\cdot 8DMF$

Block-shaped purple crystals of suitable size for X-ray single diffraction were collected from the solvothermal reaction of $Co(NO_3)_2\cdot 6H_2O$ and H_2caldc (1 : 2 molar ratio) in DMF/water. The crystal data and refinement parameters for $[Co_5(caldc)_4(OH)_2(H_2O)_4]\cdot 8DMF$ are shown in Table 3-4.

Table 3-4. Crystallographic data and refinement parameters for $[Co_5(caldc)_4(OH)_2(H_2O)_4]\cdot 8DMF$.

Empirical formula	$C_{96}H_{125}Co_{2.5}N_4O_{23}$	
Formula weight	1850.32	
Temperature	150(2) K	
Wavelength	0.71073 Å	
Crystal system	Triclinic	
Space group, Z	*P*-1, 2	
Unit cell dimensions	a = 13.7658(3) Å	α = 104.894(3)°
	b = 16.0409(5) Å	β = 89.547(3)°
	c = 22.3491(10) Å	γ = 92.223(2)°
Volume	4765.6(3) Å^3	
Density (calculated)	1.289 g/cm^3	
Crystal size	0.25 x 0.15 x 0.10 mm	
Theta range for data collection	2.93 to 26.37°	
Reflections collected/ observed (>2σ)	31341/ 9096 [R(int) = 0.0420]	
Data Completeness	0.969	
Goodness-of-fit on F^2	0.907	
Final R indices [I>2σ(I)]	$R1$ = 0.0775 $wR2$ = 0.2103	
R indices (all data)	$R1$ = 0.1369 $wR2$ = 0.2299	
Largest diff. peak and hole	1.523 and –0.536 eÅ^{-3}	

The asymmetric unit of $[Co_5(caldc)_4(OH)_2(H_2O)_4]\cdot 8DMF$ (Figure 3-26) contains 2.5 cobalt centres, two caldc anions, two DMF solvent molecules, one hydroxide and two water ligands. There was also some diffuse solvent within the lattice which was approximated to two molecules of DMF per asymmetric unit using PLATON SQUEEZE. The carbon atoms

(C89, C90 and C91) of the DMF based on N2 are equally disordered over two positions. Some carbon atoms within the propyl groups are disordered.

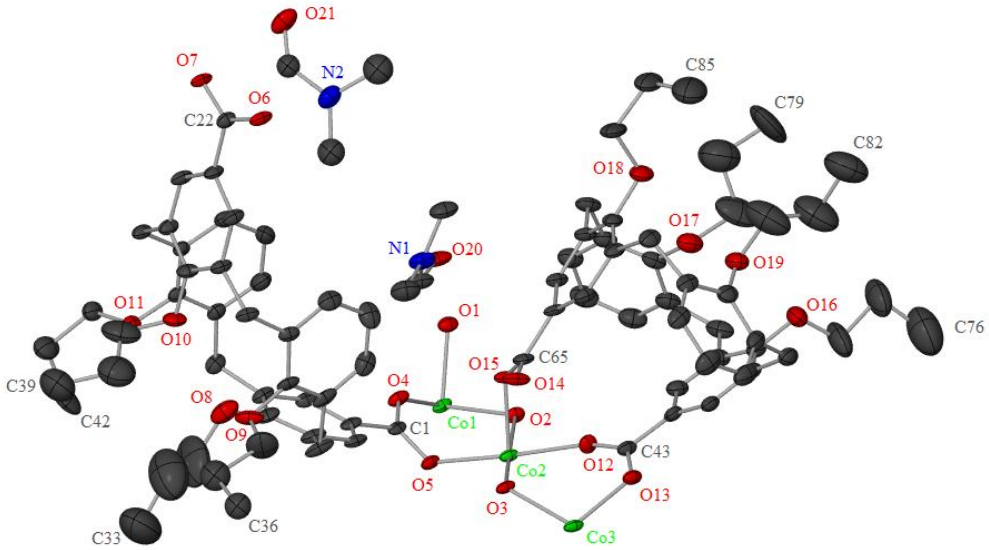

Figure 3-26. The asymmetric unit of $[Co_5(caldc)_4(OH)_2(H_2O)_4]\cdot 8DMF$ showing thermal ellipsoids at the 30% probability level. The minor disordered fragments and hydrogen atoms have been omitted for clarity.

The structure of $[Co_5(caldc)_4(OH)_2(H_2O)_4]\cdot 8DMF$ contains infinite SBUs which consist of $Co_4(\mu_3\text{-}OH)_2(O_2CR)_6(H_2O)_4$ units shown in Figure 3-27. Although the hydrogen atoms on the hydroxides and aqua ligands were not observed in the crystal structure, the identification of these groups is unambiguous, based on bond length analysis and charge balance.

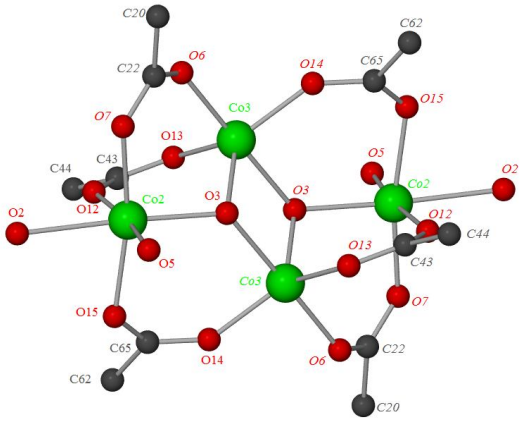

Figure 3-27. Structure of $Co_4(\mu_3\text{-}OH)_2(O_2CR)_6(H_2O)_4$ units in $[Co_5(caldc)_4(OH)_2(H_2O)_4]\cdot 8DMF$. Symmetry generated atoms are labelled in italics. The hydrogen atoms have been omitted for clarity.

There are two independent caldc dianions within the structure of $[Co_5(caldc)_4(OH)_2(H_2O)_4]\cdot 8DMF$, and these play different roles. One type of caldc anions are solely coordinated to the cobalt centres, with two of the caldc ligands being coordinated to each $Co_4(\mu_3\text{-}OH)_2(O_2CR)_6(H_2O)_4$ unit via both carboxylates, as shown in Figure 3-28.

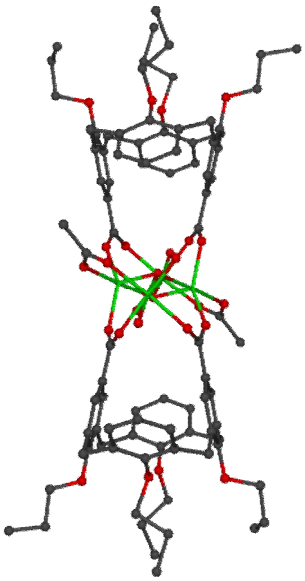

Figure 3-28. Structure of $[Co_5(caldc)_4(OH)_2(H_2O)_4]\cdot 8DMF$ showing two caldc ligands coordinated to $Co_4(\mu_3\text{-}OH)_2(O_2CR)_6(H_2O)_4$ unit. The hydrogen atoms have been omitted for clarity.

The $Co_4(\mu_3\text{-}OH)_2(O_2CR)_6(H_2O)_4$ units are linked together via single cobalt centres (Co1 atoms) into chains along *a* axis as shown in Figure 3-29. Each of the single cobalt centres is coordinated to two terminal aqua ligands and bridged by a carboxylate and an aqua ligand.

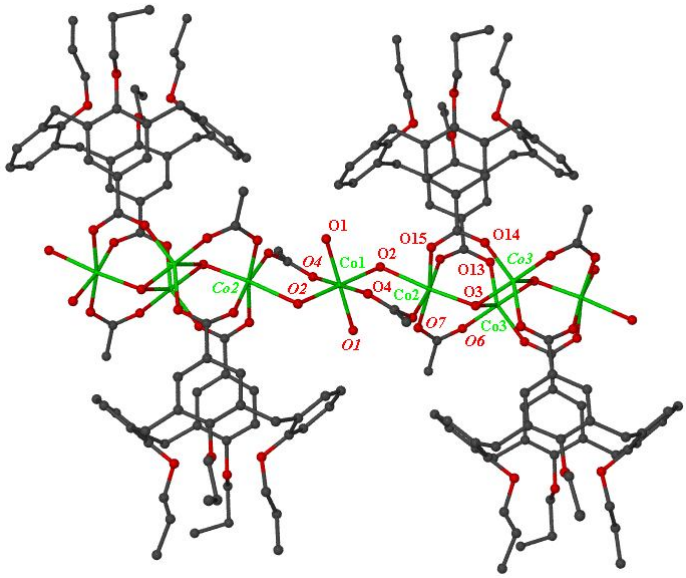

Figure 3-29. Coordination of the caldc ligands to the cobalt chain along a axis. Symmetry generated atoms are labelled in italics. The hydrogen atoms have been omitted for clarity.

The second independent caldc ligand connects the chains into sheets, as shown in Figure 3-30. There are no strong interactions between the sheets.

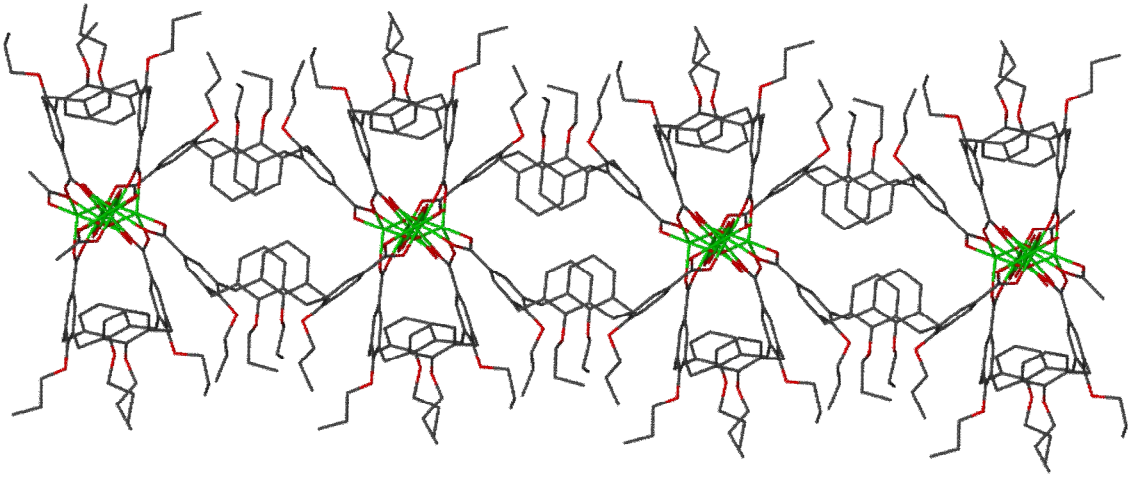

Figure 3-30. The sheets within the structure of [$Co_5(caldc)_4(OH)_2(H_2O)_4$]·8DMF. The hydrogen atoms have been omitted for clarity.

Although this appears to be the first observation of $Co_4(\mu_3\text{-}OH)_2(O_2CR)_6$ units in an extended structure, a similar core has been observed in the structure of [$Co_4(\mu_3\text{-}OH)_2(O_2CBut)_6(C_4H_6N_2O)_4$].[41]

Both independent caldc dianions in [$Co_5(caldc)_4(OH)_2(H_2O)_4$]·8DMF adopt pinched cone conformations, though they differ in orientation. Coordination of both carboxylate groups to the same chain ensures that this caldc ligand has the angle between the carboxyphenyl rings much lower (22°) than that of the phenyl rings (101°). For the caldc ligand bridging the chains, it is the phenyl rings that are almost parallel, with an angle between them of 9° whereas the carboxyphenyl rings are more splayed (101°).

The pinched cone conformations adopted by the caldc ligands within [$Co_5(caldc)_4(OH)_2(H_2O)_4$]·8DMF are represented in a simplified manner in Scheme 3-3.

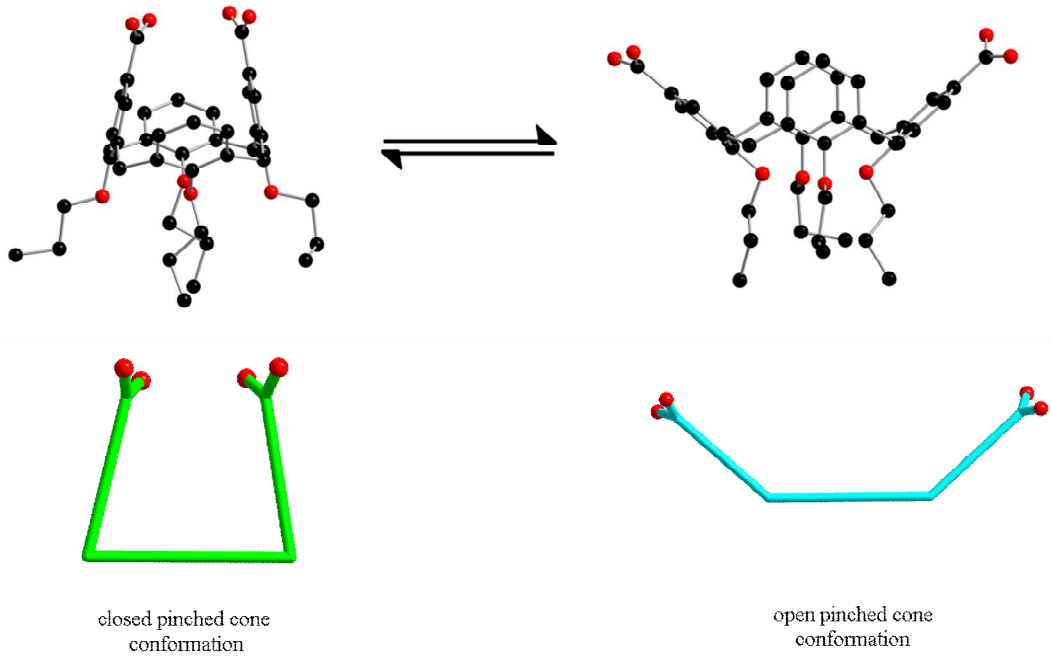

Scheme 3-3. The simplified representation of the pinched cone conformations of the caldc ligand shown in different colour.

Using the simplified representation of the caldc ligands and showing the coordination environments around the cobalt centres as blue polyhedra, the 2-D network of $[Co_5(caldc)_4(OH)_2(H_2O)_4]\cdot 8DMF$ is shown in Figure 3-31.

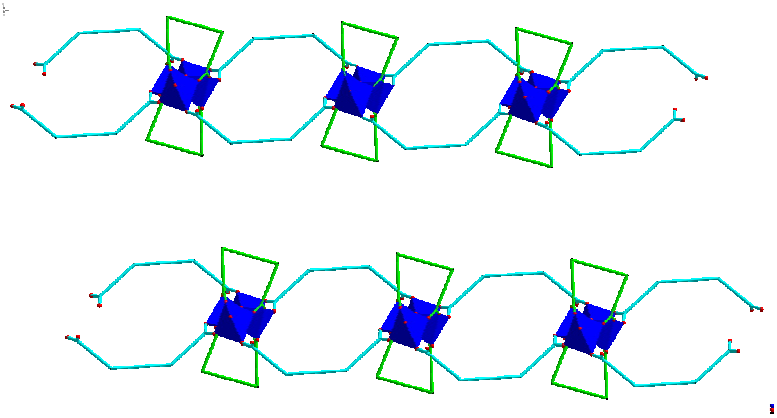

Figure 3-31. Layers within the structure of $[Co_5(caldc)_4(OH)_2(H_2O)_4]\cdot 8DMF$ viewed down the a axis using the simplified representation of caldc conformers and showing the coordination environments around Co centres as blue polyhedra.

The potentially accessible volume in the framework of $[Co_5(caldc)_4(OH)_2(H_2O)_4]\cdot 8DMF$ is 25.7% of the unit cell volume as calculated by PLATON SQUEEZE.[36] The minor

disordered fragments and all DMF solvent molecules were removed prior to these calculations.

A change in the concentration of the reaction mixture which produced purple crystals of $[Co_5(caldc)_4(OH)_2(H_2O)_4]\cdot 8DMF$, gave blue crystals which have proved by powder X-ray diffraction to be isomorphous with $Cu_2(caldc)_2(DMF)_2$ as shown in the experimental section. The $Co_2(caldc)_2(DMF)_2$ was already mentioned above as part of the isostructural $M_2(caldc)_2(DMF)_2$ series. Despite many attempts $[Co_5(caldc)_4(OH)_2(H_2O)_4]\cdot 8DMF$ could not be obtained phase pure and it seems that its formation is not as controllable as that of $Co_2(caldc)_2(DMF)_2$.

3.2.6. Molecular simulations for $Cu_2(caldc)_2(DMF)_2$, $[Cd_2(caldc)_2(DMF)_2]\cdot 3DMF$ and $[Co_5(caldc)_4(OH)_2(H_2O)_4]\cdot 8DMF$

Growing demand for hydrogen in various fields such as fuel cells and petrochemical industries has lead to finding innovative strategies for hydrogen separation and purification. Hydrogen purification is commonly carried out by steam reforming of methane[42]. CH_4/H_2 separation is also important in refinery off gas processing where equimolar CH_4/H_2 mixture is separated between 5-10 bar [43]. Unlike other impurities in H_2 stream (i.e. CO, CO_2) methane is difficult to remove due to its weaker interactions with the adsorbent. Studies carried out by our collaborators Dr. Peyman. Z. Moghadam during his PhD under the supervision of Prof. Tina Düren from Institute for Materials and Processes, University of Edinburgh[44] along with other studies in the literature[45] suggested that *p-tert*-butylcalix[4]arene displays interesting adsorptive characteristics. With this in mind our collaborators characterised and tested $Cu_2(caldc)_2(DMF)_2$, $[Cd_2(caldc)_2(DMF)_2]\cdot 3DMF$ and $[Co_5(caldc)_4(OH)_2(H_2O)_4]\cdot 8DMF$ for their adsorption and separation capabilities for methane and hydrogen.

Our collaborators obtained the pore size distribution, the surface area and pore volume measurements of $Cu_2(caldc)_2(DMF)_2$, $[Cd_2(caldc)_2(DMF)_2]\cdot 3DMF$ and $[Co_5(caldc)_4(OH)_2(H_2O)_4]\cdot 8DMF$. All water and solvent molecules were removed from the MOFs prior to their characterisations and simulations. The pore size distribution reveals pores with diameters close to 5.0 Å for all three MOFs. If in $Cu_2(caldc)_2(DMF)_2$ one pore has been identified, $[Co_5(caldc)_4(OH)_2(H_2O)_4]\cdot 8DMF$ and $[Cd_2(caldc)_2(DMF)_2]\cdot 3DMF$

form two and three pores respectively. Figure 3-32 illustrates the accessible pore space in all three MOFs studied.

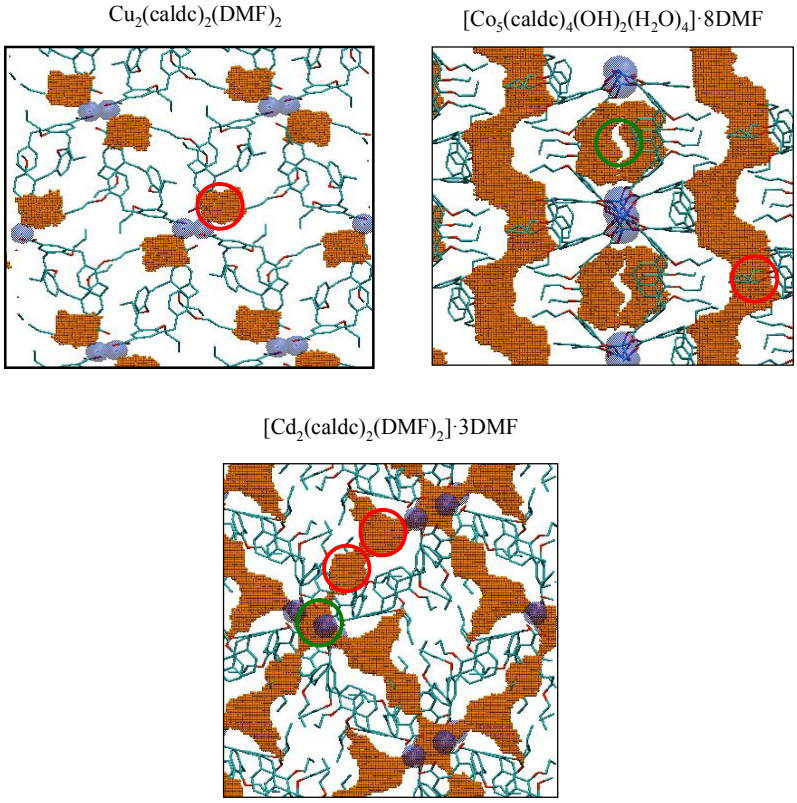

Figure 3-32. Schematic view of the pore space for all three MOFs calculated with a probe size of 2.75Å. The orange aperture shows the available pore space in the vdW representation. Metal clusters are shown in transparent blue spacefill representation. Pore diameters obtained from the pore size distribution are marked with green and red circles for large and small pores, respectively.[44]

Simulations show that the accessible surface area and void fraction for these MOFs are relatively modest with $[Cd_2(caldc)_2(DMF)_2]\cdot 3DMF$ and $[Co_5(caldc)_4(OH)_2(H_2O)_4]\cdot 8DMF$ $Cu_2(caldc)_2(DMF)_2$ showing the largest values. The experimental surface area values obtained by us and mentioned earlier in this work for $Cu_2(caldc)_2(DMF)_2$ and $[Cd_2(caldc)_2(DMF)_2]\cdot 3DMF$ were also insignificant. The accessible surface area measured with the nitrogen-sized probe molecule in general compares well with experimental BET surface area[46] for well activated samples and therefore can provide an indication about the quality of the sample and the activation procedure[47, 48].

Figure 3-33 shows the simulated adsorption isotherms for methane at 300K for $Cu_2(caldc)_2(DMF)_2$, $[Cd_2(caldc)_2(DMF)_2]\cdot 3DMF$ and $[Co_5(caldc)_4(OH)_2(H_2O)_4]\cdot 8DMF$. Although the shape of the isotherms is similar, the amount of methane adsorbed in $[Cd_2(caldc)_2(DMF)_2]\cdot 3DMF$ and $[Co_5(caldc)_4(OH)_2(H_2O)_4]\cdot 8DMF$ is higher than that in the $Cu_2(caldc)_2(DMF)_2$. This difference in adsorption can be attributed to the presence of multiple adsorption sites in the $[Cd_2(caldc)_2(DMF)_2]\cdot 3DMF$ and $[Co_5(caldc)_4(OH)_2(H_2O)_4]\cdot 8DMF$ MOFs as were identified in the pore size distribution studies.

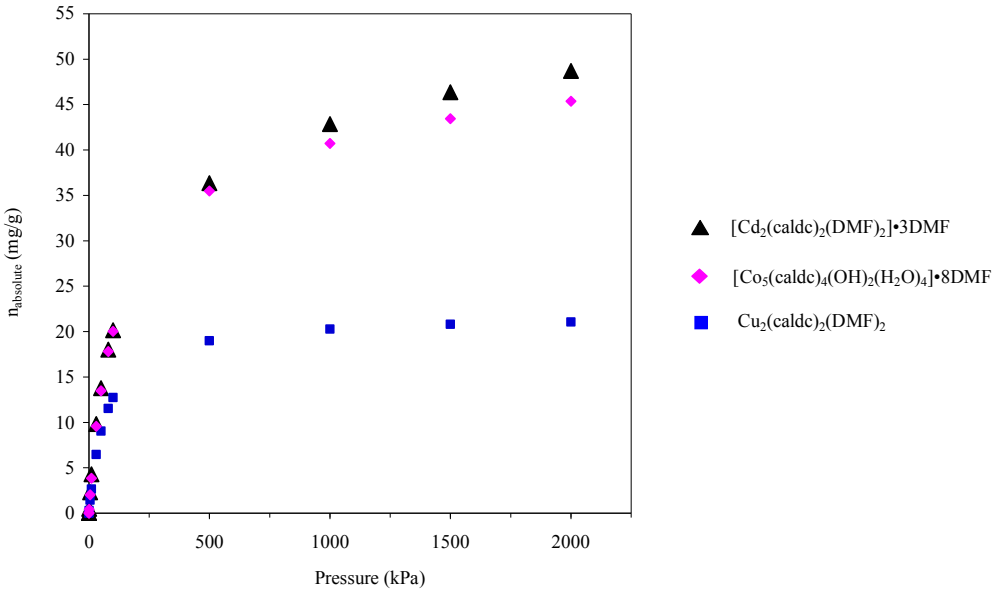

Figure 3-33. Simulated CH_4 adsorption isotherms at 300 K.[49]

A visualisation of where the methane molecules might sit within these MOF frameworks is shown in Figure 3-34. In most MOFs, preferential adsorption occurs around the metal clusters. Similarly, in the case of $Cu_2(caldc)_2(DMF)_2$, the preferential adsorption position for methane is close to the paddle-wheel metal units whereas in the $[Co_5(caldc)_4(OH)_2(H_2O)_4]\cdot 8DMF$ and $[Cd_2(caldc)_2(DMF)_2]\cdot 3DMF$ two and three respectively favourable adsorption sites, were identified as depicted by the pink and turquoise circles in Figure 3-34. These sites correspond well with the types of pores shown above in Figure 3-32. It can be observed that in all three MOFs, the calix[4]arene bowls are inaccessible to methane.

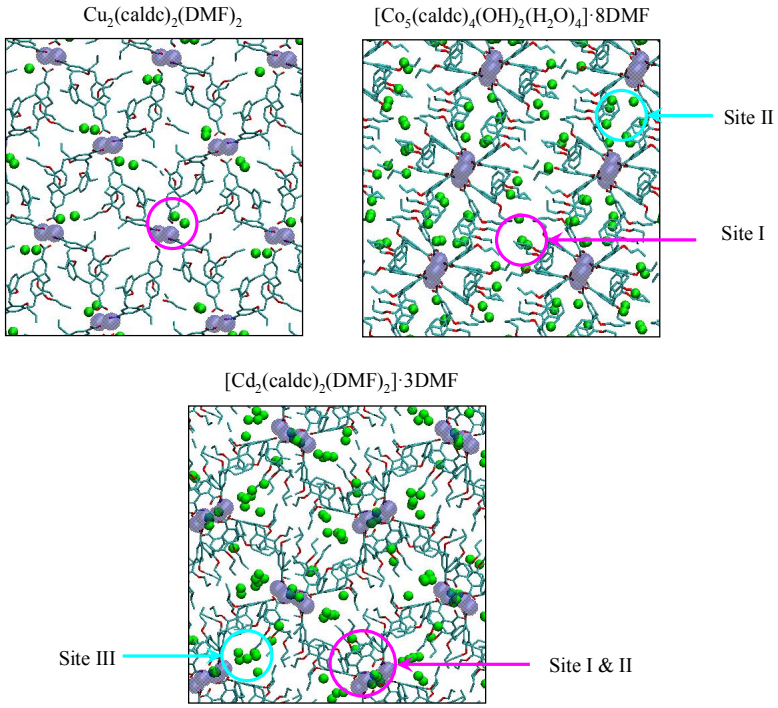

Figure 3-34 Snapshots for CH_4 adsorbed in MOFs at 2000 KPa and 300 K. The green CH_4 molecules are shown in spacefill representation; metal clusters are shown as transparent blue spheres.[49]

The simulated adsorption isotherms for H_2 at 77 K are shown in Figure 3-35. Similar to the trend observed for methane adsorption, the amount of hydrogen adsorbed is higher in the $[Cd_2(caldc)_2(DMF)_2]\cdot 3DMF$ followed by $[Co_5(caldc)_4(OH)_2(H_2O)_4]\cdot 8DMF$ and $Cu_2(caldc)_2(DMF)_2$.

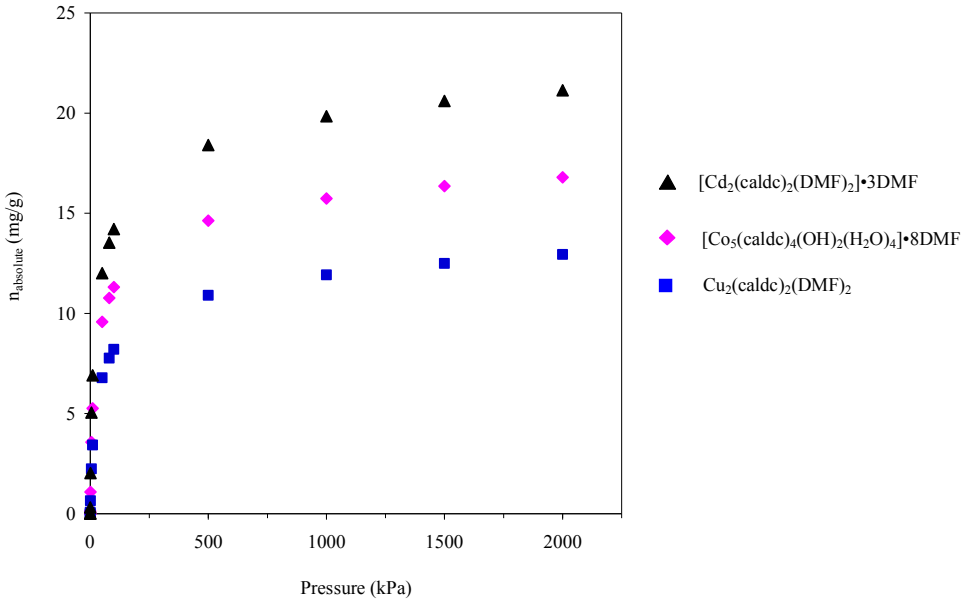

Figure 3-35. Simulated adsorption isotherms for H_2 at 77 K.[49]

The snapshots of H_2 molecules adsorbed at 77 K and 2000 KPa in all three MOFs are shown in Figure 3-36. The adsorption sites for H_2 are similar to those seen for CH_4. However, interestingly, an additional adsorption site is observed in $[Cd_2(caldc)_2(DMF)_2]\cdot 3DMF$ as illustrated by the pink circles in Figure 3-36.

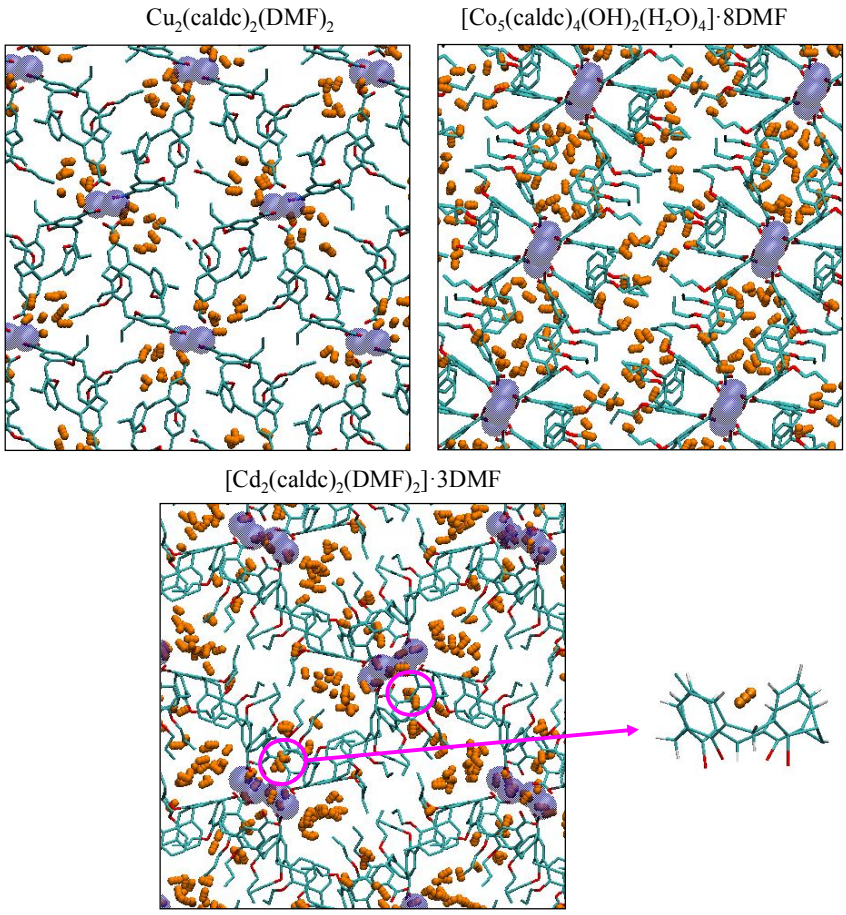

Figure 3-36. Snapshots for H_2 adsorbed in MOFs at 2000 KPa and 77 K. H_2 is represented by orange spheres, metal clusters are shown as transparent blue spheres.[49]

The bowl of the caldc ligand is not accessible to methane and only in $[Cd_2(caldc)_2(DMF)_2]\cdot 3DMF$ is accessible to hydrogen, as shown in Figure 3-37. This is consistent with the structural data that shows only $[Cd_2(caldc)_2(DMF)_2]\cdot 3DMF$ has a relatively open conformation of the calix[4]arene bowl.

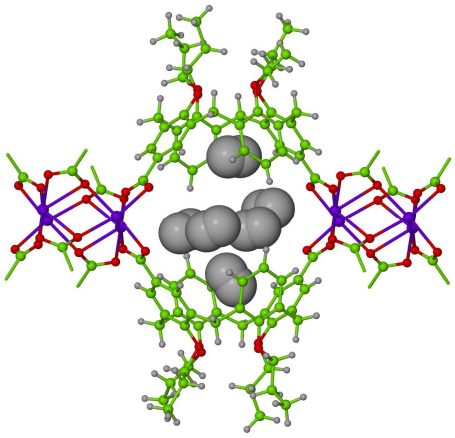

Figure 3-37. Simulated hydrogen adsorption for desolvated $[Cd_2(caldc)_2(DMF)_2]\cdot 3DMF$, showing adsorption into the calix[4]arene bowl. The hydrogen molecules adsorbed are shown in space filling representation, Colour code: Cd atoms are purple, C green, O red and H grey.[49]

Adsorption of equimolar mixture of methane and hydrogen has been simulated for all three MOFs and the adsorption selectivity for methane over hydrogen at 300 K is shown in Figure 3-38.

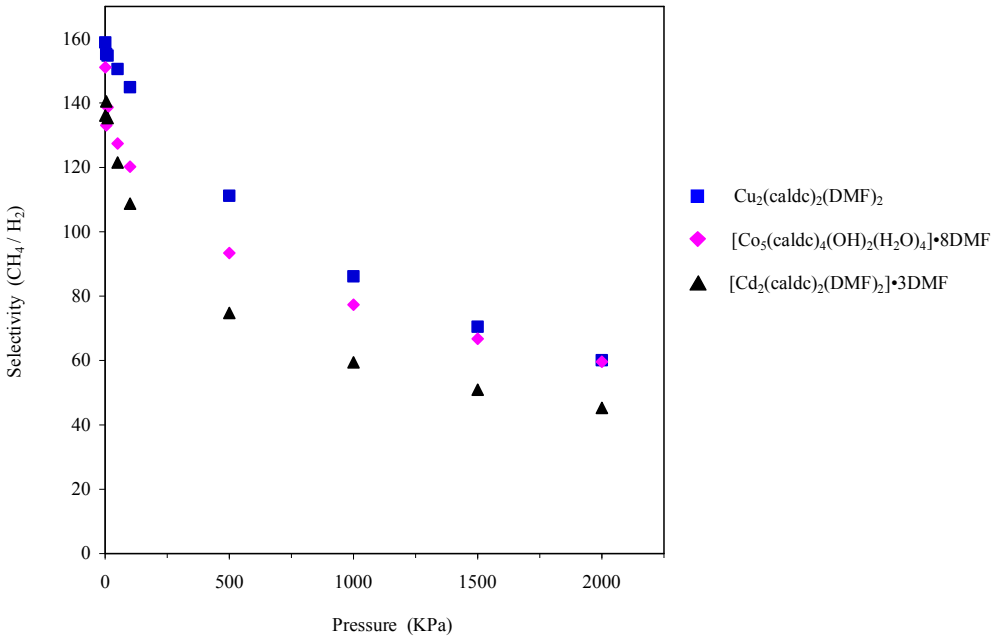

Figure 3-38. Simulated adsorption selectivity for CH_4 over H_2 at 300 K for an equimolar mixture of CH_4 and H_2.[49]

All three MOFs exhibit very similar selectivities varying between 120 and 150 at 10 KPa to between 40 and 50 at 2000 KPa, with $Cu_2(caldc)_2(DMF)_2$ showing the highest selectivity. These selectivities are higher than observed in many other MOFs by molecular simulation (e.g. $Zn_4O(1,4\text{-bdct})_3$ (IRMOF-1): ~5,[50] $Cu_3(btc)_2$ (HKUST-1, btc = 1,3,5-benzenetricarboxylate): ~18 - 12,[50] Zn(imidazolate)$_2$ (ZIF-3): ~31 – 25,[51]) and are in the same order of magnitude of what is observed in Zn(tbip) (tbip = 5-tert-butylisophthalate) where the selectivity varies between 200 and 125.[52]

Here, as in Zn(tbip), the high selectivities are mainly due to the small size of the pores. The observation that the calix[4]arene bowl in $[Cd_2(caldc)_2(DMF)_2]\cdot 3DMF$ is accessible to some but not all components of a mixture could in principle be exploited for separations. These results suggest that such networks are likely to display interesting selectivity to guest molecules.

3.3. Experimental

3.3.1. General

25,26,27,28-tetrapropoxycalix[4]arene-5,17-dicarboxylic acid (H_2caldc) were prepared using a well-developed methodology within the group of Dr. Sean Bew from University of East Anglia. The syntheses of H_2caldc and H_4caltc were reported[17, 31, 53] prior to the reactions sequence developed by our collaborators. Most of the organic compounds syntheses were performed at the University of East Anglia under guidance of Sean Thurston and repeated afterwards by myself at the University of Bath.

The reactions performed for synthesis of H_2caldc were carried out under nitrogen or argon in flame dried apparatus which were allowed to cool under an inert atmosphere. Solvents were removed using a rotary evaporator.

^{1}H NMR spectra were recorded at 300 K on an Oxford 300 MHz spectrometer at the University of East Anglia and on a Bruker Ultrashield 250 MHz or 300 MHz spectrometer at the University of Bath. Samples are prepared as solutions of $CDCl_3$ or CD_3OD and therefore the spectra were referenced to residual *protio* solvent signals for ^{1}H NMR spectra

($CDCl_3$, δ 7.26, CD_3OD δ 3.34). Chemical shifts are reported in ppm (δ) and J_{HH} values are given in Hz.

Solvothermal MOF syntheses were carried out in thick-walled glass vials (10 - 30 cm^3) purchased from Biotage or pressure tubes (15 cm^3) purchased from Aldrich and heated in programmable ovens. The reagents used for MOF syntheses were purchased commercially and used without further purification.

Microwave-assisted reactions of MOFs were carried out in a Biotage Initiator 2.0 microwave reactor where high-frequency microwaves (2.45 GHz) heat the reaction mixture. The microwave reactor was set to a normal absorption level. If stirring is unwanted the magnetic stirring bar is simply omitted. In microwave experiments the time countdown starts when the target temperature is reached, i.e. the initial time taken to reach the set temperature is not included in the heating time.
Powder X-ray diffractions (PXRDs) were recorded at the University of Bath on a Bruker AXS D8 Advance diffractometer with copper Kα radiation of wavelength 1.5406 Å at 298 K. Samples were placed in 0.5 mm diameter Lindemann capillaries, and measured with a 2θ range of 3-60°. The step size was 0.016° with time per step of 134.5 s. Simulated X-ray powder patterns were generated from single crystal data that were imported into PowderCell[54] with the step size of 0.02° and time per step of 1.00 s.

TGA experiments were performed on a Perkin Elmer TGA 4000 Thermogravimetric Analyser at the University of Bath. The samples were heated from 45°C to 600°C at a heating rate of 10°C/min, under a flow of nitrogen (20 mL/min).

Microanalysis (Carbon, Hydrogen and Nitrogen = CHN) data was recorded on a CE-440 Elemental Analyser by Alan Carver at the University of Bath. The fact that CHN data for calixarenes does not match perfectly should be of no concern as literature predicts no accurate CHN data for this type of compounds[55].

The nitrogen sorption isotherms were measured at 77 K and 101.33 KPa, using a Belsorp-mini II analyzer at the University of Bath. Prior to the nitrogen sorption measurements,

MOF samples were desolvated with the pre-treatment parameters mentioned for each measurement.

3.3.2. Single-Crystal X-Ray Crystallography

X-ray diffraction data on $(NMe_2H_2)_2$caldc, $Cu_2(caldc)_2(DMF)_2$ and $[Cd_2(caldc)_2(DMF)_2]\cdot 3DMF$ were collected on a Nonius Kappa CCD diffractometer, at the University of Bath. X-ray diffraction data on $(NMe_2H_2)_2$caldc were collected by Dr. Anna Warren whereas on $Cu_2(caldc)_2(DMF)_2$ and $[Cd_2(caldc)_2(DMF)_2]\cdot 3DMF$ were collected by me. X-ray diffraction data on $[Co_5(caldc)_4(OH)_2(H_2O)_4]\cdot 8DMF$ were collected by Dr. Mary Mahon on an Oxford Diffraction Gemini diffractometer fitted with an Atlas CCD detector, at the University of Bath. In all cases, Mo-Kα radiation of wavelength 0.71073 Å was used and data collections were carried out at 150 K.

The structures were solved using SHELXS-97[56] and refined using full-matrix least squares in SHELXL-97[56]. The final refinements were run by Dr. Mary Mahon and were generally straightforward with the following exceptions and points of note. Unless noted below, all non-hydrogen atoms were refined anisotropically in the final least squares run, and hydrogen atoms were included at calculated positions.

Search for and analysis of solvent accessible voids in the structures have been made using PLATON SQUEEZE[36]. Solvent accessible voids are defined as regions in the structure that can accommodate at least a sphere with radius 1.2 Å without intersecting with any of the van der Waals spheres assigned to each atom in the structure. The free solvent molecules from within the structure and the minor disordered atoms have been removed prior to these calculations.

The disordered fragments within $(NMe_2H_2)_2$caldc were refined subject to both C-C distance restraints and some ADP restraints in the final least squares. The hydrogens in the dimethylammonium cation were located and refined at 0.8 Å from the parent nitrogen.

In $Cu_2(caldc)_2(DMF)_2$ the approach of modelling C6, C7 and C8 as disordered atoms yielded the optimal convergence, but the disorder is somewhat smeared. Hence, C-C

distance restraints and ADP restraints were applied to these partial occupancy carbon atoms.

In the $[Cd_2(caldc)_2(DMF)_2]\cdot 3DMF$ the disorder is shown by all the carbon atoms within propyl groups containing O3 (C6, C7 and C8), O11 (C51, C52 and C53), O16 (C84, C85 and C86), whereas the containing O12 groups shown disorder just by C64 and C65 atoms. Only the major atom fractions in the disordered moieties were refined anisotropically, with the exception of the group containing O11, where the electron density was very smeared. O-C and C-C distance restraints were applied in disordered *n*-propyl functionalities to assist convergence. Strenuous efforts could not successfully render a credible model that would converge for the two solvent diffuse regions, which each approximated to one molecule of DMF, which was in agreement with the suggested quantity of solvent when PLATON SQUEEZE[36] was employed. Data presented herein take account of this 'pre-SQUEEZE' solvent. A fall off in diffraction intensity was noted, probably a function of the disordered solvent present and the small size of two (0.13 mm) of the sample dimensions and data were truncated to a maximum Bragg angle of 25°.

For $[Co_5(caldc)_4(OH)_2(H_2O)_4]\cdot 8DMF$ two X-ray data collections were required in order to get optimal data. A considerable number of distance restraints pertaining to the propoxy groups plus some ADP restraints were necessary in order to facilitate convergence of this structure. The carbon atoms C35, C36 within propoxy group containing O9 and C42 of propoxy group containing O11 are disordered in a 60: 40 ratio and 55: 45 ratio, respectively. The core is well resolved, with the exception of the hydroxide/water hydrogens atoms. The latter could not be credibly located and hence were omitted from the refinement. Although the hydrogen atoms on the hydroxides and aqua ligands were not observed in the crystal structure, the identification of these groups is unambiguous, based on bond length analysis and charge balance.

3.3.3. Molecular simulations

The accessible surface area was calculated by performing many random insertions of a nitrogen/hydrogen-sized spherical probe molecule around each MOF atom. Nitrogen and hydrogen probes were used in this study with sizes of 3.681 Å and 2.958 Å respectively. The insertions are done on a sphere whose radius is the sum of the radii of the probe and

the framework atom. The accessible surface area is then obtained from the fraction of probe insertions that do not overlap with the other framework atoms. The pore size distributions were obtained by the method described by Gelb and Gubbins[57] which determines the diameter of the largest sphere that can fit in the cavities without overlapping with framework atoms. For the pore shape studies a probe molecule with an arbitrary diameter of 2.75 Å was inserted randomly in the pore space and tested for overlap with the framework atoms as described by Sarkisov and Harrison[58]. The void fraction is the empty space of a structure divided by the total volume. To calculate the free volume, a 0 Å sized probe is randomly inserted multiple times in the unit cell and tested for overlap with the framework atoms. The pore volume can be then calculated by multiplying the void fraction (ratio of successful insertions to the total number of insertions) by the unit cell volume.

Adsorption of CH_4, H_2 and their equimolar mixture were computed from using grand canonical Monte Carlo (GCMC) simulations[59] implemented in the RASPA[60] simulation package. In the grand canonical ensemble, the chemical potential, the volume, and the temperature are kept constant while the number of molecules is allowed to fluctuate mimicking the experimental situation. This is achieved by randomly inserting, deleting, and translating and in the case of non-spherical molecules such as hydrogen also rotating the molecules. For binary mixtures, identity swap moves were also used for faster equilibration times. For all pure component isotherms, 1×10^5 equilibration and 2×10^5 production cycles were used for each point whereas for mixtures as many as 3×10^5 cycles were used for each equilibration and production run. Here, a cycle is defined as one MC move per molecule. Each simulation cell consisted of eight ($2 \times 2 \times 2$) unit cells to allow for good statistics. The MOFs were considered as rigid and the framework atoms were kept fixed at their crystallographic positions. The input fugacities for the GCMC simulations, which are related to the chemical potential by an equation of state, were calculated from the Peng-Robinson equation of state. All results are reported as absolute amount adsorbed. For the calculation of both the guest-guest and the guest-framework interactions, the Lennard-Jones potential was used with a cut-off radius of 12.8 Å. The Lennard Jones (LJ) parameters for all the framework were taken from the Dreiding force field[61] except for metal atoms which were taken from UFF force field.[62] The potential parameters for methane were taken from Goodbody *et al*.[63] In this model, the methane molecule is modelled as a single sphere. Hydrogen was modelled as a two site LJ molecule.[64] The

Lorenz-Berthelot mixing rules were used to calculate mixed LJ parameters. All electrostatic interactions between guests and guest-host molecules were neglected.
The selectivity (S) for methane relative to hydrogen is defined as:

$$S_{CH_4/H_2} = \frac{x_{CH_4} / x_{H_2}}{y_{CH_4} / y_{H_2}}$$

where x_{CH_4} and x_{H_2} are the mole fractions of methane and hydrogen in the adsorbed phase, while y_{CH_4} and y_{H2} are the mole fractions of methane and hydrogen in the bulk phase, respectively.

3.3.4. Synthesis of *p-tert*-butylcalix[4]arene

A 3 litre 3-necked round bottomed flask was flame-dried, purged with N_2 and charged with an aqueous formaldehyde solution (37%, 155 mL, 2.07 mol), *tert* butyl-phenol (250 g, 1.66 mol) and 10 M NaOH (3mL, 0.03 mol). The two remaining necks of the flask were fitted with an N_2 inlet and an N_2 outlet. The mixture was stirred using a mechanical stirrer and heated to 120ºC. Heating was ceased as the mixture became increasingly viscous and stirring was ceased just before the mixture solidified into off-white solid foam. The foam was dissolved in diphenyl ether (2 L) and heated to boiling, vapour was allowed to escape until 180°-190°C. The flask was then fitted with a condenser and the solution was refluxed at 260°C for 4 hours. The solution was allowed to cool to 60°C and ethyl acetate was added (1.5 L) and the resulting off-white crystals were filtered using a Buchner funnel. The crystals were titrated in acetic acid (200 mL), re-filtered using a Buchner funnel and washed with ethyl acetate (200 mL). The crystals were then dissolved in the minimum amount of toluene (~3 L) at 100°C and allowed to re-crystallise at room temperature. The crystals were filtered using a Buchner funnel to afford pure *p-tert*-butylcalix[4]arene as white crystals (160g, 66%). ^{1}H NMR (300MHz, $CDCl_3$): δ 10.27 (s, 4H, O*H*), 6.98 (s, 8H, *m*-HOAr*H*CH_3), 4.19 (d, 4H, ArC*Hax*HeqAr, *J* = 13.75 Hz), 3.43 (d, 4H, ArCHax*Heq*Ar, *J* = 13.75 Hz), 1.14 (s, 36H, *p*-OHArC*H*$_3$).

3.3.5. Synthesis of 25,26,27,28-tetrahydroxycalix[4]arene (1)

A 250 mL round bottomed flask with a stirrer bar was flame-dried, purged with nitrogen and charged with *p-tert*-butylcalix[4]arene (12 g, 18.4 mmol). Toluene (100 mL) was added and stirred for 10 min to give a colourless solution. Phenol (2.59 g, 27.6 mmol) was

added and the solution was stirred for 5 min. Aluminium chloride (12 g, 89.9 mmol) was slowly added over 10 min and the solution was stirred for 2 hours. Within 30 min the solution turned from colourless to red and a thick, waxy red solid formed. Adding 200 g of crushed ice quenched the reaction, the solution was transferred to a separating funnel and the flask was rinsed with CH_2Cl_2 (100 mL) and more ice (100 g). More CH_2Cl_2 (400 mL) was added and the organic layer was washed with 1 M HCl (3 x 200 mL) and distilled water (2 x 200 mL). The solvent was then removed *in vacuo* to give an orange oily residue. Diethyl ether was added to the residue and white solid precipitated. The mixture was then sealed and stored at -15°C for 1 hour. The solid was then vacuum filtered dried *in vacuo* to afford pure 25,26,27,28-tetrahydroxycalix[4]arene as a white powder (6.07 g, 77%). ^{1}H NMR (400MHz, $CDCl_3$): δ 10.16 (s, 4H, O*H*), 7.02 (d, 8H, *m*-HOAr*H*, *J* = 7.54 Hz), 6.70 (t, 4H, *p*-HOAr*H*, *J* = 7.54 Hz), 4.23 (broad, 4H, ArCHax*Heq*Ar, *J* = 13.6 Hz), 3.51 (broad, 4H, ArCHax*Heq*Ar, *J* = 13.6 Hz).

3.3.6. Synthesis of 25,27-dipropoxy-26,28-dihydroxycalix[4]arene (2)

A 100 mL round bottomed flask was flame dried and charged with **1** (4.31 g, 10.1 mmol), K_2CO_3 (3.20 g, 23.2 mmol), acetonitrile (50 mL). The flask was then fitted with a condenser and the mixture was heated at reflux for 1 hour. 1-iodopropane (6.55 mL, 22.3 mmol) was added to the solution and the reflux was continued for 16 hours. Heating was ceased and any solvent was removed *in vacuo* to afford a white powder. The solid was dissolved in CH_2Cl_2 (50 mL) and washed with 1 M HCl (2 x 50mL) and brine (50 mL). The organic layer was collected and any solvent removed *in vacuo* to afford pure 25,27-dipropoxy-26,28-dihydroxycalix[4]arene as a white solid (3.32g, 65%). ^{1}H NMR (300MHz, $CDCl_3$): δ 8.22 (s, 2H, O*H*), 6.98 (d, 4H, *m*-HOAr*H*, *J* = 7.35 Hz), 6.85 (d, 4H, *m*-PrOAr*H*, *J* = 7.54 Hz), 6.67 (t, 2H, *p*-HOAr*H*, *J* = 7.35 Hz), 6.57 (t, 2H, *p*-PrOAr*H*, *J* = 7.54 Hz), 4.25 (4H, ArC*Hax*HeqAr, *J* = 14.00 Hz), 3.91 (t, 4H, ArOC$H_2$$CH_2CH_3$, *J* = 14.00 Hz), 3.29 (4H, ArCHax*Heq*Ar, *J* = 14.00 Hz), 2.06–1.95 (sextet, 4H, ArOCH$_2$C$H_2$$CH_3$, *J* = 14.00 Hz), 1.25 (t, 6H, ArOCH$_2$CH$_2$CH_3, 3*J* = 14.00 Hz).

3.3.7. Synthesis of 5,17-diformyl-25,27-dipropoxy-26,28-dihydroxycalix[4]arene (3)

A 250 mL round bottomed flask flame dried and cooled under nitrogen, charged with a solution of **2** (2.9 g, 5.7 mmol) in anhydrous chloroform (75 mL) under an atmosphere of nitrogen was cooled to -15°C. Tin (IV) chloride (6.7 mL, 14.85 g, 57 mmol) was added in

one portion *via* syringe, followed by 1,1-dichloromethyl methyl ether (1.4 mL, 1.77 g, 15.4 mmol) in one portion *via* syringe. The reaction mixture was stirred at -15°C for a further 30 minutes and allowed to cool to room temperature with stirring over further 2 hours. The mixture was then quenched with water (40 mL). Following transfer to a 250 mL separating funnel, the resulting mixture was extracted with dichloromethane (2 x 100 mL) and the combined organic phase was washed with water (2 x 35 mL) and brine (2 x 70 mL). The resultant mixture was dried over mangnesium sulfate, filtered and concentrated *in vacuo*. Trituration of the residue with methanol afforded a pale purple solid (3.00 g, 93%). ^{1}H NMR analysis revealed the solid to be the desired 5,17-diformyl-25,27-dipropoxy-26,28-dihydroxycalix[4]arene. ^{1}H NMR (300MHz, $CDCl_3$): δ 9.72 (s, 2H, O*H*), 9.21 (s, 2H, C*H*O), 7.57 (s, 4H, *m*-HOAr*H*COH), 6.91 (d, 4H, *m*-PrOAr*H*, *J* = 7.56 Hz), 6.74 (t, 2H, *p*-PrOAr*H*, *J* = 7.56 Hz), 4.24 (d, 4H, ArC*Hax*HeqAr, *J* = 14.32 Hz), 3.95 (t, 4H, ArOC*H*$_2$CH$_2$CH$_3$, *J* = 14.32 Hz), 3.44 (d, 4H, ArCHax*Heq*Ar, *J* = 14.32 Hz), 2.08–1.96 (sextet, 4H, ArOCH$_2$C*H*$_2$CH$_3$, *J* = 14.32 Hz), 1.27 (t, 6H, ArOCH$_2$CH$_2$C*H*$_3$, *J* = 14.32 Hz).

3.3.8. Synthesis of 5,17-dimethoxy-25,27-dipropoxy-26,28-dihydroxycalix[4]arene (4)

A 250 mL round bottomed flask flame dried and cooled under nitrogen was charged with a solution of **3** (3.22 g, 5.7 mmol) in dry methanol (80 mL) under an atmosphere of nitrogen. To this solution *p*-toluene sulfonic acid (PTSA) (0.074 g, 0.38 mmol) was added under stirring followed by the addition of trimethyl orthoformate (12.5 mL, 114.02 mmol) *via* syringe. The resulting mixture was then heated at reflux overnight with stirring. To the cooled reaction mixture saturated $NaHCO_3$(aq) (30 mL) was added with stirring. The resulting mixture was then extracted with dichloromethane (3 x 30 mL), washed with distilled water (3 x 30 mL) and brine (2 x 30 mL) followed by drying over magnesium sulphate, filtered and concentrated *in vacuo* to give an off white solid (3.2 g, 85 %) which was confirmed by ^{1}H NMR to be the desired 5,17-dimethoxy-25,27-dipropoxy-26,28-dihydroxycalix[4]arene. ^{1}H NMR (250 MHz, $CDCl_3$): δ 8.36 (s, 2H, O*H*), 7.05 (s, 4H, m-HOAr*H*(OCH$_3$)$_2$), 6.88 (d, 4H, *m*-PrOAr*H*, *J* = 7.36 Hz), 6.68 (t, 2H, *p*-PrOAr*H*, *J* = 7.36 Hz), 5.21 (s, 2H, *p*-HOAr*H*(OCH$_3$)$_2$) 4.24 (d, 4H, ArC*Hax*HeqAr, *J* = 12.80 Hz), 3.90 (t, 4H, ArOC*H*$_2$CH$_2$CH$_3$, *J* = 11.20 Hz), 3.33 (d, 4H, ArCHax*Heq*Ar, *J* = 12.80 Hz), 2.07–1.93 (sextet, 4H, ArOCH$_2$C*H*$_2$CH$_3$, *J* = 11.20 Hz), 1.25 (t, 6H, ArOCH$_2$CH$_2$C*H*$_3$, *J* = 11.20 Hz).

3.3.9. Synthesis of 5,17-diformyl-25,26,27,28-tetrapropoxycalix[4]arene (5)

Sodium hydride (60% in oil, 0.71 g, 29.7 mmol) was washed with dry hexane (2 x 5 mL) before the subsequent transferral of the oil-free solid in anhydrous *N,N'*-dimethylformamide (40 mL) to a 250 mL round bottomed flask flame dried and cooled under nitrogen to 0°C. **4** (1.95 g, 2.97 mmol) was added slowly over 10 min at 0°C and allowed to warm at room temperature. The suspension was stirred under nitrogen at room temperature for 30 minutes before the addition of *n*-propyl iodide (1.45 mL, 14.8 mmol) *via* syringe, and further stirred overnight at room temperature. The resultant mixture was subsequently cooled at 0°C and quenched with 1M(aq) HCl (30 mL) very slowly with stirring after which was allowed to warm to room temperature. The product was extracted with dichloromethane (3 x 40 mL) and the combined organic layers were washed with 1 M(aq) HCl (2 x 40 mL) and with saturated solution of sodium thiosulphate (2 x 30 mL). The product was washed with distilled water (3 x 40 mL) and brine (2 x 40 mL) followed by drying over magnesium sulphate, filtered and concentrated *in vacuo* to give a pale yellow solid (1.5 g, 78%) which was confirmed by ^{1}H NMR to be the desired 5,17-diformyl-25,26,27,28-tetrapropoxycalix[4]arene. ^{1}H NMR (250 MHz, $CDCl_3$): δ 9.39 (s, 2H, C*H*O), 6.93 (s, 4H, *m*-Ar*H*CHO), 6.71–6.62 (m, 6H, *p*-Ar*H*), 4.40 (d, 4H, ArC*Hax*HeqAr, *J* = 13.6 Hz), 3.85–3.78 (m, 8H, ArOC*H*$_2$CH$_2$CH$_3$), 3.16 (d, 4H, ArCHax*Heq*Ar, *J* = 13.6 Hz), 1.92–1.77 (m, 8H, ArOCH$_2$C*H*$_2$CH$_3$), 0.99–0.87 (m, 12H, ArOCH$_2$CH$_2$C*H*$_3$).

3.3.10. Synthesis of 25,26,27,28-tetrapropoxycalix[4]arene-5,17-dicarboxylic acid (H_2caldc)

To a stirred solution of **5** (0.623 g, 0.961 mmol) in 40 mL 1:1 acetone: chloroform at 0°C was added sulfamic acid (0.560 g, 5.77 mmol). After stirring for 30 minutes, sodium chlorite (0.522 g dissolved in 2 mL H_2O) was added rapidly, and the solution was allowed to warm to room temperature over 1 h. The organic solvents were removed under reduced pressure and 60 mL H_2O and 60 mL 1M(aq) HCl were added. The resulting mixture was extracted with 4 x 50 mL ethyl acetate. The combined organics were washed with 3 x 40 mL H_2O, 2 x 40 mL brine; dried over magnesium sulphate, filtered, and the solvent removed to give a pale yellow powder (0.625 g, 96%) which was confirmed by ^{1}H NMR to be the desired H_2caldc. ^{1}H NMR (250 MHz, $CDCl_3$): δ 12.89 (s, 2H, COO*H*), 7.11 (d, 4H, *m*-Ar*H*, *J* = 7.4 Hz), 6.96 (t, 2H, *p*-Ar*H*, *J* = 7.4 Hz), 6.69 (s, 4H, *m*-Ar*H*COOH), 4.35 (d,

4H, ArC*Hax*HeqAr, *J* = 13.6 Hz), 3.92 (t, 4H, ArOC*H*$_2$CH$_2$CH$_3$, *J* = 8.5 Hz), 3.59 (t, 4H, HOOCArOC*H*$_2$CH$_2$CH$_3$, *J* = 6.5 Hz), 3.08 (d, 4H, ArCHax*Heq*Ar, *J* = 13.6 Hz), 1.80 (m, 8H, ArOCH$_2$C*H*$_2$CH$_3$), 1.03 (t, 6H, ArOCH$_2$CH$_2$C*H*$_3$, *J* = 7.4 Hz), 0.79 (t, 6H, HOOCArOCH$_2$CH$_2$C*H*$_3$, *J* = 7.4 Hz). Found (calculated for $C_{42}H_{48}O_8$): C, 72.2 (74.09); H, 7.10 (7.11) %.

The TGA analysis of as-made H$_2$caldc (Figure 3-39) shows the loss of a small amount of included solvent followed by the decomposition of the organic framework which occurred around 360°C.

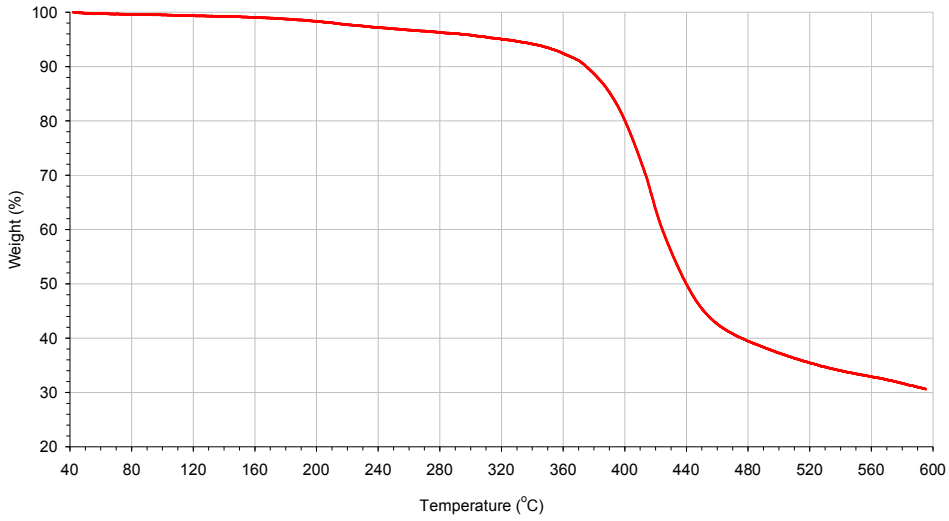

Figure 3-39. TGA trace for as-made H$_2$caldc.

3.3.11. Synthesis of (NMe$_2$H$_2$)$_2$caldc

Co(NO$_3$)$_2$·6H$_2$O (0.026 g, 0.088 mmol) and H$_2$caldc (0.120 g, 0.176 mmol) were dissolved in 20 cm^3 DMF. This solution (10 cm^3) was placed in a 30 cm^3 thick-walled glass vial and heated at 120°C for 2 days. Needle-shaped colourless crystals formed on cooling were separated by filtration, washed with DMF and air dried. Yield 0.014g (21 %). The PXRD pattern of the resultant material (Figure 3-40) matches the one simulated from the X-ray crystal structure of (NMe$_2$H$_2$)$_2$caldc.

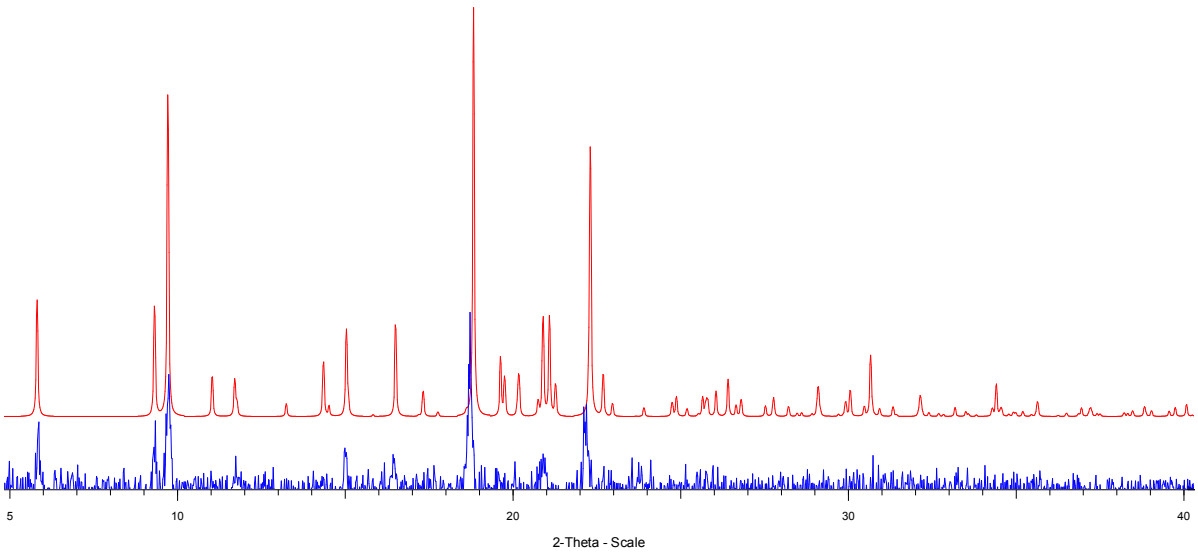

Figure 3-40. The PXRD pattern for $(NMe_2H_2)_2$caldc: experimental (bottom) and that simulated from the crystal structure (top).

Similar reactions carried out without $Co(NO_3)_2 \cdot 6H_2O$ did not produce any solid. H_2caldc has been heated at various temperatures in DMF of different ages and in DMF-water layered mixture but where crystals were formed these were identified to be the free acid by means of unit cell determinations. H_2caldc was solvothermal reacted with an excess of dimethylammonium chloride (Me_2NH_2Cl) in DMF but no solid was formed. It seems that the necessary reaction environment and amount of $Me_2NH_2^+$ cations to produce $(NMe_2H_2)_2$caldc are generated only by the presence of Co metal centres in the reaction mixture.

3.3.12. Synthesis of $Cu_2(caldc)_2(DMF)_2$

A solution of $Cu(NO_3)_2 \cdot 3H_2O$ (0.024 g, 0.10 mmol) in water (5 cm^3) was placed in a 30 cm^3 thick-walled glass vial. On top of this solution was carefully placed 5 cm^3 of DMF. H_2caldc (0.068 g, 0.10 mmol) dissolved in DMF (5 cm^3) was then carefully layered on top of the two layers. The vial was transferred to an oven and heated at 80°C for three days. The resultant turquoise powder was separated by filtration, washed with DMF and air-dried. Yield 0.074 g, (91 %). Found (calculated for $Cu_2(caldc)_2(DMF)_2$): C, 63.20 (66.28); H, 6.36 (6.55); N, 2.08 (1.72) %. The higher percentage found for nitrogen suggests the presence of more than two DMF molecules crystallographically found. This is in agreement with the remaining electron density, which can be attributed to the presence of a

small amount of diffuse DMF. The PXRD pattern of the resultant turquoise powder (Figure 3-41) matches the one simulated from the X-ray crystal structure.

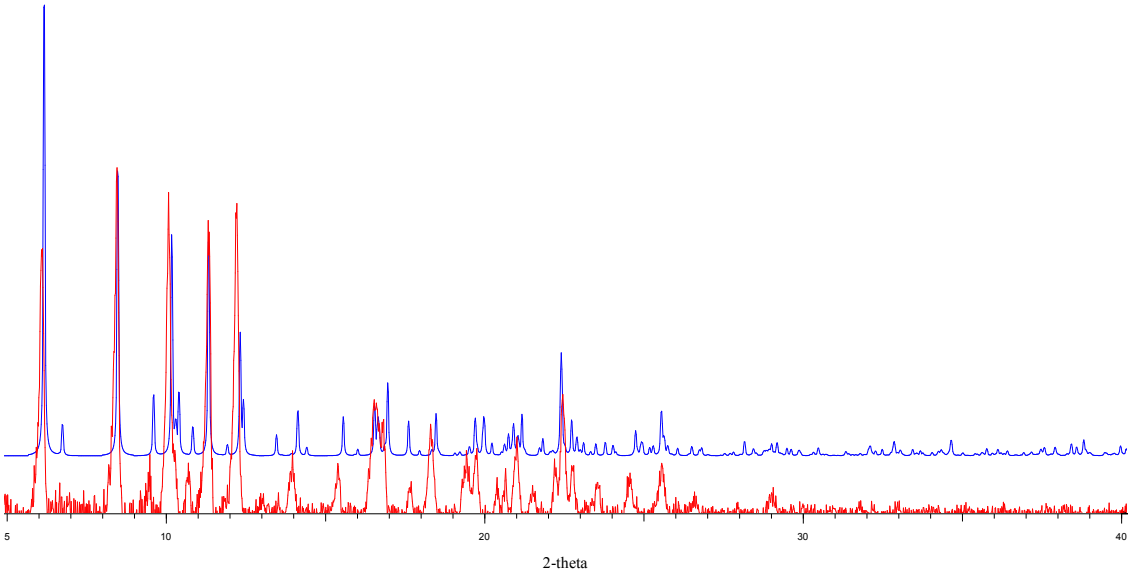

Figure 3-41. The PXRD pattern for $Cu_2(caldc)_2(DMF)_2$: experimental (bottom) and that simulated from the crystal structure (top).

PXRD investigations revealed that $Cu_2(caldc)_2(DMF)_2$ can be formed from similar reaction mixtures when using $CuCl_2$ or $Cu(SO_4)_2{\cdot}5H_2O$ instead of $Cu(NO_3)_2{\cdot}3H_2O$, though the product in this case was not phase-pure. Actually by reacting H_2caldc with $Cu(SO_4)_2{\cdot}5H_2O$ two new structures with no included $caldc^{2-}$ anions as revealed by means of single X-ray crystallography were collected which opened up further investigation reported in Chapter 5 of this thesis.

The presence of water plays an important role in $Cu_2(caldc)_2(DMF)_2$ formation even though water is not contained in the resultant structure. When no water was used in the synthesis no solid had been formed even after prolonged heating at 80°C or at higher temperatures.

3.3.13. Synthesis of $Cu_2(caldc)_2(DMF)_2$ using microwaves

A layer of DMF (2.5 cm^3) was carefully placed on top of a solution of $Cu(NO_3)_2{\cdot}3H_2O$ (0.012 g, 0.05 mmol) in water (2.5 cm^3). H_2caldc (0.034 g, 0.05 mmol) dissolved in DMF (2.5 cm^3) was then carefully placed on top of the DMF layer. The solutions were layered in a 30 cm^3 microwave vial which was then sealed with a septum and placed in the

microwave reactor. The two layered solutions were carefully manipulated with the minimum disturbance and no magnetic stirrer was added to the reaction mixture. After 1 hour heated at 100°C under microwave irradiation a turquoise powder was obtained. This was then separated by filtration, washed with DMF and air-dried. Yield 0.023 g, (57 %). The PXRD pattern of the resultant turquoise powder (Figure 3-42) matches the experimental PXRD pattern for $Cu_2(caldc)_2(DMF)_2$ suggesting that $Cu_2(caldc)_2(DMF)_2$ can be obtained in 1 hour under microwave irradiation.

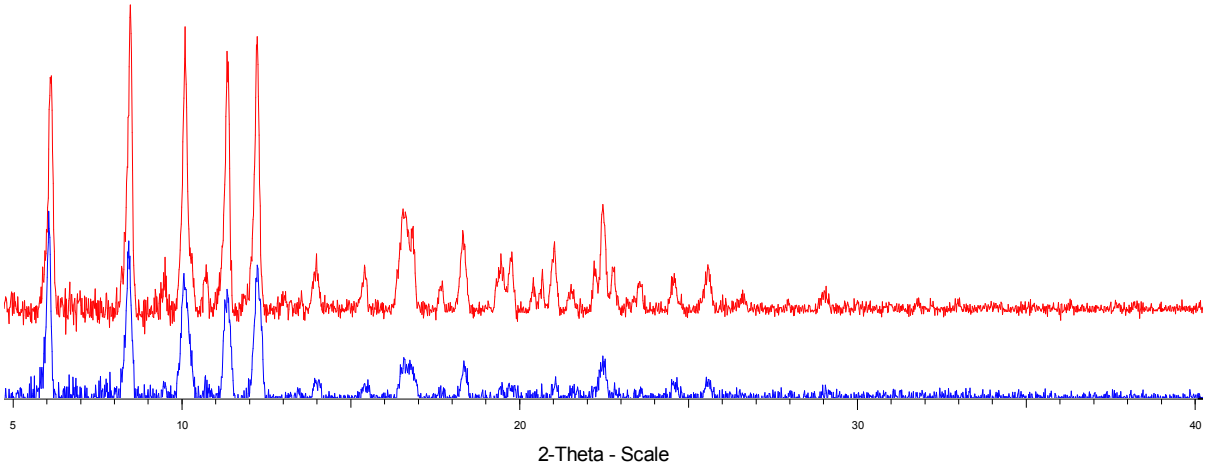

Figure 3-42. The experimental PXRD patterns of $Cu_2(caldc)_2(DMF)_2$: obtained by microwave irradiation (bottom) compared with that obtained by solvothermal reaction (top).

3.3.14. Synthesis of $Zn_2(caldc)_2(DMF)_2$

A solution of H_2caldc (0.012 g, 0.018 mmol) and $Zn(OAc)_2 \cdot 2H_2O$ (0.002 g, 0.009 mmol) in DMF (2 cm^3) was carefully placed on top of a layer of deionised water (1 cm^3) in a 10 cm^3 thick-walled glass vial. The vial was transferred to an oven and heated at 90°C for three days. The resultant small colourless crystals were separated by filtration, washed with DMF and air-dried. Yield 0.007g, (95%). The PXRD pattern (Figure 3-43) of the resultant material matches that of $Cu_2(caldc)_2(DMF)_2$ which suggests that a $Zn_2(caldc)_2(DMF)_2$ isostructural with $Cu_2(caldc)_2(DMF)_2$ has resulted. Found (calculated for $Zn_2(caldc)_2(DMF)_2$): C, 60.20 (66.13); H, 5.91 (6.54); N, 1.13 (1.71) %. It was observed that [$Zn_2(caldc)_2(DMF)_2$] formation is quite sensitive to reaction conditions and a slight change of reagents concentration or a 10°C lower reaction temperature affects the purity of $Zn_2(caldc)_2(DMF)_2$ obtained.

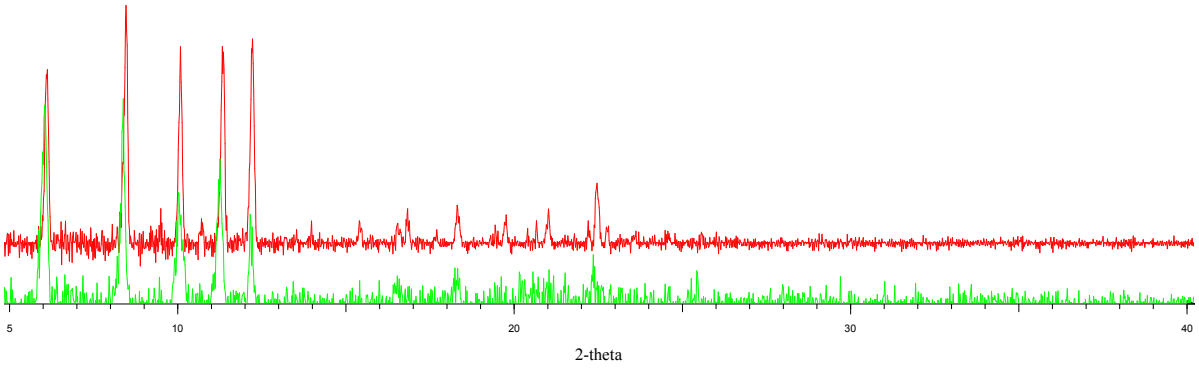

Figure 3-43. The experimental PXRD patterns for $Zn_2(caldc)_2(DMF)_2$ (bottom) and $Cu_2(caldc)_2(DMF)_2$ (top).

3.3.15. Synthesis of $Co_2(caldc)_2(DMF)_2$

A solution of $Co(NO_3)_2 \cdot 6H_2O$ (0.003 g, 0.009 mmol) and H_2caldc (0.012 g, 0.018 mmol) in DMF (2 cm^3) was carefully layered onto deionised water (1 cm^3) in a 10 cm^3 thick-walled glass vial and the mixture heated at 90°C for three days. The resultant blue, block-shaped crystals were separated by filtration, washed with DMF and air-dried. Yield 0.005 g (69 %). The PXRD analysis (Figure 3-44) revealed this product to be isostructural to $Cu_2(caldc)_2(DMF)_2$.

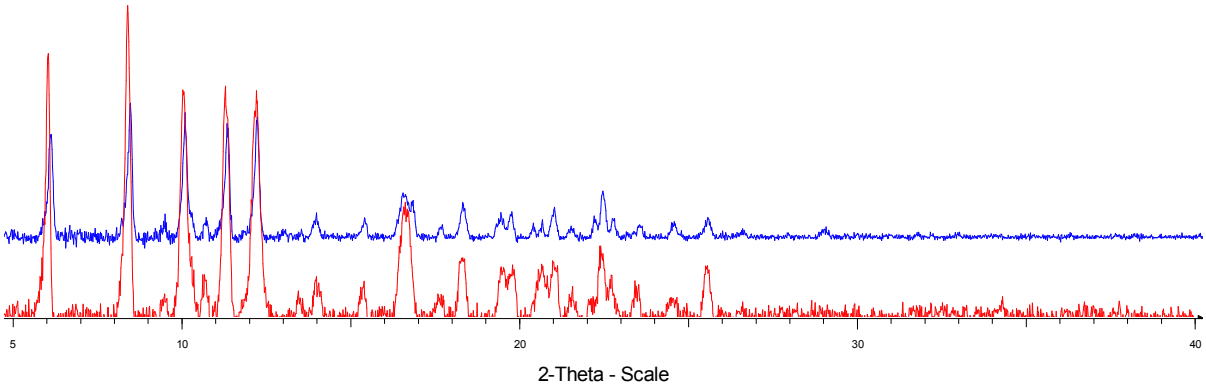

Figure 3-44. The experimental PXRD patterns for $Co_2(caldc)_2(DMF)_2$ (bottom) and $Cu_2(caldc)_2(DMF)_2$ (top).

3.3.16. Synthesis of $[Cd_2(caldc)_2(DMF)_2] \cdot 3DMF$

In a 30 cm^3 thick-walled glass vial, a layer of DMF (3 cm^3) was carefully added on top of a layer of deionised water (3 cm^3). A solution containing $Cd(NO_3)_2 \cdot 4H_2O$ (0.031 g, 0.10

mmol) and H_2caldc (0.068 g, 0.10 mmol) in DMF (10 cm^3) was carefully layered using a syringe on top of the DMF/water layers and the vial was capped with a lid. The mixture was heated in an oven at 80°C for three days. The resulting colourless needle-shaped crystals were separated by filtration, washed with DMF and air-dried. Yield 0.043 g (45 %). The PXRD pattern of the resultant material (Figure 3-45) matches the pattern simulated from the single X-ray diffraction data of $[Cd_2(caldc)_2(DMF)_2]\cdot 3DMF$ indicating that the crystal picked for single X-ray collection is representative of the whole sample. Found (calculated for $[Cd_2(caldc)_2(DMF)_2]\cdot 3DMF$): C, 59.70 (61.04); H, 5.30 (6.57); N, 2.73 (3.59) %.

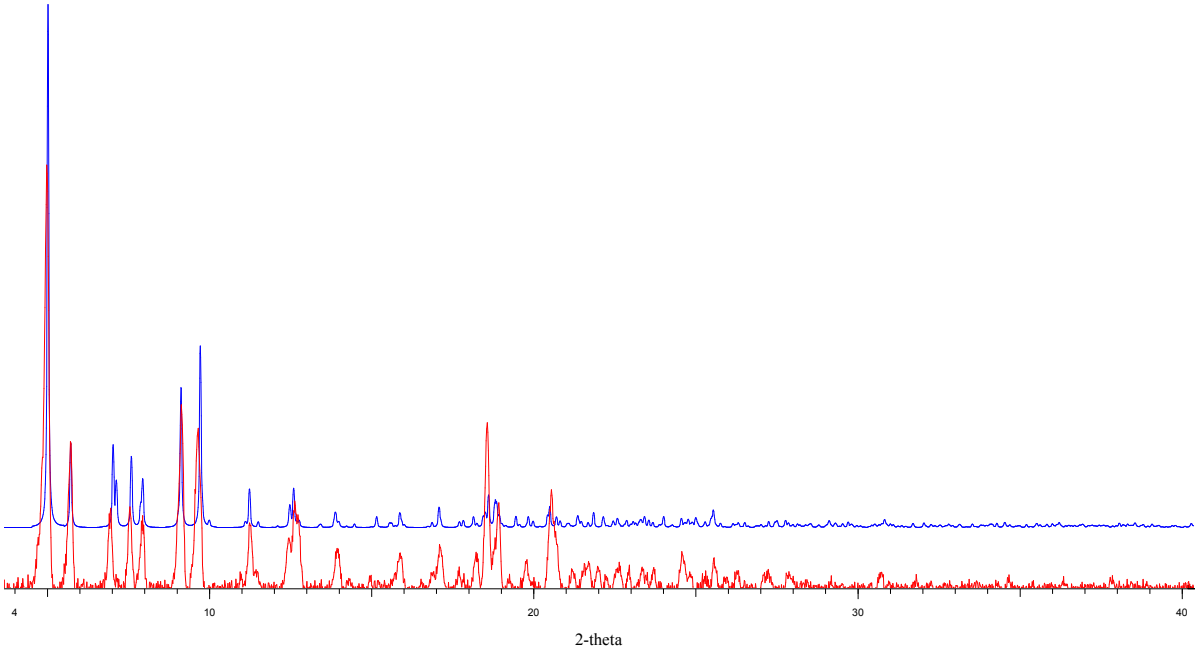

Figure 3-45. The experimental PXRD pattern for $[Cd_2(caldc)_2(DMF)_2]\cdot 3DMF$ (bottom) and that simulated from the crystal structure (top).

The layer of water plays an important role in $[Cd_2(caldc)_2(DMF)_2]\cdot 3DMF$ formation even though no water molecules are contained in the resultant structure. Without its presence no solid had been formed even when heated at 80°C for longer than the required synthesis time and further heated at 95°C for 5 days.

3.3.17. Synthesis of $[Co_5(caldc)_4(OH)_2(H_2O)_4]\cdot 8DMF$

$Co(NO_3)_2\cdot 6H_2O$ (0.013 g, 0.044 mmol) and H_2caldc (0.060 g, 0.088 mmol) were dissolved in DMF (10 cm^3). 2 cm^3 of this solution was carefully layered onto deionised water (1 cm^3) in a 10 cm^3 thick-walled glass vial. The vial was transferred to an oven and heated at 90°C

for 3 days. From the resultant mixture of white material and purple crystals, based on difference in density, purple block-shaped crystals were separated and analysed by single X-Ray crystallography. The PXRD analysis of the resultant mixture (Figure 3-46) revealed that $[Co_5(caldc)_4(OH)_2(H_2O)_4]\cdot 8DMF$ is the major product and further work will be necessary in order to obtain this MOF as phase pure.

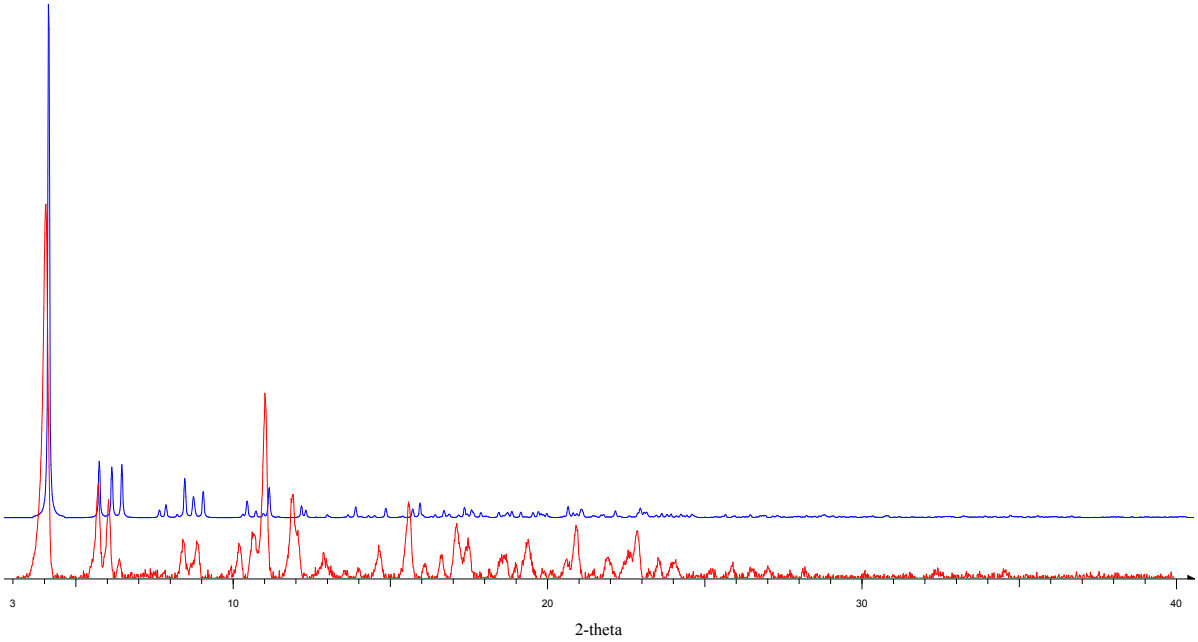

Figure 3-46. The experimental PXRD pattern for $[Co_5(caldc)_4(OH)_2(H_2O)_4]\cdot 8DMF$ (bottom) and that simulated from the crystal structure (top).

Similar results were obtained when 10 cm^3 solution made of $Co(NO_3)_2\cdot 6H_2O$ (0.026 g, 0.088 mmol) and H_2caldc (0.060 g, 0.088 mmol) in DMF (20 cm^3), was placed on top of a layer of deionised water (5 cm^3) and heated at 95°C for 3 days.

3.4. Summary and Future work

H_2caldc has been synthesised using a seven-step procedure and its incorporation as a ligand in MOFs further investigated.

Five new MOFs based on caldc linker, containing copper, zinc, cobalt and cadmium have been synthesised and characterised. The compounds $Cu_2(caldc)_2(DMF)_2$, $Zn_2(caldc)_2(DMF)_2$, $[Cd_2(caldc)_2(DMF)_2]\cdot 3DMF$, $[Co_5(caldc)_4(OH)_2(H_2O)_4]\cdot 8DMF$ and $Co_2(caldc)_2(DMF)_2$ were prepared from the reactions of the appropriate metal(II) salts with H_2caldc in DMF under solvothermal conditions. The synthesis of these MOFs was shown

to be challenging, and a layering method was adopted in order to obtain crystals suitable for X-ray diffraction. The presence of a layer of water in the reaction mixtures was found to play a major role in these MOF formations, without being present in the structure of the resultant compound. The $Cu_2(caldc)_2(DMF)_2$ was also successfully synthesised in a shorter time by using microwaves.

Compounds $Cu_2(caldc)_2(DMF)_2$, $[Cd_2(caldc)_2(DMF)_2]\cdot 3DMF$ and $[Co_5(caldc)_4(OH)_2(H_2O)_4]\cdot 8DMF$ were characterised by single crystal X-ray crystallography, whereas $Zn_2(caldc)_2(DMF)_2$ and $Co_2(caldc)_2(DMF)_2$ were shown by powder X-ray diffraction to be isomorphous with $Cu_2(caldc)_2(DMF)_2$. The $M_2(caldc)_2(DMF)_2$ (M = Cu, Zn and Co) isostructural series is among other few isostructural paddle-wheel based MOFs series containing different metals such as $M_2(1,4\text{-}bdc)_2(dabco)$ (M = Zn[38], Cu[39] and Co[40]). $Cu_2(caldc)_2(DMF)_2$ and $[Co_5(caldc)_4(OH)_2(H_2O)_4]\cdot 8DMF$ were shown to form 2-D network structures whereas $[Cd_2(caldc)_2(DMF)_2]\cdot 3DMF$ extends into a 3-D network structure. The caldc dianion adopts a closed pinched cone conformation, similar to that observed in the H_2caldc free acid[28], in all three structurally characterized calix[4]arene-based carboxylate MOFs, and in $[Co_5(caldc)_4(OH)_2(H_2O)_4]\cdot 8DMF$ it also adopts the open pinched cone conformation.

Thermogravimetric analyses (TGA) for $Cu_2(caldc)_2(DMF)_2$ and $[Cd_2(caldc)_2(DMF)_2]\cdot 3DMF$ revealed the stability of their frameworks at high temperatures similar with that of the H_2caldc linker.

The combined TGA and PXRD analysis of these MOFs on the removal of solvent molecules suggested that the DMF solvent molecules can be completely expelled from $Cu_2(caldc)_2(DMF)_2$ leaving the framework intact. $[Cd_2(caldc)_2(DMF)_2]\cdot 3DMF$ showed though a very poor crystallinity on the partial removal of DMF solvent molecules. Attempts to desolvate $[Cd_2(caldc)_2(DMF)_2]\cdot 3DMF$ by exchanging the DMF solvent molecules with MeOH or CH_2Cl_2 were resulted in collapse of the framework as was showed by the PXRD patterns. Therefore the full desolvation of $[Cd_2(caldc)_2(DMF)_2]\cdot 3DMF$ without framework collapsing was not achieved.

Molecular simulations for $[Cu_2(caldc)_2(DMF)_2]$, $[Cd_2(caldc)_2(DMF)_2]\cdot 3DMF$, $[Co_5(caldc)_4(OH)_2(H_2O)_4]\cdot 8DMF$ confirmed the presence of small pores within the

frameworks and revealed their high selectivity of CH_4 over H_2, with much higher selectivities compared to other MOFs in the literature. Remarkably, it was shown that extra voids created by calix[4]arene-based linkers, were accessible to only hydrogen molecules. These results could in principle be exploited further for separations and suggest that such networks are likely to display interesting selectivity to guest molecules.

Single crystal X-ray analysis revealed that solvothermal reaction of H_2caldc and $Co(NO_3)_2 \cdot 6H_2O$ in DMF produces the dimer $(NMe_2H_2)_2$caldc. Our investigations showed that the presence of Co^{2+} in the reaction mixture is essential for the formation of this dimer.

Changing the solvent system, adding neutral bridging co-ligands in order to prevent the formation of structures with coordinated DMF ligands and using more rigid calixarene ligands can be further investigated. An example of a rigid calix[4]arene diacid is the 1,3-monobridged calix[4]arene diacid (Figure 3-47) reported by Pochini *et al.*[31], where the interconversion between the two pinched cone conformations is inhibited.

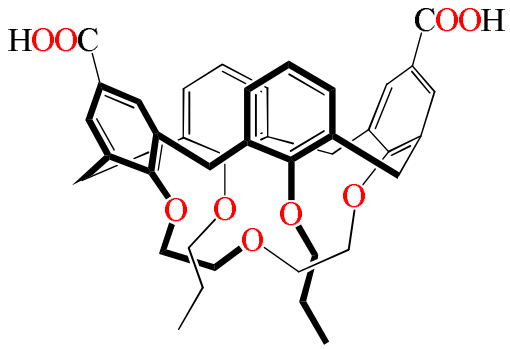

Figure 3-47. 25,27-(crown-3)-26,28-dipropoxycalix[4]arene-11,23-dicarboxylic acid.

3.5. References

[1] J. Vicens, V. Böhmer, *Calixarenes : a versatile class of macrocyclic compounds*, Springer, **1990**.

[2] C. D. Gutsche, *Calixarenes: Monographs in Supramolecular Chemistry*, 2nd ed., The Royal Society of Chemistry, Cambridge, **2008**.

[3] J. W. Cornforth, P. D. A. Hart, G. A. Nicholls, R. J. W. Rees, J. A. Stock, *British Journal of Pharmacology and Chemotherapy* **1955**, *10*, 73.

[4] C. D. Gutsche, B. Dhawan, J. A. Levine, K. Hyun No, L. J. Bauer, *Tetrahedron* **1983**, *39*, 409.

[5] G. D. Andreetti, R. Ungaro, A. Pochini, *Journal of the Chemical Society, Chemical Communications* **1979**, 1005.

[6] G. D. Andreetti, A. Pochini, R. Ungaro, *Journal of the Chemical Society, Perkin Transactions 2* **1983**, 1773.

[7] A. G. S. Hoegberg, *Journal of the American Chemical Society* **1980**, *102*, 6046.

[8] K. Araki, K. Iwamoto, S. Shinkai, T. Matsuda, *Chemistry Letters* **1989**, *18*, 1747.

[9] K. Iwamoto, K. Araki, S. Shinkai, *J. Org. Chem.* **1991**, *56*, 4955.

[10] S. Shinkai, *Tetrahedron* **1993**, *49*, 8933.

[11] S. J. Dalgarno, M. J. Hardie, C. L. Raston, *Crystal Growth & Design* **2004**, *4*, 227.

[12] W. Liao, C. Liu, X. Wang, G. Zhu, X. Zhao, H. Zhang, *CrystEngComm* **2009**, *11*, 2282.

[13] S. J. Dalgarno, M. J. Hardie, J. L. Atwood, C. L. Raston, *Inorganic Chemistry* **2004**, *43*, 6351.

[14] Y. Liu, W. Liao, Y. Bi, X. Wang, H. Zhang, *Crystal Growth & Design* **2009**, *9*, 5311.

[15] J. Olguína, A. Castilloa, V. Gómez-Vidalesa, S. Hernández-Ortegaa, R. A. Toscanoa, E. Muñozb, I. Castilloa, *Supramol. Chem.* **2009**, *21*, 502.

[16] B. Chen, D. Yuan, M. Wu, F. Jiang, M. Hong, *Z. Anorg. Allg. Chem.* **2009**, *635*, 1669.

[17] C. D. Gutsche, *Calixarenes: Monographs in Supramolecular Chemistry*, The Royal Society of Chemistry, Cambridge, **1989**.

[18] J. L. Atwood, L. J. Barbour, A. Jerga, *Science* **2002**, *296*, 2367.

[19] G. S. Ananchenko, I. L. Moudrakovski, A. W. Coleman, J. A. Ripmeester, *Angewandte Chemie International Edition* **2008**, *47*, 5616.

[20] O. Surov, N. Mamardashvili, G. Shaposhnikov, O. Koifman, *Russ. J. Phys. Chem. A* **2007**, *81*, 1936.

[21] S. Kennedy, G. Karotsis, C. M. Beavers, S. J. Teat, E. K. Brechin, S. J. Dalgarno, *Angewandte Chemie International Edition* **2010**, *49*, 4205.

[22] S. Kennedy, S. J. Teat, S. J. Dalgarno, *Dalton Trans.* **2010**, *39*, 384.

[23] Y.-J. Liu, J.-S. Huang, S. S.-Y. Chui, C.-H. Li, J.-L. Zuo, N. Zhu, C.-M. Che, *Inorganic Chemistry* **2008**, *47*, 11514.

[24] C. Redshaw, O. Rowe, D. L. Hughes, A.-M. Fuller, I. A. Ibarra, S. M. Humphrey, *Dalton Transactions* **2013**, *42*, 1983.

[25] L. V. Tsymbal, Y. D. Lampeka, V. I. Boyko, V. I. Kalchenko, S. V. Shishkina, O. V. Shishkin, *CrystEngComm* **2014**, *16*, 3707.

[26] T. Harada, J. M. RudziÇ¹ski, E. ÅŒsawa, S. Shinkai, *Tetrahedron* **1993**, *49*, 5941.

[27] P. D. J. Grootenhuis, P. A. Kollman, L. C. Groenen, D. N. Reinhoudt, G. J. Van Hummel, F. Ugozzoli, G. D. Andreetti, *Journal of the American Chemical Society* **1990**, *112*, 4165.

[28] H. Miyaji, M. Dudic, J. H. R. Tucker, I. Prokes, M. E. Light, T. Gelbrich, M. B. Hursthouse, I. Stibor, P. Lhoták, L. Brammer, *Supramolecular Chemistry* **2003**, *15*, 385.

[29] W. Verboom, S. Datta, Z. Asfari, S. Harkema, D. N. Reinhoudt, *J. Org. Chem.* **1992**, *57*, 5394.

[30] B. R. Travis, M. Sivakumar, G. O. Hollist, B. Borhan, *Organic Letters* **2003**, *5*, 1031.

[31] A. Arduini, M. Fabbi, M. Mantovani, L. Mirone, A. Pochini, A. Secchi, R. Ungaro, *J. Org. Chem.* **1995**, *60*, 1454.

[32] J. Juillard, in *Recommended methods for purification of solvents and tests for impurities* (Ed.: J.F.Coetzee), Pergamon Press, Oxford, **1982**, pp. 32.

[33] A. D. Burrows, K. Cassar, R. M. W. Friend, M. F. Mahon, S. P. Rigby, J. E. Warren, *CrystEngComm* **2005**, *7*, 548.

[34] J. Zhang, X. Bu, *Chemical Communications* **2008**, 444.

[35] D. N. Dybtsev, M. P. Yutkin, E. V. Peresypkina, A. V. Virovets, C. Serre, G. Férey, V. P. Fedin, *Inorganic Chemistry* **2007**, *46*, 6843.

[36] A. L. Spek, University of Utrecht, **1999**.

[37] K. Schlichte, T. Kratzke, S. Kaskel, *Microporous and Mesoporous Materials* **2004**, *73*, 81.

[38] K. Kim, D. N. Dybtsev, H. Chun, *Angewandte Chemie International Edition* **2004**, *43*, 5033.

[39] K. Seki, W. Mori, *The Journal of Physical Chemistry B* **2002**, *106*, 1380.

[40] L.-G. Zhu, H.-P. Xiao, *Z. Anorg. Allg. Chem.* **2008**, *634*, 845.

[41] S. Gorbunov, T. Denisova, E. Amel'chenkova, S. Nefedov, *Russian Journal of Inorganic Chemistry* **2006**, *51*, 1581.

[42] Z. R. Herm, R. Krishna, J. R. Long, *Microporous and Mesoporous Materials* **2012**, *151*, 481.

[43] D. Wu, C. Wang, B. Liu, D. Liu, Q. Yang, C. Zhong, *AIChE Journal* **2012**, *58*, 2078.

[44] P. Z. Moghadam, PhD thesis, The University of Edinburgh **2012**.

[45] J. A. Ripmeester, G. D. Enright, C. I. Ratcliffe, K. A. Udachin, I. L. Moudrakovski, *Chemical Communications* **2006**, 4986.

[46] S. Brunauer, P. H. Emmett, E. Teller, *Journal of the American Chemical Society* **1938**, *60*, 309.

[47] T. Düren, Y.-S. Bae, R. Q. Snurr, *Chemical Society Reviews* **2009**, *38*, 1237.

[48] T. Düren, F. Millange, G. Férey, K. S. Walton, R. Q. Snurr, *Journal of Physical Chemistry C* **2007**, *111*, 15350.

[49] S. P. Bew, A. D. Burrows, T. Duren, M. F. Mahon, P. Z. Moghadam, V. M. Sebestyen, S. Thurston, *Chemical Communications* **2012**, *48*, 4824.

[50] Q. Yang, C. Zhong, *J. Phys. Chem. B* **2006**, *110*, 17776.

[51] S. Keskin, *J. Phys. Chem. C* **2011**, *115*, 800.

[52] J. Liu, J. Johnson, *J. Low. Temp. Phys.* **2009**, *157*, 268.

[53] F. Sansone, S. Barboso, A. Casnati, M. Fabbi, A. Pochini, F. Ugozzoli, R. Ungaro, *Eur. J. Org. Chem.* **1998**, *1998*, 897.

[54] W. Kraus, G. Nolze, Federal Institute for Materials Research and Testing Rudower Chaussee 5, Berlin, Germany, **1999**.

[55] V. Boehmer, K. Jung, M. Schoen, A. Wolff, *J. Org. Chem.* **1992**, *57*, 790.

[56] G. Sheldrick, *Acta Cryst. A* **2008**, *64*, 112.

[57] L. D. Gelb, K. E. Gubbins, *Langmuir* **1999**, *15*, 305.

[58] L. Sarkisov, A. Harrison, *Molecular Simulation* **2011**, *37*, 1248.

[59] D. Frenkel, B. Smit, *Understanding molecular simulation: from algorithms to applications*, Academic Press, **2002**.

[60] D. Dubbeldam, S. Calero, D. E. Ellis, R. Q. Snurr, Northwestern University, Evanston, IL, **2008**.

[61] S. L. Mayo, B. D. Olafson, W. A. Goddard, *The Journal of Physical Chemistry* **1990**, *94*, 8897.

[62] A. K. Rappe, C. J. Casewit, K. S. Colwell, W. A. Goddard, W. M. Skiff, *Journal of the American Chemical Society* **1992**, *114*, 10024.

[63] S. J. Goodbody, K. Watanabe, D. MacGowan, J. P. R. B. Walton, N. Quirke, *J. Chem. Soc., Faraday Trans.* **1991**, *87*, 1951.

[64] Q. Yang, C. Zhong, *J. Phys. Chem. B* **2005**, *109*, 11862.

Chapter 4. A Molybdenum *para*-xylylenediphosphonate framework

4.1. Introduction

By far the most studied MOFs are those based on carboxylates, but "non-carboxylate" analogues[1-4] as zeolitic imidazolate frameworks (ZIFs)[1, 4], phosphonate-based MOFs[1-3] and sulfonate-based MOFs[1, 2] also show promising properties.

Phosphonate ligands have been extensively used in fundamental research but they have also found uses in industry, such as water treatment, oilfield drilling, minerals processing, corrosion control[5], metal complexation and sequestration, dental materials, enzyme inhibition, bone targeting[6] and cancer treatment.

Phosphonic acids (Figure 4-1) are derivatives of phosphoric acid in which one of the hydroxyl groups is replaced by an organic substituent(R). The phosphorus atom present in the phosphonic group is in the +5 oxidation state and the geometry of the group is approximately tetrahedral.

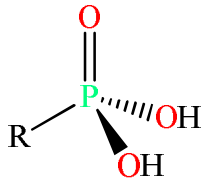

Figure 4-1. General structure of a phosphonic acid.

Demadis and Stavgianoudaki[7] outlined the similarities and differences between phosphonates and carboxylates. The phosphonic acids can be doubly deprotonated in two well defined successive steps, depending on solution pH, while the carboxylic acids can only be deprotonated once (Figure 4-2). This allows access to a variety of potential new phosphonate-based structures by simply varying the pH. In terms of bonds strength, the M–O_3PR bond is stronger than M–O_2CR bonds in carboxylate MOFs and stronger than M–NR bonds in ZIFs. This translates into higher thermal and chemical stabilities for phosphonate-based MOFs making them potentially valuable materials.

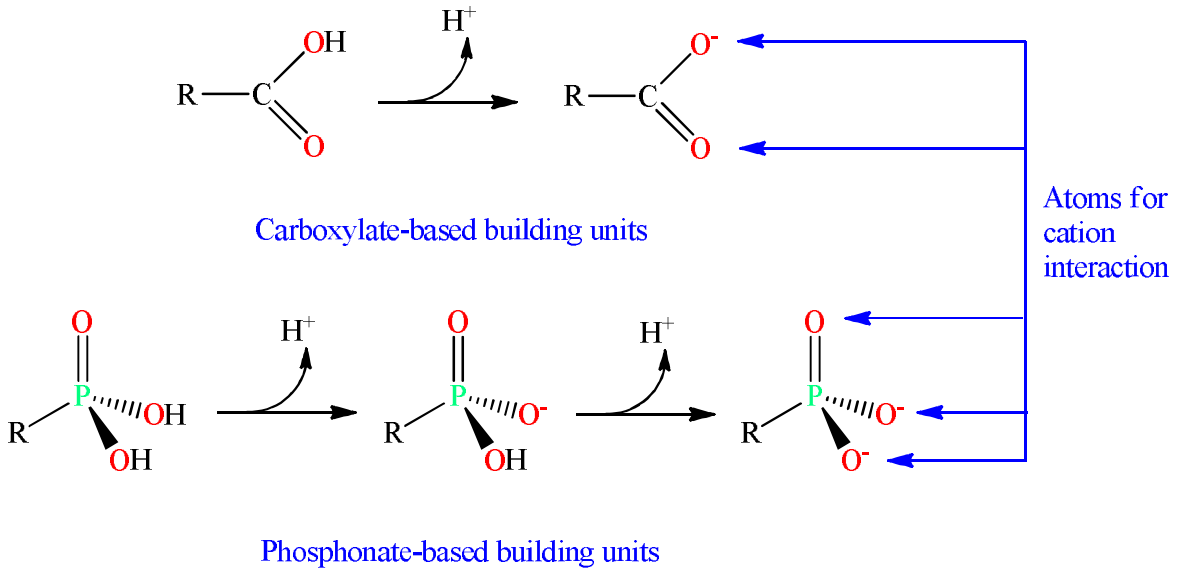

Figure 4-2. Carboxylic and phosphonic acids.[7]

Phosphonate groups possess three oxygen atoms compared to the two in carboxylates which increases the chances of obtaining a higher variety of phosphonate-based structures. On the other hand, the presence of three oxygen atoms in the phosphonate ligand can lead to more condensed structures, which makes it difficult to obtain porous phosphonate-based MOFs.

Since the pioneering work of Clearfield[8], the interest in metal phosphonate chemistry has accelerated, but mainly for the synthesis of low-dimensional compounds based on di-, tri- and tetravalent cations. Single crystals of these kind of compounds are not easy to synthesize and their structures are generally solved by powder X-ray diffraction.

Among metal organophosphonates, metal-organodiphosphonates are very common in the recent literature[9-11]. The prototypical metal-organodiphosphonate has the general formula $M_x[O_3P(\text{organic spacer})PO_3]_y$.

para-Xylylenediphosphonate (xdp^{4-}) is a good example of flexible ditopic ligand which (-CH_2-P-) can adopt cis or trans conformations with respect to benzene ring as shown in Figure 3.

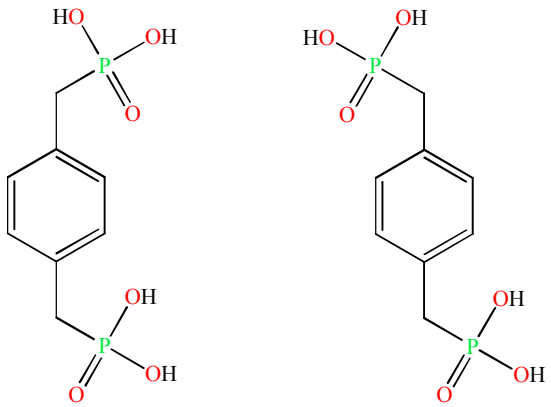

Figure 4-3. p-Xylylenediphosphonic acid (H_4xdp) showing the two possible conformations.

H_4xdp adopts a rare cis conformation in the crystal structure of two isostructural cobalt and nickel phosphonates $[M^{II}(2,2'\text{-bipy})_2(H_4xdp)]\cdot[H_2xdp]$, (2,2′-bipy = 2,2′-bipyridine)[12]. The compounds consist of 1-D $[M^{II}(2,2'\text{-bipy})_2(H_4xdp)]^{2+}$ chains and H_2xdp^{2-} anions in which H_4xdp adopts a cis conformation during its coordination to the metal centre. The corresponding trans conformation is observed in the anionic form H_2xdp^{2-}.

Attempts to obtain 3-D metal phosphonates have been rather scarce, but a few groups reached this goal by using bis(phosphonic acids) which act as pillars between the layers[13-15]. The majority of metal phosphonates, based on H_4xdp structures consist of typical (M_xO_3P) layers separated by organic spacers. The first lanthanide-organic frameworks based on H_4xdp were reported by Shi *et al.*[16] who prepared [Ln(Hxdp)(H_2O)] (Ln = Ce, Pr). They also reported the X-ray single crystal structure for H_4xdp. The Stock group investigated metal diphosphonates using H_4xdp and the corresponding tetraethyl *p*-xylylenediphosphonate as starting materials. These studies led to the diphosphonates $[M^{II}_2(xdp)]\cdot 2H_2O$ (M = Mn, Ni, Cd)[17], $Pb_2(xdp)$[18], $Sn_2(xdp)$[19], and $[Cu_2(xdp)]\cdot 2H_2O$[20]. $[V^{IV}O(H_2O)(H_2xdp)]$ (MIL-40)[21] is a 2-D MOF built up from VO^{2+} vanadyl groups and xdp units and $[(Cu^{II}(H_2O))_2xdp]$ (MIL-29)[20] both reported by Férey group. Network structures have also been prepared with other metals, including gallium(III).[22]

Molybdophosphonates as building blocks or subunits in extended structures have been reported previously.[10, 23, 24] For example, 1-D, 2-D, and 3-D materials constructed from

molybdophosphonate subunits linked through binuclear copper tetra-2-pyridylpyrazine groups have been reported by Burkholder *et al*.[24] However, there are no reports of diphosphonates containing just molybdenum.

H_4xdp was chosen for investigation as the organic bridging linker, based on the following considerations: (a) it is tetrabasic and can be successively deprotonated to generate H_3xdp^-, H_2xdp^{2-}, $Hxdp^{3-}$, xdp^{4-} depending on the pH level, and hence may supply four different valence anions; (b) it is a good example of a flexible ditopic ligand.

4.2. Results and discussion

The investigation into the use of *para*-xylylenediphosphonic acid (H_4xdp) to obtain mixed-metal MOFs was initiated by Dr. Ayi A. Ayi from Department of Pure and Applied Chemistry, University of Calabar, Nigeria, during his fellowship at the University of Bath. During these studies a new structure containing *para*-xylylenediphosphonate (xdp^{4-}) was obtained serendipitously as revealed by a single crystal X-ray analysis. It is a molybdenum *para*-xylylenediphosphonate MOF with formula $[(MoO_2)_2(xdp)(H_2O)_2]\cdot 2H_2O$. The structure of $[(MoO_2)_2(xdp)(H_2O)_2]\cdot 2H_2O$ is discussed below. The synthesis of $[(MoO_2)_2(xdp)(H_2O)_2]\cdot 2H_2O$ has been developed in this work and it has been obtained more logically by the hydrothermal reaction of sodium molybdate(VI) dihydrate ($Na_2MoO_4\cdot 2H_2O$), *para*-xylylenediphosphonic acid (H_4xdp) in the presence of hydrochloric acid.

Studies on dehydration and rehydration of $[(MoO_2)_2(xdp)(H_2O)_2]\cdot 2H_2O$ have been performed and they are detailed below. Moreover the behaviour of fully dehydrated MOF when in contact with guest molecules as methanol and ethanol has been investigated. $[(MoO_2)_2(xdp)(H_2O)_2]\cdot 2H_2O$ has been characterised through thermogravimetric analysis (TGA), powder X-ray diffraction (PXRD), infrared spectroscopy, CHN analysis and ^1H and ^{31}P NMR spectroscopy of the digested product.

4.2.1. Structure of $[(MoO_2)_2(xdp)(H_2O)_2]\cdot 2H_2O$

Colourless needle-like crystals of suitable size for X-ray single diffraction were collected from the hydrothermal reaction of sodium molybdate(VI) dihydrate ($Na_2MoO_4\cdot 2H_2O$) and *para*-xylylenediphosphonic acid (H_4xdp) in the presence of HCl. The crystal data and refinement parameters for $[(MoO_2)_2(xdp)(H_2O)_2]\cdot 2H_2O$ are given in Table 4-1.

Table 4-1. Crystallographic data and refinement parameters for $[(MoO_2)_2(xdp)(H_2O)_2]\cdot 2H_2O$.

Empirical formula	$Mo_2O_{14}P_2C_8H_{16}$	
Formula weight	590.02	
Temperature	150(2) K	
Wavelength	0.71073 Å	
Crystal system	Monoclinic	
Space group; Z	*C*2/*c*; 4	
Unit cell dimensions	a = 20.8424(8) Å	$\alpha = 90^o$
	b = 10.6114(3) Å	β = 111.686(4)°
	c = 9.0023(4) Å	γ = 90°
Volume	1850.09(12) $Å^3$	
Density (calculated)	2.118 g/cm^3	
Crystal size	0.18 x 0.05 x 0.02 mm	
Theta range for data collection	2.97 to 29.96°	
Reflections collected/ observed (>2σ)	6916/ 1821 [R(int) = 0.0284]	
Data Completeness	0.905	
Goodness-of-fit on F^2	0.902	
Final R indices [I>2σ(I)]	$R1$ = 0.0214 w$R2$ = 0.0411	
R indices (all data)	$R1$ = 0.0373 w$R2$ = 0.0424	
Largest diff. peak and hole	0.447 and -0.427 $eÅ^{-3}$	

The asymmetric unit of $[(MoO_2)_2(xdp)(H_2O)_2]\cdot 2H_2O$ (Figure 4-4) consists of one MoO_2^{2+} cation which is coordinated to a half of xdp^{4-} anion (located at a crystallographic inversion centre) and a molecule of water. One lattice water molecule is also present.

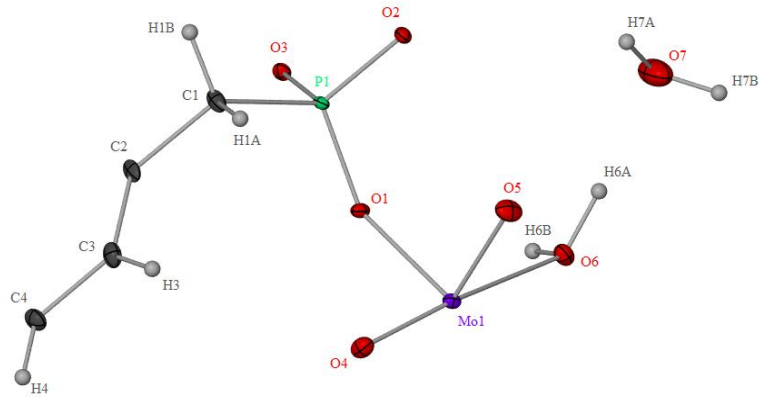

Figure 4-4. The asymmetric unit of $[(MoO_2)_2(xdp)(H_2O)_2]\cdot 2H_2O$ showing thermal ellipsoids at the 30% probability level.

Overall the $[(MoO_2)_2(xdp)(H_2O)_2]\cdot 2H_2O$ structure is 3-D, constructed by sheets containing molybdenum atoms, which are pillared by the xdp ligands. The xdp ligand is fully deprotonated and adopts a trans conformation throughout the whole structure with the phosphonate head and tail alternating in orientation.

The xdp ligand is coordinated to the molybdenum(VI) centre through all three oxygen atoms. The P–O contacts range from 1.5074(16)Å to 1.5402(17)Å with a longer P–C contact (1.783(2)Å).

The molybdenum(VI) centre is six-coordinate having a distorted octahedral geometry, bonded to three phosphonate groups ($-PO_3^{2-}$), two oxo ligands and to a water molecule. Selected bond lengths and angles are given in Table 2-14. The two oxo ligands have shorter Mo–O contacts than the other four bonds to molybdenum, while the Mo–O bond to water is the longest. The cis angles range from 73.24(6)° to 104.72(8)° and the trans angles from 158.10(7) to 170.39(7)°.

*Table 4-2. Selected bond lengths (Å) and angles (°) for $[(MoO_2)_2(xdp)(H_2O)_2]\cdot 2H_2O$.**

Atoms	Bond length (Å)	Atoms	Angle (°)
Mo1–O1	1.9944(16)	O5-Mo1-O6	84.86(7)
Mo1–O2#2	2.1108(14)	O5-Mo1-O4	104.72(8)
Mo1–O3#1	2.0083(16)	O4-Mo1-O2#2	97.18(7)

Mo1–O4	1.6823(16)	O2#2-Mo1-O6	73.24(6)
Mo1–O5	1.6932(15)	O1-Mo1-O3#1	159.45(6)
Mo1–O6	2.3298(17)	O1-Mo1-O6	82.31(6)
P1-O2	1.5074(16)	O5-Mo1-O1	96.20(7)
P1-O3	1.5402(17)	O4-Mo1-O1	95.68(8)
P1-O1	1.5387(16)	O1-Mo1-O2#2	81.20(6)
P1-C1	1.783(2)	O4-Mo1-O6	170.39(7)
		O5-Mo1-O2#2	158.10(7)
**Symmetry transformations used to generate equivalent atoms:* *#1 – x + 1/2, y + 1/2, - z + 1/2; #2 x, - y + 1, z - 1/2;*			

The octahedral molybdenum units are linked by the tetrahedral phosphonate groups of the xdp ligand forming sheets with a 4.8^2 topology (Figure 4-5). Both Molybdenum centres and phosphorus atoms act as three-connected nodes. The shortest circuits back to a three-connected Mo or P are a four-sided polygon and two eight-sided polygons.

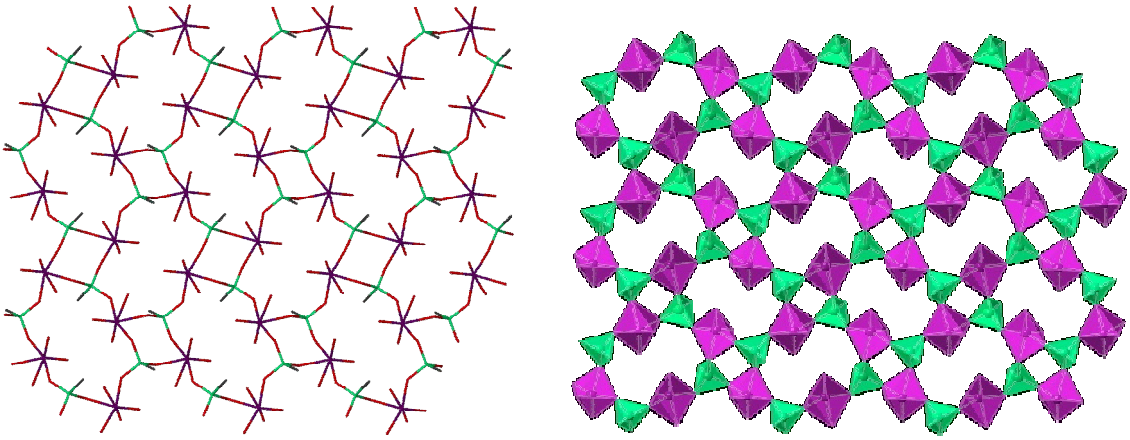

Figure 4-5. Sheets formed along bc plane with 4.8^2 topology viewed as: (left) stick and (right) polyhedral models. The lattice water and hydrogens are omitted for clarity. Only the –PO_3C group of the xdp ligand is shown.

The sheets are pillared by the xdp ligands forming a 3-D MOF with channels, which are filled with lattice water molecules (Figure 4-6).

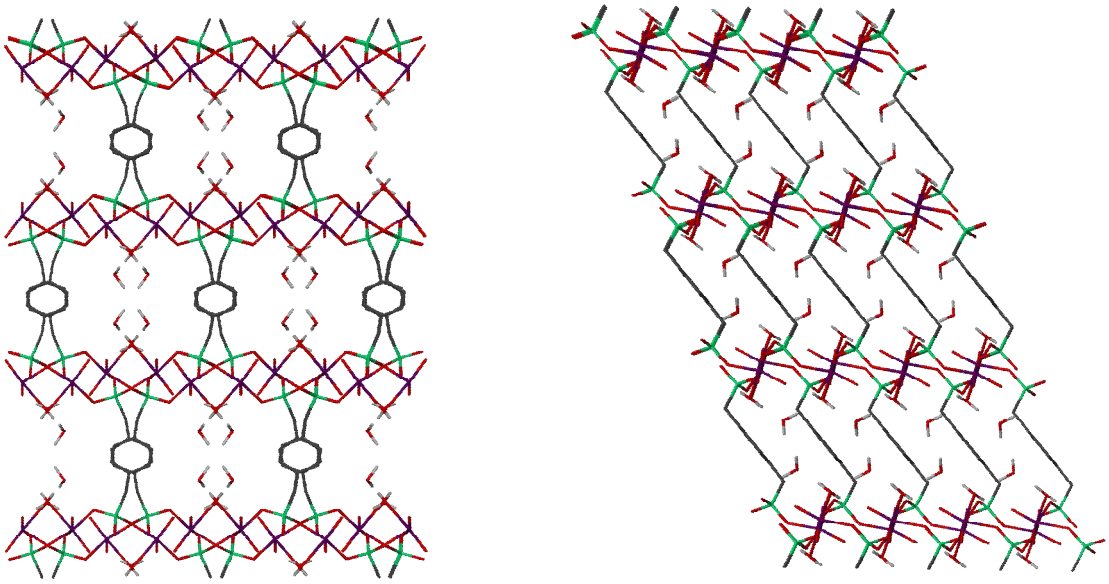

Figure 4-6. The 3-D structure of $[(MoO_2)_2(xdp)(H_2O)_2]\cdot 2H_2O$ viewed: (left) along the c axis and (right) along the b axis. The hydrogen atoms of the xdp linker have been omitted for clarity.

The removal of both coordinated and lattice water molecules would generate empty channels of 4.2 Å width (H3···H4#7[i] distance) and 4.6 Å height (O5···O5#6[i] distance) as shown in Figure 4-7. The distances are measured from centre to centre of atom with subsequent subtraction of the van der Waals radius of hydrogen and oxygen atoms, respectively.

[i] Symmetry transformations used to generate equivalent atoms: #6 -x, y,-z+1/2; #7 = -x+1, -y+2, -z+1.

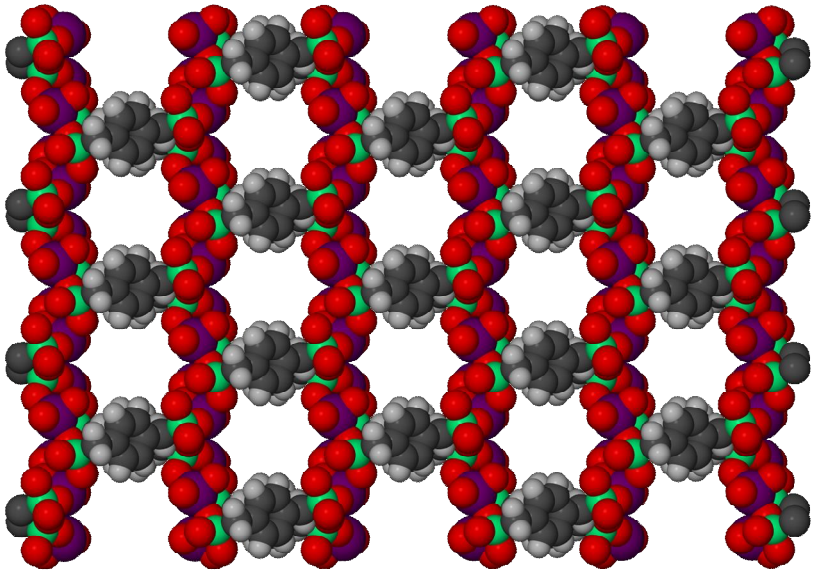

Figure 4-7. Channels of [$(MoO_2)_2$(xdp)] viewed along c axis.

The void volume and hence percentage void space within [$(MoO_2)_2$(xdp)] calculated using PLATON[25] is 17.6% of the unit cell volume when the lattice water was removed prior to these calculations and 27.3% when both the lattice and coordinated waters were removed.

Both the coordinated and lattice water molecules are involved in hydrogen bonding as shown in Figure 4-8. The coordinated water molecule based on O6 interacts through one of its hydrogen atoms (H6B) to both Mo double-bounded oxygen atoms (O4 and O5), strengthening the interactions within the sheets. Moreover, the coordinated water molecule based on O6 is hydrogen bonded to the lattice water molecule based on O7 through H7A.

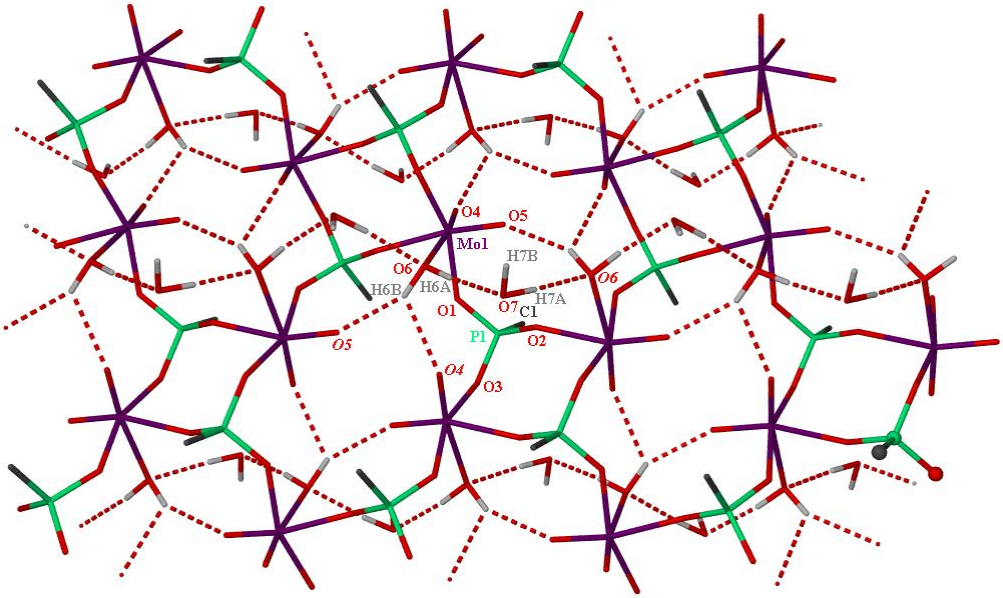

Figure 4-8. Structure of $[(MoO_2)_2(xdp)(H_2O)_2]\cdot 2H_2O$ showing hydrogen bonding. Symmetry related atoms have been labelled in italics.

The parameters of hydrogen bonding are given in Table 4-3.

*Table 4-3. Hydrogen bonding parameters for $[(MoO_2)_2(xdp)(H_2O)_2]\cdot 2H_2O$.**

Atoms	Distance N/ O···O (Å)	Distance H···O (Å)	Angle (°)
O6–H6A···O7	2.758	1.79	173
O6–H6B···O5#2	3.040	2.14	153
O6–H6B···O4#4	2.981	2.35	122
O7–H7A···O6#3	2.930	1.96	175

**Symmetry transformations used to generate equivalent atoms: #2 x,-y+1,z-1/2, #3 x,-y+1,z+1/2, #4 -x+1/2,y-1/2,-z+1/2.*

4.2.2. Dehydration-rehydration studies on $[(MoO_2)_2(xdp)(H_2O)_2]\cdot 2H_2O$

In order to see if $[(MoO_2)_2(xdp)(H_2O)_2]\cdot 2H_2O$ can be dehydrated and to what extent without loss of structural integrity, the compound was heated *in vacuo* gradually at different temperatures for various times. The evacuated samples have been analysed by TGA, PXRD and IR spectroscopy.

The TGA trace of the as-made $[(MoO_2)_2(xdp)(H_2O)_2]\cdot 2H_2O$ (Figure 4-9, trace a) shows a first mass loss of 6.5% between 45°C and 105°C attributed to the loss of lattice water (calculated 6.1%) and then loss of a further 6.5% between 105°C and 140°C attributed to the loss of coordinated water (calculated 6.1%). Up to 320°C further weight losses are relatively small, which is a strong indication that pillaring organic residue remains intact within the framework.

A sample of $[(MoO_2)_2(xdp)(H_2O)_2]\cdot 2H_2O$ was heated at 130°C under vacuum for 3 hours and the TGA analysis indicated that MOF has lost just half of the water molecules; therefore the resultant sample is a partially dehydrated MOF (Figure 4-9, trace b). Further evacuation of this sample for 1 hour at 150°C produced a fully dehydrated MOF $[(MoO_2)_2(xdp)]$ as was indicated by the TGA analysis (Figure 4-9, trace c).

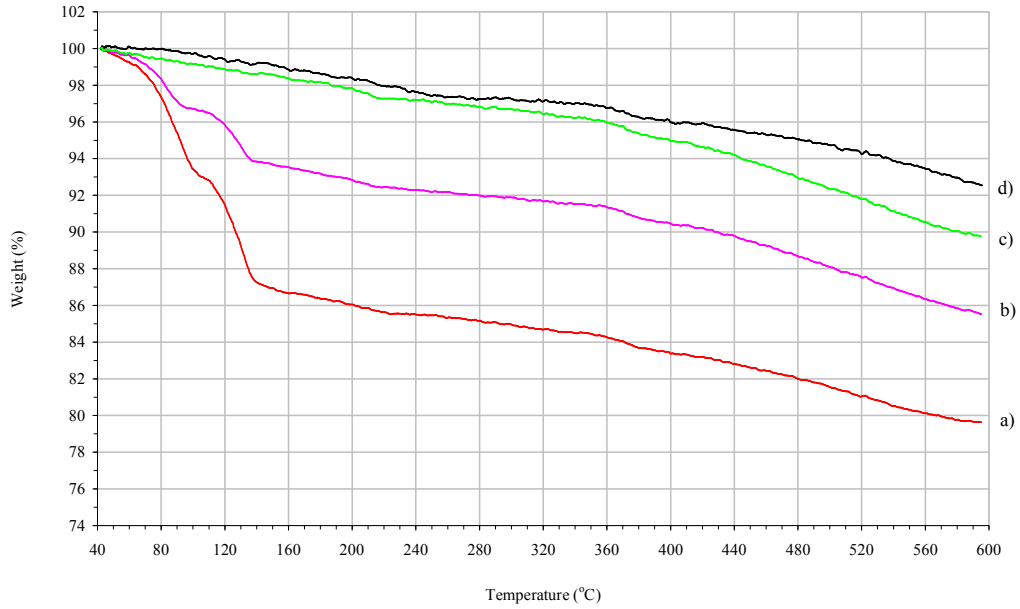

Figure 4-9. TGA traces for [(MoO$_2$)$_2$(xdp)(H$_2$O)$_2$]·2H$_2$O: a) as-made, b) vacuo-dried for 3 hours at 130°C, c) further vacuo-dried 1 hour at 150°C and d) the fully dehydrated MOF kept away from moisture.

However the TGA trace of the fully dehydrated MOF, [(MoO$_2$)$_2$(xdp)] still showed a small degree of mass loss (0.4%) up to 80°C suggesting that it might have picked up some water during handling. This was confirmed by comparing it with the TGA trace of a fully dehydrated MOF, [(MoO$_2$)$_2$(xdp)] kept away from moisture during handling (Figure 4-9, trace d).

The colour of MOF changes during heating, going from white to yellow when it is heated at 100°C, further to light orange when is heated at 130°C and finally to a light green colour when the MOF is heated at 150°C. Therefore the light green colour of the heated MOF can be associated with a fully dehydrated MOF, [(MoO$_2$)$_2$(xdp)].

To examine the structural integrity of the samples heated under vacuum at different temperatures, PXRD analyses were carried out on the heated samples as shown in Figure 4-10.

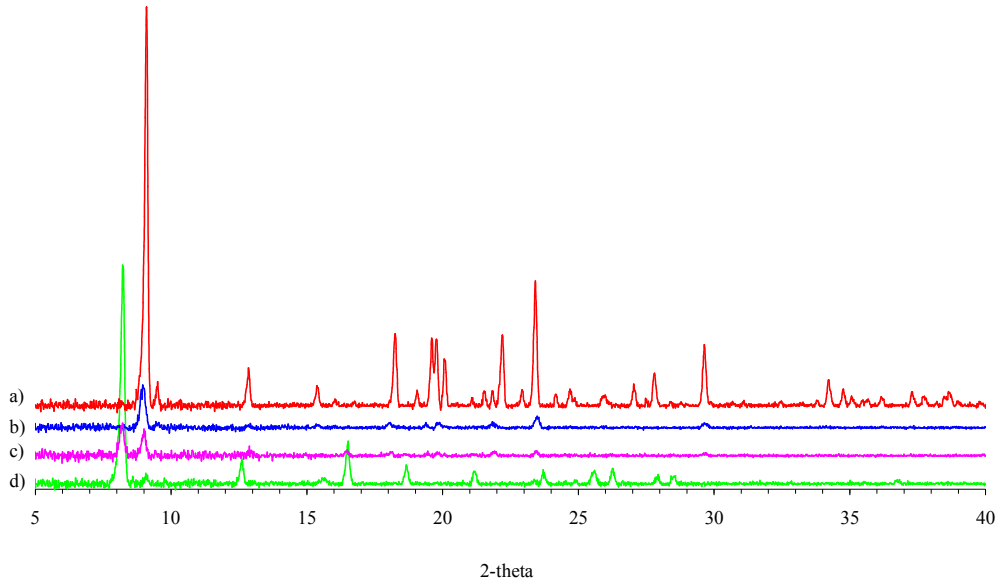

Figure 4-10. The PXRD patterns of $[(MoO_2)_2(xdp)(H_2O)_2]\cdot 2H_2O$: a) as-made, b) vacuo-dried for 3 hours at 100°C, c) vacuo-dried for 3 hours at 130°C and d) is c) further vacuo-dried 1 hour at 150°C.

PXRD analysis indicates a reduction of crystallinity for the sample heated at 100°C (Figure 4-10, trace b) and appearance of a new peak at 2-theta 8° for the MOF heated at 130°C (Figure 4-10, trace c). The peak at 2-theta 8° intensifies being the most intense peak of the PXRD for the MOF heated at 150°C (Figure 4-10, trace d). The difference between the PXRD pattern for the fully dehydrated MOF (Figure 4-10, trace d) compared to that of as-made MOF (Figure 4-10, trace a) suggests that the structure of $[(MoO_2)_2(xdp)(H_2O)_2]\cdot 2H_2O$ changes significantly on removal of the water molecules.

The difference between the as-made and fully dehydrated MOF can also be observed from their infrared spectrum. The as-made MOF (Figure 4-11, trace a) shows two bands at 3613 and 3451 cm^{-1} which are due to the asymmetric and symmetric OH stretching vibrations of the water molecules. The corresponding deformation vibration $\delta(H_2O)$ is observed at 1629 cm^{-1}. The *para*-substituted benzene ring vibration modes are observed at 1398 and 1514 cm^{-1}. As expected for *para*-substituted benzene rings, one sharp δ(CH) out-of-plane vibration at 850 cm^{-1} is found, while the in-plane vibration is found at 1258 cm^{-1}. The set of bands between 1205 and 900 cm^{-1} is due to stretching vibrations of the tetrahedral CPO groups and the band centred at 592 cm^{-1} can be assigned to MoO vibrations.

The fully dehydrated MOF (Figure 4-11, trace b) shows no bands characteristic of water at 3613, 3451 and 1629 cm^{-1} and a change of the set of bands characteristic of the tetrahedral CPO groups with broadening of the sharp δ(CH) out-of-plane vibration at 850 cm^{-1}.

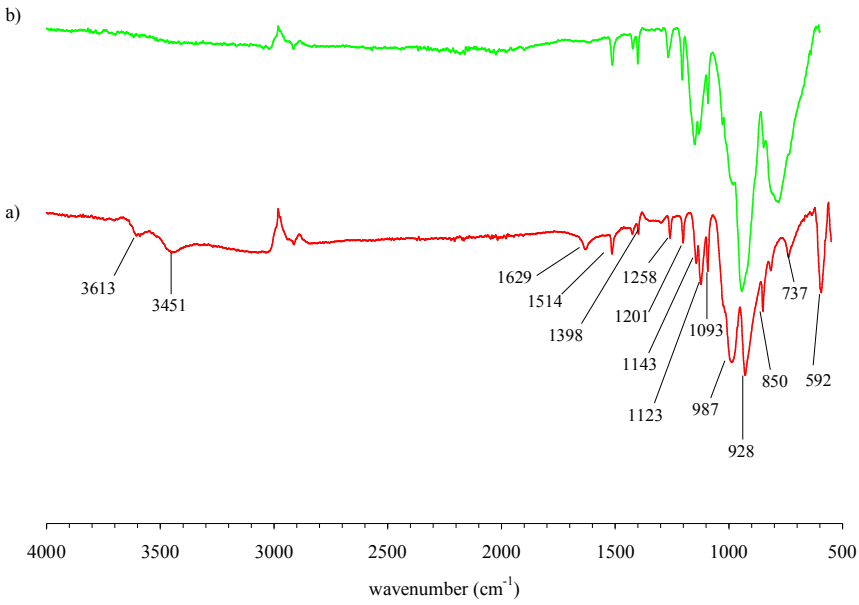

Figure 4-11. Infrared spectrum of: a) as-made $[(MoO_2)_2(xdp)(H_2O)_2]\cdot 2H_2O$ showing peak values and b) fully dehydrated $[(MoO_2)_2(xdp)]$.

N_2 sorption measurement for MOF at 77 K and 101.33 kPa produced a type III isotherm which usually indicates weak adsorbent-adsorbate interactions. The MOF sample was evacuated at 150°C for 4 hours prior to measurement. The BET surface area calculated from N_2 isotherm is 9.25 m^2/g which indicates essentially a "non-porous" MOF.

The PXRD pattern of the sample after N_2 adsorption (Figure 4-12, a) showed peaks characteristic to both fully dehydrated (Figure 4-12, b) and the as-made MOF (Figure 4-12, c). This suggests that N_2 might have been actually adsorbed into the pores of the fully dehydrated MOF and initiated re-formation of the original MOF. Another explanation can be that the sample picked up moisture during handling even though attention was paid and the PXRD analysis was carried out rapidly straight after N_2 sorption experiment. However, a careful investigation can reveal the effect of N_2 upon the fully dehydrated MOF but due to a limited time this might be for future work.

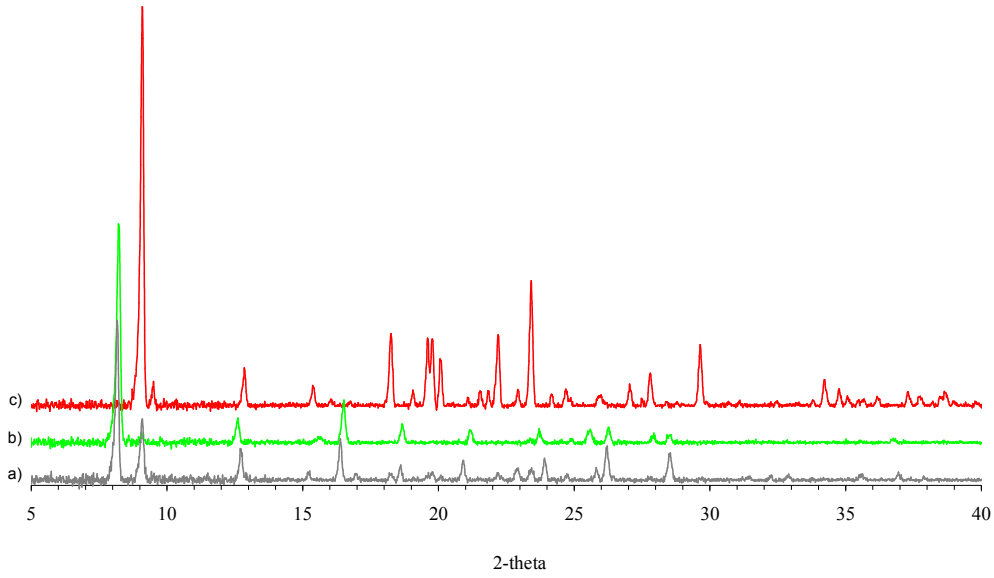

Figure 4-12. The PXRD pattern of $[(MoO_2)_2(xdp)(H_2O)_2]\cdot 2H_2O$: a) after N_2 sorption, b) fully dehydrated and c) as-made.

To examine if the fully dehydrated MOF can re-form $[(MoO_2)_2(xdp)(H_2O)_2]\cdot 2H_2O$ on hydration, a crystalline sample of $[(MoO_2)_2(xdp)(H_2O)_2]\cdot 2H_2O$ was dried under vacuum at 150°C for 3 hours and then immersed in water for 36 hours. The light green colour characteristic to the fully dehydrated MOF, changes to white in the first few hours of immersion. The resultant sample soaked in water for 36 hours was analysed by PXRD and TGA. The PXRD pattern of the sample soaked in water (Figure 4-13, a) matches the PXRD pattern of the as-made $[(MoO_2)_2(xdp)(H_2O)_2]\cdot 2H_2O$ (Figure 4-13, c) confirming that the fully dehydrated MOF has been re-hydrated, regaining the original structure.

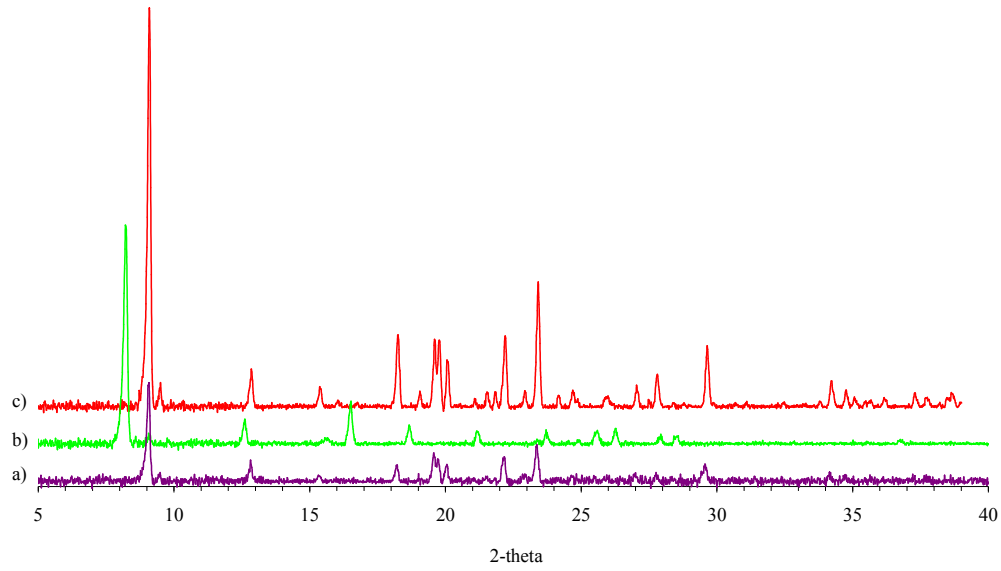

Figure 4-13. The PXRD pattern for: a) fully dehydrated [$(MoO_2)_2$(xdp)] soaked in H_2O for 36 hours, b) fully dehydrated [$(MoO_2)_2$(xdp)] and c) as-made [$(MoO_2)_2$(xdp)$(H_2O)_2$]·$2H_2O$.

The re-hydrated sample was analysed by TGA and, as can be seen from Figure 4-14, the TGA trace for the re-hydrated sample (Figure 4-14, trace a) is almost identical to that of the as-made MOF (Figure 4-14, trace b) suggesting that the fully dehydrated MOF has adsorbed in 36 hours the same amount of water lost during dehydration.

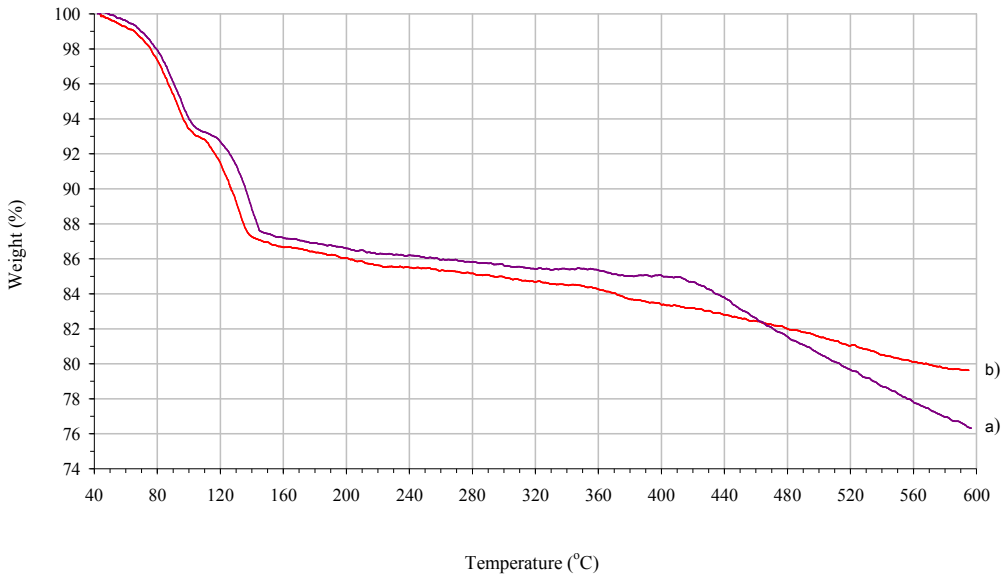

Figure 4-14. The TGA traces for: a) fully dehydrated [$(MoO_2)_2$(xdp)] soaked in H_2O for 36 hours and b) as-made [$(MoO_2)_2$(xdp)$(H_2O)_2$]·$2H_2O$.

There are reported structures that can be dehydrated and re-hydrated reversibly [26-41] with a few experiencing a phase change.[35, 36] For example, Bourne *et al.*[39, 40] demonstrates reversible dehydration and re-hydration of $(Me_2NH_2)[Zn_2(Hbtc)(btc)(H_2O)_3]\cdot 3H_2O$ (btc = 1,3,5-benzenetricarboxylate) and explains this behaviour on the basis of breathing in this structure.

Qui *et al.*[26] reported a 3-D cobalt diphosphonate $[Co_2(H_2O)_2(xdp)]$ which undergoes a reversible dehydration-rehydration process, though in this case the PXRD pattern of the dehydrated MOF is the same as that of the as-made MOF. The $[Co_2(H_2O)_2(xdp)]$ framework is related to of $[(MoO_2)_2(xdp)(H_2O)_2]\cdot 2H_2O$, being constructed of two-dimensional infinite cobalt–oxygen inorganic layers pillared by *para*-xylylenediphosphonate (xdp). The colour of the crystals changed from pink to blue when they were heated at 350°C for 2 h, and the rehydration process is accompanied by a return of the original pink colour. Therefore the coordination environment of the cobalt ion is changed from octahedral to square-pyramidal but the main framework is retained after dehydration.

The reversible dehydration- rehydration behaviour demonstrated by $[(MoO_2)_2(xdp)(H_2O)_2]\cdot 2H_2O$ with structural changes suggested by different PXRD patterns, is by our knowledge the first example of this type for a *para*-xylylenediphosphonate MOF, and is believed to be attributed to the dynamic and flexible properties of the MOF.

4.2.3. Methanol and ethanol adsorption by $[(MoO_2)_2(xdp)]$

For a porous adsorbent, both the cross-sectional size (usually referred to as the kinetic diameter, which is defined as the intermolecular distance of the closest approach for two molecules colliding with zero initial kinetic energy) and the shape of the adsorbate molecule are the ultimate factors affecting selective adsorption.

The capacity of fully dehydrated $[(MoO_2)_2(xdp)]$ to adsorb other small solvent molecules apart from water (whose kinetic diameter is 2.641 Å[42]), was further investigated for methanol and ethanol whose kinetic diameters are 3.626 Å[42] and 4.530 Å[42], respectively.

In this respect, 6 mg of fully dehydrated $[(MoO_2)_2(xdp)(H_2O)_2]\cdot 2H_2O$ was soaked in 1 mL methanol and ethanol, respectively for 36 hours. The colour of the sample soaked in methanol changed in the first few hours from light green to white with a blue tint, whereas the sample soaked in ethanol remained light green. To examine whether or not the methanol or ethanol has any effect on the as-made MOF, $[(MoO_2)_2(xdp)(H_2O)_2]\cdot 2H_2O$ was also soaked in MeOH and EtOH, respectively for 36 hours. The colour of these samples remained unchanged (white) after 36 hours and the PXRD patterns were both identical to those for the as-made samples.

Figure 4-15 shows the PXRD patterns for the two samples soaked in MeOH and EtOH, respectively, compared with the patterns for the as-made and fully dehydrated samples. The PXRD pattern of the sample soaked in MeOH (Figure 4-15, a) showed a good match with that of the as-made MOF (Figure 4-15, b) but with an extra peak of very low intensity, which is characteristic to the fully dehydrated MOF (Figure 4-15, d).

The PXRD pattern of the sample soaked in EtOH (Figure 4-15, c) showed a good match with that of the fully dehydrated MOF (Figure 4-15, d), which suggests that the fully dehydrated MOF was structurally not affected after 36 hours in EtOH.

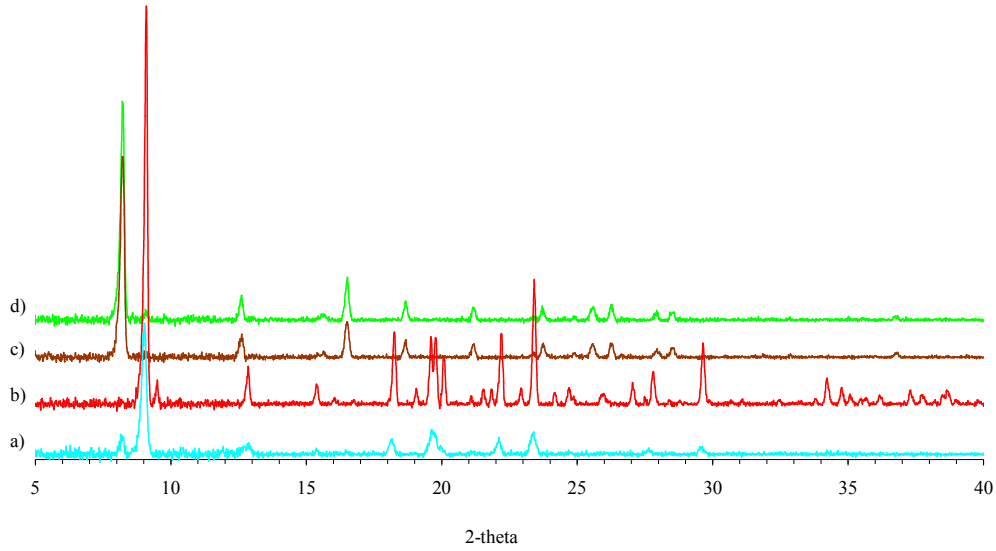

Figure 4-15. The PXRD pattern of $[(MoO_2)_2(xdp)(H_2O)_2]\cdot 2H_2O$: a) fully dehydrated soaked in MeOH for 36 hours, b) as-made, c) fully dehydrated soaked in EtOH for 36 hours and d) fully dehydrated.

The infrared spectrum of the sample soaked in MeOH (Figure 4-16, a) is identical to that of the as-made MOF (Figure 4-16, b), whereas for the sample soaked in EtOH (Figure 4-16, c) is identical to that of the fully dehydrated MOF (Figure 4-16, d). Therefore infrared analysis indicates once again that the sample soaked in MeOH re-form the original MOF while the sample soaked in EtOH retains the structure of the fully dehydrated MOF.

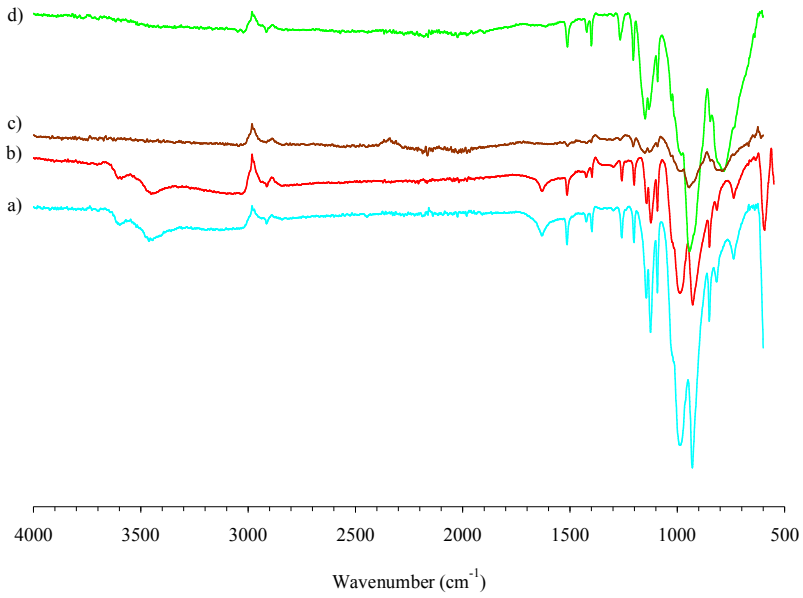

Figure 4-16. Infrared spectrum for $[(MoO_2)_2(xdp)(H_2O)_2]\cdot 2H_2O$: a) fully dehydrated soaked in MeOH for 36 hours, b) as-made, c) fully dehydrated soaked in EtOH for 36 hours and d) fully dehydrated.

Figure 4-17 shows the TGA traces of the two samples soaked in MeOH and EtOH, respectively alongside the TGA traces of the as-made and the fully dehydrated MOF. The TGA trace of the sample soaked in MeOH (Figure 4-16, a) shows a mass loss of approximate 10 % up to 150°C equally distributed over two steps. The 10 % mass loss, if calculated by adding to the fully dehydrated MOF certain amounts of methanol, represents 0.9 of a MeOH molecule per Mo centre which means that the fully dehydrated MOF adsorbed 0.9 of a MeOH molecule per Mo centre while was soaked in MeOH for 36 hours. Meanwhile, the TGA trace of the sample soaked in EtOH (Figure 4-16, c) looks like the one of the fully dehydrated MOF (Figure 4-16, d) which suggests that the fully dehydrated MOF has not picked any EtOH after 36 hours.

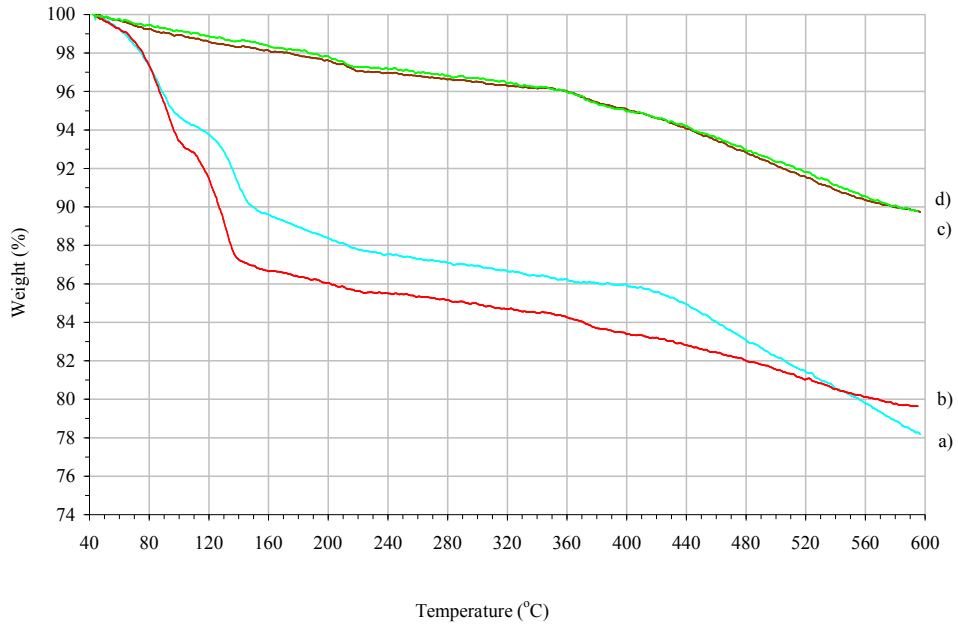

Figure 4-17. The TGA traces of $[(MoO_2)_2(xdp)(H_2O)_2]\cdot 2H_2O$: a) fully dehydrated soaked in MeOH for 36 hours, b) as-made, c) fully dehydrated soaked in EtOH for 36 hours and d) fully dehydrated.

The PXRD and IR data are consistent with the sample in MeOH picking up guests, whereas the sample in EtOH does not. The question remains of whether the dehydrated sample is adsorbing MeOH or water molecules. This was addressed by NMR analysis.

The samples that had been soaked in MeOH and EtOH were digested prior to NMR measurements using a NaOD in D_2O stock solution (0.2 mL NaOD 40% in 1 mL D_2O). The ^1H NMR spectrum of the digested sample soaked in MeOH (Figure 4-18) shows MeOH as a singlet at 2.95 ppm. The amount of MeOH calculated by integrating the peaks of the ^1H NMR spectrum suggests 0.73 of a MeOH molecule per Mo centre, knowing that the other peaks are from *para*-xylylenediphosphonic acid (H_4xdp) and they correspond to four hydrogen atoms each. The amount of MeOH contained by the sample soaked in MeOH for 36 hours, calculated from ^1H NMR spectroscopy is in broad agreement with that calculated from TGA.

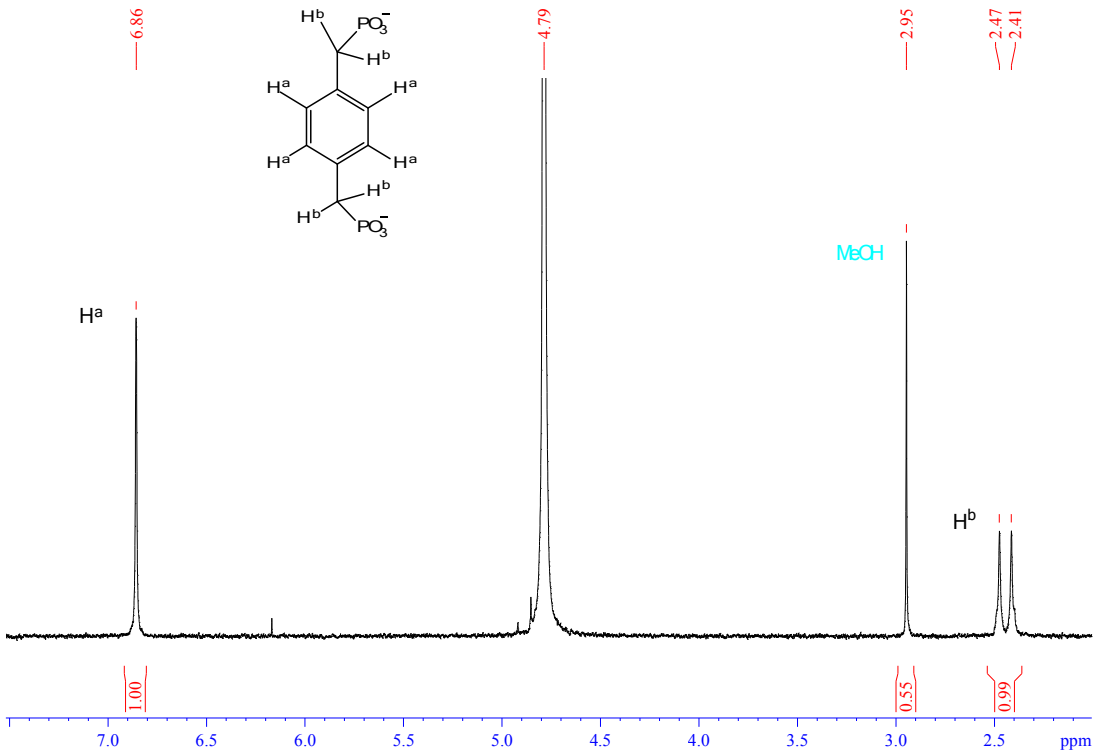

Figure 4-18. ^{1}H NMR spectrum of the digested [$(MoO_2)_2$(xdp)] soaked in MeOH for 36 hours.

The ^{1}H NMR spectrum of the digested [$(MoO_2)_2$(xdp)] soaked in EtOH for 36 hours (Figure 4-19) did not show any peaks characteristic of EtOH. The result confirms that the fully dehydrated MOF, [$(MoO_2)_2$(xdp)] did not absorb any EtOH after 36 hours.

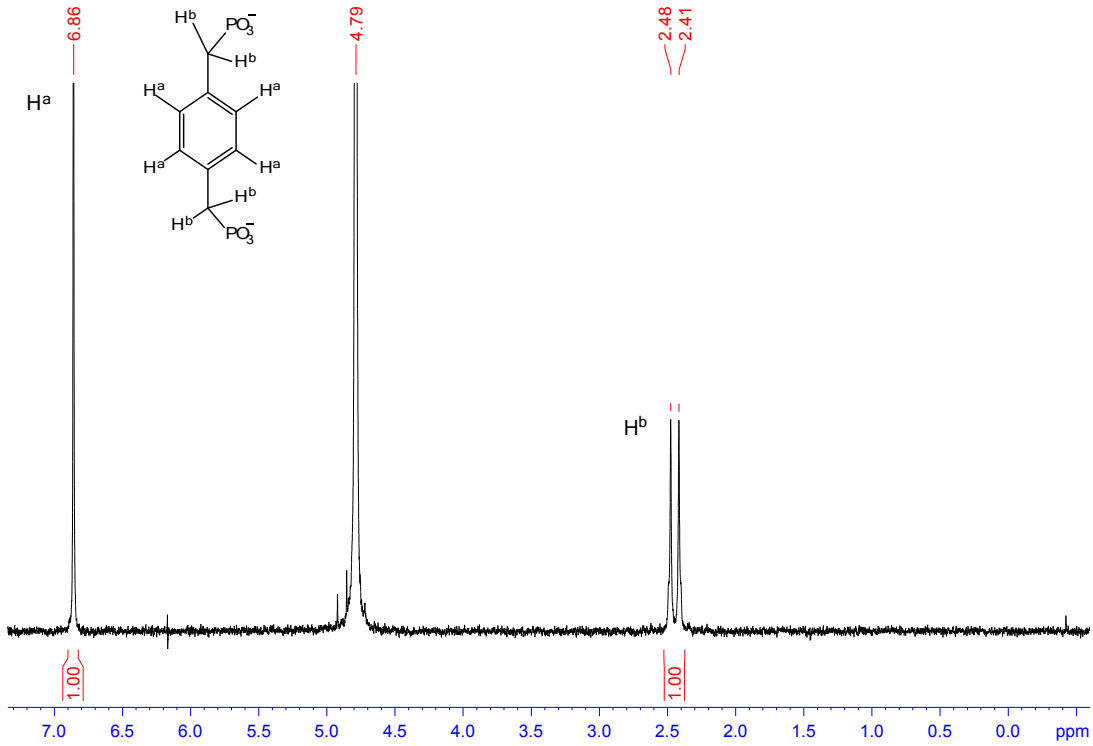

Figure 4-19. ^{1}H NMR spectrum of the digested $[(MoO_2)_2(xdp)]$ soaked in EtOH for 36 hours.

The results are consistent with $[(MoO_2)_2(xdp)(H_2O)_2]\cdot 2H_2O$ exhibiting flexibility which can be attributed to the nature of the xdp linker. This feature allows $[(MoO_2)_2(xdp)(H_2O)_2]\cdot 2H_2O$ to undergo structural changes during dehydration and re-hydration. These structural changes produce pores that are able to accommodate water and methanol molecules, but are too small to accommodate ethanol molecules.

Many MOFs have been tested for the adsorption of MeOH and EtOH molecules in the vapour phase[33, 41, 43-47], and some of them revealed significant adsorption selectivities and separation potential. The primary mechanisms involved in the observed selective adsorption were identified by Zhou[48] as: a) size/shape exclusion; b) host-guest interactions (including guest-guest interactions in some cases) and c) selective adsorption resulting from guest-adsorption induced structural transformation of the MOF. In most cases, both a) and b) mechanisms operate together and complement each other. The third mechanism c) is encountered especially in MOFs with dynamic and flexible structures.

The selective adsorption of H_2O and MeOH over EtOH vapours was observed in flexible [Cd(pzdc)(bpee)]·1.5H_2O (pzdc = pyrazine-2,3-dicarboxylate and bpee = pyridine–CH=CH–pyridine) at room temperature.[43] [Cd(pzdc)(bpee)]·1.5H_2O has a 3-D pillared-layer structure containing 1-D channels with a window size of 3.5 x 4.5 Å and each pore is occupied by three water molecules which form hydrogen bonds with protruding carboxylate moieties of pzdc ligands. Despite the framework flexibility, the adsorption selectivities were mainly attributed to the size constraints of the channels.

Having demonstrated that [$(MoO_2)_2$(xdp)] can adsorb MeOH but not EtOH, the next goal was to examine whether it can selectively adsorb methanol from a methanol-ethanol mixture. Preliminary results were promising but further investigations need to be conducted in order to conclude whether or not this compound would adsorb MeOH but not EtOH from a MeOH-EtOH mixture.

The vapour sorption studies of MeOH and EtOH by [$(MoO_2)_2$(xdp)] would be something to look at in future. The uptake of MeOH molecules, but completely exclusion of EtOH molecules, may find industrial application in discriminating the MeOH molecule from a mixture of MeOH and its higher homologues.

4.3. Experimental

4.3.1. General

The syntheses were carried out in Ace pressure tubes (15 cm^3) purchased from Aldrich and heated in programmable ovens. The reagents used for syntheses were purchased commercially and used without further purification.

Powder X-ray diffractions (PXRDs) were recorded at the University of Bath on a Bruker AXS D8 Advance diffractometer with copper Kα radiation of wavelength 1.5406 Å at 298 K. Samples were placed in 0.5 mm diameter Lindemann capillaries, and measured with a 2θ range of 3-60°. The step size was 0.016° with time per step of 134.5 s. Simulated X-ray powder patterns were generated from single crystal data that were imported into PowderCell[49] with the step size of 0.02° and time per step of 1.00 s.

TGA experiments were carried out on a Perkin Elmer TGA 4000 Thermogravimetric Analyser at the University of Bath. The samples were heated from 45°C to 600°C at a heating rate of 10°C/min, under a flow of nitrogen (20 mL/min).

Samples for NMR studies were digested using NaOD in D_2O stock solution (0.2 mL 40% NaOD/D_2O, in 1 mL D_2O). ^1H NMR spectrums were recorded at 298 K on a Bruker Advance 300 MHz Ultrashield NMR spectrometer. Chemical shifts are reported in ppm (δ) and *J* values are given in Hz. ^1H NMR spectrums were referenced to the residual *protio* peak at δ 4.79 ppm for D_2O. When the MOF was digested using a 6 times diluted NaOD in D_2O stock solution (0.1 mL 40% NaOD/D_2O in 3 mL D_2O) the chemical shifts are slightly shifted to lower field.

Infrared spectrums were recorded on a PerkinElmer Spectrum 100 spectrometer equipped with an ATR sampling accessory at the University of Bath.

Microanalysis (Carbon, Hydrogen and Nitrogen = CHN) data was recorded on a CE-440 Elemental Analyser by Mr. Alan Carver at the University of Bath.

The N_2 sorption isotherms were measured at 77 K and 101.33 kPa, using a Belsorp-mini II analyzer at the University of Bath. The MOF was heated at 150°C for 4 hours prior to the N_2 sorption measurements.

4.3.2. Single-Crystal X-Ray Crystallography

X-ray diffraction data was collected by Dr. Mary Mahon on an Oxford Diffraction Gemini diffractometer fitted with an Atlas CCD detector using Mo-Kα radiation of wavelength 0.71073 Å at 150 K, at the University of Bath.

The structure was solved using SHELXS-97[50] and refined using full-matrix least squares in SHELXL-97[50]. The final refinements were run by Dr. Mary Mahon and were generally straightforward with the following exceptions and points of note. Unless noted below, all non-hydrogen atoms were refined anisotropically in the final least squares run, and hydrogen atoms were included at calculated positions. Hydrogen atoms attached to water molecules were located and refined at 0.98 Å from the parent oxygen atoms.

Search for and analysis of solvent accessible voids in the structures have been made using PLATON SQUEEZE[25]. Solvent accessible voids are defined as regions in the structure that can accommodate at least a sphere with radius 1.2 Å without intersecting with any of the van der Waals spheres assigned to each atom in the structure.

4.3.3. Synthesis of $[(MoO_2)_2(xdp)(H_2O)_2]\cdot 2H_2O$

$Na_2MoO_4\cdot 2H_2O$ (0.12 g, 0.5 mmol) was stirred together with *p*-xylylenediphosphonic acid (H_4xdp) (0.07 g, 0.25 mmol) in 8 cm^3 deionised water. The pH of the solution was then adjusted to pH 1 by drop-wise addition of conc. HCl (HCl 32%, 0.1 mL, 1 mmol). The acidified solution was then placed in a 15 cm^3 Ace pressure tube and heated at 120°C for 15 hours in an oven. The resultant white crystalline material was thoroughly washed with deionised water (3 x 5 mL) and air-dried (0.14 g, yield 91 %).

The identity of the bulk compound was confirmed by PXRD, and the observed powder pattern matches that simulated from the crystal structure (Figure 4-20).

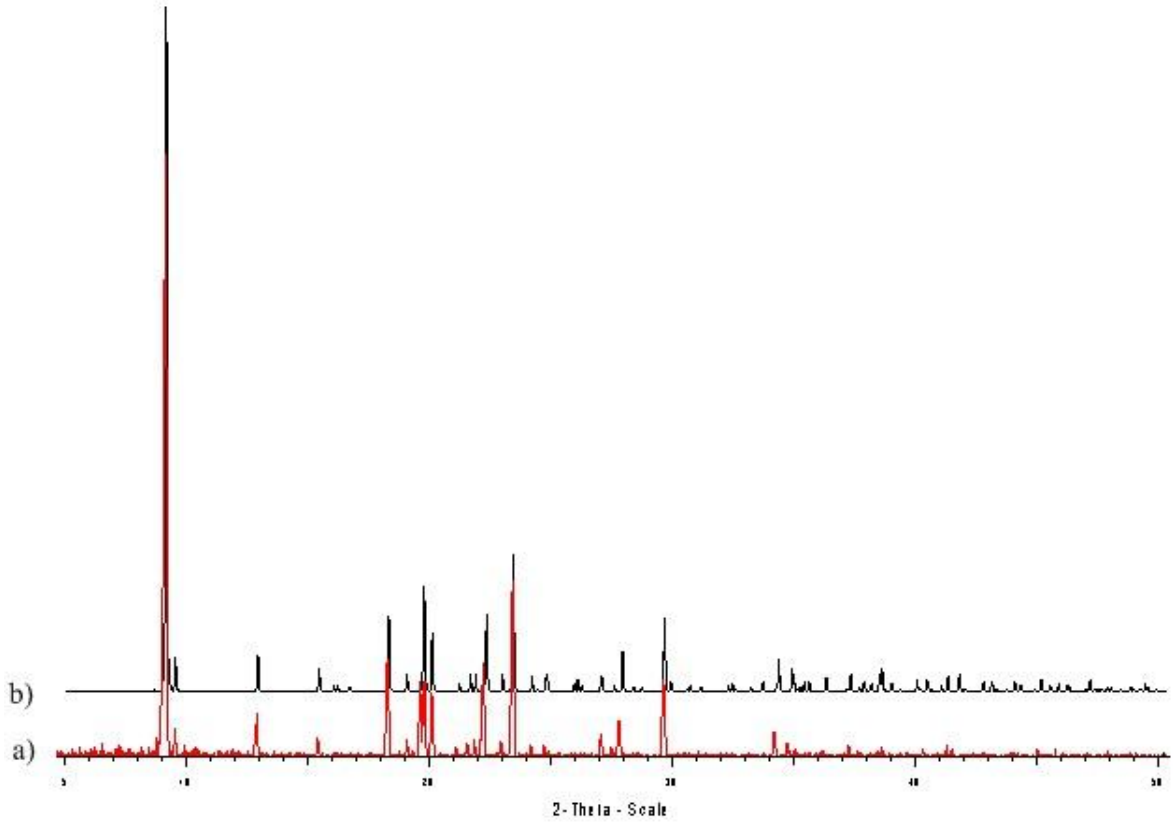

Figure 4-20. The PXRD pattern for $[(MoO_2)_2(xdp)(H_2O)_2]\cdot 2H_2O$: a) experimental and b) simulated from the crystal structure.

The presence of *para*-xylylenediphosphonate (xdp) was confirmed by NMR analysis of the digested MOF (stock solution 0.2 mL 40% NaOD/D_2O in 1 mL D_2O), ^1H NMR (300 MHz, D_2O): δ = 6.86 (s, 4 H, –C_6H_4–), δ = 2.48-2.42 (d, *J* = 18.2 Hz, 4 H, –CH_2–) and ^{31}P NMR (121 MHz, D_2O) δ = 18.96 (s).

IR (cm^{-1}): ν = 3613 (broad), 3451 (broad), 1629 (medium), 1514 (sharp), 1426 (weak), 1398 (weak, sharp), 1258 (sharp), 1201 (sharp), 1143 (sharp), 1123 (sharp), 1093 (sharp), 987 (strong), 928 (strong), 850 (sharp), 815 (weak, medium), 737 (sharp), 592 (sharp).

Found (calculated for $[(MoO_2)_2(xdp)(H_2O)_2]\cdot 2H_2O$): C, 15.50 (16.28); H, 2.71 (2.73) %.

4.4. Summary and Future work

$[(MoO_2)_2(xdp)(H_2O)_2]\cdot 2H_2O$ can be obtained from the hydrothermal reaction of sodium molybdate(VI) dihydrate ($Na_2MoO_4\cdot 2H_2O$), *para*-xylylenediphosphonic acid (H_4xdp) in the presence of hydrochloric acid. The synthesis of $[(MoO_2)_2(xdp)(H_2O)_2]\cdot 2H_2O$ was shown to be quite sensitive to the reaction conditions.

$[(MoO_2)_2(xdp)(H_2O)_2]\cdot 2H_2O$ was analysed through single crystal X-ray diffraction and shown to exhibit a 3-D structure constructed of molybdenum-phosphonate sheets pillared by the xdp ligands. The as-made MOF contains channels filled with water molecules. The coordinated water molecules form hydrogen bonds with the oxo ligands attached to molybdenum, strengthening the interactions within the sheets. The lattice water molecules also form hydrogen bonds with the coordinated water molecules.

Both types of water molecules contained by $[(MoO_2)_2(xdp)(H_2O)_2]\cdot 2H_2O$ can be removed on heating as demonstrated by TGA analysis and infrared spectroscopy but this is accompanied by a change in structure of the MOF as was shown by PXRD and infrared spectroscopy.

Rehydration of the dehydrated MOF $[(MoO_2)_2(xdp)]$ re-forms $[(MoO_2)_2(xdp)(H_2O)_2]\cdot 2H_2O$ demonstrating that the structural change observed on dehydration is reversible. The dehydration and rehydration processes are accompanied by a change of colour from white in the as-made state to light green in the fully dehydrated state. There are many reported MOFs showing reversible dehydration-rehydration

behaviour but this is by our knowledge the first example of *para*-xylylenediphosphonate MOF showing a reversible dehydration-rehydration with structural transformation of the MOF.

The PXRD analysis, TGA analysis, infrared and ^{1}H NMR spectroscopy indicates that [$(MoO_2)_2$(xdp)] behaves differently while soaked in methanol compared to ethanol. The PXRD and infrared spectrum indicate that the original MOF framework is recovered when the dehydrated MOF is soaked in methanol, while soaking in ethanol leaves the dehydrated MOF unchanged. TGA analysis and ^{1}H NMR spectroscopy of the digested sample soaked in methanol and ethanol, respectively indicate the presence of methanol but no ethanol.

Preliminary experiments suggest that [$(MoO_2)_2$(xdp)] might adsorb selectively MeOH from a MeOH-EtOH mixture but further investigations need to be done in order to be able to draw a conclusion about the selectivity of this MOF.

The N_2 sorption measurements revealed the dehydrated MOF [$(MoO_2)_2$(xdp)] to be non-porous. The results are consistent with [$(MoO_2)_2$(xdp)$(H_2O)_2$]·$2H_2O$ exhibiting flexibility which is induced by the flexible *para*-xylylenediphosphonate (xdp) linker.

The structure of the dehydrated MOF [$(MoO_2)_2$(xdp)] has not been elucidated yet and future work to identify it might help to explain the behaviour of this compound towards small guest molecules as water, methanol and ethanol.

The uptake of H_2O and MeOH molecules, but exclusion of EtOH molecules, may find an application in discriminating the MeOH molecule from a mixture of alcohols. The adsorption selectivity and separation potential of [$(MoO_2)_2$(xdp)] can be explored in future.

4.5. References

[1] S. Natarajan, P. Mahata, Current Opinion in Solid State and Materials Science **2009**, 13, 46.

[2] G. K. H. Shimizu, R. Vaidhyanathan, J. M. Taylor, Chemical Society Reviews **2009**, 38, 1430.

[3] K. J. Gagnon, H. P. Perry, A. Clearfield, Chemical Reviews **2012**, 112, 1034.

[4] J.-P. Zhang, Y.-B. Zhang, J.-B. Lin, X.-M. Chen, Chemical Reviews **2012**, 112, 1001.

[5] D.-M. Zang, D.-K. Cao, L.-M. Zheng, Inorganic Chemistry Communications **2011**, 14, 1920.

[6] M. J. Rogers, J. C. Crockett, F. P. Coxon, J. Mönkkönenb, Bone **2011**, 49, 34.

[7] K. D. Demadis, N. Stavgianoudaki, in Metal Phosphonate Chemistry: From Synthesis to Applications, The Royal Society of Chemistry, **2012**, pp. 438.

[8] A. Clearfield, Curr Opin Solid State Mater Sci **1996**, 1, 268.

[9] M. M. Gómez-Alcántara, A. Cabeza, M. Martínez-Lara, M. A. G. Aranda, R. Suau, N. Bhuvanesh, A. Clearfield, Inorganic Chemistry **2004**, 43, 5283.

[10] N. G. Armatas, D. G. Allis, A. Prosvirin, G. Carnutu, C. J. O'Connor, K. Dunbar, J. Zubieta, Inorganic Chemistry **2008**, 47, 832.

[11] Z.-C. Zhang, S. Gao, L.-M. Zheng, Dalton Transactions **2007**, 4681.

[12] B. K. Tripuramallu, R. Kishore, S. K. Das, Polyhedron **2010**, 29, 2985.

[13] V. Soghomonian, Q. Chen, R. C. Haushalter, J. Zubieta, Angewandte Chemie International Edition in English **1995**, 34, 223.

[14] D. Riou, O. Roubeau, G. Férey, Microporous and Mesoporous Materials **1998**, 23, 23.

[15] V. Soghomonian, R. C. Haushalter, J. Zubieta, Chemistry of Materials **1995**, 7, 1648.

[16] F.-N. Shi, T. Trindade, J. Rocha, F. A. A. Paz, Crystal Growth & Design **2008**, 8, 3917.

[17] N. Stock, T. Bein, Journal of Solid State Chemistry **2002**, 167, 330.

[18] E. Irran, T. Bein, N. Stock, Journal of Solid State Chemistry **2003**, 173, 293.

[19] N. Stock, N. Guillou, T. Bein, G. Férey, Solid State Sciences **2003**, 5, 629.

[20] D. Riou, F. Belier, C. Serre, M. Nogues, D. Vichard, G. Férey, International Journal of Inorganic Materials **2000**, 2, 29.

[21] F. Belier, M. Riou-Cavellec, D. Vichard, D. Riou, Comptes Rendus de l'Académie des Sciences - Series IIC - Chemistry **2000**, 3, 655.

[22] H. G. Harvey, A. C. Herve, H. C. Hailes, M. P. Attfield, Chemistry of Materials **2004**, 16, 3756.

[23] S. Jones, H. Liu, K. Schmidtke, C. C. O'Connor, J. Zubieta, Inorganic Chemistry Communications **2010**, 13, 298.

[24] E. Burkholder, V. Golub, C. J. O'Connor, J. Zubieta, Inorganic Chemistry **2003**, 42, 6729.

[25] A. L. Spek, University of Utrecht, **1999**.

[26] H. Li, G.-s. Zhu, X.-d. Guo, F.-x. Sun, H. Ren, Y. Chen, S.-l. Qiu, European Journal of Inorganic Chemistry **2006**, 2006, 4123.

[27] F. Luo, S. R. Batten, Y. Che, J.-M. Zheng, Chemistry – A European Journal **2007**, 13, 4948.

[28] N.-H. Hu, Z.-G. Li, J.-W. Xu, H.-Q. Jia, J.-J. Niu, Crystal Growth & Design **2006**, 7, 15.

[29] M. Kurmoo, H. Kumagai, M. Akita-Tanaka, K. Inoue, S. Takagi, Inorganic Chemistry **2006**, 45, 1627.

[30] Y. Cheng, A. Kondo, H. Noguchi, H. Kajiro, K. Urita, T. Ohba, K. Kaneko, H. Kanoh, Langmuir **2009**, 25, 4510.

[31] E. Y. Lee, M. P. Suh, Angewandte Chemie International Edition **2004**, 43, 2798.

[32] B. Rather, M. J. Zaworotko, Chemical Communications **2003**, 830.

[33] T. K. Maji, G. Mostafa, R. Matsuda, S. Kitagawa, Journal of the American Chemical Society **2005**, 127, 17152.

[34] H. Deng, Y.-C. Qiu, Y.-H. Li, Z.-H. Liu, R.-H. Zeng, M. Zeller, S. R. Batten, Chemical Communications **2008**, 2239.

[35] P. Li, J. Lou, Y. Zhou, X. Liu, Z. Chen, L. Weng, Dalton Transactions **2009**, 4847.

[36] M. R. Montney, S. Mallika Krishnan, R. M. Supkowski, R. L. LaDuca, Inorganic Chemistry **2007**, 46, 7362.

[37] P. Mahata, K. V. Ramya, S. Natarajan, Inorganic Chemistry **2009**, 48, 4942.

[38] Q.-X. Yao, Z.-F. Ju, W. Li, W. Wu, S.-T. Zheng, J. Zhang, CrystEngComm **2008**, 10, 1299.

[39] K. Davies, S. A. Bourne, L. Ohrstrom, C. L. Oliver, Dalton Transactions **2010**, 39, 2869.

[40] K. Davies, S. A. Bourne, C. L. Oliver, Crystal Growth & Design **2012**, 12, 1999.

[41] G. Mehlana, S. A. Bourne, G. Ramon, Dalton Transactions **2012**, 41, 4224.

[42] J.-R. Li, R. J. Kuppler, H.-C. Zhou, Chemical Society Reviews **2009**, 38, 1477.

[43] T. K. Maji, K. Uemura, H.-C. Chang, R. Matsuda, S. Kitagawa, Angewandte Chemie International Edition **2004**, 43, 3269.

[44] S. K. Ghosh, S. Bureekaew, S. Kitagawa, Angewandte Chemie International Edition **2008**, 47, 3403.

[45] S. Horike, D. Tanaka, K. Nakagawa, S. Kitagawa, Chemical Communications **2007**, 3395.

[46] W. Kaneko, M. Ohba, S. Kitagawa, Journal of the American Chemical Society **2007**, 129, 13706.

[47] S. Mohapatra, K. P. S. S. Hembram, U. Waghmare, T. K. Maji, Chemistry of Materials **2009**, 21, 5406.

[48] J.-R. Li, J. Sculley, H.-C. Zhou, Chemical Reviews **2012**, 112, 869.

[49] W. Kraus, G. Nolzeb, J. Appl. Cryst. **1996**, 29, 301.

[50] G. Sheldrick, Acta Cryst. A **2008**, 64, 112.

Chapter 5. Dimethylammonium copper(II) sulfate frameworks

5.1. Introduction

The potential of the sulfate ligand in the chemistry of 3d-metal networks has been highlighted recently[1]. A systematic search of the Cambridge Structural Database (CSD) reveals that sulfate can adopt 16 different bridging coordination modes, being capable of linking 2, 3, 4, 5, 6, 8 or even 10 metal centres.

Copper(II) sulfate exists as a series of compounds with different degrees of hydration. The most commonly encountered copper(II) sulfate salt is the bright blue pentahydrate ($CuSO_4 \cdot 5H_2O$). The anhydrous form occurs in nature as a rare mineral known as chalcocyanite. $CuSO_4 \cdot 5H_2O$ occurs in nature as chalcanthite, and two more rare hydrated copper(II) sulfate minerals are: bonattite (trihydrate) and boothite (heptahydrate). The copper(II) centres and SO_4^{2-} ligands also occur together in nature alongside other anions such as hydroxide[2, 3] or cations such as sodium.[4]

Copper(II) sulfate has many applications and is often used as a fungicide, algaecide and molluscicide,[5-7] and as an activator in the concentration by froth flotation in the mining industry.[8] It is also widely used in school chemistry classes to demonstrate dehydration-hydration processes or crystal growing and in copper plating experiments. Copper(II) sulfate is used for a series of chemical tests such as testing the blood for anemia, and the pentahydrate is used as a magnetochemical calibrant in magnetometry[9].

Reactions of $CuSO_4 \cdot 5H_2O$ with N-donor ligands including imidazolates in water have successfully produced 2-D coordination networks[10]. Five ammonium copper(II) sulfates have been synthesised under solvothermal conditions starting from copper(II) acetate and ammonium sulfate salts, in which the charges on the anions are balanced by the included ammonium cations.[11]

The first example of compounds consisting of Cu_4O-based units that contain Cu centres bridged by sulfate oxygens to form infinite 1-D networks have been reported by Li *et al.*[12] There are also examples of trinuclear copper(II) units that are bridged via sulfate anions to

give hexanuclear dimers due to a centre of symmetry. These aggregates are further linked into extended structures.

In this chapter is reported the synthesis, structures, and magnetic properties of new anionic copper(II) sulfate aggregates and chains linked into 2-D and 3-D networks involving the dimethylammonium cations ($NMe_2H_2^+$).

5.2. Results and discussion

Three new copper(II) sulfates containing dimethylammonium cations ($NMe_2H_2^+$) have been synthesised and characterised in this work.

Compound **1** has been formulated as $(NMe_2H_2)_4[Cu_6O_2(SO_4)_6(DMF)_4]$, compound **2** as $(NMe_2H_2)_4[Cu_6O_2(SO_4)_6(DMF)_2]$ and compound **3** as $(NMe_2H_2)[Cu_2(OH)(SO_4)_2(H_2O)_2]$. These compounds have been characterised by X-ray single diffraction, powder X-ray diffraction, and the magnetic properties of **1** and **3** have also been investigated.

Compounds **1** and **2** were initially obtained serendipitously from reaction mixtures containing $CuSO_4 \cdot 5H_2O$ and 25,26,27,28-tetrapropoxycalix[4]arene-5,17-dicarboxylic acid (H_2caldc) in DMF. Green crystals of **1** were harvested from this reaction mixture when it was left undisturbed at room temperature. Subsequent heating of a similar reaction mixture for 5 days at 90°C followed by a further 3 days at 120°C, produced yellow crystals of **2**. Compounds **1** and **2** were not obtained as phase pure from these reactions but alongside a blue powder of $[Cu_2(caldc)_2(DMF)_2]$, which was described in Chapter 3 of this thesis.

In order to optimise the synthesis of **1** and **2**, reaction mixtures of $CuSO_4 \cdot 5H_2O$ and DMF were investigated by altering parameters such as the temperature of the reaction, quality of the DMF and the concentration of the copper(II) sulfate solutions. The DMF used was anhydrous or ACS grade. In the presence of water, DMF hydrolyses to form dimethylamine and formic acid[13]. An aged DMF solvent is expected to be hydrolysed in a higher proportion than a fresh DMF solvent. Because of this and previous work that has shown this can lead to different products[13], the bottles of DMF used were opened no more than a few days prior to using it in the reaction. $CuSO_4 \cdot 5H_2O$ dissolves readily in DMF giving a green solution. Most of the heated mixtures produced in the first 24 hours either

pale blue, turquoise powders or very small and fragile green, yellow-green crystals. The results suggested that both anhydrous and ACS grade DMF gave the same products.

Finally, compound **2** was prepared as phase pure tiny yellow-green crystals by heating $CuSO_4 \cdot 5H_2O$ in DMF at 95 °C for 1 day.

Water was added to the reaction mixture because none of the reaction mixtures mentioned above gave **1** as a single compound. Reactions were undertaken with DMF-water in place of pure DMF. $CuSO_4 \cdot 5H_2O$ dissolves in DMF-water mixture with gentle heating. Heating $CuSO_4 \cdot 5H_2O$ in a DMF-water mixture at 95°C has produced in 1 day a turquoise powder which has a powder X-ray diffraction pattern shown in Figure 5-1 that matches that of $Cu_3(SO_4)(OH)_4$[14, 15] which is the mineral antlerite. The mineral antlerite has been previously synthesised by heating an aqueous suspension of $CuSO_4 \cdot 5H_2O$ and NaOH at 170°C for 6 days[16].

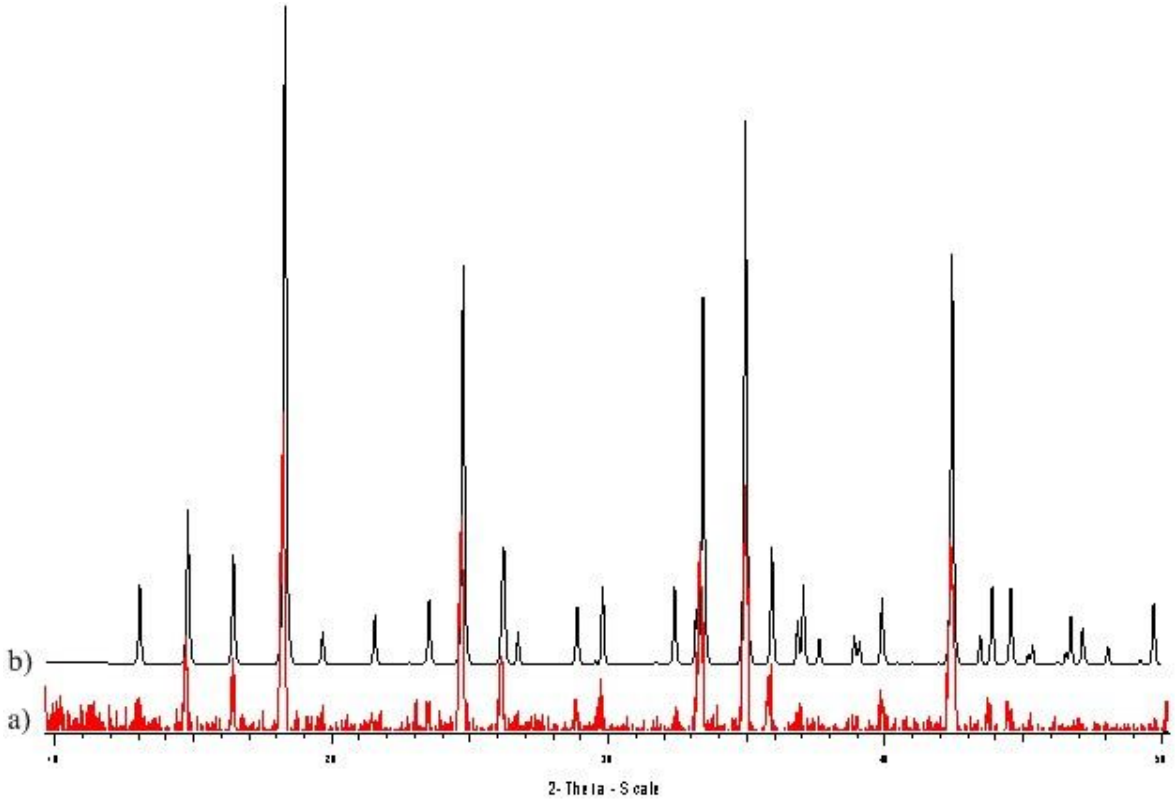

Figure 5-1. The PXRD pattern for antlerite $Cu_3(OH)_4(SO_4)$: a) as-synthesised air-dried sample and b) simulated from the X-ray crystal structure[14].

Addition of dimethylammonium chloride, $[NMe_2H_2]Cl$ has also been investigated. A mixture of $CuSO_4 \cdot 5H_2O$ and $[NMe_2H_2]Cl$ in DMF at 95 °C produced **1** as phase pure tiny green crystals in 1 day.

A more concentrated reaction mixture than that producing compound **1,** when left at room temperature gave compound **3** as phase pure turquoise crystals.

Compounds **1-3** all showed signs of decomposition on standing, with **1** and **2** decomposing rapidly in air and **3** decomposing more slowly. The products have been investigated both in their mother liquor denoted DMF-saturated samples and out of their supernatant solutions. Powder X-ray diffraction studies of the series of structural changes undergone by **1-3** are discussed later in this chapter.

Samples of **1-3** are shown in Figure 5-2, with the DMF-saturated samples of **1** and **2** being dried and stored under nitrogen whereas the DMF-saturated sample of **3** was gently air-dried and stored under atmospheric conditions. The dried samples preserve the colour of the DMF-saturated samples, namely compound **1** is green, **2** is yellow-green and **3** is turquoise, which make them easily to be differentiated.

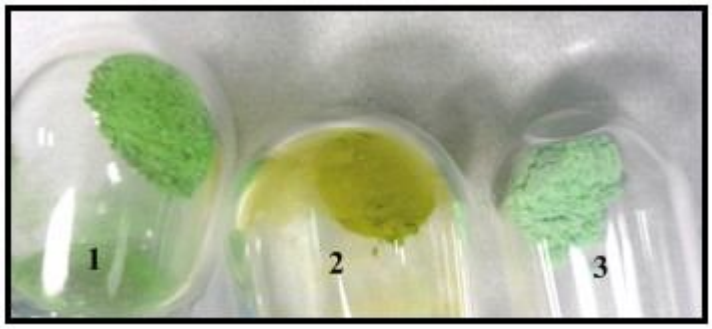

Figure 5-2. Compounds 1, 2 and 3 showing their different colours.

The anionic copper(II) sulfates of compounds **1-3** are charge balanced by dimethylammonium ions derived either from the hydrolysis of the DMF solvent or from the addition of dimethylammonium chloride ($[NMe_2H_2]Cl$).

5.2.1. Crystal structure of $(NMe_2H_2)_4[Cu_6O_2(SO_4)_6(DMF)_4]$, 1

Green block-like crystals of suitable size for X-ray single diffraction were collected from a mixture of $CuSO_4 \cdot 5H_2O$ and 25,26,27,28-tetrapropoxycalix[4]arene-5,17-dicarboxylic acid

(H_2caldc, which is reported in Chapter3 of this thesis) in DMF after several months left undisturbed at room temperature. The crystal data given in Table 5-1 revealed that the caldc anion was not incorporated in the final structure which was formulated as $(NMe_2H_2)_4[Cu_6O_2(SO_4)_6(DMF)_4]$, **1.** Green plate-like crystals which share the same unit cell with **1** were harvested from a solution of $CuSO_4 \cdot 5H_2O$ in DMF which was heated at 95°C for 1 day, but this was not phase pure either. Finally, tiny green crystals of **1** were obtained as phase pure by heating a mixture of $CuSO_4 \cdot 5H_2O$ and $[NMe_2H_2]Cl$ in DMF at 95 °C for 1 day.

*Table 5-1. Crystallographic data and refinement parameters for **1**.*

Empirical formula	$C_{20}H_{60}Cu_6N_8O_{30}S_6$	
Formula weight	1466.39	
Temperature	150(2) K	
Wavelength	0.71073 Å	
Crystal system	Monoclinic	
Space group; Z	$P2_1/n$; 2	
Unit cell dimensions	a = 13.1050(3) Å	α = 90°
	b = 10.5140(2) Å	β = 103.183(1)°
	c = 18.7530(5) Å	γ = 90°
Volume	2515.81(10) Å^3	
Density (calculated)	1.936 g/cm^3	
Crystal size	0.25 x 0.08 x 0.08 mm	
Theta range for data	3.59 to 27.51°	
Reflections collected/	39253/ 4248 [R(int) = 0.1191]	
Data Completeness	0.996	
Goodness-of-fit on F^2	1.077	
Final R indices [I>2σ(I)]	$R1$ = 0.0582 $wR2$ = 0.1230	
R indices (all data)	$R1$ = 0.0890 $wR2$ = 0.1379	
Largest diff. peak and hole	1.344 and -0.697 eÅ^{-3}	

The crystal structure of $(NMe_2H_2)_4[Cu_6O_2(SO_4)_6(DMF)_4]$ **1** consists of four dimethylammonium cations for each discrete $[Cu_6O_2(SO_4)_6(DMF)_4]^{4-}$ anion.

The asymmetric unit of **1** (Figure 5-3) contains three copper(II) centres, three sulfate anions, one oxide anion, two DMF ligands and two dimethylammonium cations.

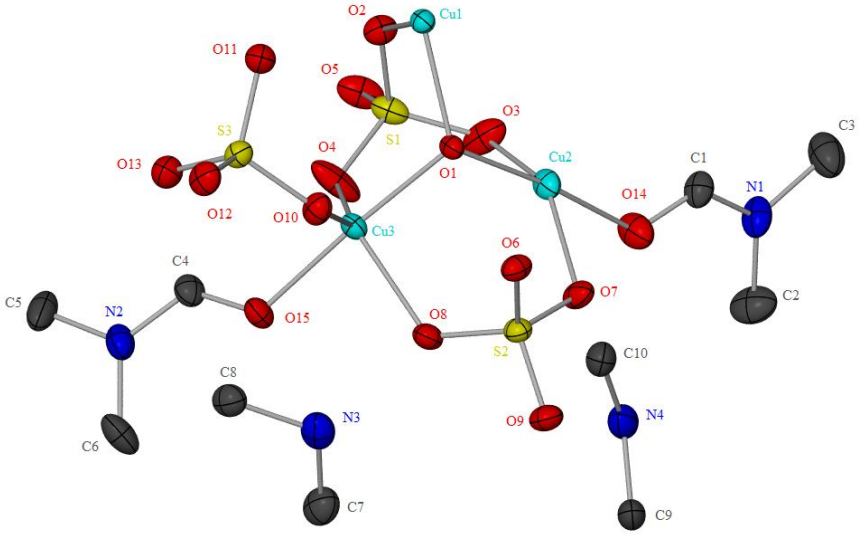

Figure 5-3. The asymmetric unit of 1 showing thermal ellipsoids at the 30% probability level. Hydrogen atoms have been omitted for clarity.

The Cu1 centre is situated near a crystallographic inversion centre leading to formation of aggregates with formulae $[Cu_6O_2(SO_4)_6(DMF)_4]^{4-}$. The aggregate contains two edge-sharing $Cu_4(\mu_4\text{-}O)$ tetrahedra (Figure 5-4) with the Cu1···Cu1#1[i] distance of 2.8404(12) Å. Two of the total of four triangular Cu_3 faces of the $Cu_4(\mu_4\text{-}O)$ tetrahedra, not involved in edge sharing are capped by a μ_3-sulfato ligand. The two edge-sharing $Cu_4(\mu_4\text{-}O)$ tetrahedra are further linked together by two μ_2-sulfato ligands through their nonshared vertices. The copper(II) centres not involved in edge-sharing (Cu2 and Cu3) are each coordinated to a DMF ligand. Hence the aggregate can be represented as $[Cu_6(\mu_4\text{-}O)_2(\mu_3\text{-}SO_4)_4(\mu_2\text{-}SO_4)_2(DMF)_4]^{4-}$. The $Cu_6O_2(SO_4)_6$ core is unusual, with the only previous example observed in the rare copper(II) sulfate mineral fedotovite, $K_2Cu_3O(SO_4)_3$,[17] which was first observed as a sublimate from the Tolbachik volcanic eruption in Kamchatka, Russia.

[i] Symmetry transformation used to generate equivalent atoms: *#1 – x + 2, - y, - z.*

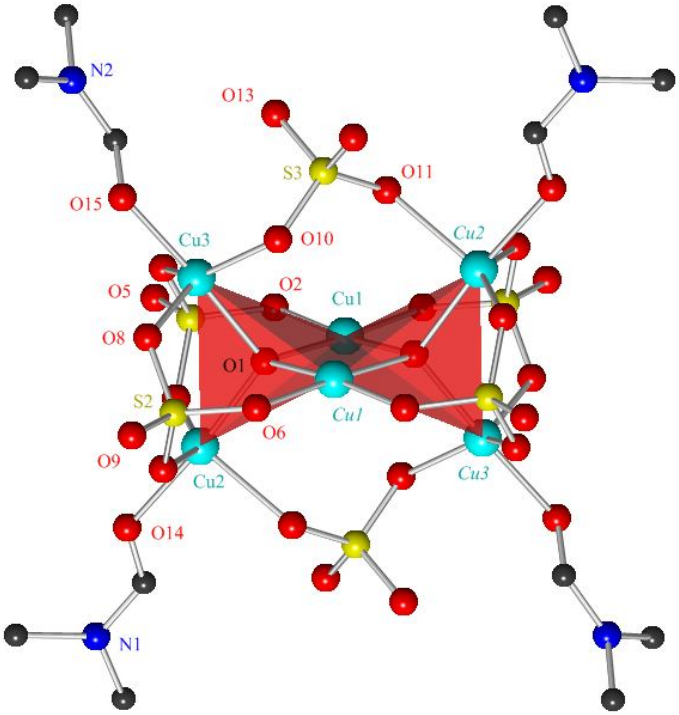

*Figure 5-4. Structure of **1** showing the $[Cu_6O_2(SO_4)_6(DMF)_4]^{4-}$ anion with the two central edge-sharing tetrahedra in red. Hydrogen atoms have been omitted for clarity. Symmetry generated atoms are labelled in italics.*

The copper(II) centres involved in edge-sharing, Cu1, are four coordinate whereas the ones not involved in edge-sharing, Cu2 and Cu3 are both five coordinate centres.

The Cu1 atom is coordinated to two oxo and two μ_3-sulfato ligands exhibiting a distorted square planar geometry. The Cu1−O bond lengths lie between 1.937(3) and 1.972(4) Å, with cis O−Cu1−O bond angles between 83.63(17) and 96.46(15)°. The Cu1 centre lies 0.072 Å from the mean plane defined by the four coordinating oxygen atoms (O1, O1#1[i], O2 and O6#1[i]). Selected bond lengths and angles for **1** are presented in Table 2-14.

The Cu2 and Cu3 centres are coordinated to an oxo ligand (O1), three sulfato ligands, and a DMF molecule. The Cu2 and Cu3 atoms, the DMF oxygen atom (either O14 or O15) and the oxo ligand (O1) are almost collinear [O1−Cu2−O14 = 174.55(18)° and O1− Cu3−O15 = 176.64(16)°], with the three oxygen atoms from the sulfato ligands approximately coplanar. Selected bond lengths and angles around Cu2 and Cu3 centres for **1** are presented

[i] Symmetry transformation used to generate equivalent atoms: *#1 – x + 2, - y, - z.*

in Table 2-14. The bond lengths and angles suggest that the coordination around Cu2 and Cu3 centres is intermediate between ideal square pyramidal and trigonal bipyramidal.

*Table 5-2. Selected bond lengths (Å) and angles (°) for **1**.**

Atoms	Bond length (Å)	Atoms	Angle (°)
Cu1−O1#1	1.937(3)	O2−Cu1−O1	93.59(16)
Cu1−O2	1.946(4)	O2−Cu1−O6#1	83.63(17)
Cu1−O1	1.949(3)	O1−Cu1−O1#1	86.08(14)
Cu1−O6#1	1.972(4)	O1#1−Cu1−O6#1	96.46(15)
		O2−Cu1−O1#1	173.55(16)
		O1−Cu1−O6#1	176.64(15)
Cu2−O1	1.943(3)	O1−Cu2−O14	174.55(18)
Cu2−O3	1.966(5)	O3−Cu2−O11#1	119.7(2)
Cu2−O14	1.988(5)	O7−Cu2−O11#1	93.46(18)
Cu2−O7	2.029(4)	O3−Cu2−O7	145.7(2)
Cu2−O11#1	2.127(4)	O1−Cu2−O3	91.71(17)
		O1−Cu2−O7	95.27(15)
		O1−Cu2−O11#1	93.00(15)
		O14−Cu2−O11#1	92.33(19)
		O14−Cu2−O3	86.6(2)
		O14−Cu2−O7	83.29(19)
Cu3−O1	1.931(3)	O1−Cu3−O15	176.64(16)
Cu3−O4	1.961(5)	O8−Cu3−O10	86.15(16)
Cu3−O15	1.972(4)	O4−Cu3−O10	143.8(2)
Cu3−O8	2.107(4)	O4−Cu3−O8	129.9(2)
Cu3−O10	2.114(4)	O1−Cu3−O8	91.49(14)
		O1−Cu3−O4	93.17(17)
		O1−Cu3−O10	87.40(15)
		O15−Cu3−O4	87.72(18)
		O15−Cu3−O10	93.80(17)
		O15−Cu3−O8	85.46(16)

**Symmetry transformation used to generate equivalent atoms: #1 – x + 2, - y, - z.*

For a five-coordinate system such as that represented in Figure 5-5, within the structural continuum between ideal square pyramidal and trigonal bipyramidal, a geometric parameter[18] $\tau = (\beta - \alpha)/60$ (β is the greater of the basal angles, BMC) has been defined and proposed as an index of the degree of trigonality. For a perfectly square pyramidal geometry τ is equal to zero, while it becomes unity for perfectly trigonal bipyramidal geometry. The donor A is chosen by the criterion that it should not be any of the four which define the two largest angles, α and β. By this criterion, the geometric parameter $\tau = (174.55 – 145.7)/60 = 0.48$ for Cu2 and $\tau = (176.64 – 143.8)/60 = 0.55$ for Cu3.

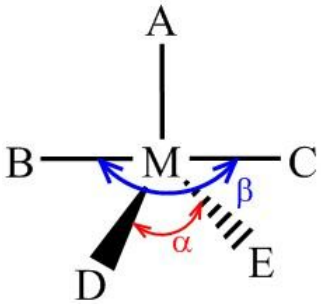

Figure 5-5. Five coordinate system.

The $[Cu_6O_2(SO_4)_6(DMF)_4]^{4-}$ anions are linked into chains along the *b* axis by hydrogen bonding to the $NMe_2H_2^+$ cations based on N3 as shown in Figure 5-6. These anionic chains $(NMe_2H_2)_2[Cu_6O_2(SO_4)_6(DMF)_4]^{2-}$ are further linked into sheets by hydrogen bonding to the $NMe_2H_2^+$ cations based on N4 as shown in Figure 5-6.

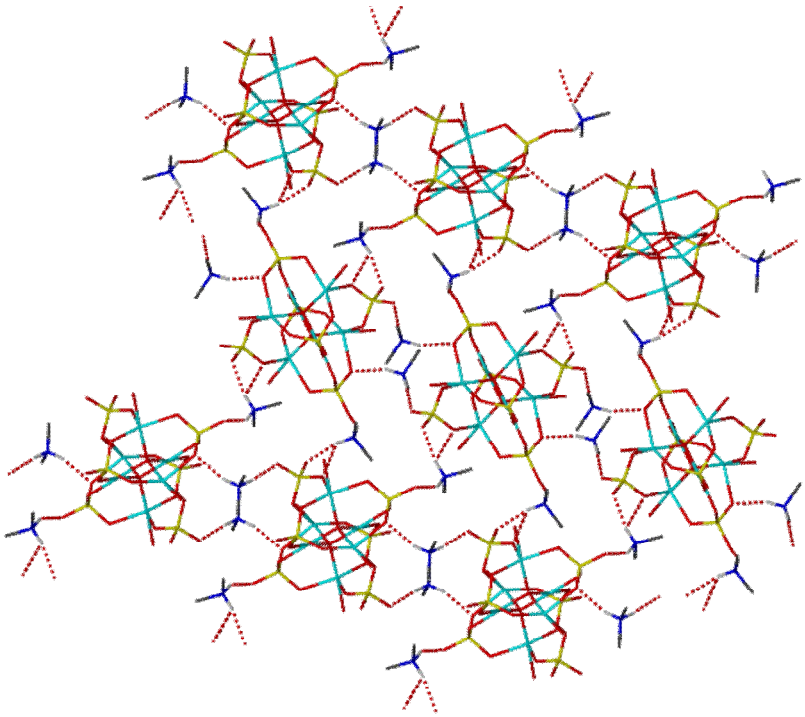

*Figure 5-6. Structure of **1** showing how the chains link into sheets. The non oxygen atoms of the DMF ligands and all hydrogen atoms except those involved in hydrogen bonding have been omitted for clarity.*

A closer overview to the hydrogen bonding within **1** is shown in Figure 5-7. The noncoordinated oxygen atoms O12, O9 and O13 and the coordinated oxygen atom O8 and O11 of the sulfato ligands act as acceptors.

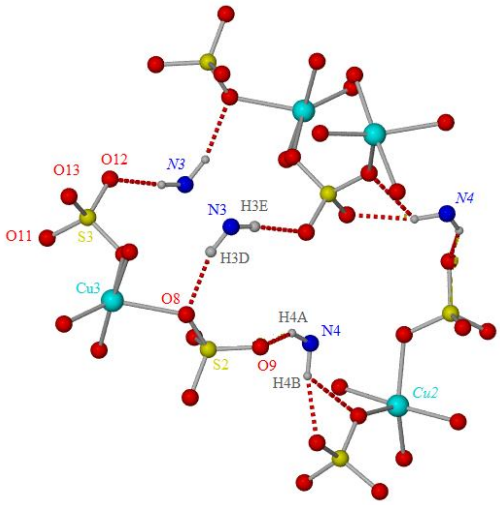

*Figure 5-7. The hydrogen bonding for **1**. The methyl groups of $NMe_2H_2^+$ cations are omitted for clarity. Symmetry generated atoms are labelled in italics.*

The parameters of hydrogen bonding are given in Table 5-3.

*Table 5-3. Hydrogen bonding parameters for **1**.**

Atoms	Distance N···O (Å)	Distance H···O (Å)	Angle (°)
N3−H3E···O12#2	2.712	1.80	170
N3−H3D···O8	2.774	1.94	149
N4−H4A···O9	2.843	2.02	149
N4−H4B···O13#3	2.800	1.90	166
N4−H4B···O11#3	3.118	2.62	114

**Symmetry transformations used to generate equivalent atoms:*
#2 – x + 2, - y - 1, - z; #3 x - 1/2, - y - 1/2, z - 1/2.

In the crystal structure of **1**, the sheets are not further connected adopting a layered arrangement with the DMF molecules pointing between sheets as can been seen in Figure 5-8.

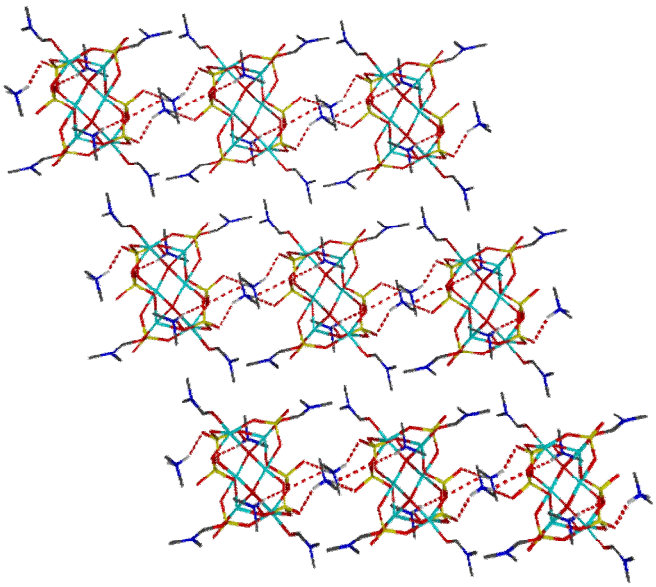

*Figure 5-8. Structure of **1** viewed along b, showing how the sheets form layers. Hydrogen atoms except those involved in hydrogen bonding have been omitted for clarity.*

5.2.2. Crystal structure of $(NMe_2H_2)_4[Cu_6O_2(SO_4)_6(DMF)_2]$, 2

Yellow-green block-like crystals of suitable size for X-ray single diffraction were collected from the solvothermal reaction of $CuSO_4 \cdot 5H_2O$ with H_2caldc in DMF. The crystal data revealed that the $(caldc)^{2-}$ anion is not been incorporated in the structure which was formulated as $(NMe_2H_2)_4[Cu_6O_2(SO_4)_6(DMF)_2]$, **2**. The crystal data and refinement parameters for **2** are given in Table 5-4.

Attempts to synthesise **2** with no addition of H_2caldc have subsequently been developed and its synthesis can be found in the experimental section of this chapter.

*Table 5-4. Crystallographic data and refinement parameters for **2**.*

Empirical formula	$C_{14}H_{46}Cu_6N_6O_{28}S_6$	
Formula weight	1320.17	
Temperature	150(2) K	
Wavelength	0.71073 Å	
Crystal system	Triclinic	
Space group; Z	$P\bar{1}$; 1	
Unit cell dimensions	a = 8.5880(2) Å	α = 106.496(1)°
	b = 10.6840(3) Å	β = 104.593(1)°
	c = 12.8170(3) Å	γ = 105.935(2)°
Volume	1012.49(4) Å^3	
Density (calculated)	2.165 g/cm^3	
Crystal size	0.28 x 0.15 x 0.08 mm	
Theta range for data	3.55 to 27.49°	
Reflections collected/	15974/ 3823 [R(int) = 0.0492]	
Data Completeness	0.992	
Goodness-of-fit on F^2	1.068	
Final R indices [I>2σ(I)]	$R1$ = 0.0326 $wR2$ = 0.0760	
R indices (all data)	$R1$ = 0.0450 $wR2$ = 0.0813	
Largest diff. peak and hole	1.263 and -0.907 eÅ^{-3}	

The crystal structure of $(NMe_2H_2)_4[Cu_6O_2(SO_4)_6(DMF)_2]$ **2** has some similarities to that of $(NMe_2H_2)_4[Cu_6O_2(SO_4)_6(DMF)_4]$ **1** consisting of four dimethylammonium cations for each discrete $[Cu_6O_2(SO_4)_6(DMF)_4]^{4-}$ anion. However from their formulae it can be observed that the number of DMF ligands per Cu_6 unit is reduced to two in **2**.

The asymmetric unit of **2** (Figure 5-9) consists of three copper(II) centres, three sulfate anions ligands, one oxide anion, one DMF ligand and two dimethylammonium cations. The dimethylammonium cation based on N3 is disordered in a 80 : 20 ratio.

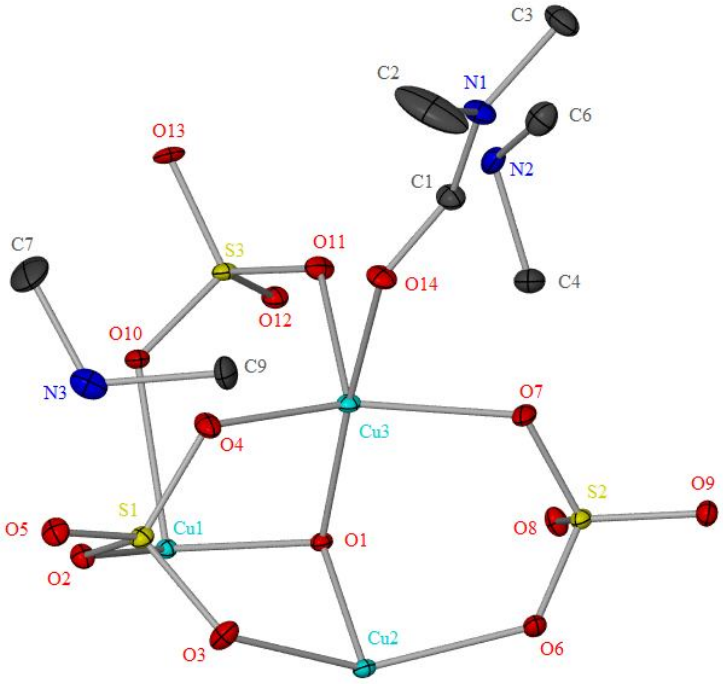

*Figure 5-9. The asymmetric unit of **2** showing thermal ellipsoids at the 30% probability level. Hydrogen atoms and the minor disordered component of the $NMe_2H_2^+$ cation have been omitted for clarity.*

The Cu1 centre is situated, near a crystallographic inversion centre leading to formation of aggregates with formulae $[Cu_6O_2(SO_4)_6(DMF)_2]^{4-}$. The structure of each $[Cu_6O_2(SO_4)_6(DMF)_2]^{4-}$ aggregate is broadly similar to the discrete $[Cu_6O_2(SO_4)_6(DMF)_4]^{4-}$ aggregates in **1**. The $[Cu_6O_2(SO_4)_6(DMF)_2]^{4-}$ aggregate in **2** contains two edge-sharing $Cu_4(\mu_4\text{-}O)$ tetrahedra (Figure 5-10) with a Cu1···Cu1#1[i] distance of 2.8592(7) Å. As in case of **1,** two triangular Cu_3 faces of the $Cu_4(\mu_4\text{-}O)$ tetrahedra are each capped by a μ_3-

[i] Symmetry transformation used to generate equivalent atoms: *#1 – x + 2, - y, - z.*

sulfato ligand and the two edge-sharing $Cu_4(\mu_4\text{-}O)$ tetrahedra are linked together by two μ_2-sulfato ligands through their nonshared vertices (Cu2 and Cu3).

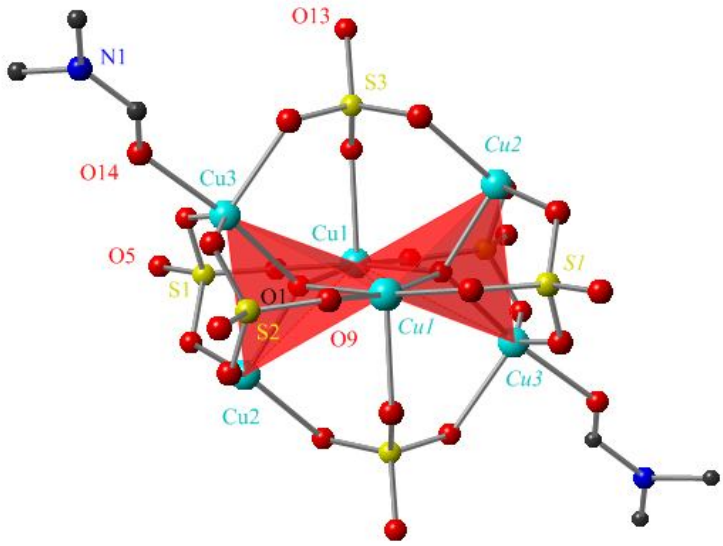

*Figure 5-10. Structure of **2** showing the $[Cu_6O_2(SO_4)_6(DMF)_2]^{4-}$ anion with the two central edge-sharing tetrahedra in red. Hydrogen atoms have been omitted for clarity. Symmetry generated atoms are labelled in italics.*

However, there are two major differences between the aggregates in **1** and **2**. Firstly in **2** the copper(II) centres involved in edge-sharing, Cu1, are five coordinate in contrast to the equivalent four coordinate centres in **1**. In **2**, Cu1 is additionally coordinated to an oxygen atom (O10) from the sulfato ligand bridging between the copper(II) centres (Cu2 and Cu3) at the ends of the two $Cu_4(\mu_4\text{-}O)$ tetrahedra. The axial contact, Cu1−O10 of 2.214(2) Å, is longer than those in the basal plane [1.952(2) − 1.999(2) Å], but significantly shorter than the analogous nonbonded contact in **1** [Cu1···O10#1[i] = 2.666(4) Å]. Selected bond lengths and angles for **2** are presented in Table 5-5.

*Table 5-5. Selected bond lengths (Å) and angles (°) for **2**.**

Atoms	Bond length	Atoms	Angle (°)

[i] Symmetry transformation used to generate equivalent atoms: #1 – x + 2, - y, - z.

Cu1−O1	1.952(2)	O2−Cu1−O1#1	172.19(8)
Cu1−O8#1	1.972(2)	O1−Cu1−O8#1	169.88(9)
Cu1−O1#1	1.990(2)	O1−Cu1−O2	94.90(8)
Cu1−O2	1.999(2)	O2−Cu1−O8#1	82.22(9)
Cu1−O10	2.214(2)	O1−Cu1−O1#1	86.99(8)
		O1#1−Cu1−O8#1	94.62(8)
		O2 −Cu1−O10	92.78(8)
		O1−Cu1−O10	97.79(8)
		O8#1 −Cu1−O10	92.05(8)
		O1#1 −Cu1−O10	94.47(8)
Cu2−O1	1.9494(19)	O13#2−Cu2−O1	168.09(9)
Cu2−O13#2	1.946(2)	O13#2−Cu2−O6	85.90(9)
Cu2−O6	2.021(2)	O13#2−Cu2−O3	81.94(9)
Cu2−O3	2.102(2)	O13#2−Cu2−O12#1	92.62(9)
Cu2−O12#1	2.122(2)	O6−Cu2−O3	138.44(9)
		O3−Cu2−O12#1	98.86(9)
		O6−Cu2−O12#1	121.35(8)
		O1−Cu2−O3	93.21(8)
		O1−Cu2−O6	90.67(8)
		O1−Cu2−O12#1	98.89(8)
Cu3−O1	1.956(2)	O14−Cu3−O1	171.96(9)
Cu3−O4	1.985(2)	O14−Cu3−O7	84.09(9)
Cu3−O14	1.991(2)	O14−Cu3−O4	82.64(9)
Cu3−O7	2.021(2)	O14−Cu3−O11	87.13(9)
Cu3−O11	2.143(2)	O4−Cu3−O7	146.40(10)
		O11−Cu3−O7	99.69(9)
		O4−Cu3−O11	110.28(9)
		O1−Cu3−O7	94.10(8)
		O1−Cu3−O11	100.90(8)
		O1−Cu3−O4	94.78(9)

**Symmetry transformation used to generate equivalent atoms: #1 – x + 2, - y, - z.*

By the criterion described above for a five coordinate centre, the geometric parameter τ for the Cu1 centre in **2** is (172.2 – 169.9)/60 = 0.04 which indicates a square pyramidal geometry for the Cu1 centre. The Cu2 and Cu3 centres in **2** are five coordinate as well but with coordination geometries between those expected for ideal square pyramidal and trigonal bipyramidal geometries, as indicated by their geometric parameter τ values. The geometric parameter for Cu2 equals (168.1 – 138.45)/60 = 0.49 having a similar value to the one for Cu3 which is (171.97 – 146.4)/60 = 0.43. Therefore the coordination geometries of Cu2 and Cu3 in **2** are broadly similar to Cu2 and Cu3 in **1**.

The Cu2 and Cu3 centres are both coordinated to an oxo ligand (O1), three sulfato ligands and a DMF molecule in case of Cu3 but not for Cu2 which is not solvated. In contrast the Cu2 is coordinated to a μ_3-sulfato ligand from a neighbouring aggregate. As a result the number of DMF ligands per anion is reduced to two, which constitute the second major difference between the aggregates in **1** and **2**. A consequence of these changes is that the μ_2-sulfato ligand in **1** is replaced by a μ_4-sulfato ligand in **2**, which plays herein an additional role linking the $[Cu_6O_2(SO_4)_6(DMF)_2]^{4-}$aggregates into chains that run along the *a* axis (Figure 5-11). In this case the aggregates in **2** can be represented as $[Cu_6(\mu_4\text{-}O)_2(\mu_3\text{-}SO_4)_4(\mu_4\text{-}SO_4)_2(DMF)_2]^{4-}$.

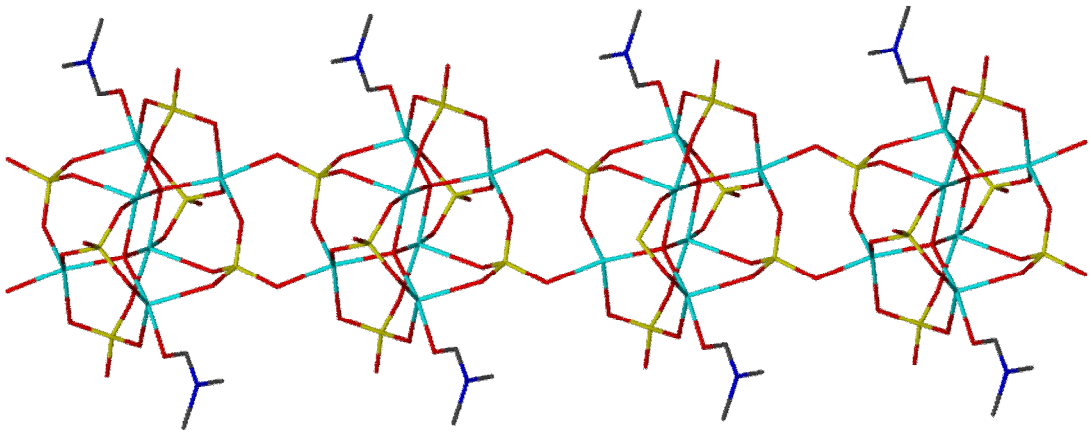

*Figure 5-11. Structure of **2** showing how the $[Cu_6O_2(SO_4)_6(DMF)_2]^{4-}$ anions link into chains. Hydrogen atoms have been omitted for clarity.*

The Cu2, the oxygen atom (O13) of the μ_3-sulfato ligand from the neighbouring aggregate and oxo ligand (O1) are almost collinear [O1−Cu2−O13#2[i] = 168.09(9)°], with the three oxygen atoms from the sulfato ligands approximately coplanar. The Cu3 with the DMF oxygen atom (O14) and oxo ligand (O1) are almost collinear [O1−Cu2−O14 = 171.96(9)°], with the three oxygen atoms from the sulfato ligands approximately coplanar. Selected bond lengths and angles for **2** are presented in Table 5-5.

The chains are further linked into sheets by hydrogen bonding to the $NMe_2H_2^+$ cations based on N2 as can be seen in Figure 5-12. The hydrogen bonds primarily involve the noncoordinated (O9) and the coordinated (O6 and O12) oxygen atoms of the sulfato ligands acting as acceptors.

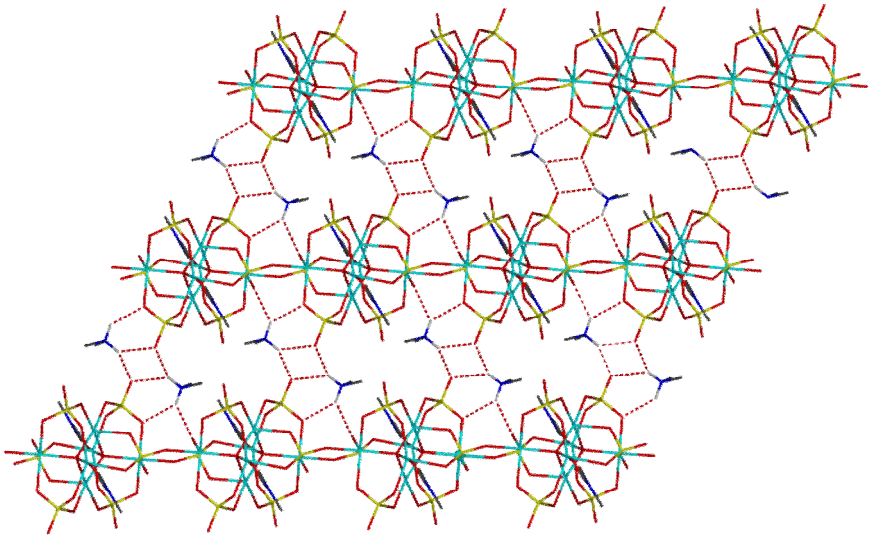

*Figure 5-12. Sheets of **2** in the ab plane. All hydrogen atoms except those involved in hydrogen bonding have been omitted for clarity.*

The remaining noncoordinated oxygen atom of the sulfato ligand (O5) acts as a hydrogen bond acceptor along with the coordinated oxygen atom O3 in hydrogen bonding with the $NMe_2H_2^+$ cation based on N3 to form sheets as can be seen in Figure 5-13.

[i] Symmetry transformation used to generate equivalent atoms: #2 x + 1, y, z.

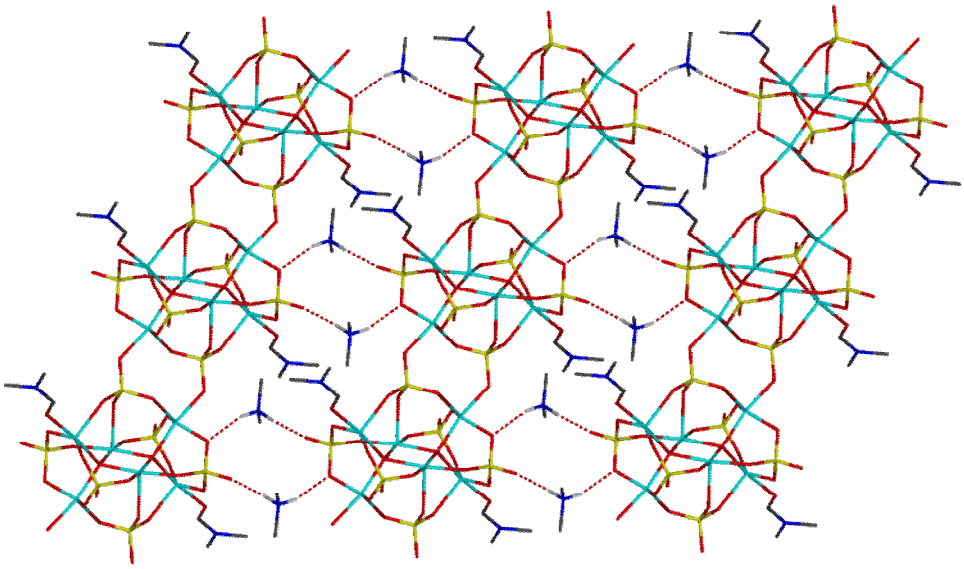

*Figure 5-13. Structure of **2** showing chains linked into sheets. All hydrogen atoms except those involved in hydrogen bonding have been omitted for clarity.*

The parameters of hydrogen bonding except those involving the minor disordered component of the dimethylammonium cation based on N3 are given in Table 5-6.

*Table 5-6. Hydrogen bonding parameters for **2**.**

Atoms	Distance N···O (Å)	Distance H···O (Å)	Angle (°)
N2–H5A···O9#3	3.037	2.51	117
N2–H5A···O9#4	2.808	1.98	148
N2–H5B···O12	2.983	2.28	133
N2–H5B···O6#3	2.886	2.18	132
N3–H3D···O5	2.790	1.88	170
N3–H3E···O3#5	3.033	2.14	163

**Symmetry transformations used to generate equivalent atoms:*
#3 x - 1, y, z; #4 – x + 2, - y + 1, - z; #5 – x + 3, - y, - z + 1.

The hydrogen bonding in the gross structure of **2** renders a 3-D supramolecular network as shown in Figure 5-14.

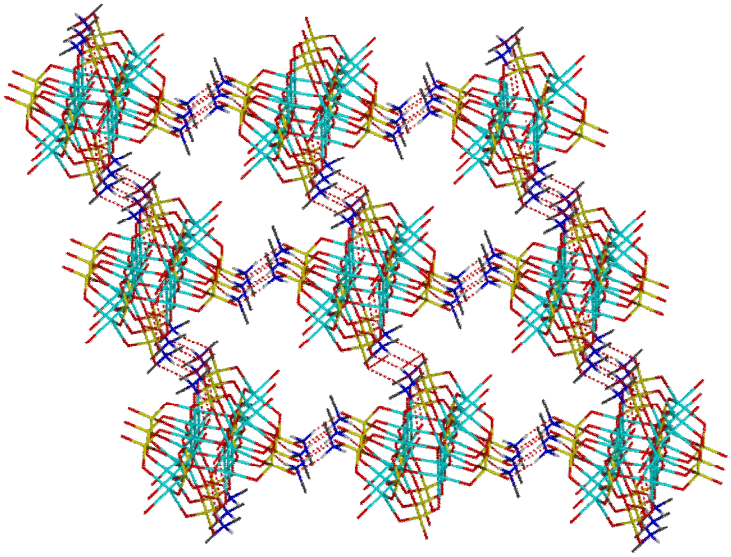

*Figure 5-14. The 3-D supramolecular network of **2**. DMF molecules and all hydrogen atoms except those involved in hydrogen bonding have been omitted for clarity.*

Both crystal structures of **1** and **2** have features in common with the structure of the rare copper(II) sulfate mineral fedotovite, $K_2Cu_3O(SO_4)_3$[17]. All three structures contain the same unusual core $[Cu_6(\mu_4\text{-}O)_2(\mu_3\text{-}SO_4)_4(SO_4)_2]^{4-}$. However the two μ_2-sulfato groups in **1** and in fedotovite are replaced by μ_4-sulfato groups in **2**. The μ_4-sulfato groups in **2** and the μ_2-sulfato groups in fedotovite, bridge between the $[Cu_6(\mu_4\text{-}O)_2(\mu_3\text{-}SO_4)_4(SO_4)_2]^{4-}$ units to form 2-D networks which is not the case for the μ_2-sulfato groups in **1**. All three structures extend into 2-D networks through extensive hydrogen bonding which involves the dimethylammonium ions (NMe_2H_2) in both **1** and **2** and the potassium ions in fedotovite. The number of DMF ligands per $[Cu_6(\mu_4\text{-}O)_2(\mu_3\text{-}SO_4)_4(SO_4)_2]^{4-}$ unit is reduced to two in **2** from four in **1**, which promotes linking the $[Cu_6(\mu_4\text{-}O)_2(\mu_3\text{-}SO_4)_4(\mu_4\text{-}SO_4)_2(DMF)_2]^{4-}$ aggregates in **2** into tapes, hence increasing its dimensionality. Notably, like **1** and **2**, fedotovite has been observed to be unstable in air.

5.2.3. Crystal structure of $(NMe_2H_2)[Cu_2(OH)(SO_4)_2(H_2O)_2]$, 3

Turquoise plate-like crystals of suitable size for X-ray single diffraction were collected from a DMF solution of $CuSO_4 \cdot 5H_2O$ and dimethylammonium chloride $[NMe_2H_2]Cl$ after three weeks at room temperature. The compound **3** was formulated as $(NMe_2H_2)[Cu_2(OH)(SO_4)_2(H_2O)_2]$ and its crystal data and refinement parameters are given in Table 5-7.

*Table 5-7. Crystallographic data and refinement parameters for **3**.*

Empirical formula	$C_2H_{13}Cu_2NO_{11}S_2$	
Formula weight	418.33	
Temperature	150(2) K	
Wavelength	0.71073 Å	
Crystal system	Monoclinic	
Space group; Z	$P2_1/n$; 4	
Unit cell dimensions	a = 6.8990(1) Å	α = 90°
	b = 17.0780(4) Å	β = 90.779(1)°
	c = 10.3860(3) Å	γ = 90°
Volume	1223.58(5) Å^3	
Density (calculated)	2.271 g/cm^3	
Crystal size	0.15 x 0.10 x 0.10 mm	
Theta range for data collection	3.52 to 27.53°	
Reflections collected/	22218/ 2105 [R(int) = 0.0879]	
Data Completeness	0.994	
Goodness-of-fit on F^2	1.069	
Final R indices [I>2σ(I)]	$R1$ = 0.0389 $wR2$ = 0.0811	
R indices (all data)	$R1$ = 0.0636 $wR2$ = 0.0910	
Largest diff. peak and hole	0.587 and -0.898 eÅ^{-3}	

The asymmetric unit of **3** (Figure 5-15) contains one full-occupancy copper(II) centre (Cu1), two half-occupancy copper(II) centres (Cu2 and Cu3 located at inversion centres),

two sulfate anions, one dimethylammonium cation, two water ligands and one hydroxy group, which acts as a ligand.

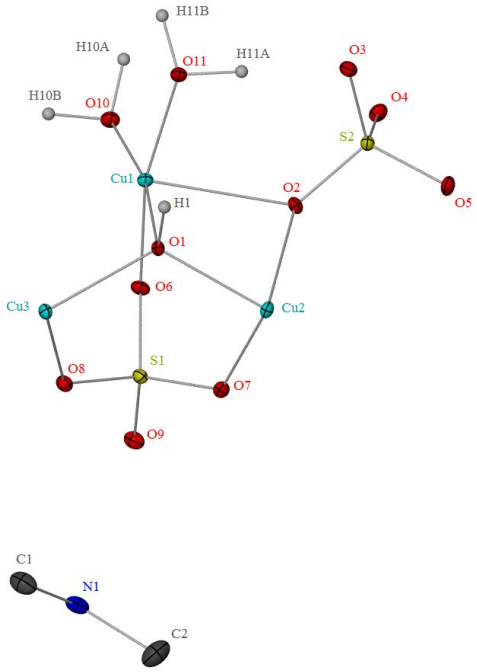

Figure 5-15. The asymmetric unit of ***3,*** *showing thermal ellipsoids at the 30% probability level. Hydrogen atoms of the dimethylammonium cations have been omitted for clarity.*

In the crystal structure of **3**, each $[Cu_2(OH)(SO_4)_2(H_2O)_2]^-$ anion is charge balanced by a $NMe_2H_2^+$ cation. The copper(II) centres in **3** are not solvated by DMF molecules as in **1** and **2** but by water ligands and the tetrahedral μ_4-O is replaced by the trigonal pyramidal μ_3-OH. In **3,** the building block represented by the trigonal pyramid $Cu_3(\mu_3\text{-OH})$ is extended by the virtue of Cu2 and Cu3 being located at crystallographic inversion centres, into tapes along the crystallographic *a* axis (Figure 5-16).

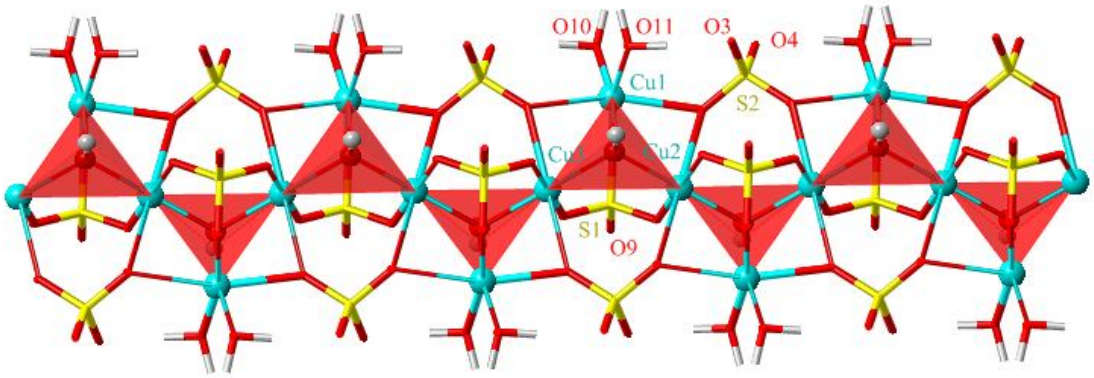

*Figure 5-16. Structure of **3** showing the $[Cu_2(OH)(SO_4)_2(H_2O)_2]^-$ tapes with the $Cu_3(OH)$ triangles in red.*

The intra-trimeric Cu···Cu distances are in the range of 3.21−3.45 Å (average of 3.33 Å). The hydroxo O1 atom deviates by 0.567 Å from the plane defined by the three copper atoms and this plane is also capped by a sulfato group acting as a tripod bridge bonding to all three copper atoms through three oxygen atoms. Hence the trimeric units can be formulated as $Cu_3(\mu_3\text{-}OH)(\mu_3\text{-}SO_4)$. The second sulfato group is acting as a tetrapod bridge bonding through two oxygen atoms, each to two different copper atoms. Thus the anion in **3** can be represented as $[Cu_2(\mu_3\text{-}OH)(\mu_3\text{-}SO_4)(\mu_4\text{-}SO_4)(H_2O)_2]^-$ because of the two half-occupancy copper(II) centres (Cu2 and Cu3), where the water ligands are both coordinated to Cu1.

In the pyramidal $Cu_3(\mu_3\text{-}OH)$ core, the three Cu−O1 bond lengths range from 1.941(3) to 2.019(3) Å and the average of the Cu−O1−Cu angles are 112.1°.

All three copper(II) centres are six coordinate; each one exhibiting tetragonally distorted octahedral geometries. The octahedral geometries for copper(II) complexes are always distorted due to the Jahn-Teller effect. The Cu1 centre is coordinated to a hydroxyl group through O1, two aqua ligands (through O10 and O11) and a μ_3-sulfato oxygen atom (O6) in the equatorial plane, and to two μ_4-sulfato oxygen atoms (O2 and O5#1[i]) in the axial positions. The contacts to the oxygen atoms (O2 and O5#1[i]) situated in the axial positions

[i] Symmetry transformation used to generate equivalent atoms: #1 x + 1, y, z.

are the longest ones with the bond lengths in the equatorial plane being in the range of 1.970(3) to 2.012(3) Å. Selected bond lengths and angles for **3** are presented in Table 5-8.

*Table 5-8. Selected bond lengths (Å) and angles (°) for **3**.**

Atoms	Bond length (Å)	Atoms	Angle (°)
Cu1−O10	1.970(3)	O1−Cu1−O6	91.00(11)
Cu1−O6	1.984(3)	O1 −Cu1−O11	88.69(12)
Cu1−O11	1.985(3)	O10−Cu1−O6	86.65(12)
Cu1−O1	2.012(3)	O10 −Cu1−O11	95.92(12)
Cu1−O5#1	2.281(3)	O1 −Cu1−O10	169.40(12)
Cu1−O2	2.384(3)	O6−Cu1−O11	166.99(12)
		O1 −Cu1−O2	85.93(10)
		O6 −Cu1−O2	80.10(11)
		O10−Cu1−O2	103.81(11)
		O11 −Cu1−O2	86.90(11)
		O10−Cu1−O5#1	90.85(11)
		O11−Cu1−O5#1	98.62(12)
		O1 −Cu1−O5#1	79.00(10)
		O6 −Cu1−O5#1	94.08(12)
		O2−Cu1−O5#1	163.78(10)
Cu2−O1	1.941(3)	O1−Cu2−O7	90.84(12)
Cu2−O7	1.960(3)	O1#2−Cu2−O7	89.16(12)
Cu2−O2	2.579(3)	O1−Cu2−O2	82.1(1)
		O7−Cu2−O2	86.3(1)
		O1#2−Cu2−O2	97.9(1)
		O7#2−Cu2−O2	93.7(1)
Cu3−O8	1.932(3)	O1−Cu3−O8	92.33(11)
Cu3−O1	2.019(3)	O8−Cu3−O1#3	87.67(11)
Cu3−O5#1	2.377(3)	O1−Cu3−O5#1	76.60(10)
		O8−Cu3−O5#1	93.58(11)
		O1#3−Cu3−O5#1	103.40(10)

		O8#3−Cu3−O5#1	86.42(11)

**Symmetry transformations used to generate equivalent atoms: #1 x + 1, y, z; #2 -x, -y + 2, -z + 2; #3 –x + 1, -y + 2, -z + 2.*

The copper(II) centres Cu2 and Cu3 are coordinated to two hydroxyl oxygen atoms (O1 and O1#2[i] and O1 and O1#3[i], respectively) and two μ_3-sulfato oxygen atoms (O7 and O7#2[i], and O8 and O8#3[i]) in the equatorial plane, with two longer contacts to the μ_4-sulfato oxygen atoms (O2 and O2#2[i], and O5#1[i] and O5#2[i], respectively) in the axial positions. The Cu2 and Cu3 centres link the triangular $Cu_3(\mu_3\text{-OH})$ units together into the tapes.

The tapes are supported by the presence of intramolecular hydrogen bonds between the coordinated aqua ligands (O11) and the noncoordinated oxygen atoms of the μ_4-sulfate (O3) as can be seen in Figure 5-17. There are also intermolecular hydrogen bonds between the tapes which link them into sheets as also shown in Figure 5-17. The intermolecular hydrogen bonds involve the aqua ligands (O10 and O11) and the noncoordinated oxygen atoms of the μ_4-sulfate (O3 and O4). The aqua ligands act as hydrogen bond donors and the oxygens of the μ_4-sulfate ligands act as hydrogen bond acceptors.

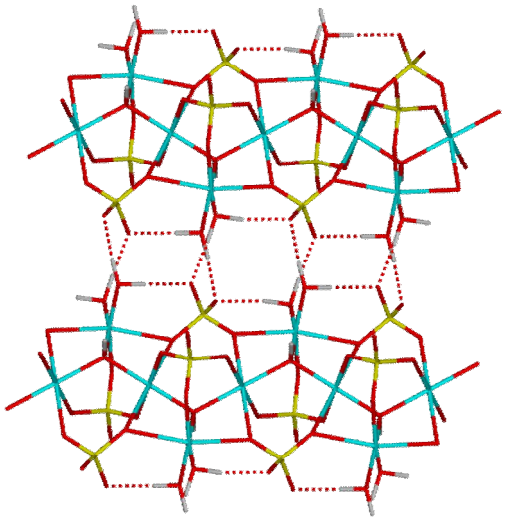

*Figure 5-17. The $[Cu_2(OH)(SO_4)_2(H_2O)_2]^-$ tapes in **3** linked into sheets.*

[i] Symmetry transformations used to generate equivalent atoms: *#2 -x, -y + 2, -z + 2; #3 –x + 1, -y + 2, -z + 2.*

The parameters of hydrogen bonding are given in Table 5-9.

*Table 5-9. Hydrogen bonding parameters for **3**.**

Atoms	Distance N/ O···O (Å)	Distance H···O (Å)	Angle (°)
O10−H10A···O3#5	2.670	1.70	171
O10−H10B···O4#1	2.754	1.78	174
O11−H11A···O3	2.682	1.76	157
O11−H11B···O4#5	2.718	1.74	177
N1−H1A···O2#6	2.993	2.21	142
N1−H1A···O6#6	3.037	2.28	140
N1−H1B···O9	2.771	1.90	158

**Symmetry transformations used to generate equivalent atoms: #1 x + 1, y, z; #5 – x, - y + 2, - z + 3; #6 x + 1/2, - y + 3/2, z - 1/2.*

Furthermore, H-bonds involving the $NMe_2H_2^+$ cations link the sheets into a 3-D supramolecular network (Figure 5-18) which is similar to that observed in **1**. These hydrogen bonds involve the dimethylammonium cations and both the coordinated (O2#6[i] and O6#6[i]) and noncoordinated (O9) sulfato oxygen atoms, though notably the hydroxyl O1−H1 group does not act as a hydrogen bond donor.

[i] *Symmetry transformation used to generate equivalent atoms: #6 x + 1/2, - y + 3/2, z - 1/2.*

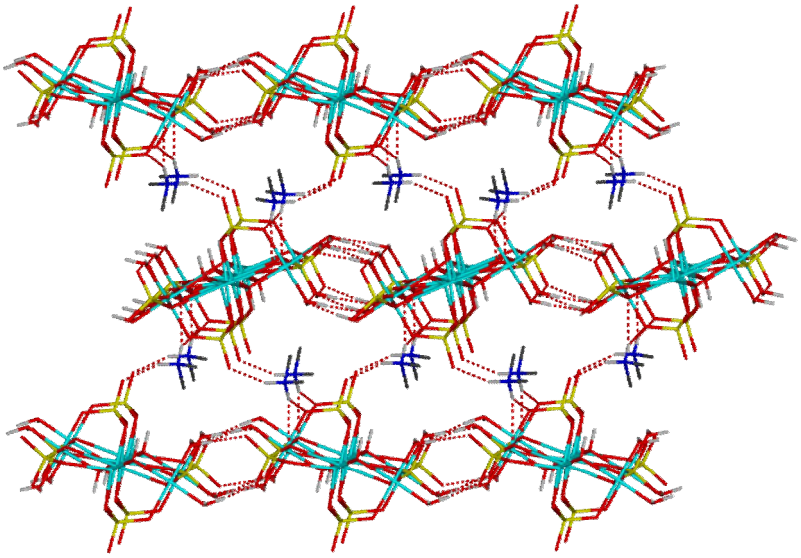

*Figure 5-18. The 3-D network of **3**. All hydrogen atoms except those involved in hydrogen bonding have been omitted for clarity.*

Triangular $Cu_3(\mu_3\text{-}OH)$ units including the mineral antlerite $Cu_3(OH)_4SO_4$[16] are relatively well-known[19] but there are only three previously reported examples of compounds containing $Cu_3(\mu_3\text{-}OH)(\mu_3\text{-}SO_4)$ units, in which the plane defined by the three copper(II) atoms is capped by a μ_3-sulfato ligand. Previously reported compounds containing $Cu_3(\mu_3\text{-}OH)(\mu_3\text{-}SO_4)$ units are a discrete Cu_3 compound that was reported by Beckett and Hoskins in 1972,[20] and more recently two $Cu_{10}(SO_4)_8$ aggregates.[21, 22]

5.2.4. Magnetic studies

The proximity of the $3d^9$ copper(II) centres in **1**–**3** prompted us to study their magnetic behaviour. In that respect, magnetic susceptibility χT and magnetization M have been measured for compounds **1** and **3**. These measurements were carried out by Dr. Yanhua Lan working with Prof. Annie Powell from Institut für Anorganische Chemie der Universität Karlsruhe, Karlsruhe Institute of Technology, Germany.

Plots of magnetic susceptibility χT against temperature for **1** and **3** in an external magnetic field of 1000 Oe (1 Oe = 79.6 A/m) are shown in Figure 5-19a and Figure 5-20a, respectively. It can be observed that at temperatures above 60 K for both compounds the magnetic susceptibility χT increases with the increase of temperature which indicates the presence of antiferromagnetic interactions at high temperatures. The greater temperature

dependence is observed for **1** which suggests stronger antiferromagnetic interactions in this compound.

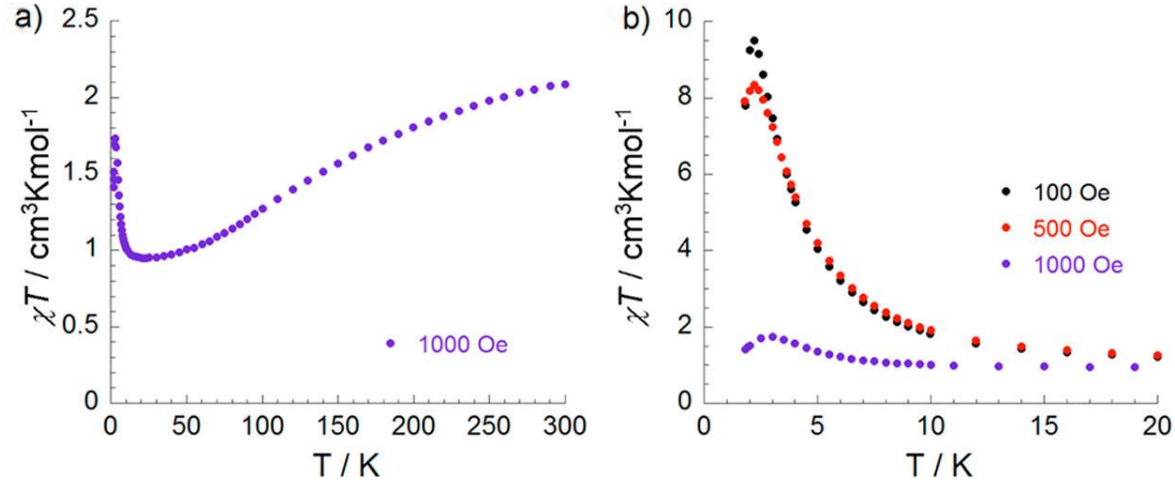

*Figure 5-19. Magnetic susceptibility (χT) vs temperature for **1**: a) at 1000 Oe and b) below 20 K for the indicated applied magnetic fields.*

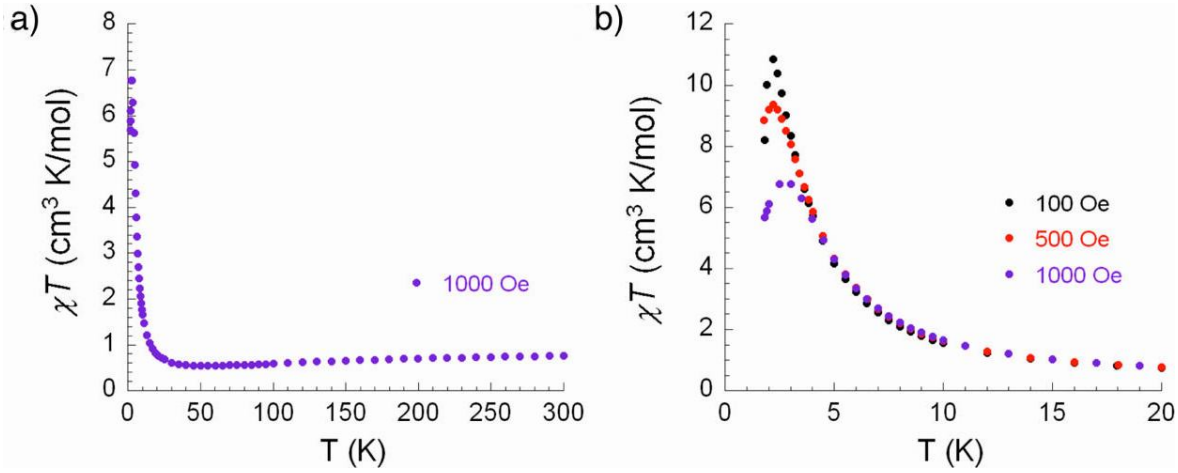

*Figure 5-20. Magnetic susceptibility (χT) vs temperature for **3**: a) at 1000 Oe and b) below 20 K for indicated applied magnetic fields.*

For both **1** and **3**, the presence of antiferromagnetic interactions at high temperatures is confirmed by the negative Weiss constants (θ) of −82.0 K and −18.7 K for **1** and **3**, respectively (Figure 5-21).

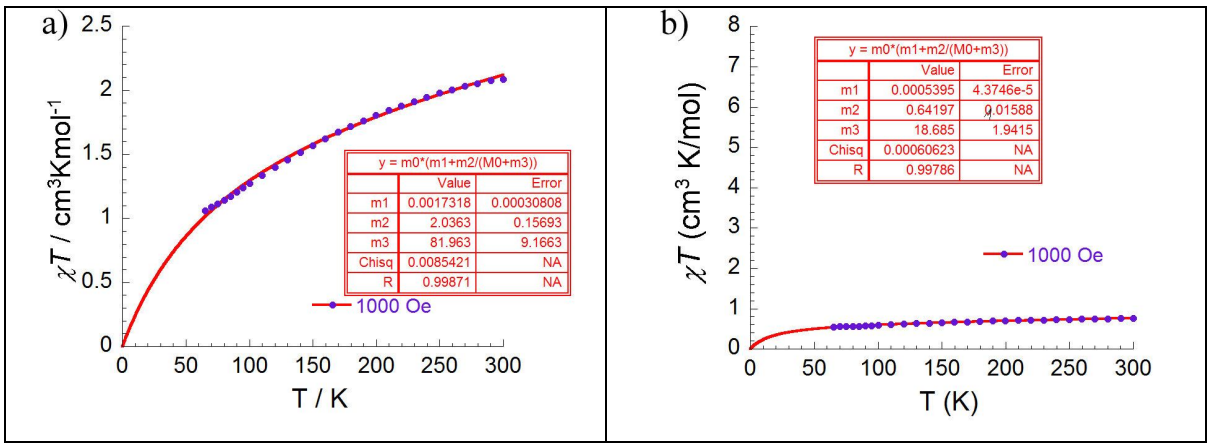

*Figure 5-21. Curie-Weiss fit to the data of: a) **1** and b) **3**, above 60 K.*

Plots of magnetic susceptibility χT against temperature below 20 K for **1** and **3** in a variable external applied magnetic field of 1000 Oe, 500 Oe and 100 Oe are shown in Figure 5-19b and Figure 5-20b, respectively. It can be observed that for both compounds **1** and **3**, below 20 K the magnetic susceptibility χT increases rapidly with the decrease of temperature and reaches a maximum at approximate 3 K. The maximum value of magnetic susceptibility χT increases with the decrease of the external applied magnetic field from 1000 Oe to 100 Oe. This type of field-induced response in the susceptibility is related to the unpaired spins of the d^9 copper(II) centres canting to each other at very low temperatures.

Magnetization curves for compounds **1** and **3** (Figure 5-22a and Figure 5-23a) at temperatures of 2 K, 3 K and 5 K show a rapid increase of magnetization, M, with the external magnetic field, H. For **1,** the magnetization M increases slowly with the external magnetic field H reaching approximately 1.2 μB at 70 000 Oe though no saturation point was observed. For **3**, the magnetization M increases more rapidly and almost reaches a saturation of 1.1 μB at 70 000 Oe. The first derivative plots of the magnetization M against external magnetic field H show for both compounds **1** and **3** (Figure 5-22b and Figure 5-23b, respectively) the presence of an inflection point at a field of 110 Oe. This suggests a metamagnetic behaviour for both compounds **1** and **3** with the field of 110 Oe representing the characteristic field at which the magnetic field overcomes antiferromagnetic interactions, allowing for the parallel alignment of the spins.

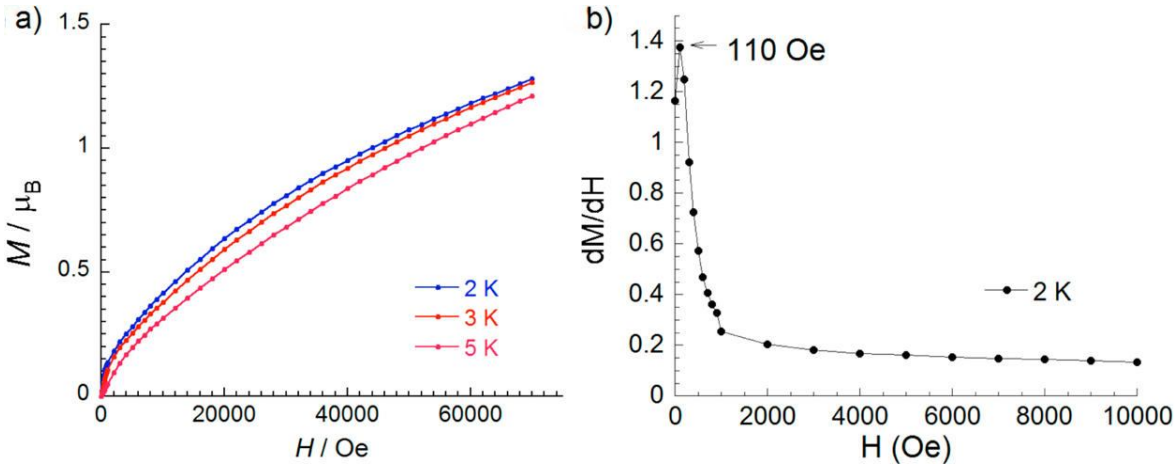

*Figure 5-22. Magnetization (M) vs external magnetic field (H) for **1**: a) at indicated temperatures and b) its first derivative at 2 K showing an inflection point at a field of 110 Oe.*

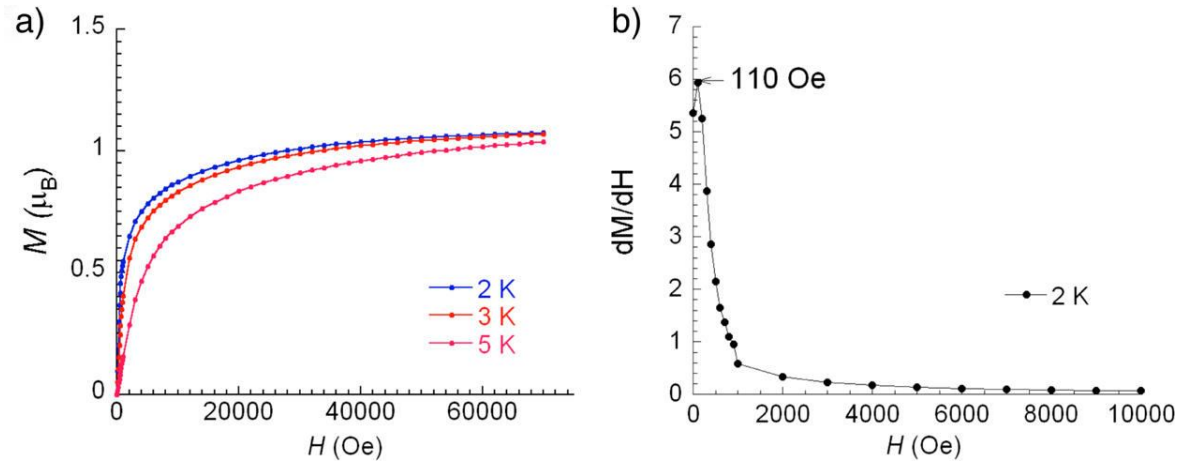

*Figure 5-23. Magnetization (M) vs external magnetic field (H) for **3**: a) at indicated temperatures and b) its first derivative at 2 K showing an inflection point at a field of 110 Oe.*

AC (alternating current) magnetic susceptibility studies, which monitor the response of a material's magnetic moment to an applied oscillating magnetic field, were also undertaken for the two compounds. The plots of the AC susceptibility for both **1** and **3** (Figure 5-24 and Figure 5-25, respectively), for in-phase (χ′) component (Figure 5-24a and Figure 5-25a) and out-of-phase (χ″) component (Figure 5-24b and Figure 5-25b) show the absence of out-of-phase (χ″) component. These results suggest the presence of a small canting

angle for both compounds **1** and **3**. Therefore the magnetization is almost cancelled when the spin carriers are antiferromagnetically coupled and only slightly canted.

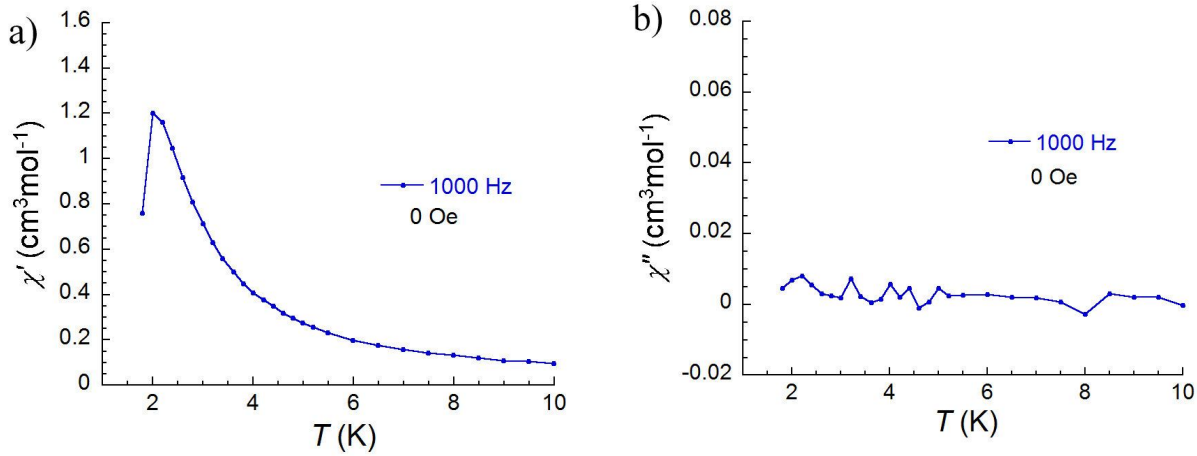

*Figure 5-24. AC susceptibility vs. temperature for the a) in-phase signal χ' and b) out-of-phase signal χ'' for **1**, in a AC field oscillating frequency of 1000 Hz with a DC field of 0 Oe.*

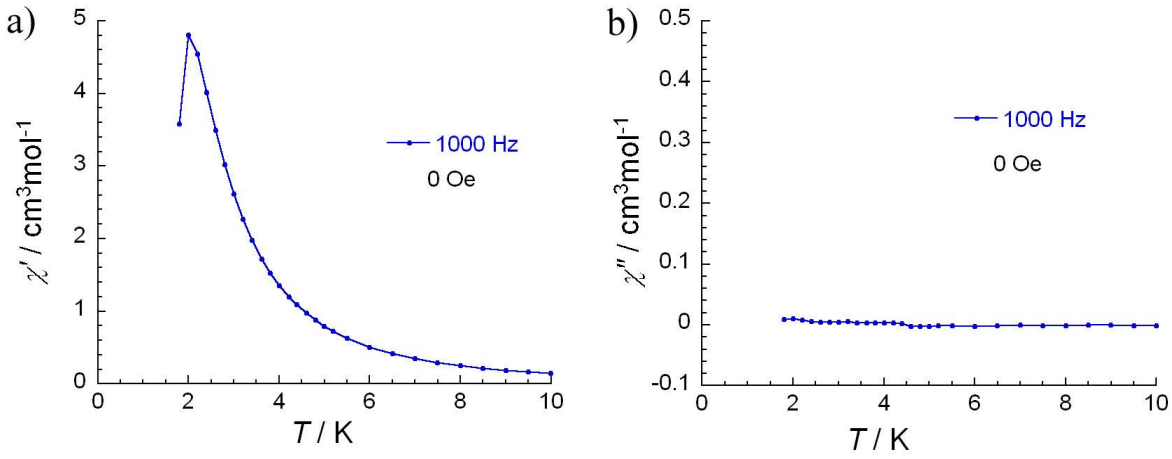

*Figure 5-25. AC susceptibility vs. temperature for the a) in-phase signal χ' and b) out-of-phase signal χ'' for **3**, in a AC field oscillating frequency of 1000 Hz with a DC field of 0 Oe.*

There have been a few previous magnetic studies on compounds containing octahedral magnetic transition metals as copper(II) and tetrahedral nonmagnetic sulfate anions. Vilminot *et al.* [23] reported canted-antiferromagnetic behaviour for $Cu_3(OH)_4SO_4$ (antlerite) and $Cu_4(OH)_6SO_4$ (brochantite).

Although canted antiferromagnetism has been reported recently for some copper(II) compounds[24-26], compounds **1** and **3** are the first examples of copper(II) sulfate frameworks containing dimethylammonium cations shown to exhibit spin-canting metamagnetic behaviour.

The magnetic measurement of a copper(II) coordination polymer $Cu_2(cpa)_2$ (H_2cpa= 4-carboxyphenoxyacetic acid) in different magnetic fields suggest a weak ferromagnetic ordering taking place below 20 K, arising from spin canting phenomenon due to the non-coplanar basal planes of copper ions.[27]

Sulfato-bridged Cu(II) materials are known to yield anti- or ferromagnetic exchange coupling, with long-range order exhibited in some cases[10, 28] but there are scarcer examples of sulfate compounds exhibiting spin canting behaviour as was reported by Weng *et al* [29].

5.3. Experimental

5.3.1. General

The solvothermal syntheses were carried out in thick-walled glass vials (10 - 30 cm^3) purchased from Biotage and heated in programmable ovens. The reagents used for syntheses were purchased commercially and used without further purification. Unless otherwise noted, the DMF was an A.C.S. reagent.

Powder X-ray diffractions (PXRDs) were recorded at the University of Bath on a Bruker AXS D8 Advance diffractometer with copper Kα radiation of wavelength 1.5406 Å at 298 K. Samples were placed in 0.5 mm diameter Lindemann capillaries, and measured with a 2θ range of 3-60°. The step size was 0.016° with time per step of 134.5 s. Simulated X-ray powder patterns were generated from single crystal data that were imported into PowderCel [30] with the step size of 0.02° and time per step of 1.00 s.

Magnetic measurements were carried out by Dr. Yanhua Lan working in the group of Prof. Annie Powell from Institut für Anorganische Chemie der Universität Karlsruhe, Karlsruhe Institute of Technology, Germany. Magnetic susceptibility measurements were obtained using a Quantum Design SQUID (superconducting quantum interference device) MPMS-

XL susceptometer. This magnetometer works between 1.8 and 400 K for direct current (DC) applied fields ranging from -70 to 70 kOe. Measurements were performed on polycrystalline samples of **3** (36.7 mg) and **1** (33.0 mg), respectively. Alternating current (AC) susceptibility measurements were measured with an oscillating AC field of 3 Oe and AC frequencies at 1000 Hz. The magnetic data were corrected for the sample holder.

The sensitivity of **1-3** reduced the number of analyses which could have been undertaken for these compounds (IR, UV-VIS, TGA) and prevented accurate microanalysis from being obtained too, though in all cases the powder X-ray diffraction patterns of the DMF-saturated samples (Figure 5-26 to Figure 5-27) show a good correspondence to those simulated from the X-ray single crystal analyses.

5.3.2. Single-Crystal X-Ray Crystallography

X-ray diffraction data on structures were collected by me on a Nonius Kappa CCD diffractometer, using Mo-Kα radiation of wavelength 0.71073 Å at 150 K, at the University of Bath.

The structures were solved using SHELXS-97[31] and refined using full-matrix least squares in SHELXL-97[31]. The final refinements were run by Dr. Mary Mahon and were generally straightforward with the following exceptions and points of note. All non-hydrogen atoms were refined anisotropically in the final least squares run, and hydrogen atoms were included at calculated positions.

Nitrogen bound hydrogen atoms for all three structures were located and refined at 0.92 Å from the relevant parent atoms.

For compound **1** only the major occupancy fragment atoms within the dimethylammonium cation based on N3 were refined anisotropically.

For compound **3** the oxygen bound hydrogens were located and refined at 0.98 Å from the relevant parent atoms.

5.3.3. Synthesis of antlerite, $Cu_3(OH)_4(SO_4)$

$CuSO_4 \cdot 5H_2O$ (0.06 g, 0.24 mmol) was dissolved with stirring and gentle heating in a DMF-water mixture (8 mL DMF ACS and 4 mL deionised water). This solution was placed in a 30 cm^3 tick-walled glass vial and heated at 95°C for 24 hours. The resultant turquoise solid was separated by filtration, washed with DMF ACS and air-dried to produce 0.026 g (yield = 93 %) turquoise powder.

5.3.4. Synthesis of $(NMe_2H_2)_4[Cu_6O_2(SO_4)_6(DMF)_4]$, 1

$CuSO_4 \cdot 5H_2O$ (0.060 g, 0.24 mmol) and $[NMe_2H_2]Cl$ (0.013 g, 0.16 mmol) were dissolved with stirring in 12 cm^3 DMF. The reaction mixture was placed in a 30 cm^3 thick-walled glass vial and heated at 95°C for 24 hours to yield tiny green crystals. The PXRD pattern of the DMF-saturated sample matches that of the simulated X-ray single crystal structure (Figure 5-26). The DMF-saturated sample was carefully dried straight after synthesis under a flow of nitrogen and stored in a sealed flask under nitrogen.

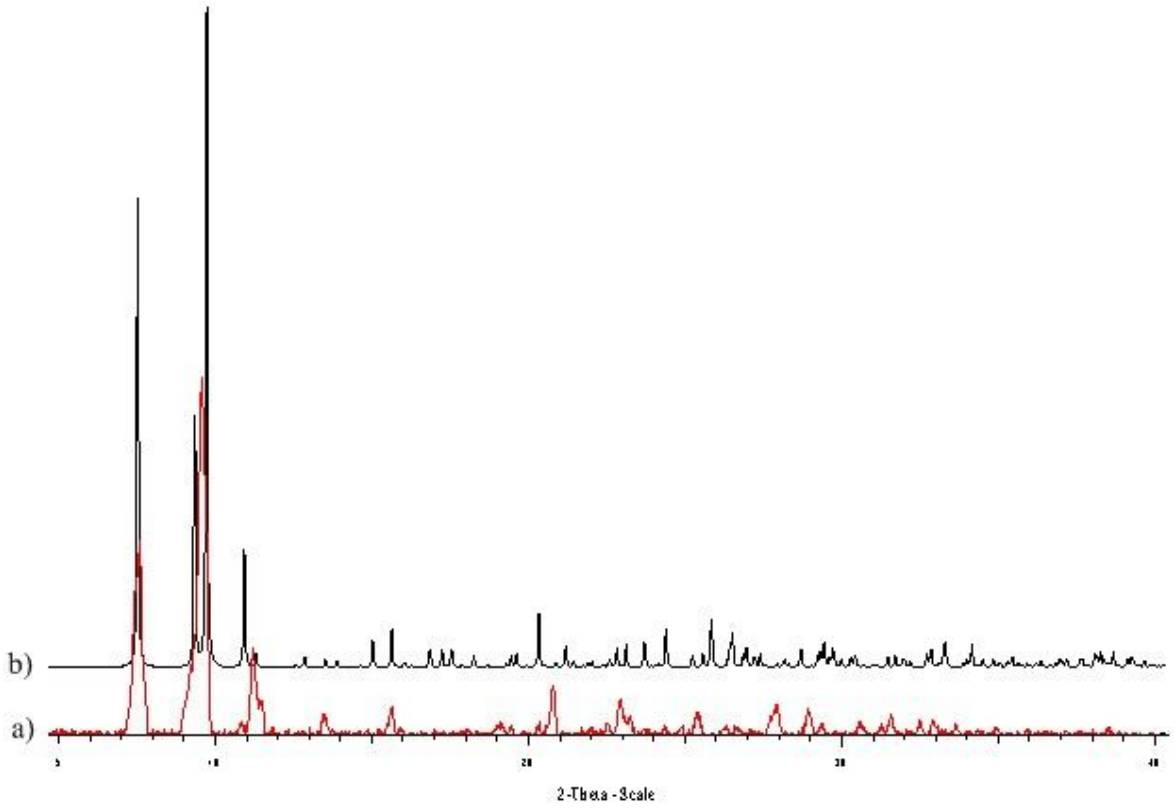

*Figure 5-26. The PXRD pattern for **1**: a) as-synthesised DMF-saturated sample and b) simulated from the X-ray crystal structure.*

5.3.5. Synthesis of $(NMe_2H_2)_4[Cu_6O_2(SO_4)_6(DMF)_2]$, 2

$CuSO_4 \cdot 5H_2O$ (0.60 g, 2.4 mmol) was dissolved with stirring in 12 cm^3 DMF. This solution was placed in a 30 cm^3 thick-walled glass vial and heated at 95°C for 24 hours to yield yellow-green tiny crystals. The PXRD pattern of the DMF-saturated sample matches that simulated from the X-ray crystal structure (Figure 5-27). After synthesis the DMF-saturated sample was carefully dried immediately under a flow of nitrogen and stored in a sealed flask under nitrogen.

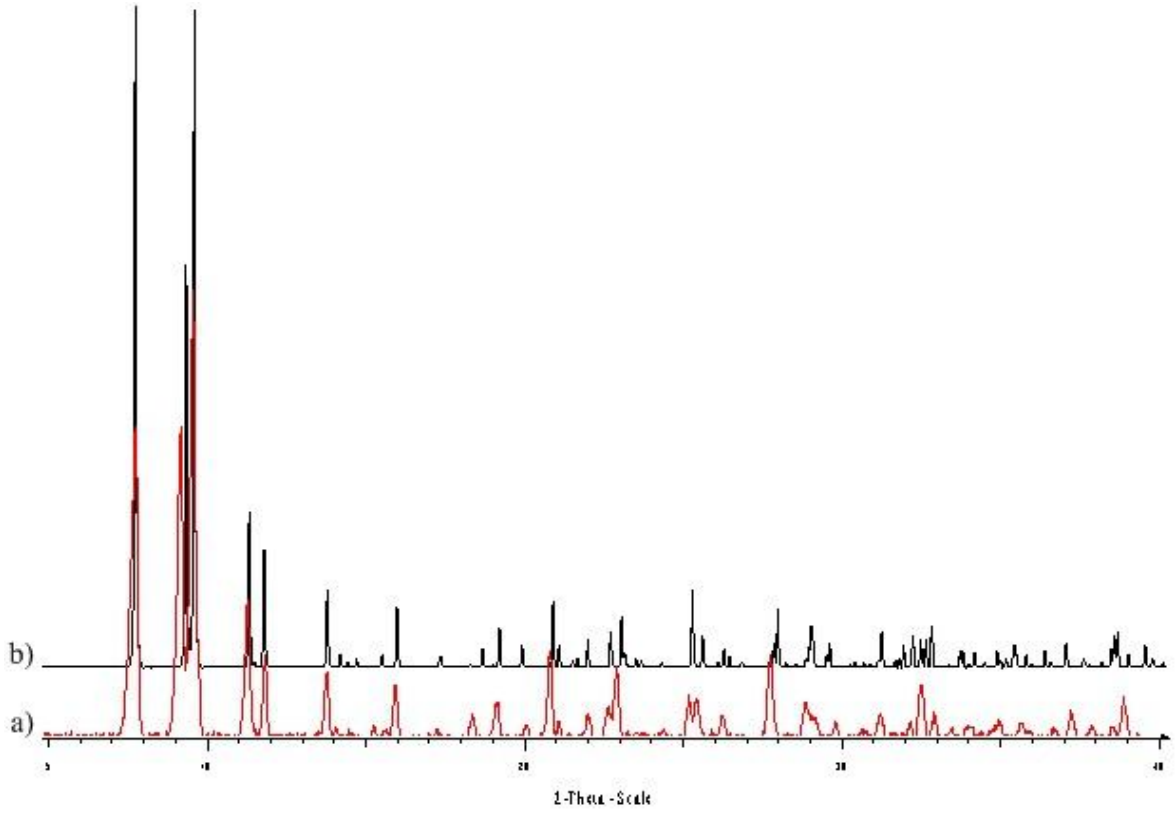

*Figure 5-27. The PXRD pattern for **2**: a) as-synthesised DMF-saturated sample and b) simulated from the X-ray crystal structure.*

5.3.6. Synthesis of $(NMe_2H_2)[Cu_2(OH)(SO_4)_2(H_2O)_2]$, 3

$CuSO_4 \cdot 5H_2O$ (0.6 g, 2.4 mmol) and $[NMe_2H_2]Cl$ (0.13 g, 1.6 mmol) were dissolved with stirring in 12 cm^3 DMF. This solution was placed in a vial and left undisturbed at room temperature. Turquoise crystals started to appear after a week, but the crystals were left in the mother liquor for a further two weeks after which they were harvested and analysed by X-ray single crystallography and powder X-ray diffraction. The PXRD pattern for the DMF-saturated sample matches that simulated from the X-ray crystal structure (Figure

5-28). Furthermore, if left to dry gently under atmospheric pressure, **3** shows a PXRD pattern identical to the DMF-saturated sample.

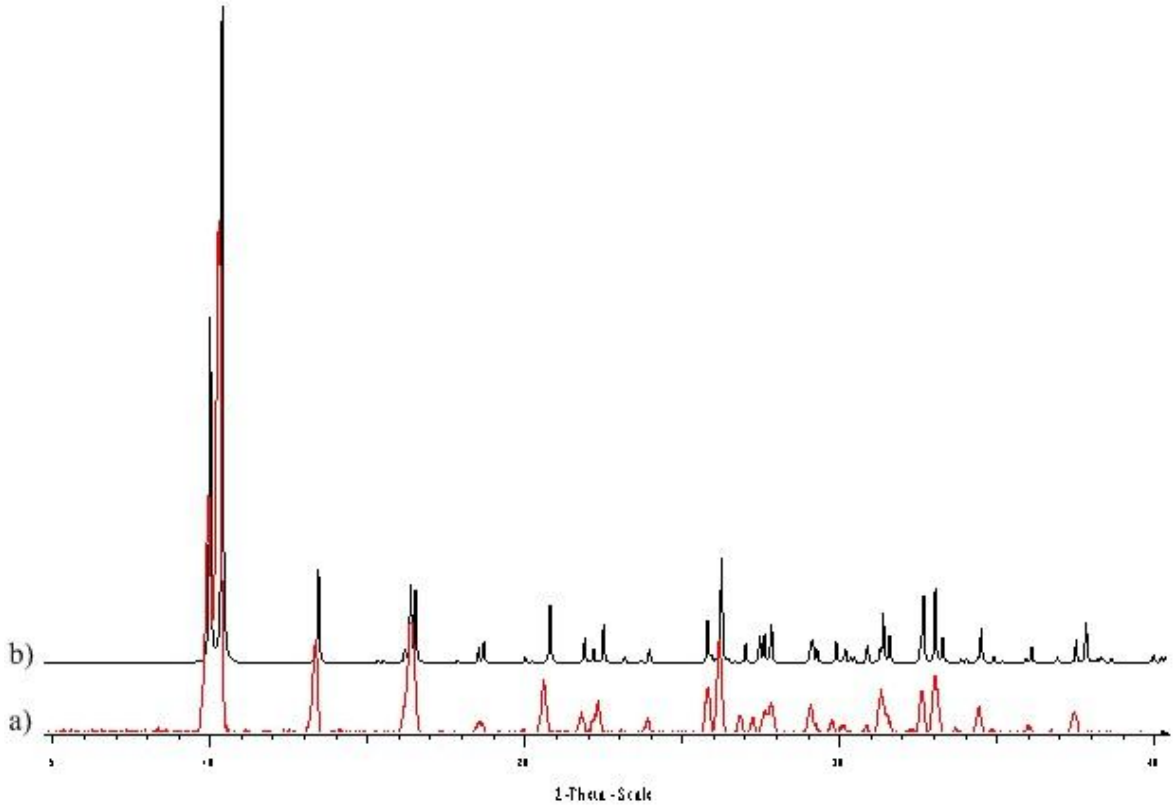

*Figure 5-28. The PXRD pattern for **3**: a) as-synthesised air-dried sample and b) simulated from the X-ray crystal structure.*

5.4. Structural changes

As mentioned above compounds **1-3** are all moisture-sensitive; with **1** and **2** undergoing structural changes rapidly while **3** changes more slowly.

In general the products were gently air-dried before running the powder X-ray diffraction measurements or other analyses and in the end the resulting solids were stored under ambient conditions. In this case it was observed that most of the samples changed their aspect or colour. PXRD investigations revealed that most of these samples suffered structural changes when taken out of the mother liquor. The only samples showing no structural changes whilst air-dried were the as-synthesised $Cu_3(SO_4)(OH)_4$ (antlerite) and **3**. However the PXRD experiments revealed that if the samples are gently dry under a flow of nitrogen and stored under nitrogen then they are able to retain their structural integrity.

A sample of **1** carefully dried under a flow of nitrogen and stored under nitrogen has been checked by means of PXRD. A decrease in peaks intensity and appearance of a new peak in the PXRD pattern of this sample of **1** (Figure 5-29) indicates a degradation of this sample. If a sample of **1** was left at ambient conditions, after one hour its PXRD pattern matches that of **3**, which further left at ambient conditions for one week converts into an unknown pale blue solid.

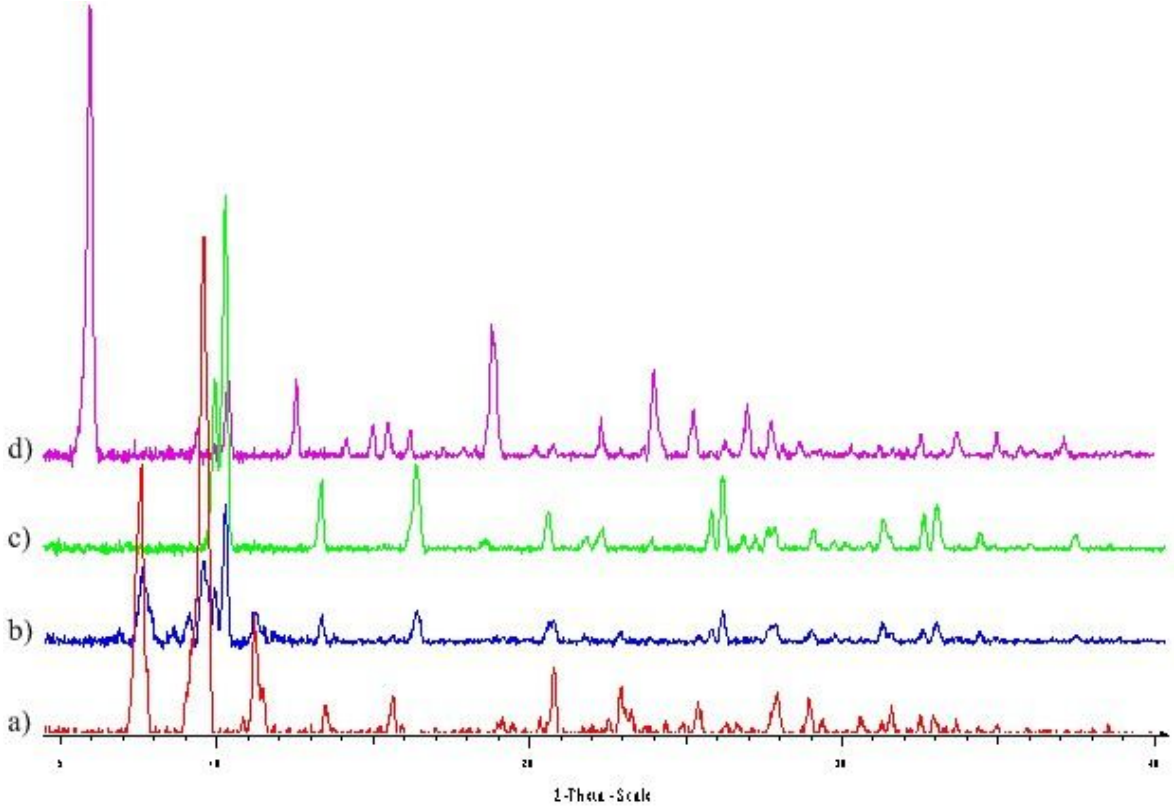

*Figure 5-29. The PXRD patterns changes suffered by **1**: a) as made **1**, b) as made **1** left one month under N_2, c) as made **1** left one hour at ambient conditions and d) the PXRD pattern of the unknown pale blue solid.*

When a sample of **2** is stored under nitrogen for one month its colour changes from yellow-green to blue-green and its PXRD pattern changes as shown in Figure 5-30, matching the PXRD pattern of the air-dried sample of **2**. Moreover this sample of **2** stored under nitrogen, shows different PXRD patterns if left few hours at ambient conditions and changes to the unknown pale blue solid when further left at ambient conditions for another week.

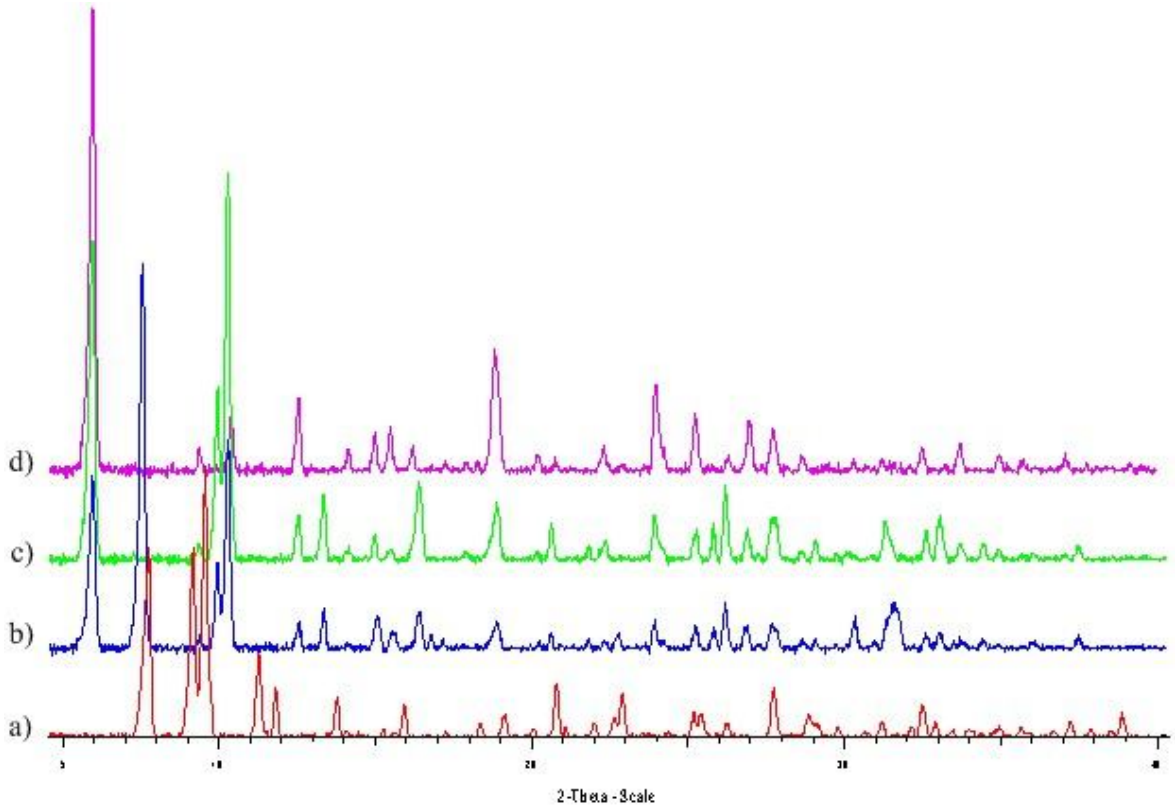

*Figure 5-30. The PXRD patterns changes suffered by **2**: a) as made **2**, b) as made **2** left one month under N_2, c) as made **2** left few hours at ambient conditions and d) the PXRD pattern of the unknown pale blue solid.*

An identical mixture with that producing **2** when left for a week at ambient conditions produced dark-blue large crystals but attempts to collect the X-ray single data on them were not been successful. The PXRD pattern of this DMF-saturated sample does not match any known PXRD patterns but the air-dried sample has a PXRD pattern matching that of $CuSO_4 \cdot 5H_2O$ as shown in Figure 5-31.

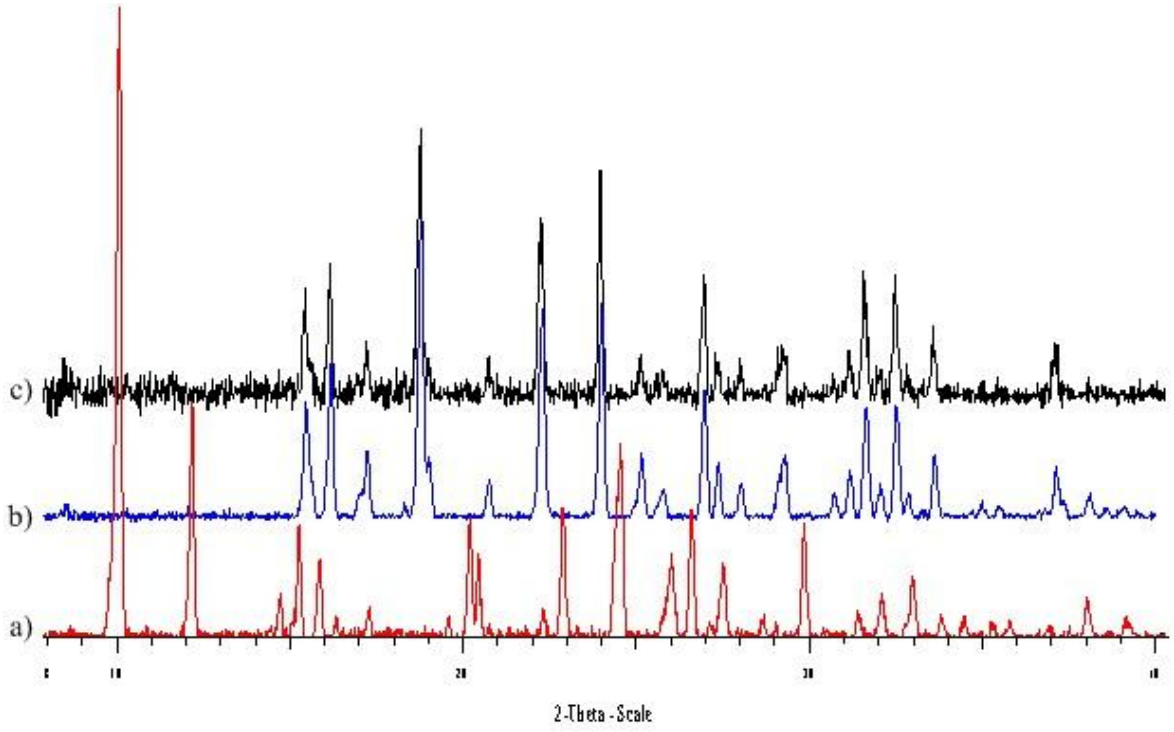

Figure 5-31. The PXRD pattern for the unknown dark blue crystals: a) DMF-saturated and b) air-dried; in comparison with c) crude $CuSO_4 \cdot 5H_2O$.

The PXRD patterns of DMF-saturated and air-dried samples of turquoise crystals of 3 harvested after 3 weeks are the same which indicates that 3 is stable at ambient conditions but the PXRD pattern of the DMF-saturated sample harvested from the same reaction mixture two weeks earlier does not match that of 3 (Figure 5-32).The air-dried sample of 3 stored at ambient conditions turned into a blue paste after approximate a month.

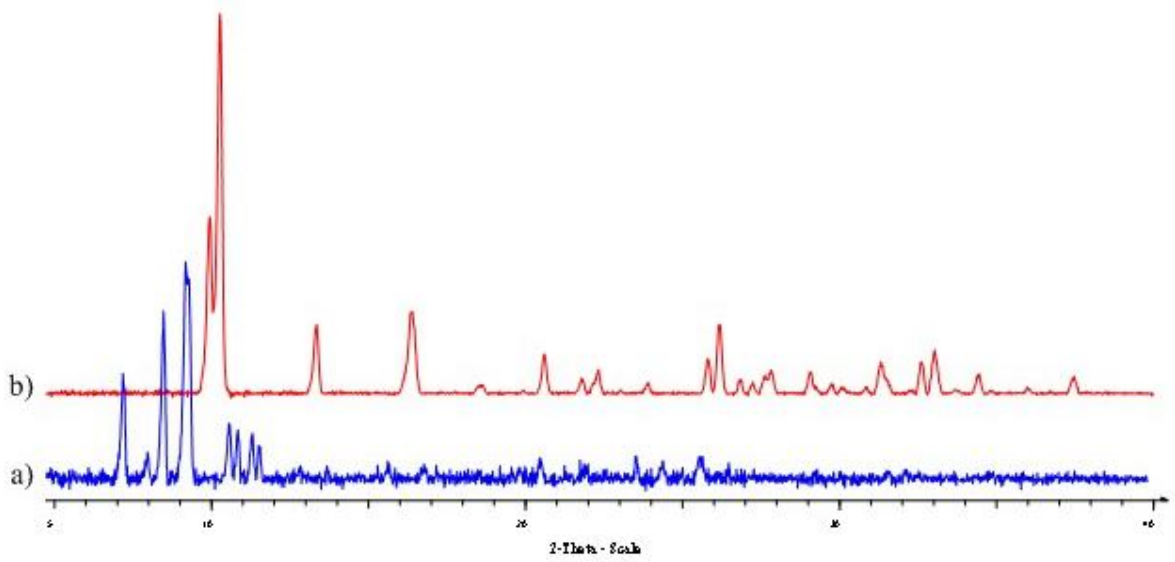

*Figure 5-32. The experimental PXRD pattern for the DMF-saturated sample of **3** harvested after: a) one week and b) three weeks.*

5.5. Summary and Future work

Three new dimethylammonium copper(II) sulfates have been prepared, in which the anionic copper(II) sulfate aggregates or chains are charge balanced by $NMe_2H_2^+$ cations derived either from the hydrolysis of the DMF solvent or from the addition of $[NMe_2H_2]Cl$.

These compounds have been crystallographically characterised as $(NMe_2H_2)_4[Cu_6O_2(SO_4)_6(DMF)_4]$ **1**, $(NMe_2H_2)_4[Cu_6O_2(SO_4)_6(DMF)_2]$ **2** and $(NMe_2H_2)[Cu_2(OH)(SO_4)_2(H_2O)_2]$ **3**. Compounds **1** and **2**, contain the unusual $Cu_6O_2(SO_4)_6$ core with the only previous example observed in the rare copper(II) sulfate mineral fedotovite, $K_2Cu_3O(SO_4)_3$.[17] In compound **2**, in contrast to **1**, the $Cu_6O_2(SO_4)_6$ aggregates are connected to form chains. In compound **3,** triangular $Cu_3(\mu_3\text{-}OH)(\mu_3\text{-}SO_4)$ units are linked through copper(II) centres to form tapes.

Compounds **1-3** are all moisture-sensitive as indicated by their colour and aspect changes and from PXRD investigations, with **1** and **2** undergoing rapidly structural changes while **3** changed slowly into a paste.

Magnetic measurements revealed that **1** and **3** are both spin-canting metamagnetic systems. Field-induced responses were observed below 5 K, with the critical field indicating metamagnetic behaviour from antiferromagnetic to ferromagnetic equal to 110 Oe for both compounds.

A thorough investigation of these products in a controlled-humidity environment could provide a better understanding of the structural changes undergone by these compounds.

5.6. References

[1] C. Papatriantafyllopoulou, E. Manessi-Zoupa, A. Escuer, S. P. Perlepes, Inorganica Chimica Acta 2009, 362, 634.

[2] J. J. Pluth, I. M. Steele, A. R. Kampf, D. I. Green, Mineral. Mag. 2005, 69, 973.

[3] P. Orlandi, E. Bonaccorsi, Can. Mineral. 2009, 47, 143.

[4] F. C. Hawthorne, R. B. Ferguson, Acta Crystallographica Section B 1975, 31, 1753.

[5] D. Jančula, B. Maršálek, Chemosphere 2011, 85, 1415.

[6] A. Reddy, E. L. Ponder, B. Fried, Journal of Parasitology 2004, 90, 1332.

[7] A. R. Jacobson, S. Dousset, N. Guichard, P. Baveye, F. Andreux, Environmental Pollution 2005, 138, 250.

[8] J. Wiese, P. Harris, D. Bradshaw, Minerals Engineering 2011, 24, 995.

[9] B. F. Abrahams, C. T. Abrahams, M. G. Haywood, T. A. Hudson, B. Moubaraki, K. S. Murray, R. Robson, Dalton Transactions 2012, 41, 4091.

[10] W. Zhao, J. Fan, Y. Song, H. Kawaguchi, T.-a. Okamura, W.-Y. Sun, N. Ueyama, Dalton Transactions 2005, 1509.

[11] J. Lin, D.-W. Guo, Y.-Q. Tian, Crystal Growth & Design 2008, 8, 4571.

[12] G. Li, Y. Xing, S. Song, N. Xu, X. Liu, Z. Su, Journal of Solid State Chemistry 2008, 181, 2406.

[13] A. D. Burrows, K. Cassar, R. M. W. Friend, M. F. Mahon, S. P. Rigby, J. E. Warren, CrystEngComm 2005, 7, 548.

[14] F. C. Hawthorne, L. A. Groat, R. R. Eby, The Canadian Mineralogist 1989, 27, 205.

[15] J. J. Finney, T. Araki, Nature 1963, 197, 70.

[16] S. Vilminot, M. Richard-Plouet, G. André, D. Swierczynski, M. Guillot, F. Bourée-Vigneron, M. Drillon, Journal of Solid State Chemistry 2003, 170, 255.

[17] G. L. Starova, S. K. Filatov, V. S. Fundamensky, L. P. Vergasova, Mineralogical Magazine 1991, 55, 613.

[18] A. W. Addison, T. N. Rao, J. Reedijk, J. van Rijn, G. C. Verschoor, J. Chem. Soc., Dalton Trans. 1984, 1349.

[19] S. Ferrer, F. Lloret, E. Pardo, J. M. Clemente-Juan, M. Liu-González, S. García-Granda, Inorganic Chemistry 2012, 51, 985.

[20] R. Beckett, B. F. Hoskins, Journal of the Chemical Society, Dalton Transactions 1972, 0, 291.

[21] J. Wu, H.-W. Hou, Y.-X. Guo, Y.-T. Fan, X. Wang, European Journal of Inorganic Chemistry 2009, 2009, 2796.

[22] F. Pan, J. Wu, H. Hou, Y. Fan, Crystal Growth & Design 2010, 10, 3835.

[23] S. Vilminot, G. André, F. Bourée-Vigneron, M. Richard-Plouet, M. Kurmoo, Inorganic Chemistry 2007, 46, 10079.

[24] L. Deakin, A. M. Arif, J. S. Miller, Inorganic Chemistry 1999, 38, 5072.

[25] D. Kong, Y. Li, J. H. Ross Jr, A. Clearfield, Chemical Communications 2003, 1720.

[26] Y.-S. Ma, Y. Song, W.-X. Du, Y.-Z. Li, L.-M. Zheng, Dalton Transactions 2006, 3228.

[27] A. Aijaz, E. C. Sañudo, P. K. Bharadwaj, Inorganica Chimica Acta 2009, 362, 4246.

[28] F. Cariati, G. Micera, A. Scozzafava, G. Minghetti, G. Banditelli, Inorganic Chemistry 1982, 21, 3843.

[29] D.-F. Weng, Z.-M. Wang, S. Gao, Chem. Soc. Rev. 2011, 40, 3157.

[30] W. Kraus, G. Nolze, Federal Institute for Materials Research and Testing Rudower Chaussee 5, Berlin, Germany, 1999.

[31] G. Sheldrick, Acta Cryst. A 2008, 64, 112.